

**FAKULTA MATEMATIKY, FYZIKY A INFORMATIKY  
UNIVERZITA KOMENSKÉHO V BRATISLAVE  
&  
ÉCOLE DOCTORALE SCIENCES PHYSIQUES ET DE L'INGÉNIEUR  
UNIVERSITÉ DE BORDEAUX**

**SuperNEMO Experiment: Study of Systematic  
Uncertainties of Track Reconstruction and Energy  
Calibration. Evaluation of Sensitivity to  $0\nu\beta\beta$  with  
Emission of Majoron for  $^{82}\text{Se}$ .**

Dissertation

Bordeaux, 2018

MGR. MIROSLAV MACKO



JADROVÁ A SUBJADROVÁ FYZIKA  
KATEDRA JADROVEJ FYZIKY A BIOFYZIKY  
FAKULTA MATEMATIKY, FYZIKY A INFORMATIKY  
UNIVERZITA KOMENSKÉHO V BRATISLAVE

université  
de BORDEAUX

ASTROPHYSIQUE, PLASMAS, NUCLÉAIRE  
ÉCOLE DOCTORALE SCIENCES PHYSIQUES  
ET DE L'INGÉNIEUR  
UNIVERSITÉ DE BORDEAUX

---

**SuperNEMO Experiment: Study of Systematic  
Uncertainties of Track Reconstruction and Energy  
Calibration. Evaluation of Sensitivity to  $0\nu\beta\beta$  with  
Emission of Majoron for  $^{82}\text{Se}$ .**

Dissertation

MGR. MIROSLAV MACKO

---

**Supervisors:** doc. Ing. Ivan Štekl, CSc. and Dr. Fabrice Piquemal  
Bordeaux, 2018



## ZADANIE ZÁVEREČNEJ PRÁCE

**Meno a priezvisko študenta:** Mgr. Miroslav Macko  
**Študijný program:** jadrová a subjadrová fyzika (Jednoodborové štúdium, doktorandské III. st., denná forma)  
**Študijný odbor:** jadrová a subjadrová fyzika  
**Typ záverečnej práce:** dizertačná  
**Jazyk záverečnej práce:** anglický  
**Sekundárny jazyk:** slovenský

**Názov:** SuperNEMO Experiment: Study of Systematic Uncertainties of Track Reconstruction and Energy Calibration. Evaluation of Sensitivity to  $0\nu\beta\beta$  with Emission of Majoron for  $^{82}\text{Se}$   
*SuperNEMO experiment: Štúdiá systematických neistôt rekonštrukcie dráh a energetickej kalibrácie. Odhad citlivosti detektora na  $0\nu\beta\beta$  s emisiou Majorónu pre  $^{82}\text{Se}$*

**Anotácia:** V súčasnej fyzike sa veľká pozornosť venuje problematike neutrín (jednoduchý beta rozpad, dvojitý beta rozpad, oscilácie neutrín). Meranie dvojitého beta rozpadu je dôležité pre ďalší rozvoj teórie jadra (výpočty jadrových maticových elementov) a pre stanovenie povahy neutrína (Majoranovská alebo Diracovská častica). V súčasnej dobe existuje niekoľko experimentálnych prístupov v oblasti týchto meraní (napr. [1]). Jeden z experimentálnych prístupov bol použitý v detektore NEMO-3 (napr. [2]), kde bola tenká fólia študovaného izotopu obklopená dráhovým detektorom (určenie dráhy častíc) a kalorimetrom zo scintilačných detektorov (určenie energie častíc). Celý detektor bol tienový proti časticiam gama a neutrónom. Experiment SuperNEMO je založený na rovnakom princípe ako NEMO-3 a jeho hlavným cieľom je meranie  $0\nu\beta\beta$  v  $^{82}\text{Se}$  na úrovni času polpremeny  $1 \times 10^{26}$  rokov. To zodpovedá efektívnej hmotnosti neutrína na úrovni 0,04 – 0,1 eV. Detektor SuperNEMO sa bude skladať z 20 identických modulov, pričom každý z nich bude obsahovať 5 kg obohateného izotopu. V súčasnej dobe prebieha výstavba prvého modulu v podzemnom laboratóriu v Modane (LSM) a jeho úplne dokončenie sa očakáva v roku 2019.

**Cieľ:** - Zoznámte sa s celkovou konštrukciou detektora SuperNEMO a fyzikálnymi procesmi, ktoré ním budú detekované.

- Spolupracujte pri výstavbe a testovaní prvého modulu detektora SuperNEMO (demonštrátor) v podzemnom laboratóriu LSM (Francúzsko). Zamerajte sa predovšetkým na dve oblasti: i) príprava a testovanie scintilačných, optických modulov pre hlavný kalorimeter demonštrátora s cieľom optimalizácie energetického rozlíšenia detektora a ii) vykonanie meraní kalibračných zdrojov  $^{207}\text{Bi}$ , s cieľom určenia polohy zdroja pomocou pixelových detektorov a ich aktivít pomocou HPGe detektorov.

- Zoznámte sa so simuláciami Monte Carlo a softvérom pre spracovanie nameraných dát pre detektor SuperNEMO (Falaise), s dôrazom na pochopenie



Univerzita Komenského v Bratislave  
Fakulta matematiky, fyziky a informatiky

---

jeho funkcionality, vlastností a spôsobom spracovania experimentálnych dát. Pri simuláciách sa zamerajte na dve oblasti: i) presnosť určenia miesta rozpadu vo fólii  $^{82}\text{Se}$  v závislosti na parametroch akými sú magnetické pole, energia či smery výletu elektrónov; ii) optimalizáciu neutrónového tienenia pre SuperNEMO demonštrátor za použitia reálneho spektra neutrónov v podzemnom laboratóriu LSM, ako aj odhad počtu zachytených neutrónov v materiáloch detektora.

- Na základe výsledkov simulácií pozadia (predovšetkým z  $^{208}\text{Tl}$  a  $^{214}\text{Bi}$ ), detekčnej účinnosti a vlastností demonštrátora (rekonštrukcie dráh elektrónov, energetické rozlíšenie kalorimetra) stanovte experimentálne limity pre čas polpřemeny  $0\nu\beta\beta$  s emisiou jedného alebo dvoch Majorónov.

**Literatúra:** [1] F.T. Avignone III, S.R. Elliot a J. Engel, Rev. Mod. Phys. 80 (2008) 481.  
[2] R. Arnold et al., Nucl. Inst. Meth. A 536 (2005) 79.

**Školiteľ:** doc. Ing. Ivan Štekl, CSc.  
**Školiteľ:** Dr. Fabrice Piquemal  
**Konzultant:** Mgr. Rastislav Hodák, PhD.  
**Katedra:** FMFI.KJFB - Katedra jadrovej fyziky a biofyziky  
**Vedúci katedry:** prof. RNDr. Stanislav Tokár, DrSc.  
**Dátum zadania:** 02.03.2015

**Dátum schválenia:** 29.10.2018

prof. RNDr. Jozef Masarik, DrSc.  
garant študijného programu

.....  
študent

.....  
školiteľ



## THESIS ASSIGNMENT

**Name and Surname:** Mgr. Miroslav Macko  
**Study programme:** Nuclear and Subnuclear Physics (Single degree study, Ph.D. III. deg., full time form)  
**Field of Study:** Nuclear And Subnuclear Physics  
**Type of Thesis:** Dissertation thesis  
**Language of Thesis:** English  
**Secondary language:** Slovak

**Title:** SuperNEMO Experiment: Study of Systematic Uncertainties of Track Reconstruction and Energy Calibration. Evaluation of Sensitivity to  $0\nu\beta\beta$  with Emission of Majoron for  $^{82}\text{Se}$

**Annotation:** In contemporary physics large attention is paid to problematics of neutrinos (single beta decay, double beta decay, neutrino oscillations). Measurement of double beta decay is important for further development of nuclear theory (calculations of nuclear matrix elements) and for specification of nature of neutrino (Majorana or Dirac particle). Currently, several different experimental approaches are applied in the field (e.g. [1]). NEMO-3 is such an example (e.g. [2]). In NEMO-3, thin foil made of studied isotope was surrounded by tracking detector (information about particle tracks) and by calorimeter made of scintillating detectors (information about particle energy). The detector was shielded against gamma particles and neutrons. SuperNEMO experiment is based on the same principle and its main goal is to perform a measurement of half-life of  $0\nu\beta\beta$  in  $^{82}\text{Se}$  at the level of  $1 \times 10^{26}$  years. It corresponds to an effective neutrino mass on the level of  $0.04 - 0.1$  eV. SuperNEMO detector will be composed of 20 identical modules, each of them will contain 5 kg of enriched isotope. Currently, the construction of the first module in underground laboratory in Modane (LSM) is ongoing. Its finalisation is scheduled for year 2019.

**Aim:** - Familiarize with the construction of SuperNEMO detector and with the physical processes which it is capable to detect.

- Contribute to the construction and testing of the first SuperNEMO module (demonstrator) in underground laboratory LSM (France). Focus mainly on two tasks: i) assembly and testing of scintillating optical modules for the demonstrator's main calorimeter with the focus on the optimisation of detector's energy resolution and ii) measurements of  $^{207}\text{Bi}$  calibration sources with the main focus on the specification of the position of the source droplet (using pixel detectors) and the measurements of their activities (using HPGe detectors).

- Familiarize with the Monte Carlo simulations and with the software for the analysis of data from SuperNEMO (Falaise), with the stress on the understanding of its functionalities, properties and the method of data processing. Within the simulations, focus on two tasks: i) evaluation of precision of decay position in  $^{82}\text{Se}$  foil in dependence on parameters such as magnetic



Comenius University in Bratislava  
Faculty of Mathematics, Physics and Informatics

---

field, energy of electrons or the direction of electron emission; ii) optimisation of neutron shielding for SuperNEMO demonstrator by using realistic neutron spectrum in underground laboratory LSM, as well as the estimation of captured neutrons in detector materials.

- Based on the simulation results of background processes (mainly  $^{208}\text{Tl}$  and  $^{214}\text{Bi}$ ), detection efficiencies and detector parameters (particle track reconstruction, energy resolution of calorimeter), estimate experimental limits for half-lives of  $0\nu\beta\beta$  with emission of one or two Majorons.

**Literature:** [1] F.T. Avignone III, S.R. Elliot a J. Engel, Rev. Mod. Phys. 80 (2008) 481.  
[2] R. Arnold et al., Nucl. Inst. Meth. A 536 (2005) 79.

**Tutor:** doc. Ing. Ivan Štekl, CSc.

**Tutor:** Dr. Fabrice Piquemal

**Consultant:** Mgr. Rastislav Hodák, PhD.

**Department:** FMFI.KJFB - Department of Nuclear Physics and Biophysics

**Head of department:** prof. RNDr. Stanislav Tokár, DrSc.

**Assigned:** 02.03.2015

**Approved:** 29.10.2018                      prof. RNDr. Jozef Masarik, DrSc.  
Guarantor of Study Programme

.....  
Student

.....  
Tutor

# Čestné prehlásenie

Čestne prehlasujem, že dizertačnú prácu som vypracoval samostatne, na základe konzultácií s vedúcimi dizertačnej práce a štúdia odbornej literatúry, ktorej úplný prehľad je uvedený v zozname použitej literatúry.

.....

# Acknowledgments

First of all, I would like to thank my both supervisors Ivan Štekl and Fabrice Piquemal for all the discussions, guidance and help during these three years. A collaboration with you was truly beneficial for development of my skills and abilities in physics. At the same time, I would like to express my gratitude to my consultant Rastislav Hodák who is familiar with all the smaller or bigger issues I was facing during my Ph.D. studies and was always there prepared to help with advise or to offer helping hand. I would like to thank also to my (as I informally called him) "shadow supervisor" Fedor Šimkovic. I appreciate all the support he provided to me whenever I needed some help.

Furthermore, I want to express my "remerciements" to the neutrino team in CENBG, namely Cristine Marquet, Frédéric Perrot, Emmanuel Chauveau, Cédric Cerna, Arnaud Huber and Jean Jouve for introducing me into their institute, a cosy château, and for hosting me there during my three half-year stays. It was my pleasure to spend that time in Bordeaux. Special thanks go to Bertram Blank who allowed me to use his detector for measurements of absolute activities of calibration sources. I want to thank as well to my friends on a Czech side, except for already mentioned Rastislav Hodák, also to Lukáš Fajt, Adam Smetana, Jakub Vlášek and Ekaterina Rukhadze for helping me to accomodate myself at my new home institute. I wish to acknowledge staff of LSM, in particular Guillaume Warot for offering me helping hand with the calibration source measurements which I performed in the underground laboratory.

Moja veľmi špeciálna vďaka ide takisto administratíve na FMFI UK a ÚTEF ČVUT, za oboje spomeniem hlavne Helenu Patrikovú, Martinu Vanišovou či Soňu Štichovú. Bez ich neustáleho trpezlivého naprávania mojich administratívnych prešľapov by som tento administratívne náročný model dvojitého doktorátu asi ani nezvládol.

Nakoniec by som chcel poďakovať tým pre mňa najdôležitejším ľuďom, ktorými sú moja mama Anna Macková, sestry Betka a Mária Mackové, babka Mária Macková a moja najmilšia Oleksandra Vesel'ská. Vašu bezhraničnú podporu som neustále cítil počas týchto rokov a hlavne v závere bola jedným z kľúčových faktorov, ktoré mi dodali silu nevzdať sa.

V úplnom závere by som chcel venovať zopár riadkov svojmu otcovi Mariánovi Mackovi. Tým čím som sa stal, je minimálne z polovice tvoja obrovská zásluha. Bol si vždy mojím (nielen) intelektuálnym vzorom a poradcom na všetko. "Niektorí ľudia sa nikdy nič nenaučia, pretože veľmi skoro všetkému rozumejú," túto tvoju zásadu si vždy opakujem a stala sa mi dôležitým oporným bodom v mojej profesionálnej kariére. Ďakujem ti za tvoj humor, intelekt a oporu. Táto práca je venovaná práve tebe.





*Venované môjmu ocinovi*  
*Dedicated to my Dad*  
*Dédié à mon papa*

# SuperNEMO experiment: Štúdia systematických neistôt rekonštrukcie dráh a energetickej kalibrácie. Odhad citlivosti detektora na $0\nu\beta\beta$ s emisiou Majorónu pre $^{82}\text{Se}$ .

## Abstrakt

Predkladaná dizertačná práca je zložená z projektov rôzneho charakteru, na ktorých som pracoval vo fáze výstavby SuperNEMO demonštrátora v období rokov 2015-2018.

Experiment SuperNEMO, umiestnený v podzemnom laboratóriu LSM, je zameraný na hľadanie  $0\nu\beta\beta$  v  $^{82}\text{Se}$ . Experiment je založený na technológii rekonštrukcie dráh elektrónov vznikajúcich v rozpade. Tento prístup je jedinečný v oblasti  $0\nu\beta\beta$  experimentov. Rekonštrukcia topológie udalostí je silným nástrojom na potlačenie pozad'ovej aktivity vyskytujúcej sa v laboratóriu, ako aj v konštrukčných materiáloch detektora.

Časť práce je venovaná experimentálnym úlohám. Zúčastnil som sa na konštrukcii optických modulov - súčasti hlavného kalorimetra. Práca obsahuje výsledky prípravy a testovania 520 optických modulov, a takisto výsledky kompletného mapovania kalibračných  $^{207}\text{Bi}$  zdrojov vykonaného za pomoci pixelových detektorov. V tejto časti sú odprezentované aj výsledky merania ich aktivít za pomoci HPGe detektorov. Štúdia zohrávala kľúčovú úlohu pri výbere 42 zdrojov, ktoré boli nainštalované do prvého SuperNEMO modulu, do demonštrátora, a budú použité na jeho energetickú kalibráciu.

V roku 2018 som takisto vypracoval štúdie neutrónového tienenia. Očakávané toky neutrónov za tienením boli odhadnuté pomocou Monte Carlo simulácie. Kvalita odtienenia neutrónov z realistického pozad'ového spektra, nameraného v LSM, bola skúmaná pre tri rôzne materiály rôznych hrúbok. Výsledky ukázali, že neutrónový tok prechádzajúci tienením bude primárne zachytávaný na komponentoch detektora zhotoveného zo železa. V rámci štúdie neutrónového tienenia je takisto diskutovaný problém simulácie deexcitačných gama kaskád, produkovaných jadrami, po záchyťte termálnych neutrónov. Štandardné simulačné softvérové balíčky využívajú generátory gama kaskád nepostačujúce pre potreby štúdie. Navrhol som nový generátor, ktorý je schopný tieto problémy vyriešiť. Funkčnosť generátora bola preukázaná na príklade jednoduchého systému.

Okrem štandardného  $0\nu\beta\beta$  je SuperNEMO experiment schopný hľadať aj jeho exotickjšie verzie. V práci sa nachádzajú odhady limitov času polpremeny  $0\nu\beta\beta$  s emisiou jedného alebo dvoch Majorónov, dosiahnuteľné SuperNEMO demonštrátorom. Tieto limity sú študované v závislosti na aktivite izotopov  $^{208}\text{Tl}$  a  $^{214}\text{Bi}$ , ktoré kontaminujú zdrojovú  $^{82}\text{Se}$  fóliu. Bola odhadnutá doba merania, za ktorú bude SuperNEMO schopný vylepšiť limity času polpremeny, pre dva spomenuté rozpadové módy, dosiahnutých experimentom NEMO-3.

**Kľúčové slová:** bezneutrínový dvojitý beta rozpad, SuperNEMO, Majorón, simulácie, hmotnosť neutrína, neutrónové tienenie, kalibračný systém, optický modul, systematické neistoty

# SuperNEMO Experiment: Study of Systematic Uncertainties of Track Reconstruction and Energy Calibration. Evaluation of Sensitivity to $0\nu\beta\beta$ with Emission of Majoron for $^{82}\text{Se}$ .

## Abstract

Presented thesis is composed of variety of projects which I performed within the construction phase of SuperNEMO demonstrator during the period 2015-2018.

SuperNEMO experiment, located at underground laboratory LSM, is designed to search for  $0\nu\beta\beta$  of  $^{82}\text{Se}$ . Its technology, which takes advantage of particle tracking, is unique in the field of double beta decay experiments. Event topology reconstruction is powerful tool for suppression of naturally-occurring background radiation.

Part of the thesis is dedicated to experimental work. I took part in assembly and testing of optical modules - the integral part of SuperNEMO calorimeter. Results of tests after assembly of 520 optical modules are presented in the thesis. Furthermore, I present results of complete mapping of  $^{207}\text{Bi}$  sources performed using pixel detectors. I also present precise measurements of their activities for which I used HPGe detectors. These  $^{207}\text{Bi}$  sources will be used for calibration of the calorimeter. Study played a key role in choice of 42 sources which were installed in the demonstrator and will take part in calibration of the demonstrator.

In 2018, I also performed simulations of neutron shielding. Variety of shielding materials with different thicknesses were (in the simulation) exposed to realistic neutron spectrum from LSM and the fluxes behind the shielding were estimated. It was shown that the parts of the detector made of Iron should be expected to capture vast majority of neutrons passing the shielding. I also discuss a problem with simulation of deexcitation gamma radiation, emitted after thermal neutron capture, which arises in standard software packages. I proposed new extended generator capable to resolve the problem and demonstrate the concept in analytically solvable example.

Along with standard  $0\nu\beta\beta$ , SuperNEMO will be capable of searching for more exotic modes of the decay. In the thesis, I present possible half-life limits achievable by SuperNEMO for  $0\nu\beta\beta$  with emission of one or two Majorons. The study is performed as a function of activity of internal contamination from  $^{208}\text{Tl}$  and  $^{214}\text{Bi}$  isotopes. Measurement period after which SuperNEMO should be able to improve half-life limits of NEMO-3 (in case the decay would not be observed) are estimated.

**Keywords:** Neutrino-less Double Beta Decay, SuperNEMO, Majoron, simulations, neutrino mass, neutron shielding, calibration system, optical module, systematic uncertainties

# Expérience SuperNEMO: Études des incertitudes systématiques sur la reconstruction de traces et sur l'étalonnage en énergie. Evaluation de la sensibilité de la $0\nu\beta\beta$ avec émission de Majoron pour le $^{82}\text{Se}$ .

## Résumé

La thèse présentée est composée de divers projets que j'ai réalisés au cours de la phase de construction du démonstrateur SuperNEMO pendant la période 2015-2018.

L'expérience SuperNEMO, située dans le laboratoire souterrain LSM, est conçue pour rechercher  $0\nu\beta\beta$  de  $^{82}\text{Se}$ . Sa technologie, qui tire parti du suivi des particules, est unique dans le domaine des expériences de double désintégration bêta. La reconstruction de la topologie des événements est un outil puissant pour la suppression de fond naturel.

Une partie de la thèse est consacrée à un travail expérimental. J'ai participé à la préparation de modules optiques, partie intégrante du calorimètre SuperNEMO. Les résultats de la préparation et des tests de 520 modules optiques sont présentés dans la thèse. En outre, je présente les résultats de la cartographie complète des sources  $^{207}\text{Bi}$  effectuée à l'aide de pixel détecteurs. Je présente également des mesures précises de leurs activités pour lesquelles j'ai utilisé des détecteurs HPGe. Ces sources  $^{207}\text{Bi}$  seront utilisées pour l'étalonnage du calorimètre. L'étude a joué un rôle clé dans le choix des 42 sources qui participeront à l'étalonnage du démonstrateur.

En 2018, j'ai également effectué les simulations du blindage contre les neutrons. Différents matériaux de blindage d'épaisseurs différentes ont été (dans la simulation) exposés à un spectre de neutrons réaliste provenant du LSM et les flux situés derrière le blindage ont été estimés. Il a été démontré que les parties du détecteur en fer devraient capturer la grande majorité des neutrons passant le blindage. Je discute également un problème de simulation des rayonnements gamma de désexcitation après capture de neutrons thermiques, apparaissant dans les logiciels standard. Je propose un nouveau générateur étendu capable de résoudre le problème et de démontrer le concept dans un exemple analytiquement résolu.

Avec le standard  $0\nu\beta\beta$ , SuperNEMO sera capable de rechercher des modes plus exotiques de la décroissance. Dans cette thèse, je présente les limites de demi-vie possibles que SuperNEMO peut atteindre pour  $0\nu\beta\beta$  avec l'émission d'un ou deux Majorons. L'étude est réalisée en fonction de l'activité de contamination interne par les isotopes  $^{208}\text{Tl}$  et  $^{214}\text{Bi}$ . La période de mesure après laquelle SuperNEMO devrait pouvoir améliorer les limites de demi-vie de NEMO-3 (au cas où la décroissance ne serait pas observée) est estimée.

**Mots-clés:** décroissance double beta bêta sans émission des neutrino, SuperNEMO, Majoron, simulations, la masse des neutrinos, blindage contre les neutrons, système d'étalonnage, module optique, incertitudes systématiques

# Contents

<b>List of Abbreviations</b>		<b>4</b>
<b>Introduction</b>		<b>6</b>
<b>1 Neutrino Physics and Its History</b>		<b>10</b>
1.1	Neutrino Postulate . . . . .	10
1.2	Discovery of Neutrino . . . . .	11
1.3	Neutrinos in Standard Model . . . . .	11
1.3.1	Neutrino Flavours . . . . .	13
1.4	Neutrinos Beyond the Standard Model . . . . .	13
1.4.1	Solar Neutrino Problem . . . . .	13
1.4.2	Neutrino Mixing and Oscillations . . . . .	15
1.4.3	Supernova Neutrinos . . . . .	16
1.4.4	Neutrino Hierarchies . . . . .	17
1.4.5	Neutrino Masses and Their Nature . . . . .	17
1.5	Double Beta-Decay Processes . . . . .	19
1.5.1	Two-Neutrino Double Beta-Decay . . . . .	19
1.5.2	Neutrino-Less Double Beta-Decay . . . . .	20
1.5.3	Nuclear Matrix Elements . . . . .	21
1.5.4	Experimental Status of Double Beta-Decay . . . . .	22
<b>2 SuperNEMO Experiment</b>		<b>28</b>
2.1	Laboratoire Souterrain de Modane . . . . .	28
2.2	Description of the Detector . . . . .	29
2.2.1	$^{82}\text{Se}$ Source Foils . . . . .	30
2.2.2	Tracking Detector . . . . .	31
2.2.3	Calorimeters . . . . .	31
2.2.4	Status of the Demonstrator . . . . .	33
2.3	Construction of Main Calorimeter Walls . . . . .	33
2.3.1	Optical Module Production Procedure . . . . .	33
2.3.2	Optical Module Resolution Test and Finalization . . . . .	34
<b>3 Measurements of <math>^{207}\text{Bi}</math> Calibration Sources</b>		<b>37</b>
3.1	SuperNEMO Calibration System . . . . .	37
3.1.1	Automatic Calibration Source Deployment System . . . . .	37
3.1.2	Description of Calibration Sources . . . . .	38

3.2	Mapping of $^{207}\text{Bi}$ Deposition Distribution in Calibration Sources . . . . .	39
3.2.1	Timepix Pixel Detectors . . . . .	40
3.2.2	Detector Energy Calibrations . . . . .	41
3.2.3	Test Measurements . . . . .	45
3.2.3.1	Data Analysis . . . . .	45
3.2.3.2	Study of the Energy Spectra . . . . .	47
3.2.4	Detector Spatial Calibrations . . . . .	49
3.2.4.1	Source Placement Convention . . . . .	54
3.2.5	Results . . . . .	55
3.2.5.1	Uncertainty Estimation . . . . .	57
3.3	Measurements of Source Activities . . . . .	58
3.3.1	Relative Measurements . . . . .	59
3.3.1.1	First Phase . . . . .	61
3.3.1.2	Second Phase . . . . .	61
3.3.1.3	Distribution of Calibration Sources in SuperNEMO Detector . . . . .	62
3.3.2	Absolute Measurements . . . . .	63
3.3.2.1	Measurements of Source Depths . . . . .	64
3.3.2.2	Activity Measurements and Analysis . . . . .	66
3.3.2.3	Discrepancy Between Results . . . . .	68
3.4	Conclusions . . . . .	71
<b>4</b>	<b>Simulations of SuperNEMO Neutron Shielding</b>	<b>72</b>
4.1	Simulations of the Shielding . . . . .	73
4.1.1	Phase One: Neutrons Passing Through Shielding . . . . .	74
4.1.2	Phase Two: Mapping of Demonstrator . . . . .	79
4.2	Problem of Neutron Capture Generators . . . . .	89
4.2.1	Thermal Neutrons in Geant4 . . . . .	90
4.2.2	Stair Generator . . . . .	92
4.2.3	Possible Solution . . . . .	94
4.2.3.1	Naming Convention . . . . .	95
4.2.3.2	Description of Generator . . . . .	96
4.2.3.3	Solution for a System with Two Intermediate States . . . . .	99
4.2.3.4	Proof of the Concept by Analytical Solution . . . . .	102
4.3	Conclusions . . . . .	106
<b>5</b>	<b>Estimation of Sensitivity of SuperNEMO to <math>0\nu\beta\beta</math> with Majoron Emission</b>	<b>107</b>
5.1	Calculation of Half-Life of Rare Processes . . . . .	107
5.2	Statistical Nature of Observed Counts . . . . .	110
5.2.1	Experiments Without Background . . . . .	110
5.2.2	Experiments with Background - Collapse of Classical Method . . . . .	112
5.3	Feldman-Cousins Method . . . . .	112
5.3.1	Ordering Principle . . . . .	115
5.3.1.1	Likelihood Ratio Ordering Principle . . . . .	116
5.3.1.2	Numerical Artefacts . . . . .	117
5.3.2	Experiments with no Discovery . . . . .	118
5.4	Calculation of Half-Life Limits . . . . .	120
5.4.1	Calculation of Detection Efficiencies $\epsilon$ . . . . .	120
5.4.2	Calculation of Signal-to-Background Ratios . . . . .	121
5.4.3	Sensitivity Results . . . . .	126

5.5 Conclusions . . . . .	128
<b>Conclusions</b>	<b>132</b>
<b>A Complete Results of Measurements of <math>^{207}\text{Bi}</math> Calibration Sources</b>	<b>134</b>
A.1 Mapping Results . . . . .	134
A.2 Results of Activity Measurements . . . . .	137
A.2.1 Results of Relative Activity Measurements . . . . .	137
A.2.2 Results of Absolute Activity Measurements . . . . .	139
<b>B Numerical Values of Half-Life Limits for <math>0\nu\beta\beta\chi^0</math> and <math>0\nu\beta\beta\chi^0\chi^0</math></b>	<b>142</b>
<b>Bibliography</b>	<b>145</b>

# List of Abbreviations

**BSM** - (physics) **beyond Standard Model**  
**CAT** - **cellular automaton tracker**  
**CD** (bank) - **calibrated data**  
**CENBG** - **Centre Etudes Nucléaires de Bordeaux Gradignan**  
**CERN** - **Conseil Européen pour la Recherche Nucléaire**  
**CKM** (matrix) - **Cabibbo–Kobayashi–Maskawa**  
**CL** - **Confidence Level**  
**CTU** - **Czech Technical University**  
**DONUT** - **Direct Observation of the Nu Tau**  
**EC** - **electron capture**  
**FWHM** - **full width at half maximum**  
**GERDA** - **Germanium Detection Array**  
**GID** - **geometry identifier**  
**HdM** - **Heidelberg - Moscow (experiment)**  
**HWHM** - **half width at half maximum**  
**IBM** - **Interacting Boson Model**  
**IEAP** - **Institute of Experimental and Applied Physics**  
**IGEX** - **International Germanium Experiment**  
**IMB** (detector) - **Irvine–Michigan–Brookhaven**  
**ISM** - **Interacting Nuclear Shell Model**  
**ITEP** (Moscow) - **Institute for Theoretical and Experimental Physics**  
**KamLAND-Zen** (experiment) - **KamLAND-Zero Neutrino**  
**LAPP** - **Laboratoire d'Annecy-le-Vieux de Physique des Particules**  
**LEGEND** - **Large Enriched Germanium Experiment for Neutrinoless Decay**  
**LEP** - **Large Electron–Positron Collider**  
**LNGS** **Laboratori Nazionali del Gran Sasso**  
**LSM** - **Laboratoire Souterrain de Modane**  
**LUCIFER** - **Low-background Underground Cryogenic Installation For Elusive Rates**  
**MSSL** - **Mullard Space Science Laboratory**  
**MSW** (effect) - **Mikheyev–Smirnov–Wolfenstein**  
**m.w.e.** - **meter water equivalent**  
**NEMO** - **Neutrino Ettore Majorana Observatory**  
**PMNS** (matrix) - **Pontecorvo–Maki–Nakagawa–Sakata**  
**PMT** - **photomultiplier tube**  
**PTD** (bank) - **particle track data**



**PS** - polystyrene  
**QED** - Quantum Electrodynamics  
**QRPA** - Quasiparticle Random Phase Approximation  
**RMS** - root mean square  
**ROI** - region of interest  
**SAGE** - The Soviet–American Gallium Experiment  
**SD** (bank) - simulated data  
**SDBDC** - Standard Double Beta Decay Reconstruction Criteria  
**SLAC** - Stanford Linear Accelerator Center  
**SM** - Standard Model (of elementary particles)  
**SNO** - Sudbury Neutrino Observatory  
**SNU** - solar neutrino unit  
**SSM** - Standard Solar Model  
**ToT** - Time over Treshold  
**TPC** - time projection chamber  
**UCL** - University College London

# Introduction

The Standard Model of particle physics (SM) is a theory of fundamental particles and their interactions. Theoreticians in its Lagrangian formalism managed to merge Electromagnetic, Weak and Strong interactions into one theoretical framework. It precisely describes a vast range of interaction processes between quarks and leptons. It is undeniably the most precise theory of fundamental particles of contemporary physics. However, despite the enormous effort of brightest theoretical physicists supported by results of very complex and sophisticated experiments, the gravity was not yet included in unified theory of electroweak and strong interactions framework. Furthermore, the observations of kinematics of certain galaxies have shown mismatch of their dynamics and predictions based on our current knowledge. The difference is caused by presence of new, unknown type of particles - dark matter and unknown force - dark energy. The unsolved problem with quantization of gravity and existence of dark matter are typical examples of so-called physics beyond the Standard Model (BSM). The SM managed to describe all the currently known particles and in the past it even succeeded to predict existence of many of them. The SM, however, is "only" a low energy approximation of more general physics, thus, it is not surprising that the picture it offers is not complete.

Contemporary particle physics is currently hunting for a bridge between SM and BSM. Key to the success might be hidden in the physics of neutrinos. The SM describes the neutrinos as Weakly interacting massless particles. However, the observation of neutrino oscillations brings a modification to the SM. Although small, the mass of the neutrino is not zero. Unfortunately, the oscillation experiments, by their nature, cannot provide values of three neutrino masses, because their observables depend only on their squared mass differences.

In 1935, Maria Goeppert-Mayer proposed the existence of two-neutrino double beta decay ( $2\nu\beta\beta$ ). It is a nuclear transition when two neutrons bounded in nucleus are suddenly transformed into two protons emitting two electrons and two electron anti-neutrinos. This rare decay is typically overshadowed by its simpler version - the standard beta decay with significantly shorter half-life ( $\sim 900$  s). Nevertheless, there are examples of nuclei where single beta decay is either suppressed by spin selection rules or totally forbidden by law of energy conservation. With the half-life values of  $10^{18}$  years up to  $10^{21}$  years,  $2\nu\beta\beta$  is nowadays the rarest process observed by physicists.  $2\nu\beta\beta$  preserves lepton number. It is a process permitted by Standard Model. In 1939, it was Wendell H. Furry who proposed an idea of even rarer nuclear transition - Neutrino-less double beta decay ( $0\nu\beta\beta$ ). As the name suggests, the process is similar to  $2\nu\beta\beta$  with one important difference. In  $0\nu\beta\beta$ , no neutrinos are expected to be emitted. Such a process would violate lepton number conservation which is forbidden in SM.  $0\nu\beta\beta$  clearly represents a candidate for a process beyond

the SM. Furthermore, its half-life depends on so-called effective neutrino mass (this is not true for  $2\nu\beta\beta$ ) which is a value obtained from known superposition of neutrino mass eigenstates. Observation of  $0\nu\beta\beta$  would provide value of neutrino masses, which are currently still not known. However, the main importance of  $0\nu\beta\beta$  lies in the potential to discover a bridge from SM towards BSM physics.  $0\nu\beta\beta$  can exist only if neutrino would be its own antiparticle or, so-called Majorana particle. The concept of Majorana particle does not exist in Standard Model and would provide one of its possible extensions. To our present knowledge, no other process than  $0\nu\beta\beta$  could prove the Majorana character of neutrinos.

Despite the fact that  $0\nu\beta\beta$  could be an important first step beyond the SM, unfortunately, it was not yet observed. Enormous effort is invested into the search for this rare decay mode. Typically,  $0\nu\beta\beta$  experiments (as well as the other neutrino-related experiments) are placed underground, where omnipresent natural radioactivity is suppressed by several magnitudes. We can divide  $0\nu\beta\beta$  experiments into two basic categories.

Firstly, there are experiments in which the source isotope serves at the same time as detector. In this group, we can find Germanium detectors such as GERDA or MAJORANA which will soon merge into the biggest - ton scale  $0\nu\beta\beta$  experiment - LEGEND.  $^{76}\text{Ge}$  is one of the candidate isotopes for  $0\nu\beta\beta$  found in natural Ge. At the same time Germanium crystals serve as a HPGe detectors. In the past, it was Heidelberg-Moscow experiment (which also used Germanium) which drew lot of attention of community by announcement of observation of  $0\nu\beta\beta$ . It was proven false by results of GERDA. Another type of source = detector experiment use huge vessels of liquid Xenon which serves as a source (especially isotopes  $^{134}\text{Xe}$  and  $^{136}\text{Xe}$ ) and as a scintillator at the same time. EXO with its upgrade nEXO are examples of such experiments. In source = detector category we can find also bolometric experiments. For instance, experiment CUORE uses  $\text{TeO}_2$  crystals cooled down to few mK.  $^{130}\text{Te}$  is another potential  $0\nu\beta\beta$  isotope. The electrons emitted in the decay heat up the crystal and the heat excess can be measured thanks to the change of the electrical resistance of crystal. There is a whole range of other  $0\nu\beta\beta$  experiments which typically belong to one of the mentioned subcategories.

Secondly, there are experiments which take advantage of approach when source is separated from the detection system. SuperNEMO and its predecessor NEMO-3 are such examples. Energy of electrons from the decay are detected by plastic scintillators. Their most unique feature, however, is the reconstruction of topology of the events. Grid of wires in Geiger mode are employed for particle tracking. The source isotope has a form of thin foil. The foil can be exchanged for other isotope of interest. It is an unique feature of the experiments where source and detector are separated. NEMO-3 was capable to study seven isotopes simultaneously (it was:  $^{48}\text{Ca}$ ,  $^{82}\text{Se}$ ,  $^{96}\text{Zr}$ ,  $^{100}\text{Mo}$ ,  $^{116}\text{Cd}$ ,  $^{130}\text{Te}$  and  $^{150}\text{Nd}$ ). SuperNEMO experiment is using  $^{82}\text{Se}$ ,  $^{150}\text{Nd}$  might be employed in future.

Presented thesis sums up all the work which I performed during three years (2015-2018) of my Ph.D. studies within the SuperNEMO collaboration. Let me briefly summarize the contents of each chapter.

- **Chapter 1** contains a brief overview of the history of neutrino physics. The story begins with Pauli's famous neutrino postulate and its discovery 26 years later. Historical overview offers description of variety of key experiments in history of neutrinos, such as first detection of muon neutrino or the experiments resolving decades long Solar neutrino problem. On top of them, some of the most important theoretical concepts important for neutrino physics are discussed. Chapter ends with a brief introduction into the physics of Double beta decay and short review of the experiments performed in the field.

- **Chapter 2** offers short description of all the integral parts of SuperNEMO demonstrator module. SuperNEMO is divided into three main parts: source foil, tracking detector and the calorimeter. In 2016, I took part in assembly and testing of optical modules used to build main SuperNEMO calorimeters. The process of preparation with results is described at the end of the chapter.
- **Chapter 3** is dedicated to measurements of  $^{207}\text{Bi}$  sources which will be used for the energy calibration of demonstrator. The goal of this work is to reduce systematics uncertainties coming from energy calibration by knowing better the source characteristics. At the beginning of the chapter, a brief description of automatic source deployment system is provided. Calibration sources are presented. This chapter is divided into two parts. First part of the chapter contains extensive description of measurement which I performed in order to map the deposition of  $^{207}\text{Bi}$  droplet in the sources. In the measurements, I used three Si Timepix detectors. The whole process of their calibration and preparation of the measurements is presented. I calibrated the detectors in IEAP CTU in Prague in October 2017. First trial measurements, I performed in LSM at the end of October 2017. Final measurements were performed in December 2017 also in LSM. The analysis method and the software algorithms, that I used for extraction of quantities of interest, are explained in detail. Finally, at the end of first part, the results are presented and summarized. The second part of the chapter contains discussion of activity measurements which I performed for the calibration sources during summer 2018 in CENBG. Measurements were performed using two different HPGe detectors. One was employed in order to measure relative activities of all the available sources (40 + 2 measured in LSM) while the second was used for precise measurement of absolute activities of chosen (25) sources. Results are discussed in the form of summarizing plots at the end of the chapter. Full database of all the values measured in both the source mapping and activity measurements are included in Appendix A.
- **Chapter 4** covers the topic of neutron shielding of SuperNEMO demonstrator. In 2018, I performed comparative studies of materials capable to shield neutrons as a contribution to a discussion about shielding design. The study presented in the chapter takes advantage of realistic neutron spectrum measured in LSM. Behaviour of neutrons (fluxes and energy losses) passing through the shielding is simulated in details. Obtained fluxes and energy spectra are compared for nine shielding scenarios using software package Geant4. For each scenario, neutron fluxes passing the wall are simulated using Falaise (SuperNEMO software package). Detector materials which tend to capture most of the neutrons are identified. Second part of the chapter is dedicated to generators of thermal neutron capture used in standard software packages for simulations. Problems with proper generation of gamma cascades are discussed. New generator is proposed and its functionality is demonstrated on an illustrative example.
- **Chapter 5** discusses the topic of detector sensitivity calculations. Firstly, the method of Feldman-Cousins is extensively described. Several aspects and peculiarities of the method are commented and demonstrated. Secondly, the full process of sensitivity calculation is performed. The goal of the chapter was to obtain sensitivity estimation to  $0\nu\beta\beta$  with emission of one or two Majoron(s) for SuperNEMO demonstrator. The process of calculation is initiated by simulation of detection efficiencies and search for region of interest (ROI) with the best signal-to-background ratio. Such ROI can provide the most precise half-life measurement if the decay was observed. If the decay remains unobserved, the half-life limit can be extracted using Feldman-Cousins

method. Half-life limits to Majoron modes of  $0\nu\beta\beta$  were studied as a function of activity of  $^{208}\text{Tl}$  and  $^{214}\text{Bi}$  (present in the foil) and experiment's exposure. Measurement period, after which, SuperNEMO should improve limits of NEMO-3 for both decay modes, are estimated. Full database of the results obtained in the chapter is presented in Appendix B.

The thesis is a balanced compilation of experimental tasks (calibration source measurements) and simulation tasks (neutron shielding and Majoron studies) completed by purely mathematical tasks (e.g. analysis algorithms for spatial calibration of pixel detectors or neutron capture generator proposal).

# Neutrino Physics and Its History

## 1.1 Neutrino Postulate

In the beginning of the 20<sup>th</sup> century, the radioactivity was already known thanks to discovery of Antoine Henri Becquerel in 1896 [1, 2]. It was already Ernest Rutherford, in 1899, who was able to distinguish between  $\alpha$ - and  $\beta$ -decay by the ability to penetrate paper or Aluminium. Later, particle emitted in  $\beta$ -decay was identified as a electron. In that time, they understood  $\beta$ -decay as a process where only the electron is emitted (Equation 1.1).



After discovery of gamma radiation, it was known that alpha and gamma radiation have one feature in common - their spectra are composed of narrow peaks. It is caused by the fact that the particle is carrying all the energy from the difference between states of initial and final nucleus. In contrary, in 1914 James Chadwick showed that beta spectrum behaves differently. It has a continuous spectrum [3]. This indicated that the energy of  $\beta$ -decay is lost somewhere. Apparent non-conservation of spin was another important issue which was needed to be accounted for. It was known that  $\beta$ -decay leaves nucleus mass number unchanged which implies that nuclear spin should be integer number for nuclei with even number of nucleons. Spin of electron is  $1/2$ , so it was obvious that spin could not be conserved for nuclei with even number of nucleons. Neils Bohr suggested that the energy might not be conserved for every decay but only in statistical sense. However, Charles Drummond Ellis and Nevill Francis Mott in [4] ruled out that idea by determination of upper bound of beta energy spectrum. The limit should not exist if Bohr's assumption was right.

In 1930, Wolfgang Pauli sent his famous letter to Physical Institute of the Federal Institute of Technology in Zürich in which he postulated existence of new light particle [5]. He described it as a neutral particle of maximal mass of 0.01 proton masses, different from light quanta, with spin  $1/2$ , thus obeying exclusion principle. He named the particle neutron. He proposed that it is emitted in the  $\beta$ -decay along with electron. However, he did not fully believe in the scenario assuming that the particle would probably already had been discovered. The name neutron was later given to much heavier particle discovered by James Chadwick in 1932. In 1934, Enrico Fermi developed theory of  $\beta$ -decay giving the particle the name it has today - the neutrino. The name was a pun: ending -one has a augmentative purpose in Italian language giving impression that neutrone (the Italian version of neutron) is denoting "something large and neutral". He replaced ending -one with suffix -ino giving the name diminutive sense. Fermi's theory of  $\beta$ -decay was analogy of the quantum electrodynamics

(QED). He assumed that proton is transformed into neutron by emission of electron along with anti-neutrino (Equation 1.2).

$$(A, Z) \rightarrow (A, Z + 1) + e^- + \bar{\nu} \quad (1.2)$$

## 1.2 Discovery of Neutrino

It was already Wolfgang Pauli who expected that the detection of the particle which he postulated would be a very difficult task. He expressed his scepticism in the statement, "I have done a terrible thing, I have postulated a particle that cannot be detected." Finally, the task was not impossible. It took 26 years after the postulate to detect neutrino. In 1956, Clyde Cowan and Frederick Reines published article claiming the neutrino discovery [6]. They achieved this important milestone by taking advantage of beta capture process proposed by Wang Ganchang in 1942 [7]:

$$\bar{\nu}_e + p^+ \rightarrow n^0 + e^+ \quad (1.3)$$

The Reines-Cowan experiment, as it is called, used the nuclear reactor in Savannah river in South Carolina (USA) as a source of the anti-neutrinos. The experimental device was composed of two large tanks of water (200 l each) surrounded by tanks of liquid scintillator. Positron in beta capture (Equation 1.3), created when the anti-neutrino from reactor hits the proton in the water, annihilates fast. As a result, two gammas, with the energy of 511 keV each, are produced. The gammas caused flashes in scintillator tanks and the light was collected in photomultiplier tubes. After they realized that the method is not conclusive enough they added 40 kg of cadmium chloride into each tank with water. Cadmium has a big cross section for the capture of neutron. When neutron is captured, gammas are emitted. The gamma from neutron capture was expected 5  $\mu$ s after the annihilation pair (Figure 1.1). The measurement in coincidence allowed Reines and Cowan to recognize neutrino captures more reliably. The results were compared to data with reactor turned off. During 1371 hours of measurements (including the background data taking) they were able to measure 1-3 anti-neutrinos per hour out of the flux of order  $10^{13}$  anti-neutrinos per  $\text{cm}^2$  every second. Only Frederic Reines was awarded the Nobel prize for this discovery in 1995 because Clyde Cowan died in 1974.

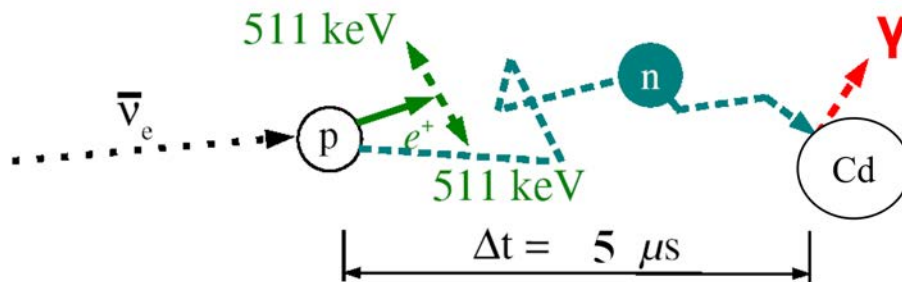


Figure 1.1: Scheme of detection principle in Reines-Cowan experiment.

## 1.3 Neutrinos in Standard Model

Currently, physics distinguishes four types of fundamental forces in nature: Sstrong, Electromagnetic, Weak and Gravity. Standard Model of particle physics (SM) is theory unifying first three: Strong, Electromagnetic and Weak interaction. However, despite an effort

of theorists, gravity was not incorporated yet. In 1961, Sheldon Glashow found a way how to combine electromagnetic interaction with weak interaction [8]. In 1967, Higgs mechanism [9, 10, 11] was incorporated into Glashow's electroweak theory by Steven Weinberg [12] and Abdus Salam [13] giving it the modern form we know today. Formulation of SM was finalized in 1970s after experimental proof of existence of quarks. Since 1970s, SM is considered as very reliable model of fundamental particles. SM gained even more credence after experimental discoveries of top quark in 1995 [14, 15], tau neutrino in 2000 [16] and Higgs boson in 2012 [17, 18]. However, SM is only low energy approximation of more general physics and extension is inevitable. Experimental evidence inconsistent with SM was already found - this physics is called physics beyond Standard Model - BSM physics.

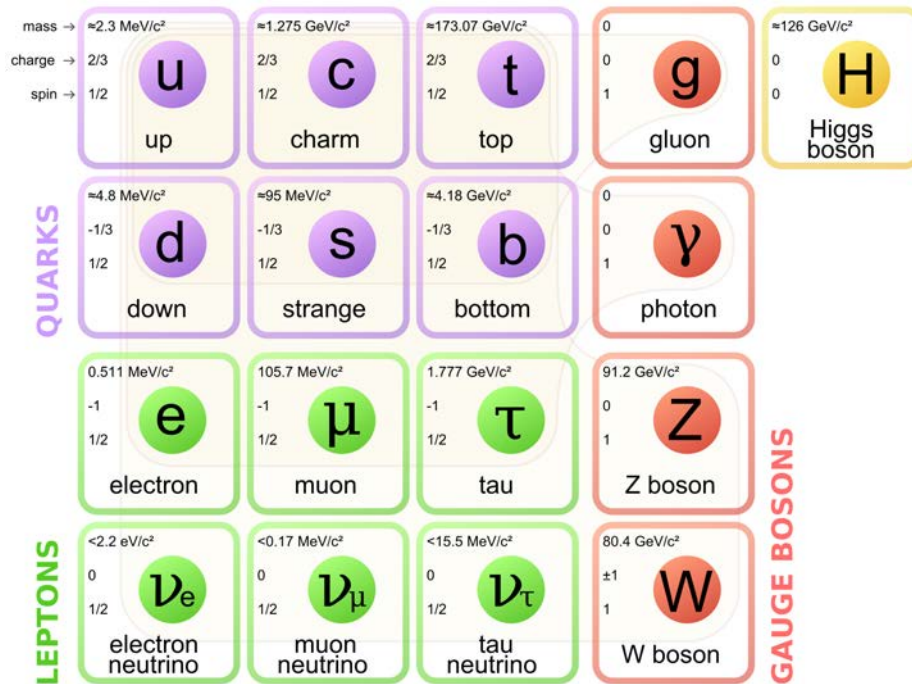


Figure 1.2: All particles of Standard Model.

SM is formulated in form of Lagrangian formalism and describes theoretically interaction of fermions with half integer spin via gauge bosons (integer spin) which act as force carriers. The electromagnetic force is provided by photon, weak interaction by  $W^\pm$  and  $Z^0$  bosons and strong force is mediated by eight gluons. Gravity as a part of BSM physics is not included. Inclusion of Higgs boson explained why gauge bosons have mass. Fermions in SM are divided into two main groups. Six quarks (up, down, charm, strange, top, bottom) are undergoing all interactions (Strong, Electromagnetic, Weak and also Gravity) while electromagnetically charged leptons (electron, muon and tau lepton) only Electromagnetic, Weak and Gravity. Neutrinos, the last three fermions, have no electromagnetic charge, thus they interact only weakly in the framework of SM. The diagram showing all SM particles within the categories can be seen in Figure 1.2.

Analogically to quarks, leptons are divided into three families (generations). In each family there is charged fermion and its neutrino, i.e. electron and electron neutrino, muon and muon neutrino, tau and tau neutrino. The neutrinos in SM are massless. This was proven wrong experimentally by observation of neutrino oscillations [19] (see Section 1.4.1). It is one of the aforementioned proofs that SM needs extension and neutrinos might hide the key to BSM physics.



### 1.3.1 Neutrino Flavours

The discovery of neutrino opened an important chapter in history of experimental particle physics. Knowing that neutrino was a real particle, physicist were interested to know it better. In 1962, new type of neutrino was observed, so-called  $\mu$ -neutrino, in experiment performed by Leon Lederman, Melvin Schwartz and Jack Steinberger [20]. This type of neutrino was already theoretically predicted in 1940 by several people and named "neutretto" [21]. In the experiment,  $\pi$ -mesons (so-called pions) were accelerated which made it possible to study the nature of weak forces in higher energies. Positive (negative) pion is decaying (in more than 99% of cases) into positive (negative) muon and anti-neutrino (neutrino) (Equation 1.4).



The pions from accelerator were decaying during the flight. Created muons were absorbed by 13.5 m thick wall and neutrinos continued to detector (Figure 1.3). If there would be only one type of neutrino, electrons and muons caused by impact of neutrinos would be created randomly, in equal rate. However, they observed significant excess of muons. This led them to conclusion, that neutrino from pion decay have identity designated by the nature of interaction by which they were created. New neutrino was named  $\mu$ -neutrino (and designated

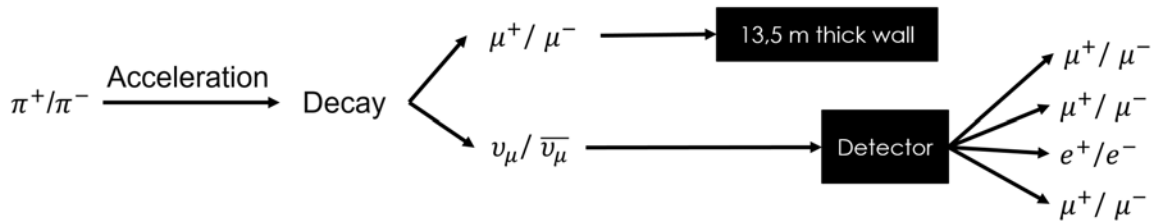


Figure 1.3: Simplified scheme of detection principle in muon neutrino discovery experiment.

$\nu_\mu$ ) because in the lepton vertex it is always created along with  $\mu$ -lepton. This implies that the neutrino from beta decay is of electron type and designated  $\nu_e$ . The Nobel prize for discovery of  $\nu_\mu$  was awarded in 1988.

In 1975, when the third type of lepton was discovered - the  $\tau$ -lepton - in SLAC [22], analogically, the existence of third type of neutrino -  $\tau$ -neutrino ( $\nu_\tau$ ) - was expected. Its discovery was achieved by DONUT collaboration from Fermilab in 2000 [16]. The data were confirmed later by post-analysis from LEP in CERN. Up to date, we distinguish three types (so-called flavours) of neutrinos -  $\nu_e$ ,  $\nu_\mu$  and  $\nu_\tau$ . The existence of other types of neutrinos is being experimentally investigated (for example [23]).

## 1.4 Neutrinos Beyond the Standard Model

As mentioned before, neutrinos in Standard Model are massless. This is, however, inconsistent with experimental observations. Neutrinos are not, obviously, described fully by SM and they hold information about BSM physics.

### 1.4.1 Solar Neutrino Problem

The sources of neutrinos are divided into two main groups - natural and artificial. Artificial sources are made by human, for example nuclear reactors (reactor anti-neutrinos)

and particle accelerators (accelerator neutrinos). Group of natural sources include neutrinos from neutrino cosmic background one second after Big Bang (cosmological/relic neutrinos), neutrinos produced in nuclear reactions in the Sun (solar neutrinos), neutrinos from the supernovae explosions (supernova neutrinos), neutrinos originating inside of the Earth (geoneutrinos), neutrinos created in atmosphere of the Earth by interaction of cosmic radiation (atmospheric neutrinos), neutrinos from active galactic nuclei (AGN neutrinos) and cosmogenic neutrinos produced by interaction of ultra-high energy cosmic rays with cosmological photon background. Plot depicting fluxes of neutrinos of different origin can be found in Figure 1.4.

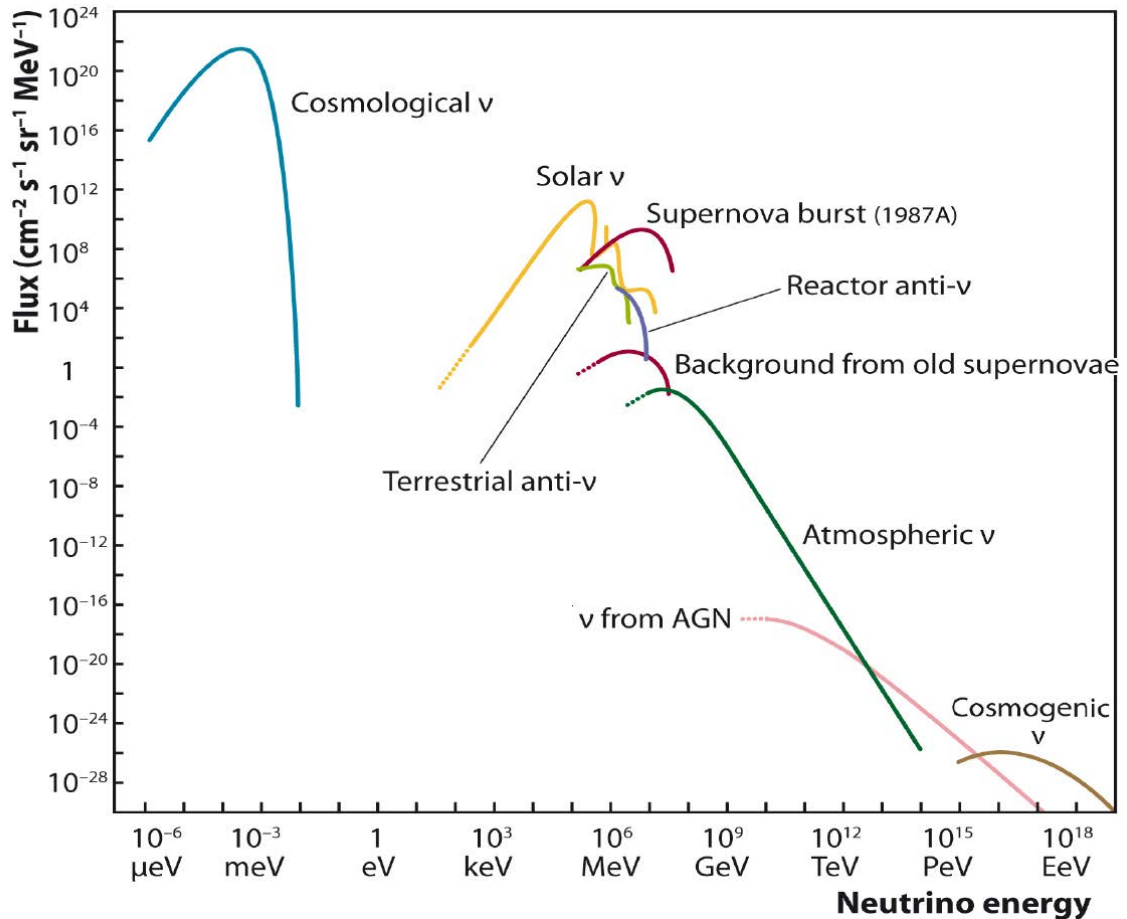


Figure 1.4: Distribution of known neutrino types among the energy range. Plot represents flux of neutrinos of different origin separately. Source: [24].

Solar neutrinos were puzzling neutrino physicists for three decades. Proton-proton chain reaction (so called P-p cycle), which takes place in the core of the Sun [25], is accompanied by emission of  $\nu_e$ . These neutrinos travel without interaction through the Sun and are emitted uniformly into the space. Some of them reach the Earth. In 1960s, Raymond Davis, Jr. and John N. Bahcall prepared experiment focused on the detection of these neutrinos - the Homestake experiment. It was placed in golden mine in South Dakota in the depth of 1.5 km in order to be shielded from cosmic ray radiation occurring on the surface. Homestake experiment started the era of underground neutrino experiments. It was continuously in operation from 1970 to 1994. Experimental technique was based on 615 t of tetrachloroethylene ( $C_2Cl_4$ ) which is total of  $2.2 \times 10^{30}$  nuclei of  $^{37}Cl$ . Electron neutrino, which came from the Sun, underwent capture by  $^{37}Cl$  which was transformed into  $^{37}Ar$  accompanied by emission

of electron (Equation 1.5).



Every few weeks, Davis and Bahcall bubbled Helium through the tank to extract Argon. Few  $\text{cm}^3$  were extracted including the stable Argon isotopes. Then the decay of  ${}^{37}\text{Ar}$  was observed. This helped to determine the rate of neutrino events. Bahcall calculated that according to the Standard Solar Model (SSM), the expected rate should be  $9.3 \pm 1.3 \text{ SNU}^1$ . However, they measured only  $2.56 \pm 0.32 \text{ SNU}$  [26]. The theoretical predictions were revised several times by theoreticians improving the precision of the model but the difference seemed not to lie in the theoretical refinement. Experiment was also checked for errors, but conclusion was that it works correctly. There was lack of neutrinos in the detector. This problem is called the solar neutrino problem.

It was not clear whether the processes in the Sun are understood properly, thus the main interest of theoreticians was pointed towards SSM. Several experiments were constructed in order to account for this question. Kamiokande [27] in Japan (1985 - 1995), SAGE [28] in Baksan, Russia (1989 - 2007) or Gallex [29] in Gran Sasso, Italy (1991 - 1997). All of them have seen lack of neutrinos. Kamiokande was capable of measuring the momentum of the neutrinos. It confirmed that these neutrinos really originate in the Sun. The lack of solar neutrinos was, finally, explained by occurrence of so-called neutrino oscillations. Their existence was proposed in 1958 by Bruno Pontecorvo [30].

## 1.4.2 Neutrino Mixing and Oscillations

Under the term neutrino oscillations we understand the continuous change of the flavour of neutrino along the trajectory of flight. In contrary to assumption of Standard Model of particle physics, it would be only possible if neutrino had non-zero mass. The reason is as follows: if we assume three neutrino mass eigenstates (denoted  $\nu_1, \nu_2, \nu_3$ ) to be different from flavour eigenstates (denoted  $\nu_e, \nu_\mu, \nu_\tau$ ) there is a unitary transformation between the bases<sup>2</sup>:

$$\begin{aligned} |\nu_\alpha\rangle &= \sum_i U_{\alpha i} |\nu_i\rangle \\ |\nu_i\rangle &= \sum_\alpha U_{\alpha i}^* |\nu_\alpha\rangle \end{aligned} \quad (1.6)$$

Rewritten into matrix form:

$$\begin{pmatrix} |\nu_e\rangle \\ |\nu_\mu\rangle \\ |\nu_\tau\rangle \end{pmatrix} = \begin{pmatrix} U_{e1} & U_{e2} & U_{e3} \\ U_{\mu1} & U_{\mu2} & U_{\mu3} \\ U_{\tau1} & U_{\tau2} & U_{\tau3} \end{pmatrix} \begin{pmatrix} |\nu_1\rangle \\ |\nu_2\rangle \\ |\nu_3\rangle \end{pmatrix} \quad (1.7)$$

The unitary matrix providing transformation between two bases is called PMNS (Pontecorvo – Maki – Nakagawa – Sakata) matrix [31, 32]. It is an analogue to CKM (Cabibbo – Kobayashi – Maskawa) matrix for quark mixing. If we limit our discussion only to case of two neutrino mixing of flavours  $\nu_\alpha$  and  $\nu_\beta$ , it has form:

$$\begin{pmatrix} |\nu_\alpha\rangle \\ |\nu_\beta\rangle \end{pmatrix} = \begin{pmatrix} \cos(\theta) & \sin(\theta) \\ -\sin(\theta) & \cos(\theta) \end{pmatrix} \begin{pmatrix} |\nu_1\rangle \\ |\nu_2\rangle \end{pmatrix} \quad (1.8)$$

<sup>1</sup>SNU - Solar neutrino unit denotes one neutrino capture per  $10^{36}$  nuclei every second.

<sup>2</sup>Greek index  $\alpha$  is used to denote flavour states and Latin  $i$  to denote mass states.

Here  $\theta$  is called mixing angle. When neutrinos are propagated, their state evolve along the trajectory. We can assume, that the momentum of neutrino is far bigger than its rest mass. In that case probability for neutrino with energy  $E$  to change flavour from  $\nu_\alpha$  to  $\nu_\beta$  is:

$$P(\nu_\alpha \rightarrow \nu_\beta) = \sin^2(2\theta)\sin^2\left(\frac{\Delta m_{ij}^2 L}{4E}\right), \quad \alpha \neq \beta \quad (1.9)$$

Here,  $L$  is the distance travelled by neutrino,  $\theta$  is neutrino mixing angle and  $\Delta m_{ij}^2$  mass squared difference of  $i$ -th and  $j$ -th mass state, i.e.  $\Delta m_{ij}^2 = m_i^2 - m_j^2$ . From Equation 1.9 we can easily see that probability of oscillation  $P(\nu_\alpha \rightarrow \nu_\beta)$  is non-zero only if  $\Delta m_{ij}^2 \neq 0$  holds (assuming that first sine in the product is non-zero which was observed). In other words, it means that neutrino oscillations are possible only in case when at least one of the mass eigenstates of neutrino would be non-zero. This breaks apart the assumption of mass-less neutrinos in Standard Model.

In the case of Solar neutrinos they are produced uniquely as the electron neutrinos but oscillations make them change their flavour during the flight towards the Earth. All the experiments mentioned above, which have seen lack of neutrinos, were capable to detect only electron neutrinos. In 1996, experiment Super-Kamiokande (upgrade of Kamiokande) started data collection. In 1998, they provided the first evidence of neutrino oscillations by observation of atmospheric  $\nu_\mu$  oscillating into  $\nu_\tau$  [33]. One year later, in 1999, SNO (Sudbury Neutrino Observatory) came into operation. SNO was focused on the measurement of neutrinos coming from decay of  ${}^8\text{B}$  (around 10 MeV). These electron-neutrinos are not very affected by vacuum neutrino oscillations rather than by so-called MSW effect [34] which has influence on the neutrino oscillations in matter (in this case solar matter). SNO was able to count the number of detected electron-neutrinos and number of neutrinos of all flavours collectively. In 2001, their results supported the existence of neutrino oscillations [19]. In 2015, Nobel prize was given to Takaaki Kajita (Super-Kamiokande) and Arthur B. McDonald (SNO) "for the discovery of neutrino oscillations, which shows that neutrinos have mass".

### 1.4.3 Supernova Neutrinos

Neutrino oscillations provided clear evidence that Standard Model of particle physics is not complete. However, the hint that neutrino has non-zero mass came even sooner. In 1987, unique explosion of Supernova 1987A was observed [35]. This supernova is approximately 168 000 light years away in our galactic neighbourhood (in Large Magellanic Cloud). It was the first supernova explosion observable by naked eye since 1604 [36]. In the explosion, estimated  $10^{58}$  anti-neutrinos were created. Three neutrino observatories were capable to measure anti-neutrinos from this burst. In Kamiokande, they detected 12 anti-neutrinos [37], in IMB (Irvine – Michigan – Brookhaven) detector 8 [38] and Baksan measured 5 anti-neutrinos [39]. The most interesting result was obtained by Kamiokande. Their 12 measured anti-neutrinos arrived in two pulses by 9 and 3 while anti-neutrinos from second pulse were delayed by 9.219 to 12.439 seconds after the first pulse [37]. This was hint, although not a evidence, that neutrinos might have mass. In other case, they would arrive all together propagating at the speed of light in vacuum. Although, 25 detected anti-neutrinos is not a huge number, it was significant increase to background values. It was the first observation of supernova anti-neutrinos and the beginning of neutrino astronomy. The observations were consistent with theoretical supernova models and also allowed physicists to set upper limits on neutrino mass and number of neutrino flavours [40].

### 1.4.4 Neutrino Hierarchies

The existence of neutrino oscillations serves as a clear signature of neutrinos with non-zero mass. As it was already shown in Equation 1.9, by oscillation experiments, it is possible to extract only the square mass differences  $\Delta m_{ij}^2 = m_i^2 - m_j^2$ . These values are measured. However, the three neutrino mass states  $\nu_1$ ,  $\nu_2$  and  $\nu_3$  remain unknown.

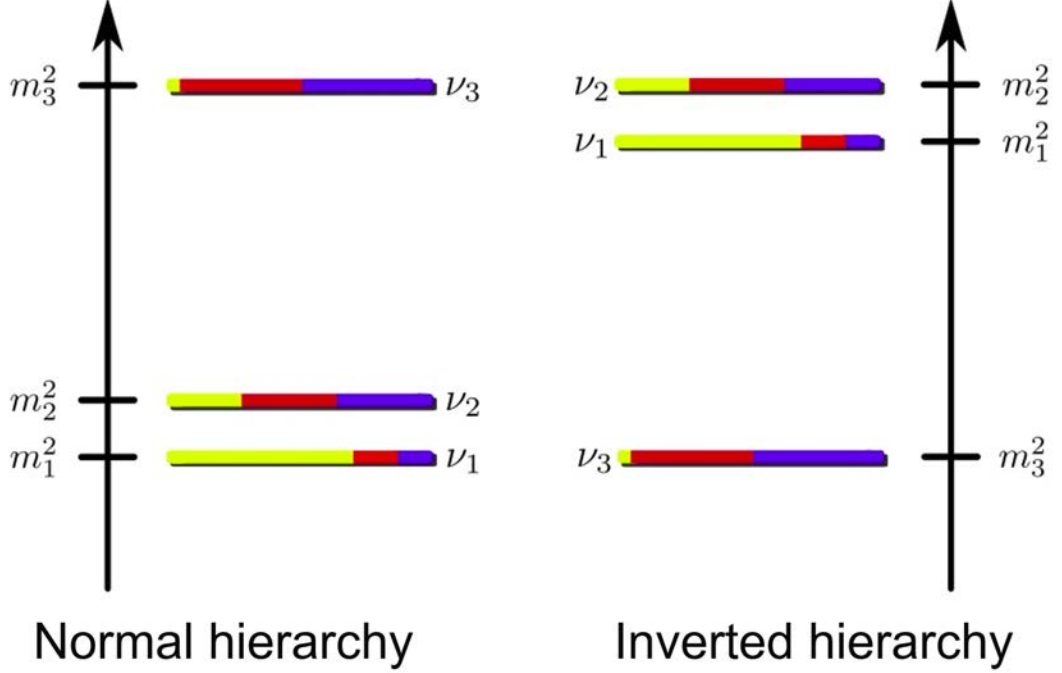


Figure 1.5: Two possible neutrino mass hierarchies. The case of  $\nu_1 < \nu_2 < \nu_3$  (with one heavier neutrino state) depicted on the left - is called "Normal" hierarchy while the case on the right, fulfilling  $\nu_3 < \nu_1 < \nu_2$  (with two heavier neutrino states), is called "Inverted" hierarchy.

Furthermore, the ordering of the states - so-called neutrino hierarchy - can not be provided by oscillation experiments. From solar neutrino observations and measurements of atmospheric neutrinos we know the values of  $\Delta m_{21}^2$  and  $|\Delta m_{32}^2|$  [41]:

$$\begin{aligned} \Delta m_{Sun}^2 = \Delta m_{21}^2 &= (7.53 \pm 0.18) \times 10^{-5} eV^2 \\ |\Delta m_{atm}^2| = |\Delta m_{32}^2| &= (2.44 \pm 0.06) \times 10^{-3} eV^2 \end{aligned} \quad (1.10)$$

The convention  $m_1 < m_2$  is adopted which allows us to narrow possible neutrino hierarchies to two cases depicted in Figure 1.5. They differ only by number of heavier states. The case with one heavier neutrino state is called "Normal" hierarchy while the case with two heavier neutrino states is so-called "Inverted" hierarchy.

### 1.4.5 Neutrino Masses and Their Nature

Based on previous discussion, new terms generating neutrino masses are needed as an extension of Lagrangian of SM. Depending on chirality of particles we recognize left-handed

(spin and momentum of particle are parallel) and right-handed (spin and momentum of particle are anti-parallel) particles. In Standard Model, only the left-handed neutrinos and right-handed anti-neutrinos enter into interactions.

Let us have a look on three possible extensions of SM Lagrangian generating neutrino masses:

### Dirac mass term

Assuming the existence of both, left-handed ( $\nu_\alpha^L$ ) and right-handed ( $\nu_\alpha^R$ ) neutrino fields, we are able to compose so-called Dirac mass term of Lagrangian given in Equation 1.11.

$$\mathcal{L}^D = - \sum_{\alpha, \alpha'} \bar{\nu}_{\alpha'}^R M_{\alpha, \alpha'}^D \nu_\alpha^L + \text{h.c.} \quad (1.11)$$

Indices  $\alpha$  and  $\alpha'$  stand for neutrino flavours (e,  $\mu$  and  $\tau$ ) and  $M^D$  is complex  $3 \times 3$  matrix coupling left-handed and right-handed neutrino. In respect to equation of neutrino mixing (Equation 1.6), the  $\nu_\alpha^L$  are mixed in the following way:

$$\nu_\alpha^L = \sum_{i=1}^3 U_{\alpha i} \nu_i^L, \quad (1.12)$$

Here,  $i$  ( $i = 1, 2$  or  $3$ ) denotes the Dirac mass state with mass  $m_i$  and  $U_{\alpha i}$  is unitary neutrino mixing matrix. If matrix  $M^D$  is non-diagonal, the individual lepton numbers  $L_e, L_\mu, L_\tau$  are not conserved. However, this mass term does not mix particles with anti-particles, thus the total lepton number  $L = L_e + L_\mu + L_\tau$  is conserved.

### Majorana mass term

Another possibility to construct neutrino mass term was proposed by Ettore Majorana. His mass term is coupling neutrinos with anti-neutrinos as follows:

$$\mathcal{L}^M = - \sum_{\alpha, \alpha'} (\bar{\nu}_{\alpha'}^L)^c M_{\alpha \alpha'}^M \nu_\alpha^L + \text{h.c.} \quad (1.13)$$

Index  $c$  denotes charge conjugated neutrino spinor  $\nu^c = C\bar{\nu}^T$ , where  $C$  is charge conjugation operator.  $M^M$  is complex symmetric  $3 \times 3$  matrix. Majorana mass fields  $\chi_i^L$  are mixed into flavour fields in following way:

$$\nu_\alpha^L = \sum_{i=1}^3 U_{\alpha i} \chi_i^L, \quad (1.14)$$

where again  $U_{\alpha i}$  is unitary neutrino mixing matrix. Charge conjugated mass fields  $\chi_i^c$  differ to  $\chi_i^L$  only by a phase factor  $\xi_i$ :  $\chi_i^c \xi_i = \chi_i$ . Neutrinos are indistinguishable to anti-neutrinos and processes violating total lepton number are allowed<sup>3</sup>. Majorana mass term, as already mentioned, is coupling neutrinos with anti-neutrinos. As a result, Majorana mass term violates even total lepton number  $L = L_e + L_\mu + L_\tau$ . The existence of such mass term in quark sector or for charged leptons is impossible because the charge conservation would be violated, which is not the case for neutrinos.

---

<sup>3</sup>For example neutrino-less double beta-decay, see Section 1.5.2

### Dirac - Majorana mass term

The last possibility is relatively simple combination of previous two. It is the most general and, thanks to presence of Majorana part, it does not conserve total lepton number.

$$\mathcal{L}^{D+M} = - \sum_{\alpha\alpha'} \left[ \frac{1}{2} (\bar{\nu}_{\alpha'}^L)^c M_{\alpha\alpha'}^{M,L} \nu_{\alpha}^L + \frac{1}{2} \bar{\nu}_{\alpha'}^R M_{\alpha\alpha'}^{M,R} (\nu_{\alpha}^R)^c + \bar{\nu}_{\alpha'}^R M_{\alpha\alpha'}^D \nu_{\alpha}^L \right] + \text{h.c.} \quad (1.15)$$

$M^{M,L}$  and  $M^{M,R}$  are complex non-diagonal symmetric  $3 \times 3$  matrices. In this general case, the flavour fields  $\nu_{\alpha}^L$  and  $\nu_{\alpha}^R$  are composed of six Majorana mass fields:

$$\nu_{\alpha}^L = \sum_{i=1}^6 U_{\alpha i}^L \chi_i^L, \quad \nu_{\alpha}^R = \sum_{i=1}^6 U_{\alpha i}^R \chi_i^R. \quad (1.16)$$

For mixing matrices  $U_{\alpha i}^L, U_{\alpha i}^R$  we have these orthonormalization conditions:

$$\sum_{i=1}^6 U_{\alpha i}^L U_{\alpha' i}^R \xi_i = 0, \quad \sum_{i=1}^6 U_{\alpha i}^L (U_{\alpha' i}^L)^* = \delta_{\alpha\alpha'}, \quad \sum_{i=1}^6 U_{\alpha i}^L (U_{\alpha' i}^R)^* = \delta_{\alpha\alpha'}. \quad (1.17)$$

According to the mass generation process, neutrino can be either of Dirac ( $\nu \neq \bar{\nu}$ ) or of Majorana nature ( $\nu = \bar{\nu}$ ).

## 1.5 Double Beta-Decay Processes

Unknown neutrino masses as well as the problem of neutrino hierarchies are important problems of contemporary neutrino physics. The possible solutions might be hidden in a processes called by generalized name of double beta-decay.

### 1.5.1 Two-Neutrino Double Beta-Decay

Two-neutrino double beta-decay is nuclear decay proposed in 1935 by Maria Goeppert-Mayer [42]. It is a nuclear transition where two neutrons are instantaneously transformed into two protons by emission of two electrons and two electron anti-neutrinos (Equation 1.18).

$$(A, Z) \rightarrow (A, Z + 2) + 2e^{-} + 2\bar{\nu}_e \quad (1.18)$$

It is the double analogy of ordinary  $\beta^{-}$ -decay (Equation 1.2), usually denoted by  $2\nu\beta\beta$ . However, the term double beta-decay with two neutrinos (anti-neutrinos) might be used to name also one of the following combinations of  $\beta^{+}$ -decay or electron capture (EC):

$$\begin{aligned} (A, Z) &\rightarrow (A, Z - 2) + 2e^{+} + 2\nu_e, & (2\nu\beta^{+}\beta^{+}) \\ e^{-} + (A, Z) &\rightarrow (A, Z - 2) + e^{+} + 2\nu_e, & (2\nu\beta^{+}/EC) \\ 2e^{-} + (A, Z) &\rightarrow (A, Z - 2) + 2\nu_e + 2\gamma, & (2\nu EC/EC) \end{aligned} \quad (1.19)$$

In next, if not stated otherwise,  $2\nu\beta\beta$  would stand for the process described by Equation 1.18. This process is rare compared to ordinary  $\beta$ -decay, so its half-life  $T_{1/2}^{2\nu}$  reaches  $10^{19} - 10^{25}$  years and can be calculated as follows:

$$\frac{1}{T_{1/2}^{2\nu}} = \frac{\Gamma_{2\nu}}{\ln(2)} = G^{2\nu}(Q, Z) |M^{2\nu}|^2 \quad (1.20)$$

Decay	Q-value [keV]	$T_{1/2}$ [yr]
$^{48}\text{Ca} \rightarrow ^{48}\text{Ti}$	4267	$4.4^{+0.6}_{-0.5} \times 10^{19}$
$^{76}\text{Ge} \rightarrow ^{76}\text{Se}$	2039	$1.65^{+0.14}_{-0.12} \times 10^{21}$
$^{82}\text{Se} \rightarrow ^{82}\text{Kr}$	2996	$(0.92 \pm 0.07) \times 10^{20}$
$^{96}\text{Zr} \rightarrow ^{96}\text{Mo}$	3349	$(2.3 \pm 0.2) \times 10^{19}$
$^{100}\text{Mo} \rightarrow ^{100}\text{Ru}$	3034	$(7.1 \pm 0.4) \times 10^{18}$
$^{100}\text{Mo} \rightarrow ^{100}\text{Ru}(0_1^+)$	1905	$6.7^{+0.5}_{-0.4} \times 10^{20}$
$^{116}\text{Cd} \rightarrow ^{116}\text{Sn}$	2813	$(2.87 \pm 0.13) \times 10^{19}$
$^{128}\text{Te} \rightarrow ^{128}\text{Xe}$	867	$(2.0 \pm 0.3) \times 10^{24}$
$^{130}\text{Te} \rightarrow ^{130}\text{Xe}$	2528	$(6.9 \pm 1.3) \times 10^{20}$
$^{136}\text{Xe} \rightarrow ^{136}\text{Ba}$	2458	$(2.19 \pm 0.06) \times 10^{21}$
$^{150}\text{Nd} \rightarrow ^{150}\text{Sm}$	3371	$(8.2 \pm 0.9) \times 10^{18}$
$^{150}\text{Nd} \rightarrow ^{150}\text{Sm}(0_1^+)$	2626	$1.2^{+0.3}_{-0.2} \times 10^{20}$
$^{238}\text{U} \rightarrow ^{238}\text{Pu}$	1144	$(2.0 \pm 0.6) \times 10^{21}$

Table 1.1: Recommended averaged values of half-lives for several  $2\nu\beta\beta$  nuclei [43]. Q values are taken from National Nuclear Data Center website [44].

$\Gamma_{2\nu}$  is a decay width, Q is total energy released in  $2\nu\beta\beta$ ,  $G^{2\nu}(Q, Z)$  is kinematical phase space factor and  $M^{2\nu}$  is nuclear matrix element. This decay mode was already observed in case of several candidate nuclei. Their list along with their Q-values and measured half-lives can be found in the Table 1.1.

## 1.5.2 Neutrino-Less Double Beta-Decay

In 1939, Wendell H. Furry proposed possibility of neutrino-less mode of double beta-decay [45]. This would be only possible if neutrino is its own antiparticle, so-called Majorana particle. The process would look similar to  $2\nu\beta\beta$  but without anti-neutrinos in final state (Equation 1.21).

$$(A, Z) \rightarrow (A, Z + 2) + 2e^- \quad (1.21)$$

Interest in this decay mode lies in the possibility to prove that neutrino is of Majorana nature. For now, it is the only known possible way to prove it. Moreover, the half-life ( $T_{1/2}^{0\nu}$ ) of  $0\nu\beta\beta$  is in the direct relation with neutrino mass values (Equation 1.22).

$$\frac{1}{T_{1/2}^{0\nu}} = \frac{\Gamma_{0\nu}}{\ln(2)} = |m_{\beta\beta}|^2 |G^{0\nu}(Q, Z)| |M^{0\nu}|^2 \quad (1.22)$$

$\Gamma_{0\nu}$  is decay width of  $0\nu\beta\beta$ , Q is kinetic energy emitted in the process,  $G^{0\nu}(Q, Z)$  is a phase space factor and  $M^{0\nu}$  is nuclear matrix element of  $0\nu\beta\beta$ . Here,  $m_{\beta\beta}$  is so-called effective



neutrino mass given by linear combination of all three neutrino masses (Equation 1.23).

$$m_{\beta\beta} = \sum_{i=1}^3 U_{ei}^2 m_i \quad (1.23)$$

Due to the fact that this decay channel was not experimentally observed yet, the lower limits were set for the half-lives. The best limits for four isotopes are presented in Table 1.2. They also yield the upper limit for effective neutrino mass.

Decay	Q-value [keV]	$T_{1/2}$ [yr]	$ m_{\beta\beta} $ [eV]	Experiment
$^{76}\text{Ge} \rightarrow ^{76}\text{Se}$	2039.0	$> 2.1 \times 10^{25}$	$< 0.26-0.62$	GERDA-I [46]
$^{100}\text{Mo} \rightarrow ^{100}\text{Ru}$	3034.4	$> 1.1 \times 10^{24}$	$< 0.33-0.62$	NEMO-3 [47]
$^{130}\text{Te} \rightarrow ^{130}\text{Xe}$	2527.5	$> 2.8 \times 10^{24}$	$< 0.3-0.7$	CUORICINO [48]
$^{136}\text{Xe} \rightarrow ^{136}\text{Ba}$	2458.7	$> 1.9 \times 10^{25}$	$< 0.12-0.25$	KamLAND-Zen [49]

Table 1.2: List of the best lower limits set for the half-life of  $0\nu\beta\beta$  and upper limits on effective neutrino mass [43]. Limits are at 90% C.L. Uncertainty of the mass upper limit is caused by limited knowledge of  $0\nu\beta\beta$  matrix elements  $M^{0\nu}$ .

In  $0\nu\beta\beta$  experiments, two electrons coming from one vertex are expected to be observed. However, the same signal is expected from  $2\nu\beta\beta$  decay because the two neutrinos are not detected. This fact puts  $2\nu\beta\beta$  decay into position of background event when searching for  $0\nu\beta\beta$ . Luckily, this problem is possible to solve just by looking at the spectrum. If we look at the sum of kinetic energies of both electrons, in case of  $2\nu\beta\beta$  decay, some energy from  $Q_{\beta\beta}$  value is taken away by neutrinos. Analogically to the simple beta-decay, energy spectrum of  $2\nu\beta\beta$  is thus continuous. In contrary, in case of  $0\nu\beta\beta$  there are no neutrinos, and all energy from  $Q_{\beta\beta}$  is transformed into kinetic energy of both electrons. So the theoretical  $0\nu\beta\beta$  signal is expected to be a peak at the end of  $2\nu\beta\beta$  spectrum as depicted in Figure 1.6a. In real experimental situation, this peak has a shape of Gaussian distribution because of the non-zero energy resolution (Figure 1.6b). In case of poor energy resolution this peak might overlap with the  $2\nu\beta\beta$  continuum. The detection techniques with sufficiently high energy resolution in the region of  $Q_{\beta\beta}$  is thus required for  $0\nu\beta\beta$  experiments.

### 1.5.3 Nuclear Matrix Elements

The knowledge of nuclear matrix elements of  $0\nu\beta\beta$  is inevitable in order to extract effective neutrino mass from half-life of  $0\nu\beta\beta$ . Unfortunately, these matrix elements can be measured independently only partially, thus they have to be calculated. This fact underlines the importance of having precise theoretical nuclear models. The matrix elements are crucial for planning of future experiments. The uncertainty of factor of two is projected into four-fold raise in amount of isotope needed to reach some certain neutrino mass limit.

In order to calculate the nuclear matrix elements, the many-body wave-functions of nuclei in question should be known precisely. Many different approaches are currently used in order to address this question. Let us briefly present three of them.

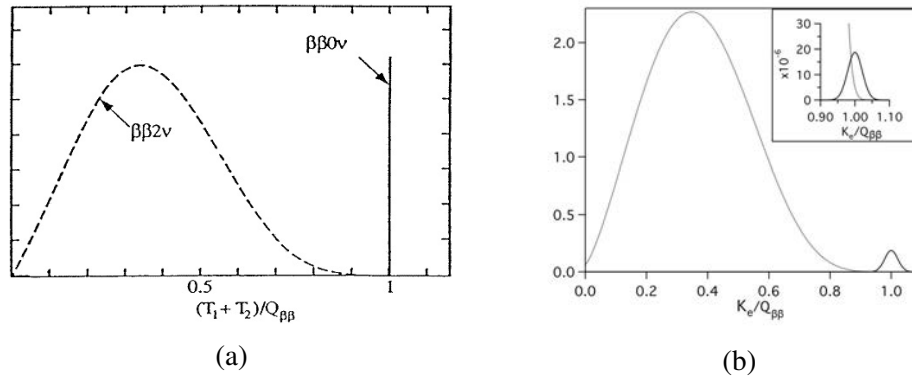


Figure 1.6: Double beta-decay spectra. X-axis in both figures represents sum of kinetic energies of both electrons in units of  $Q_{\beta\beta}$  value. Y-axis is the amplitude in arbitrary units in both cases. (a): Theoretical spectrum of double beta-decay.  $2\nu\beta\beta$  continuous spectrum is in dashed line while  $0\nu\beta\beta$  is represented as a delta function at the end of the spectrum. Its height is exaggerated. (b): Theoretical double beta-decay spectrum. The effect of non-zero energy resolution of detector is taken into account. Peak which belongs to  $0\nu\beta\beta$  is of Gaussian shape and its height is exaggerated. In top right corner the zoom of the region around  $Q_{\beta\beta}$  value is displayed. In this case,  $0\nu\beta\beta$  peak is shown in its real relative size compared to  $2\nu\beta\beta$  continuum. Clear overlap is visible. This effect can be inhibited by improvement in the energy resolution of detection.

First one is the ISM (Interacting Nuclear Shell Model). This model treats only limited number of orbits which are not far from Fermi level. All the possible correlations are included and treated exactly. The disadvantage of this approach is that it could result into quite robust calculation where basis as big as  $10^{11}$  Slater determinants is needed to be treated. This is the reason why this method is suitable mainly for smaller nuclei such as  $^{48}\text{Ca}$  [50].

Another model is the Quasiparticle Random Phase Approximation (QRPA). Compared to ISM, QRPA is using much large valence space but it is not able to take into account all possible configurations. The single particle states are obtained from solution of Schrödinger equation in mean-field approximation using Woods-Saxon potential. BCS (Bardeen – Cooper – Schrieffer) approximation is employed, so proton and neutron numbers are not exactly conserved. This method generally works the best for bigger nuclei but further development is needed in order to achieve sufficient precision for calculation of nuclear matrix elements for  $0\nu\beta\beta$ . One of such attempts was a topic of my master thesis where the approach of possible non-linear extension of phonon operator was studied [51].

Third commonly used model is so-called Interacting Boson Model (IBM). This model is building the nuclear wave-function in terms of nucleon pairs with  $L = 0$  and  $L = 2$ . The double beta-decay is modelled in terms of  $0^+$  and  $2^+$  neutron pairs transferring into proton pair. This model was used for both small and large nuclei.

A full discussion of different contemporary nuclear models is far beyond the scope of this thesis. Let us, at least, present the current status of nuclear matrix elements for  $0\nu\beta\beta$  in form of the Figure 1.7.

### 1.5.4 Experimental Status of Double Beta-Decay

In past decades, several experiments were using different approaches to observe  $0\nu\beta\beta$ . These experiments, belonging to a first generation, e.g. Heidelberg-Moscow, NEMO-3,

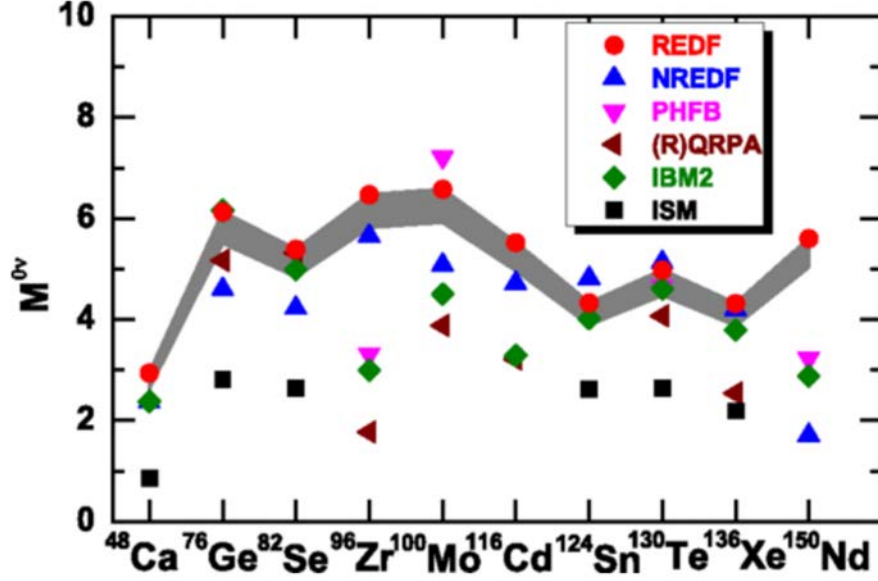


Figure 1.7: Current status of theoretical calculations of nuclear matrix elements for  $0\nu\beta\beta$  [52]. Except for IBM, ISM and QRPA methods, results of PHFB (Projected Hartree - Fock - Bogoliubov) and EDF (Energy Density Functional) methods are presented. The differences are still relatively big despite of the theoretical effort invested into this topic.

CUORICINO are now history and many second generation experiments are either developed or planned. Even though, the variety of approaches is relatively wide, there are still few principles which are followed by all  $0\nu\beta\beta$  experiments. First of all, good resolution of electron energies is needed to be able to recognize the  $0\nu\beta\beta$  in the energy spectrum from  $2\nu\beta\beta$  and other types of background. It is also important to achieve high spatial resolution to be able to distinguish the  $0\nu\beta\beta$  vertex from other possible events mimicking this decay channel, thus lowering background. The mass of studied isotope is the key parameter which increases expected experimental sensitivity of neutrino-less double beta-decay half-life. Sensitivity can be calculated by Equation 1.24.

$$T_{1/2}^{0\nu\beta\beta} > \ln(2) \frac{N_A}{W} \varepsilon \frac{am_s t}{\alpha \sqrt{b}} \quad (1.24)$$

The parameters in the equation are as following:  $T_{1/2}^{0\nu\beta\beta}$  - neutrino-less double beta-decay half-life,  $\alpha$  - number of standard deviations for given confidence level,  $\varepsilon$  - efficiency of detection and identification of true events,  $a$  - isotopic abundance of studied  $0\nu\beta\beta$  isotope in investigated sample,  $W$  - is molecular weight of source isotope,  $m_s$  - total mass of studied sample,  $t$  - duration of data taking period and  $b$  - number of expected background events. Detailed discussion about origin of this equation and calculation of half-life limits takes place in Chapter 5. Some examples of techniques used to search for  $0\nu\beta\beta$  are presented in next sections.

### Germanium experiments

This type of experiments aim to study the  $0\nu\beta\beta$  of  $^{76}\text{Ge}$ . They belong to the type of experiments where source is the detector at the same time. They use Ge semiconductor diodes enriched at about 86% in  $^{76}\text{Ge}$ , having high detection efficiency. At the level of 2 039 keV

( $Q_{\beta\beta}$  value of  $^{76}\text{Ge}$ ) the energy resolution can be as small as few keV when using cooling system, for example liquid Argon. The detection principle is relatively simple. A particle, interacting with detector, produces charge carriers which are collected, amplified and turned into a voltage signal. The signal is proportional to energy deposited in detector. The most known experiments of first generation based on Germanium are Heidelberg-Moscow (HdM) and International Germanium Experiment (IGEX). The low limit on  $0\nu\beta\beta$  half-life was set to level of  $1.9 \times 10^{25}$  yr (90% C.L.) by HdM [53] and  $1.57 \times 10^{25}$  yr (90% C.L.) by IGEX [54]. Part of HdM collaboration announced the observation of  $0\nu\beta\beta$  signal in 2004 [55] but the proof is not convincing enough and the result is considered as controversial. GERDA (Germanium Detection Array) is next generation experiment. One of the design goal in first phases was to verify results of HdM. In following several phases progressive increase of the isotope mass is planned. GERDA have not completely ruled out possible observation of  $0\nu\beta\beta$  by HdM but it strongly disfavours it. The low limit on  $0\nu\beta\beta$  half-life was set to level of  $2.1 \times 10^{25}$  yr (90% C.L.) by GERDA in Phase I of its run [46]. MAJORANA is another experiment in preparation which aims to employ 40 kg of selenium. Collaboration with GERDA in its Phase III is being prepared under the name LEGEND (Large Enriched Germanium Experiment for Neutrino-less Decay).

### **Bolometer experiments**

Bolometers are calorimeters at very low temperatures. This type of detection technique also takes advantage of source being the detector. Particle passing through the detector leaves the heat proportional to its energy in bolometer. Heat is then measured by very sensitive semiconductor thermistors. The bolometers should be cooled down to 10 mK. In general, the deposition efficiency of energy in bolometers is high, but the data collection is slow. There are several  $0\nu\beta\beta$  experiments using bolometric method. CUORICINO was located in the LNGS (Laboratori Nazionali del Gran Sasso, Italy) and ran from March 2003 to July 2008. It used 40.7 kg of enriched and also natural  $\text{TeO}_2$  crystals at the temperature of 8 mK. The limit on  $0\nu\beta\beta$  half-life was set by CUORICINO at the level of  $2.8 \times 10^{24}$  yr (90% C.L.) for  $^{130}\text{Te}$  [56]. CUORE is next generation bolometer  $0\nu\beta\beta$  experiment and successor of CUORICINO. Its prephase CUORE-0 is now in operation. The aim is to increase the mass from 40.7 kg (CUORICINO) to 741 kg which corresponds to 206 kg of  $^{130}\text{Te}$ . The expected sensitivity assuming low background of 0.01 cts/(keV · kg · y) during five years of operation is on the level of  $9.5 \times 10^{25}$  yr (90% C.L.) [57]. LUCIFER (Low-background Underground Cryogenic Installation For Elusive Rates) is  $0\nu\beta\beta$  bolometer experiment aimed to study  $^{82}\text{Se}$  in the form of crystals of ZnSe. LUCIFER will be composed of 15 kg of enriched  $^{82}\text{Se}$ . The expected sensitivity of  $0\nu\beta\beta$  half-life after 5 years of running and the background level of  $10^{-3}$  cts/(keV · kg · y) is on the level of  $6.0 \times 10^{25}$  yr (90% C.L.) [58].

### **TPC and liquid scintillator experiments**

Time projection chambers are particle detectors taking advantage of ionisation of gas (liquid) filling the volume of the detector. This ionisation is caused when charged particle passes the volume of detector. Anode wires attract the ionisation electrons and collect them. These electrons carry information about the track of initial ionising particle which can be reconstructed in three dimensions if the anode wires are organized in specific pattern inside of the chamber. These experiments also belong to the category of the source = detector experiments. EXO-200 is a cylindrical liquid xenon time projection chamber (TPC) aimed to study

200 kg of 80.6% enriched  $^{136}\text{Xe}$ . The data taking started in 2011. After two years of data taking, the limit on  $0\nu\beta\beta$  half-life (for  $^{136}\text{Xe}$ ) was reached at the level of  $1.1 \times 10^{25}$  yr (90% C.L.) [59]. KamLAND-Zen (KamLAND-Zero neutrino) is the liquid scintillator experiment and successor of KamLAND detector. Its interest is in  $^{136}\text{Xe}$ . It went into operation in 2011 in Kamioka mine (Japan). The whole setup comprises 330 kg of  $^{136}\text{Xe}$  in form of 13 tons of Xe-loaded liquid scintillator. Neither this experiment have seen an excess in the energy region of  $0\nu\beta\beta$  setting the low limit on  $0\nu\beta\beta$  half-life (for  $^{136}\text{Xe}$ ) at the level of  $1.9 \times 10^{25}$  yr (90% C.L.) [49]. The aim of next experiment - the SNO+ - is to become the largest scintillator detector in the world. It will be placed in the Sudbury Neutrino Observatory - 2 km deep underground laboratory inside Vale's Creighton Nickel mine near Sudbury, Ontario, Canada. It is the deepest facility in the world of this type. The object of study is  $^{130}\text{Te}$ . 780 tonnes of LAB (Linear AlkylBenzene) scintillator will be installed and loaded with  $^{130}\text{Te}$ . The signal will be read out by 9 500 8" PMTs. The experiment will aim to reach sensitivity of neutrino mass on the level of 0.1 eV.

### Tracker-Calorimeter experiments

This type of  $0\nu\beta\beta$  take advantage from the information about particle energy from calorimeters with position and momentum information obtained from trackers. This method is very important step towards background rejection. It is capable to reject the events based simply on a event topology.

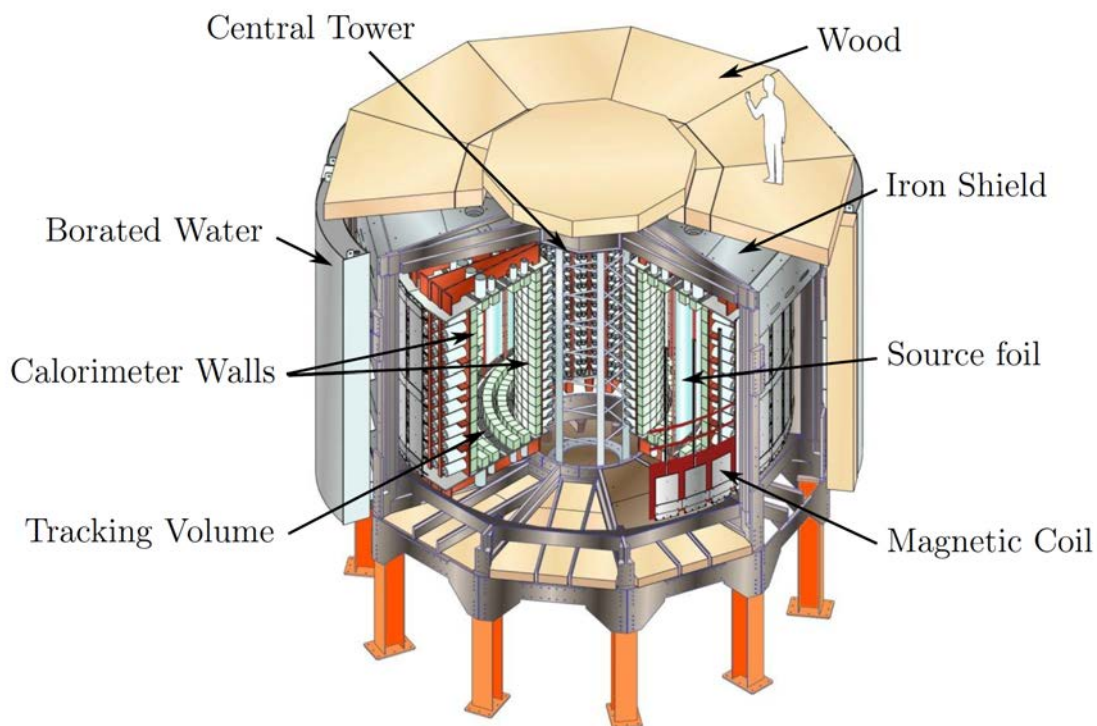


Figure 1.8: Schematic section of NEMO-3 experiment [60].

Main aim of NEMO-3 (The Neutrino Ettore Majorana Observatory) experiment was precise measurement of  $2\nu\beta\beta$  half-lives of several isotopes as well as search for  $0\nu\beta\beta$ . From all 11 different isotopes known to be  $2\nu\beta\beta$  radioactive it was NEMO-3 which managed to measure 7 of them including one measurement of  $2\nu\beta\beta$  transition to excited state. Whole

project started in 1990s with two prototypes NEMO-1 [61] and NEMO-2 [62].

In NEMO-3 [63, 64] electrons coming from  $0\nu\beta\beta$  were detected by scintillating calorimeters and tracked by tracking wires in Geiger mode (Figure 1.8).

The geometry of detector was of cylindrical shape divided into 20 sectors. These sectors were dedicated to different  $0\nu\beta\beta$  isotopes, namely:  $^{100}\text{Mo}$  (12 sectors),  $^{82}\text{Se}$  (2 sectors),  $^{130}\text{Te}$  (2 sectors),  $^{116}\text{Cd}$  (1 sector). Small volumes of  $^{150}\text{Nd}$ ,  $^{96}\text{Zr}$  and  $^{48}\text{Ca}$  were also measured. Finally, sectors composed of Copper and very pure oxide of natural Tellurium were used for measurements of external background in the experiment. The distribution of the sources in the experiment and their amounts are shown in the Figure 1.9.

Energy and time-of-flight of electrons was acquired from 1 940 plastic scintillator blocks. Data from blocks were read out by 3" and 5" photomultiplier tubes (PMT). The information about electron tracks were obtained by 270 cm long vertical Geiger wires enclosing the source foils positioned in the center of each sector (see Figure 1.8). The tracking method is very effective way to reduce background based on rejection by the event topology. Solenoid surrounding the detector produced 25 G magnetic field (parallel to the Geiger wires) inside the experiment. The whole detector was enclosed in 20 cm thick external shield made of low radioactivity iron in order to reduce  $\gamma$ -rays and thermal neutrons. Another layer of shielding, made of borated water, was applied on top of the iron. It served for thermalisation of fast neutrons and capture of thermal neutrons.

NEMO-3 was placed in LSM (Laboratoire Souterrain de Modane) in Fréjus tunnel on the French - Italian border. The laboratory is in the depth of 1 700 m protected by rock which corresponds to 4 800 m.w.e. During the run period of 8 years (January 2003 - January 2011) which corresponds to 5 years of data taking,  $0\nu\beta\beta$  was not observed. NEMO-3 managed to

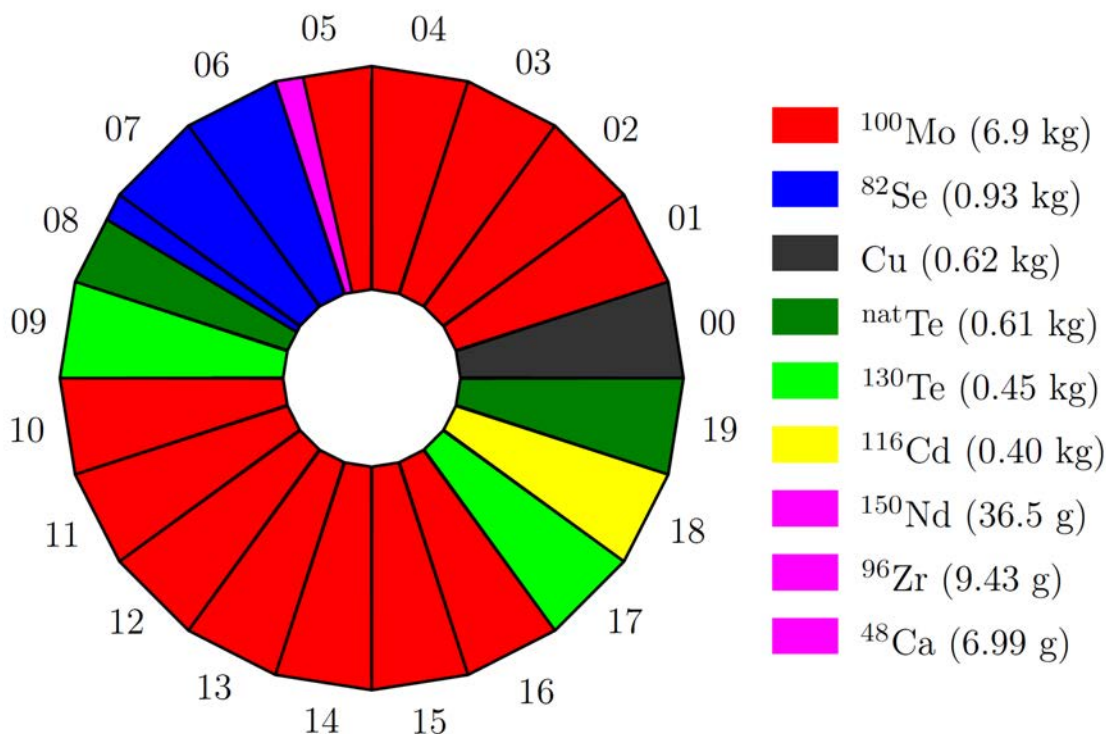


Figure 1.9: Composition of sectors containing measured isotopes in NEMO-3 experiment [60].

set the lower limit for  $0\nu\beta\beta$  on the level of  $10^{24}$  yr [47]. Moreover,  $2\nu\beta\beta$  half-lives of many isotopes were measured for the first time in history. Their full list can be found in Table 1.3.

Decay	Q-value [keV]	$T_{1/2}$ [yr]	Ref.
$^{48}\text{Ca} \rightarrow ^{48}\text{Ti}$	4267	$[6.4_{-0.6}^{+0.7}(\text{stat})_{-0.9}^{+1.2}(\text{syst})] \times 10^{19}$	[65]
$^{82}\text{Se} \rightarrow ^{82}\text{Kr}$	2996	$[(9.93 \pm 0.14(\text{stat}) \pm 0.72(\text{syst})) \times 10^{19}]$	[60]
$^{96}\text{Zr} \rightarrow ^{96}\text{Mo}$	3349	$[2.35 \pm 0.14(\text{stat}) \pm 0.16(\text{syst})] \times 10^{19}$	[66]
$^{100}\text{Mo} \rightarrow ^{100}\text{Ru}$	3034	$[0.716 \pm 0.001(\text{stat}) \pm 0.054(\text{syst})] \times 10^{19}$	[67]
$^{100}\text{Mo} \rightarrow ^{100}\text{Ru}(0_1^+)$	1905	$[5.7_{-0.9}^{+1.3}(\text{stat}) \pm 0.8(\text{syst})] \times 10^{20}$	[68]
$^{116}\text{Cd} \rightarrow ^{116}\text{Sn}$	2813	$[2.74 \pm 0.04(\text{stat}) \pm 0.18(\text{syst})] \times 10^{19}$	[69]
$^{130}\text{Te} \rightarrow ^{130}\text{Xe}$	2528	$[7.0 \pm 0.9(\text{stat}) \pm 1.1(\text{syst})] \times 10^{20}$	[70]
$^{150}\text{Nd} \rightarrow ^{150}\text{Sm}$	3371	$[9.11_{-0.22}^{+0.25}(\text{stat}) \pm 0.63(\text{syst})] \times 10^{18}$	[71]

Table 1.3: Values of half-lives of  $2\nu\beta\beta$  nuclei measured by NEMO-3. Q-values are taken from National Nuclear Data Center website [44].

## SuperNEMO Experiment

SuperNEMO represents a new generation of  $0\nu\beta\beta$  experiments. Taking advantage from experience with its predecessor, NEMO-3, its detection principle is based on the detection of two electrons coming from double beta-decay. The aim is to study  $0\nu\beta\beta$  of  $^{82}\text{Se}$ . Technology which allows to reconstruct the topology of double beta decay events is unique in the field. It improves the background rejection and measurement of otherwise unobservable quantities, for instance the angular distribution of the electrons. It might be a crucial step towards a new physics.

### 2.1 Laboratoire Souterrain de Modane

$0\nu\beta\beta$  experiments are very sensitive experiments and it is important to protect them against natural radioactivity occurring on the Earth's surface. SuperNEMO experiment is, therefore, placed in Laboratoire Souterrain de Modane (LSM). LSM is underground laboratory and it is the deepest of its kind in Europe. It is placed in South-East of France on the border between France and Italy near Modane. LSM is located in Fréjus highway tunnel 1.7 km underground under the peak of mount Fréjus which represents 4800 m.w.e. The scheme of the tunnel and the mount Fréjus can be seen in Figure 2.1. As it is visible in the scheme, the laboratory is placed near the border, on the French side. Throughout the thesis, I follow

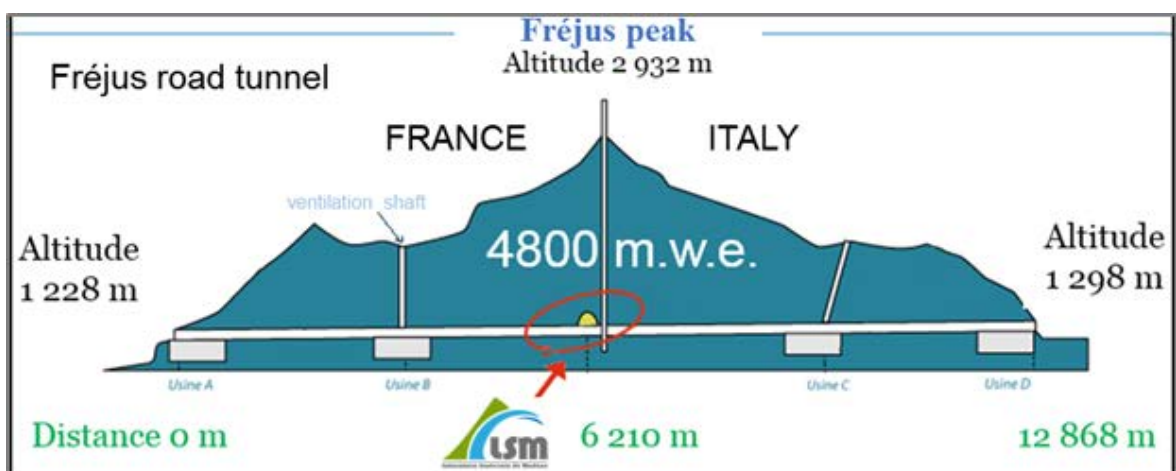


Figure 2.1: Scheme of mount Fréjus and the Fréjus highway tunnel. Laboratory LSM is placed roughly in the middle of the tunnel, right under the peak of the mountain.



naming convention normally used by collaboration. Parts of the detector are given adjectives based on the country they are closer to. Therefore, the terms like "Italian calorimeter" or "French calorimeter" designate the calorimeter wall on Italian side or French side, respectively. Same convention applies for tracker, as well as for other parts of the detector. The atmospheric muons are in the laboratory attenuated by a factor of million. Only 4-5 muons pass to the laboratory per day.

## 2.2 Description of the Detector

Since 2005, large effort was invested into the research and development of SuperNEMO experiment. The main improvements in comparison to its predecessor NEMO-3, were achieved in the enrichment and radiopurity of  $^{82}\text{Se}$  source foils, the energy resolution of calorimeters and the reduction of problematic Radon background.

SuperNEMO experiment aspires to reach sensitivity of  $10^{26}$  years to half-life of  $0\nu\beta\beta$  in  $^{82}\text{Se}$ . The SuperNEMO is designed to measure 100 kg of  $^{82}\text{Se}$  distributed among 20 modules [72, 73].

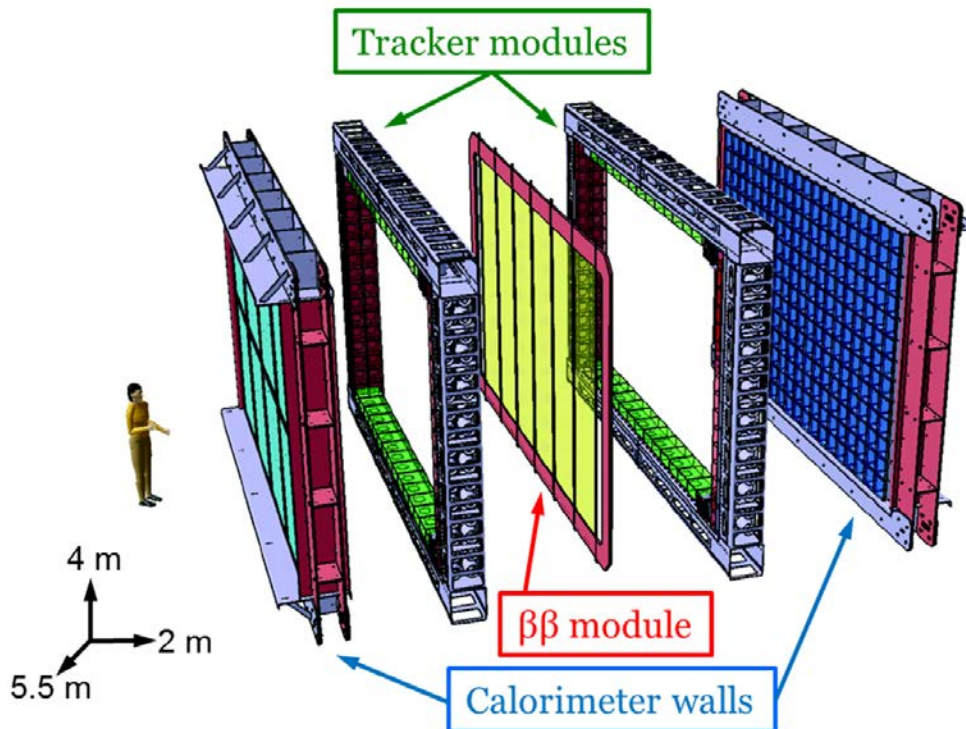


Figure 2.2: Schematic picture of one SuperNEMO module designed to study 7 kg of  $^{82}\text{Se}$  in form of foils ( $\beta\beta$  module).

The first module, the demonstrator, will start phase of data taking in early 2019. The aim of demonstrator is to prove the concept and to fine tune all the systems. Demonstrator with roughly 6 kg of  $^{82}\text{Se}$  should be able to reach sensitivity of  $4.9 \times 10^{24}$  years to half-life of  $0\nu\beta\beta$  in  $^{82}\text{Se}$ .

A SuperNEMO module is composed of three main parts organized in a planar geometry. The source foil ( $\beta\beta$  module) composed of enriched Selenium is in its center sandwiched by tracking detector. This is all encapsulated between ensemble of scintillating block calorimeters (Figure 2.2).

### 2.2.1 $^{82}\text{Se}$ Source Foils

$0\nu\beta\beta$  experiments observing isotopes such as  $^{76}\text{Ge}$ ,  $^{130}\text{Te}$ ,  $^{134}\text{Xe}$  or  $^{136}\text{Xe}$  typically take advantage of approach when the source isotope serves as the detector at the same time. SuperNEMO plays unique role in the field because its source is independent of detection system. Such an approach has an advantage of variability. Experiment of this type can measure various different isotopes. The approach, naturally, brings the question of the choice of the most suitable source isotope. In NEMO-3, seven different isotopes ( $^{48}\text{Ca}$ ,  $^{82}\text{Ca}$ ,  $^{96}\text{Zr}$ ,  $^{100}\text{Mo}$ ,  $^{116}\text{Cd}$ ,  $^{130}\text{Te}$  and  $^{150}\text{Nd}$ ) were measured in parallel, however, the one with the most observed mass was  $^{100}\text{Mo}$ . There are several important requirements which have to be met in order to choose a suitable  $0\nu\beta\beta$  decay candidate to be observed. First of all, it is important to consider  $Q_{\beta\beta}$  value of the decay of the isotope. Gamma radiation from natural background can reach up to 2.615 MeV ( $^{208}\text{Tl}$  from  $^{232}\text{Th}$  chain). The higher, the  $Q_{\beta\beta}$  value is above this value, the better chance is to eliminate the background in the region of interest. Natural elements are usually composed of several different isotopes. High abundance of isotope of interest in the natural (or already enriched) sample increases the exposure and gives higher chances to observe  $0\nu\beta\beta$ . If the abundance is not sufficient in the composition of naturally occurring element of choice, the enrichment should take place. The efficiency and difficulty of enrichment technology differs from isotope to isotope. It is another factor to be considered. Large phase-space of  $0\nu\beta\beta$  results into lower half-lives. In process of choice of the isotope, one should also take into account the phase-space factor of the isotope. Finally, it is also important to choose isotope with long half-lives of  $2\nu\beta\beta$ .  $2\nu\beta\beta$  is the main, and what is the most important, irreducible, background for  $0\nu\beta\beta$ . Long half-lives of the process for



Figure 2.3: Left: Source foil prepared in ITEP in Russia. Right: Source foil prepared in LAPP in France.

the isotope of choice can increase the chances to observe  $0\nu\beta\beta$ .

Isotope  $^{82}\text{Se}$  was chosen for SuperNEMO demonstrator thanks to its natural abundance and high value of  $Q_{\beta\beta}$  (2996 keV). Approximately 7 kg of enriched isotope will be placed in demonstrator in form of the foil strips whose thickness will reach 40-55 mg/cm<sup>2</sup>. The isotope is enriched by centrifugation method which can enrich natural Selenium up to 90% to 99% content of  $^{82}\text{Se}$ . After a development, the method might be applicable to  $^{150}\text{Nd}$  with  $Q_{\beta\beta}$  value of 3371 keV which would make  $^{150}\text{Nd}$  an isotope of choice for future SuperNEMO modules.

$^{82}\text{Se}$ , after the enrichment is finished, has a form of powder. The powder is deposited on a very thin Mylar foil. The foils were prepared in ITEP (Institute for Theoretical and Experimental Physics) in Moscow and LAPP (Laboratoire d'Annecy-le-Vieux de Physique des Particules) in Annecy (Figure 2.3). The source foils are already installed in the LSM.

### 2.2.2 Tracking Detector

Source foil is, from both sides, surrounded by tracking detector (tracker). The tracker is composed of 14 970 wires operating in Geiger mode. Research and development of the tracker took place at University of Manchester in Great Britain. Majority of the (Geiger) wires are made of steel with diameter of 40  $\mu\text{m}$  to 50  $\mu\text{m}$ . The wires were assembled at the Manchester University and sent to Mullard Space Science Laboratory (MSSL) of the University College London (UCL). There, they were assembled into form of 2034 cells with a help of robot (Figure 2.4). The tracker module is divided into four parts named C0, C1, C2 and C3. Each quarter was assembled in MSSL in a large clean tent. The tracker will be encapsulated in a radon-tight chamber filled with a gas. The gas will be composed of 94.85% of Helium, 4% of Ethanol 1% of Argon and 0.15% of water. The tracker is already installed in LSM.



Figure 2.4: Photos of robot developed for the preparation of the tracker cells.

### 2.2.3 Calorimeters

The energy of the electrons emitted in double beta decay events is measured by calorimeter made of plastic scintillators. The calorimeter is composed of three main parts, the "main calorimeter (walls)", the "X-calo" (xcalo) and "gveto". The three parts surround the detector

in all five sides except for the bottom as it can be seen in scheme in Figure 2.5. The scheme is for simplicity missing one main calorimeter wall and one xcalo wall. In the figure also the definition of coordinate system is shown. The definition is strictly followed throughout the whole thesis. Basic calorimeter unit is so-called optical module. The main parts of the optical module are plastic scintillator (in our case polystyrene) and PMT which is glued to the plastic scintillator for tight connection. Xcalo walls are placed at the smaller, vertical, sides of the tracker. The calorimeters were directly connected to the tracker, its production was, therefore done at UCL in Great Britain. Xcalo consists of 128 optical modules, each with resolution of roughly 12% at 1 MeV. In contrary, gveto, on top of the module, is composed of 64 optical modules with resolution of 15% at 1 MeV. Both xcalo and gveto are using 5" PMTs resued from NEMO-3. Finally, the main calorimeter, covers the detector from both sides parallel to source foil. It consists of two main walls composed of 520 optical modules. One wall is on the Italian side while the opposite one on French side. Their assembly took place in CENBG (Centre Etudes Nucléaires de Bordeaux Gradignan). Plastic scintillator in optical module is based on the polystyrene. 0.6% of para-terphenyl (pTP) and 0.05% of 1,4-bis(5-phenyloxazol-2-yl) benzene (POPOP) fluorescent additives are serving as wavelength shifters for better detection efficiency. The optimization of content of pTP and POPOP with respect to the energy resolution was achieved in IEAP CTU (Institute of Experimental and Applied Physics Czech Technical University) in Prague. In [74] it was shown that PS blocks with 1.5% of pTP and 0.05% of POPOP can reach better energy resolution. The production process was switched to these enhanced PS blocks after the study was done. The production process of main calorimeter walls is presented in Section 2.3. PMTs used to build main calorimetric walls are 8" in diameter with resolution of 8% at 1 MeV.

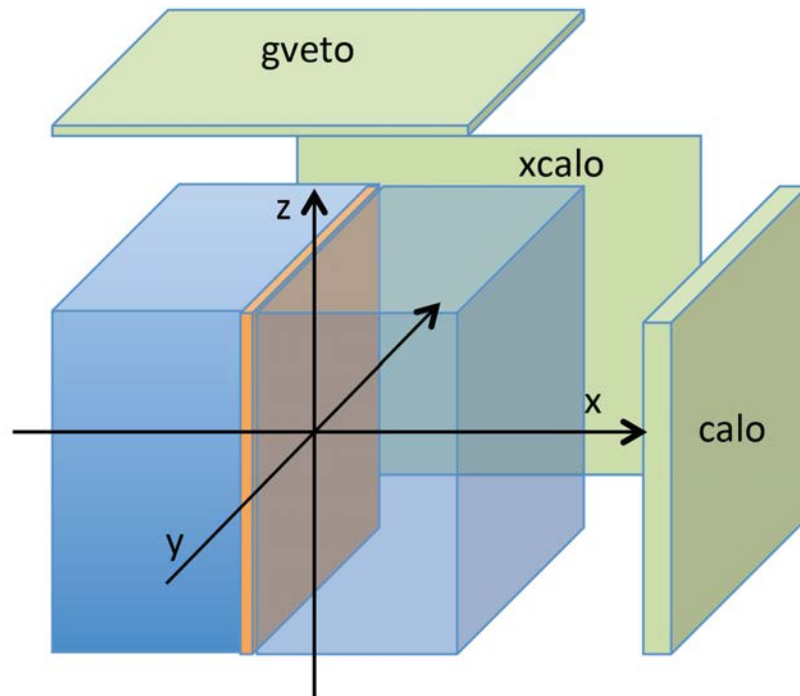


Figure 2.5: The scheme of SuperNEMO calorimetric walls. Except for main walls ("calo") SuperNEMO module will be composed of x-calorimeter walls ("xcalo") on the short side and g-veto on top ("gveto"). The picture also shows standard definition of coordinates, used for example for simulation purposes, where y and z direction are defining the plane of source foil and x is perpendicular.

### 2.2.4 Status of the Demonstrator

The goal of the demonstrator is to achieve sensitivity of  $0\nu\beta\beta$  half-life at the level of  $6 \times 10^{24}$  yr, which is equal to upper neutrino mass limit of 0.2 - 0.4 eV. Furthermore, in full design (20 modules) with more than 100 kg of  $^{82}\text{Se}$ , the limit on  $0\nu\beta\beta$  half-life is expected at the level of  $10^{26}$  yr, yielding the upper limit on neutrino mass on the level of 0.04 - 0.11 eV.

Currently, the works on construction of demonstrator parts (source foil, tracker and calorimeters) are finished and they are all already present in LSM. The cabling works are in progress and should be finished at the beginning of 2019. Automatic calibration source deployment system (see also Chapter 3) was already installed. The SuperNEMO should obtain first data in 2019. In parallel, the works on shielding design are taking place.

## 2.3 Construction of Main Calorimeter Walls

Assembly of the optical modules for main calorimeter walls was performed in CENBG and finished in summer 2016. In autumn 2016, the main calorimeter walls were already built at the LSM. During my first stay in CENBG in first half of 2016, I took part in the assembly of optical modules. Let me briefly present the procedure in following sections.

### 2.3.1 Optical Module Production Procedure

The basic constituent of each optical module is a polystyrene block of 10 kg produced in company NUVIA (former ENVINET) in Kralupy nad Vltavou near Prague, Czech Republic. As waveshifters, para-terphenyl (pTP) and 1,4-bis(5-phenyloxazol-2-yl) benzene (POPOP) fluorescent additives were mixed into polystyrene (PS) in the process of production. These

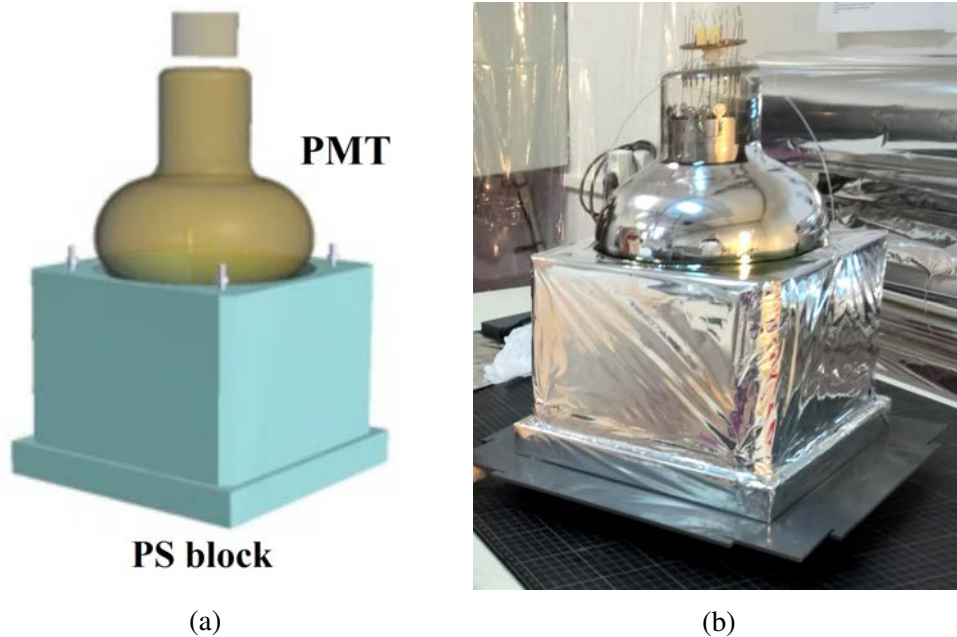


Figure 2.6: (a): Simplified layout of optical module consisting of polystyrene block and photomultiplier tube. (b): Real optical module after wrapping into Teflon and Mylar is finished.



Figure 2.7: (a): Picture of real PS block produced by NUVIA. (b): Production number placed on top of each block.

blocks were shipped to CENBG (near Bordeaux) and their production of optical modules was finalized there along with tests of the performance.

One finalized optical module consists of two main parts: aforementioned PS block and 8" (or 5", for xcalo and gveto) PMT glued to the block (Figure 2.6).

In order to avoid impurities in the preparation process, whole production was placed in a clean room. At the beginning, the polystyrene modules were cleaned with acetone, isopropanol and distilled water. After drying, the dimensions of the PS block were measured and visually checked for impurities in polystyrene. Each block was labelled on top by production number (Figure 2.7b). In next step, optical fibres were glued on top (Figure 2.8a). The fibres serve for LED calibration of optical modules.

Subsequently, Hamamatsu PMT was glued on top into the spherical cut-out in the block (Figure 2.8b). The drying process took 24 hours. The glue used for this step was chosen with regard to its radiopurity (same applies to all materials used in construction of SuperNEMO demonstrator) and its refractive index close to the refractive indices of PS block and PMT. Two different types of PMTs are used in the SuperNEMO demonstrator. For main walls 8" Hamamatsu PMTs were employed while for x-calorimeter and g-veto it was 5" PMTs previously used in NEMO-3 experiment. After the PMT was in the place, the optical module was wrapped into three layers of teflon tape (0.6 mm of total thickness) from sides (Figure 2.8c) and two layers of mylar foil (total thickness 12  $\mu\text{m}$ ) from bottom and from sides (Figure 2.8d). This procedure was done in order to improve the light yield of the optical module. Thanks to wrapping, the photons were confined inside the module and guided to PMT more effectively. Moreover, it prevented outside photons to enter the optical module. In the process, electronics responsible for data collection from PMT was soldered on top.

### 2.3.2 Optical Module Resolution Test and Finalization

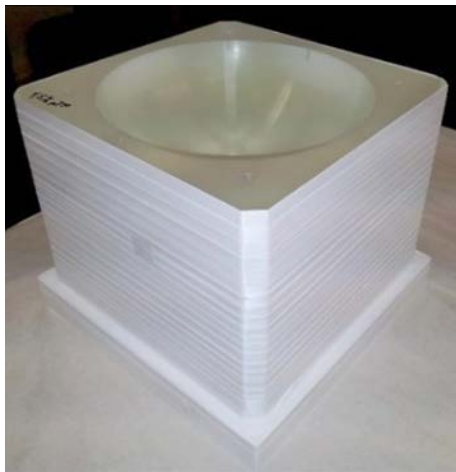
The modules which went through all previous procedure steps were subsequently tested for their resolution with  $^{90}\text{Sr}$  source [75]. Electrons from  $^{90}\text{Sr}$  were bent towards the collimator by electromagnet and 1 MeV electrons were chosen. These electrons impacted into the optical module from the bottom and spectrum was obtained. Whole testing process took place in light-tight box to prevent unwanted light to be registered. The value of resolution



(a) Gluing of optical fibres.



(b) PMT gluing.



(c) Teflon wrapping.



(d) Mylar wrapping.



(e) Encapsulation of eight optical modules into the shielding.



(f) Final brick prepared to be packed, shipped and assembled.

Figure 2.8: Different steps of optical module preparation process. Note that in steps c) and d) PMT is missing on top. These optical modules were used for testing and PMT was glued to them after they were wrapped in Teflon and Mylar.

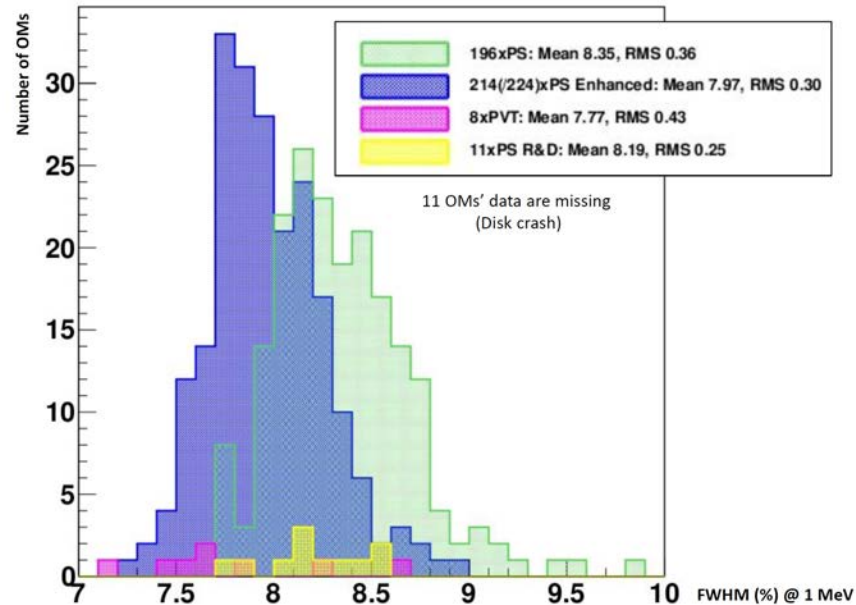


Figure 2.9: Histogram of resolution of optical modules with 8'' PMTs used in the main wall of SuperNEMO demonstrator (data about eleven of them are missing due to disc crash). Modules of standard quality (PS - green) were produced before the composition of pTP and POPOP was optimized [74]. Enhanced optical modules (PS Enhanced - blue) are produced after the mentioned optimization. Eight modules (PVT - pink) were participating in process of research on composition of pTP and POPOP and their composition differs slightly. Eleven optical modules (PS R&D - yellow) were used to develop the optical module preparation procedure.

of each module was obtained. Histogram showing the resolution of all optical modules with 8'' PMTs can be seen in Figure 2.9. After the resolution measurement, eight optical modules were grouped on the preparation table in two rows of four modules. Very high radiopurity glue was applied on top of each. A metallic shielding protecting optical modules from magnetic field was placed on top in a way that only bottom faces of each optical module was sticking out (Figures 2.8e and 2.8f). The connection between modules was strengthened by 32 plastic screws. Such optical brick was then packed in the box and shipped to LSM.

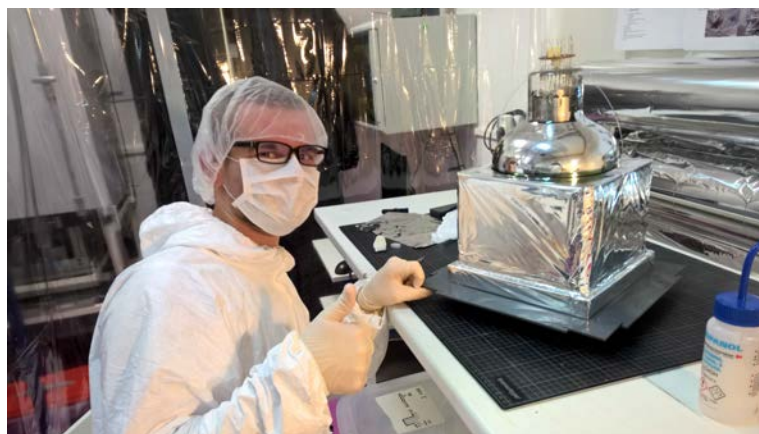


Figure 2.10: Me, in clean room in CENBG, with my first completed optical module.



## Measurements of $^{207}\text{Bi}$ Calibration Sources

In order to calibrate NEMO-3 calorimeters,  $^{207}\text{Bi}$  sources were employed. The same strategy was chosen for SuperNEMO experiment. However, experience with NEMO-3 have shown that insufficient knowledge of calibration source properties can give rise to large experimental uncertainties on the half-life of  $2\nu\beta\beta$  as well as lower the sensitivity for half-life of  $0\nu\beta\beta$ . These effects can be removed by precise investigation of calibration sources. In this chapter I will describe in detail all the necessary measurements which I performed in order to better quantify calibration sources.

### 3.1 SuperNEMO Calibration System

Before opening the discussion about the sources, let me briefly describe SuperNEMO calibration system. Calibration of a SuperNEMO module is a process which will take place several times per month. For this purpose, the calibration sources have to be placed and removed regularly from well defined positions inside the module. However, during the operation a SuperNEMO module should be sealed, preventing any leak of the atmosphere which is inside of the tracker. This limits the access inside, which makes manual operation of calibration system impossible. Therefore, SuperNEMO calibration will be performed by automatic deployment developed by group from University of Texas at Austin [76].

#### 3.1.1 Automatic Calibration Source Deployment System

Between some of the adjacent pairs of  $^{82}\text{Se}$   $\beta\beta$  source foil stripes there is a narrow gap (Figure 3.1 - Left) designed for the insertion of  $^{207}\text{Bi}$  calibration sources. The automatic calibration source deployment system will consist of six Copper plumb bobs suspended by steel wires from SuperNEMO source frame. Each wire will be wrapped on a wheel on top of the SuperNEMO module. Wheel can be rotated by a stepper motor. Between the plumb bob on the bottom and wheel on top 7 calibration sources will be attached to steel wire. Stepping motor is able to vertically adjust the position of the sources or to remove them completely from the SuperNEMO module. Symbolic scheme of the deployment system can be found in Figure 3.1 - Right.

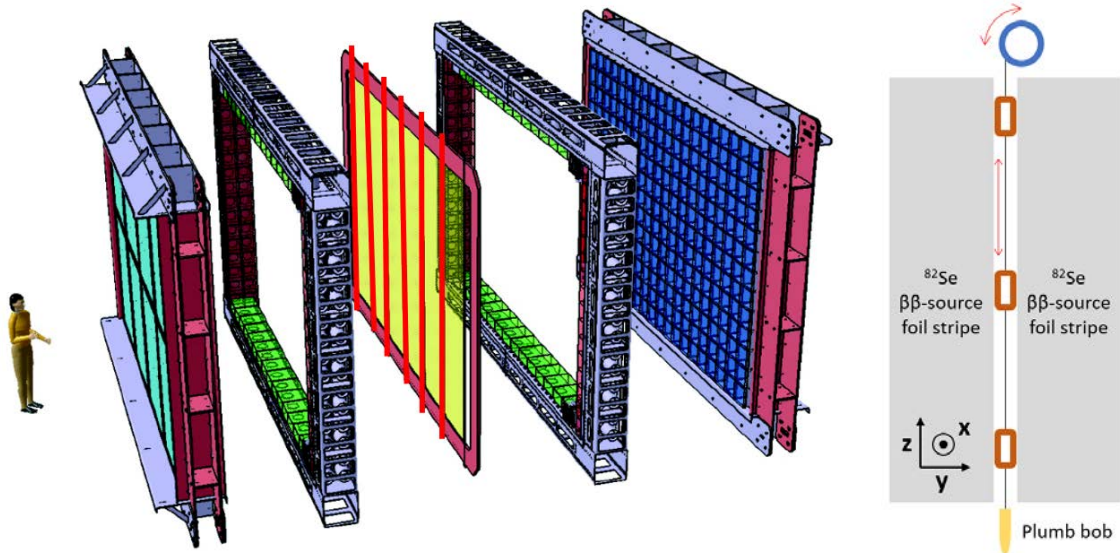


Figure 3.1: Left: Red vertical lines symbolize six gaps between  $\beta\beta$  source foil strips where automatic deployment system deploys the calibration sources. Right: Simplified scheme of  $^{207}\text{Bi}$  deployment system. In the gap between  $^{82}\text{Se}$   $\beta\beta$  source foil the sources (brown rectangles) can be vertically (red arrows) deployed by automatic system. Deployment will be controlled by stepping motor connected to wheel on top (blue colour) which is able to wrap the steel wire. Plumb bob has a role of load keeping the wire straight. It is marked by light orange colour at the bottom. Note that the scheme is only symbolic, the number of sources is incorrect and the dimensions in the figure are not to scale.

### 3.1.2 Description of Calibration Sources

SuperNEMO calibration sources have a rectangular shape (Figure 3.2). A source has a form of  $^{207}\text{Bi}$  droplet deposited between two transparent mylar foils and sealed by radiopure Copper frame. Example of such source is on the right side of Figure 3.2. Sources in these form will be used in SuperNEMO calibration for the automatic deployment system. However, as I have already mentioned, the sources were inherited from NEMO-3 experiment. Figure 3.3 shows all available sources from NEMO-3 experiment. Large part of the available sources had extra plastic envelope glued to them resulting into slight change in the geometry of the source. For the purpose of this thesis I will refer to them as to sources "with plastic envelope" while the former type I will naturally call "without plastic envelope". The plastic envelope was useful as a holder in NEMO-3 experiment and will be removed from the sources before using them for calibration of SuperNEMO experiment. However, during the studies described in the thesis, some of the sources had still the envelope on which I had to take into account in the process of data analysis and comparison of the sources. More about the naming convention and the practical difference between these two types of sources will be discussed in the following sections of this chapter.

Dimensions of the sources were measured by two different methods so it was possible to cross check the results. First method which I performed myself was indirect. I took photos of source of choice with a ruler. The ruler gave a scale. Number of pixels per centimeter counted thanks to the ruler in the photo served as scaling coefficient. Then I counted number of pixels representing individual dimensions introduced in Figure 3.2. Using the scale coefficient I represented these dimensions in cm. As one can imagine, such a methodology is dependent on the perspective distortion introduced when taking the photo.

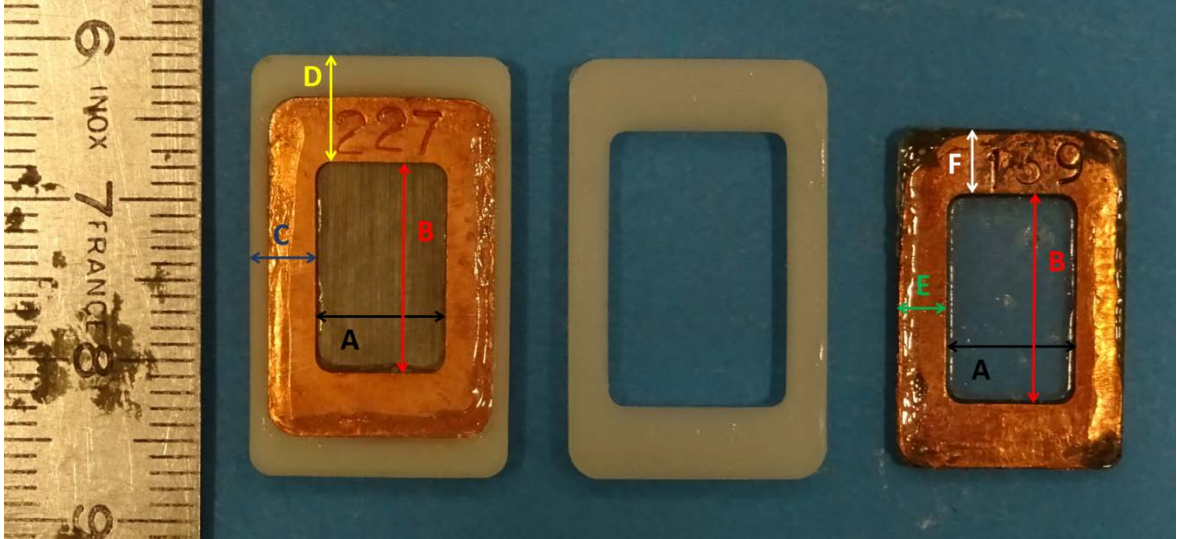


Figure 3.2: Photo of the SuperNEMO calibration sources. The source on the right is what I call "without plastic envelope" and the one on the left, next to the ruler is source which I will call "with plastic envelope" because the white plastic frame (in the middle of the photo) was glued to them. Dimensions defined in the photo are listed in Tables 3.1 and 3.2.

Even though, I took the picture perpendicularly to the plane of the source and assumed the distortions to be negligible, it is still non-trivial to satisfactorily quantify them. Therefore, I asked my colleague Ramon Salazar to perform direct measurement using calliper. Both methods are within reasonable difference consistent with each other. Measured values can be found in Tables 3.1 and 3.2.

	A [mm]	B [mm]	C [mm]
Pixel counting	8.2	13.11	4.14
Direct measurement (calliper)	7.91	12.99	4.15

Table 3.1: Source dimensions A, B and C defined in Figure 3.2 measured by pixel counting and direct measurement with calliper.

	D [mm]	E [mm]	F [mm]
Pixel counting	6.61	3.12	3.98
Direct measurement (calliper)	6.66	3.2	4.01

Table 3.2: Source dimensions D, E and F defined in Figure 3.2 measured by pixel counting and direct measurement with calliper.

### 3.2 Mapping of $^{207}\text{Bi}$ Deposition Distribution in Calibration Sources

As it was mentioned in the introduction to this chapter, it is important to have sufficient knowledge of calibration sources. Mapping of the calibration sources can provide a lot of

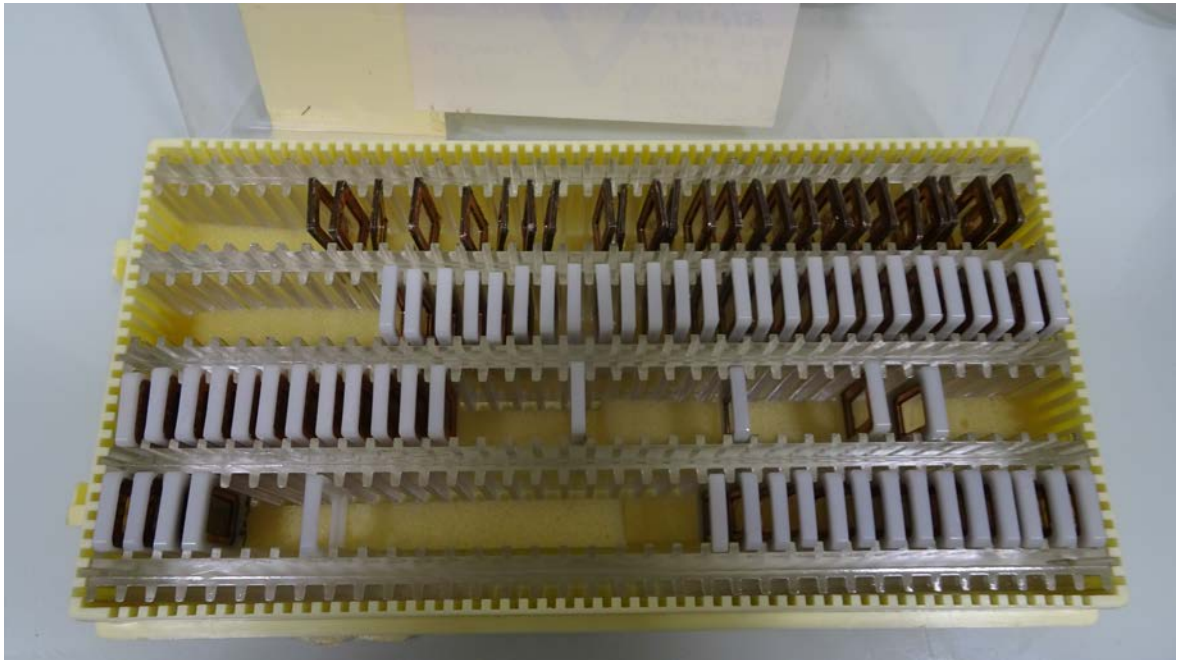


Figure 3.3: Case with all available  $^{207}\text{Bi}$  calibration sources.

information about deposition quality of radioactive isotope in the production process. Moreover, deposition distribution maps for each sample of calibration source can be used as an input for Monte Carlo simulation to improve quality of calibration. Between September 2017 and January 2018, I performed complete deposition distribution study of 49  $^{207}\text{Bi}$  calibration sources. The section is dedicated to the description of methodology, data analysis and results of this study.

#### 3.2.1 Timepix Pixel Detectors

Pixel semiconductor detector is a tool of choice in a broad range of imaging applications. One of its biggest advantages lies in the design. Each pixel contains separate electronics with digital counter which allows each particle to be processed separately. One pixel is composed of semiconductor diode with reverse bias voltage applied to both ends. The voltage causes the depletion zone between two semiconductors in the diode to become wider. When particle passes through the depletion zone, charge is created by electric field, collected at the contacts and afterwards processed by the read-out electronics. More information about semiconductor pixel detectors and their applications can be found in [77].

Timepix pixel detectors which I used in the study belong to category of so called hybrid pixel device. Hybrid pixel detector consist of two chips. First chip is the sensor which is composed of semiconductor diode with one common and one pixelated contact. Second chip contains read-out electronics for all pixels. Their advantage to the monolithic pixel detectors (with one chip) is that their sensor can be made of range of materials (e.g. Si, GaAs, CdTe, etc.) while monolithic are limited uniquely to Silicon. However, in the study, I used three Timepix detectors with Silicon chip. Their photos can be seen in the Figure 3.4. The chip thickness of first two detectors (H04-W0163 and H11-W0163) was  $300\ \mu\text{m}$  while the last one (L05-W0163) had chip of  $1\ \text{mm}$  thickness. All three consisted of 65536 pixels aligned in  $256 \times 256$  square matrix. Size of one pixel is  $55 \times 55\ \mu\text{m}^2$ . Full chip covers the area of  $1.4 \times 1.4\ \text{cm}^2$ .



Figure 3.4: Photos of the Timpepix pixel detectors used in the study. From left: H04-W0163 (300  $\mu\text{m}$  Silicon sensor), H11-W0163 (300  $\mu\text{m}$  Silicon sensor) and L05-W0163 (1 mm Silicon sensor). The chip is located in the top part of the detector, lower, blue part is USB interface developed in IEAP CTU in Prague [78].

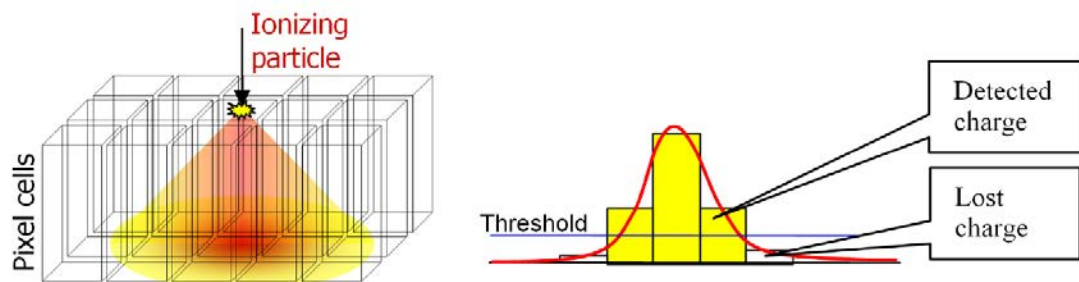


Figure 3.5: Scheme of charge sharing effect in pixel detector. Picture taken from [77]. Left: Charge cloud created by ionizing particle is expanding into adjacent pixels due to electromagnetic repulsion and diffusion. Right: Plot of charge distribution detected by central pixel (peak in the middle) and adjacent pixels (tails) due to charge sharing effect. If charge in adjacent pixels is lower than threshold in the pixel the charge is lost and energy of the particle is underestimated.

#### 3.2.2 Detector Energy Calibrations

Timepix detector family is a successor of Medipix detector family developed by Medipix collaboration [79, 80]. Medipix detectors were used as a counting detectors capable of counting particles in individual pixels. The essential upgrade which Timepix detector family received was a clock counting in each pixel. Each pixel in Timepix detector can be configured to operate in one of three following modes: Medipix mode, Timepix mode and Time over threshold (ToT) mode. In Medipix mode, as the name suggest, the particles numbers are counted in each pixel without any extra information about particle. Timepix mode allows to study the coincidences of the impacting particles, as it is capable of measuring time of arrival of the particle. In ToT mode, Timepix detector is able to provide information about the energy left by the particle in individual pixels. A limitation for this type of detector is caused by effect called charge-sharing. In the case when pixels are small and/or sensor is thick, the collected charge cloud created in one pixel expands due to charge repulsion and diffusion and can be collected by adjacent pixels (Figure 3.5 - Left). In the adjacent pixels the tail of

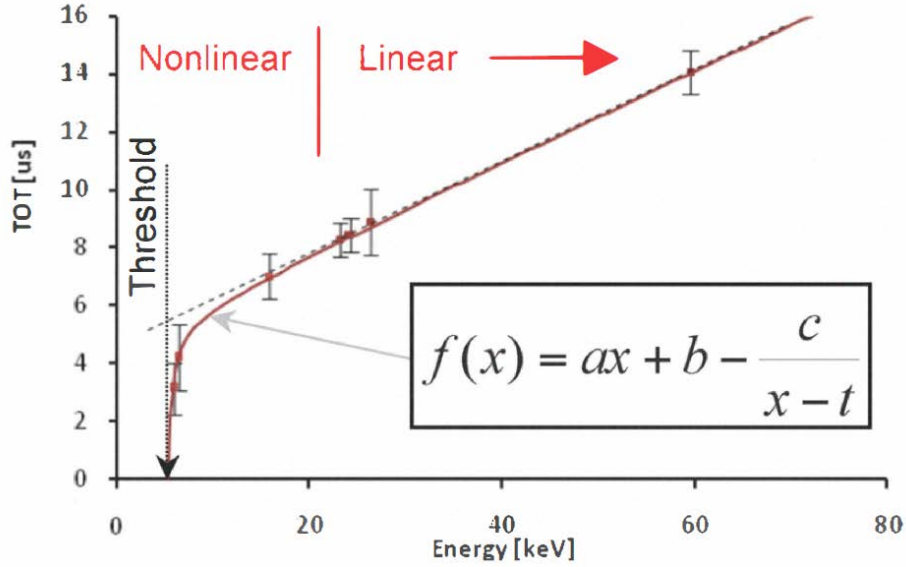


Figure 3.6: Relation between time over threshold and energy used for energy calibration of pixel detectors. Source of image: [81].

the charge might not exceed the threshold value and therefore it becomes lost (Figure 3.5 - Right). In consequence, collected charge is often lower than its original value which affects the energy resolution. In ToT mode, energy is not obtained by direct measurement and calibration is needed. The principle of measurement in the ToT mode is as following: clock in the pixel measures the period during which charge signal caused by impacting particle exceeded pre-set threshold in the pixel. This quantity is called Time over Threshold (ToT). There is a relation between energy deposited in the pixel and ToT which was measured and modelled by surrogate function given by Equation 3.1.

$$\text{ToT}(E) = aE + b - \frac{c}{E - t}. \quad (3.1)$$

The equation represents Time over Threshold as a function of the energy deposited in the pixel by incident particle.  $a$ ,  $b$ ,  $c$  and  $t$  are the parameters of the function. While  $t$  represents an energy threshold in the pixel,  $a$  and  $b$  define the linear part of the curve valid as a good approximation for majority of the energy range. The function is depicted in the Figure 3.6. Due to a complexity of the sensor, it is natural to expect different response in different pixels. Therefore, energy calibration has to be performed separately for each pixel. In the process of energy calibration, detector is exposed to X-ray fluorescent radiation taking only clusters<sup>1</sup> of one pixel size into the account. Current leaked into the adjacent pixels due to the charge sharing effects can be estimated based on the simulations and corrected. More information about the calibration and charge sharing effect can be found in [81, 82, 83].

Before I could perform the measurements I needed to calibrate each one of the three detectors. As it was already mentioned, energy calibration has to be done for each pixel individually. In practice, this means to find set of parameters  $a$ ,  $b$ ,  $c$  and  $t$  in Equation 3.1, for each pixel separately. This can be really time consuming process taking into account a fact that we need to provide enough statistics for calibration to each one of the 65536 pixels in order to make fitting possible. As a first step before the calibration itself, I had to find

<sup>1</sup>Cluster is a group of adjacent pixels representing one particle which deposited energy in each pixel. Size of a cluster is given by number of pixels included in the cluster.

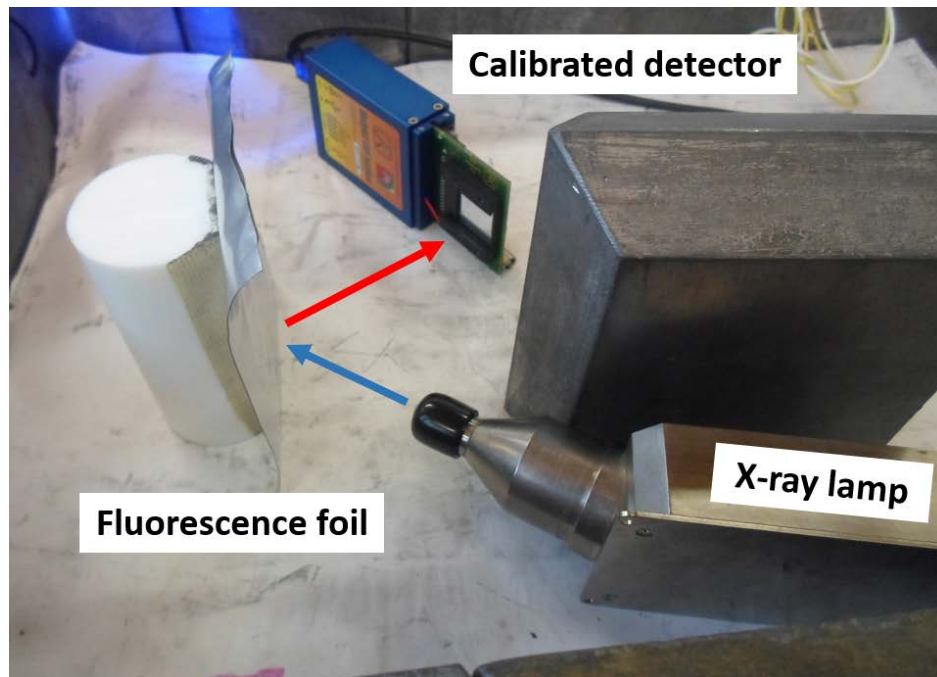


Figure 3.7: Photo of Timepix detector calibration setup. The X-ray lamp irradiates Fluorescent foil with spectrum of X-ray radiation (blue arrow). Atoms in the foil are excited and subsequently deexcited by X-rays of unique energy (red arrow). These rays impact the detector and provide the calibration.

appropriate value of biasing voltage for each detector. Biasing voltage (bias) is increasing the size of a depletion zone in the pixel (diode) improving the detection sensitivity of the pixel. After it reaches maximum, it saturates. I irradiated the chip with X-ray fluorescent radiation and measured rates while I was changing the bias of the detector supplied by voltage source. At the saturation point, I obtained value of the bias which I used for all the process of calibration and measurements. For 300  $\mu\text{m}$  thick Timepix detectors H04-W0163 and H11-W0163 I obtained bias value of 90 V and 100 V, respectively. It is provided by the USB interface in the Figure 3.4 [78]. However, for 1 mm detector, one needs extra voltage supply capable to deliver bias of 460 V (L05-W0163).

After setting the biases one needs to do so-called "threshold equalization". In Timepix detector, the pixels are designed to be identical to one another. However, in reality the differences occur. In threshold equalization, the global threshold value is fine tuned for each pixel in a way that the dispersion is as small as possible. Pixelman [84], a software interface for Timepix detectors, provides simple plugin which performs threshold equalization. It also gives possibility to mask noisy (faulty) pixels. After the equalization is finished, it is important to save and use always the same configuration in calibration and measurements.

Detectors are in this point prepared for calibration. As I mentioned above, X-ray fluorescent radiation was employed. I used three different fluorescent foils irradiated by Amptek Mini-X X-ray lamp. During the calibration, X-ray lamp was irradiating fluorescent foil (Fe, Cu or Cd) initiating X-ray fluorescence in the target foil. The energy of the X-rays coming from the foil have sharp value (Fe: 6.398 keV, Cu: 8.04 keV, Cd: 23.106 keV), therefore it is suitable for calibration of the detector. The photo of calibration setup can be found in Figure 3.7. The output from the calibration measurements is a set of files containing spectra in terms of ADC channels (time over threshold) for each individual pixel. Each spectrum is fitted and the peak value is assigned to be the ToT value representing energy of fluorescence

### 3.2: Mapping of $^{207}\text{Bi}$ Deposition Distribution in Calibration Sources

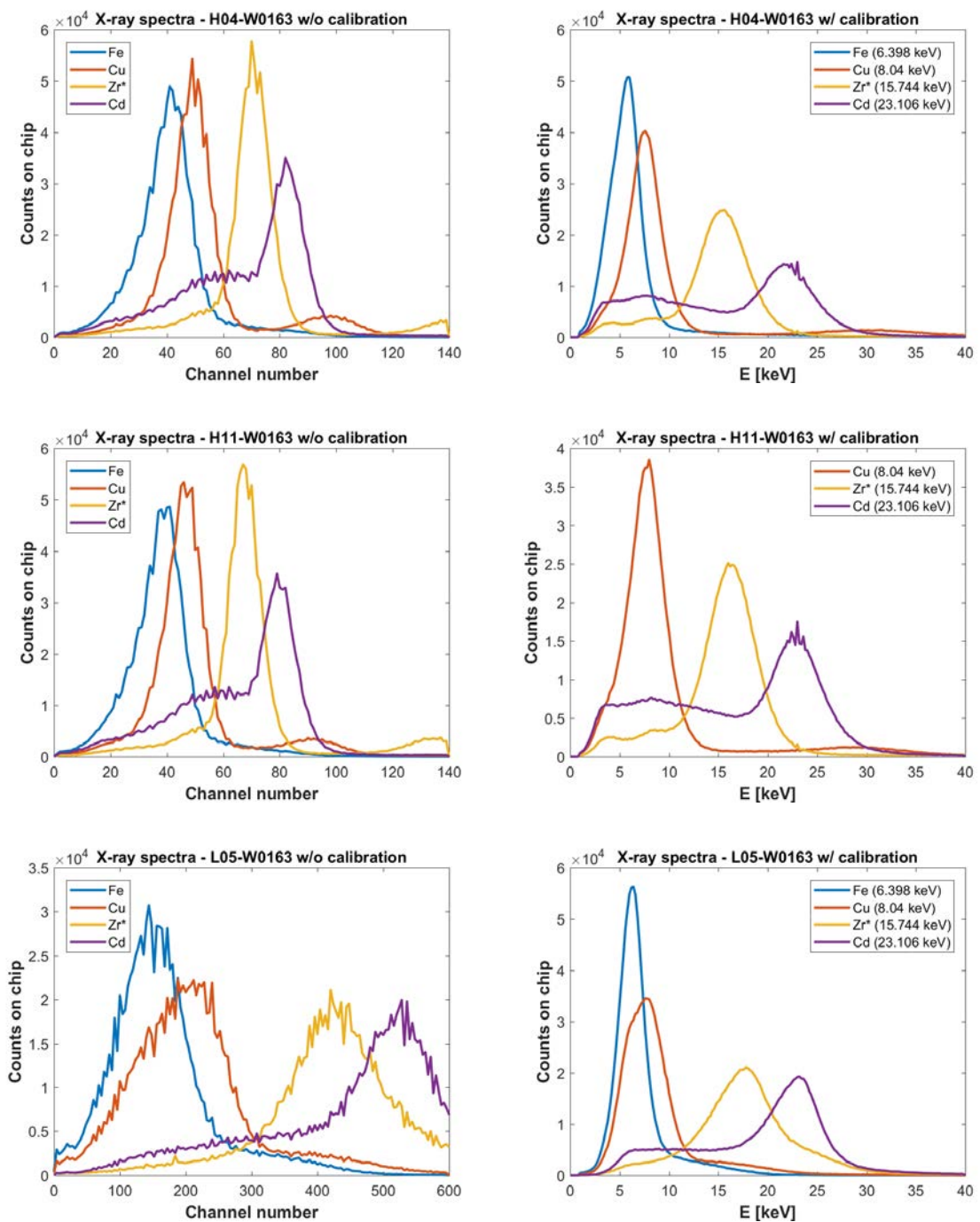


Figure 3.8: Calibration test spectra. All three detectors were tested with fluorescence foils before (left column) and after (right column) calibration. Similarly to calibration, only one pixel clusters were accepted regardless of the position on the chip. Each row represents detectors H04-W0163, H11-W0163 and L05-W0163 respectively. The spectra before calibration are represented in channel number (ToT). All three fluorescent foils from calibration were employed in the test. Asterisk represents Zirconium foil measurement which was not used for the calibration. In case of H11-W0163, data after calibration for Fe foil were lost due to disk failure. The spectrum can be found in the screenshot after the measurement in Figure 3.9.



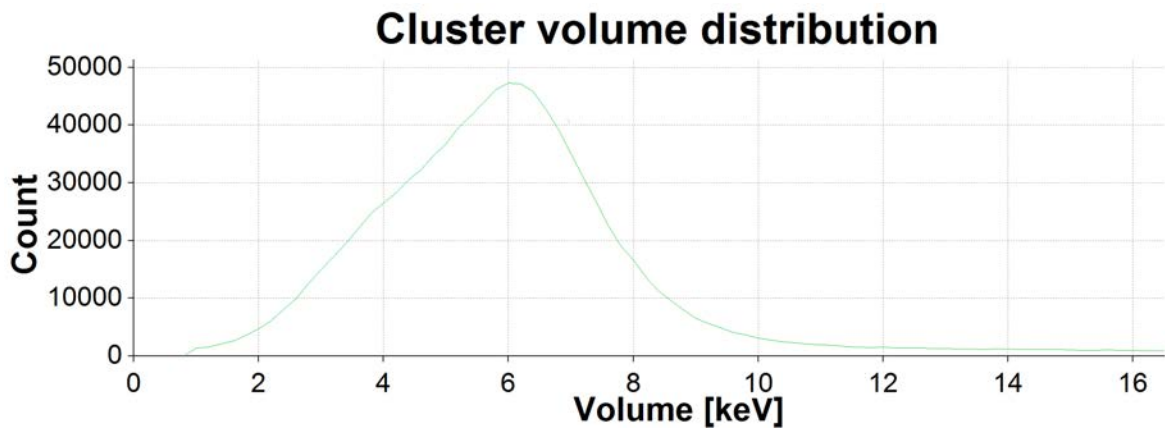


Figure 3.9: Energy from Fe foil as seen by detector H11-W0163 after the calibration. The picture represent Pixelman screenshot after the test as the data from the measurement were lost, therefore not included in Figure 3.8.

X-rays. Such a couple of values represent a point on the calibration curve from Figure 3.6. Each fluorescence foil dataset yields one such point for each pixel. As a last step, the points are fitted by function given by Equation 3.1, giving parameters  $a$ ,  $b$ ,  $c$  and  $t$ . Each quadruplet of the parameters is unique for individual pixel. Therefore, resulting calibration files are four  $256 \times 256$  matrices containing calibration parameters  $a$ ,  $b$ ,  $c$  and  $t$ .

In the Figures 3.8 and 3.9 one can find global spectra (i.e. all pixels combined) from all three used detectors before and after calibration. The calibration tests were performed using the same fluorescence foils as during the calibration (i.e. Fe, Cu and Cd) and one extra foil made of Zr (15.744 keV). From the figures one can also extract the values of energy resolution, typically on the order of few keV. The calibration was performed with success and detectors prepared for measurements.

### 3.2.3 Test Measurements

After the completion of calibration it was necessary to investigate the possibilities of the measurement and develop the most suitable and effective method. The best possibility was to perform short measurements with various setups. In October 2017 I spent one week in LSM in order to perform test measurements with the calibration sources.

#### 3.2.3.1 Data Analysis

Before a discussion about the measurements, let me talk about the data extracted from the detector and the software I developed for the analysis. Timepix detectors produce data in form of cyclic snapshots of a given acquisition time (frames) followed typically by 200 ms of dead time reserved for data storage. As it was already discussed, each pixel is capable to detect particle independently. With proper calibration provided, data in each pixel are saved in a simple form of three columns storing  $x$  and  $y$  coordinates of pixel and energy deposited in the pixel, respectively. Only the pixels with detected signal are written in the file in order to eliminate redundant data. This type of output I call "raw output" and it can be represented in a form of frame image in Figure 3.10. It is possible to recognize different particle tracks in the figure. In case when the particle deposited all its energy in the detector, the sum of all energies detected in the pixels belonging to its track should be equal to initial energy of the particle. Except for the raw data output, which I already described, Pixelman

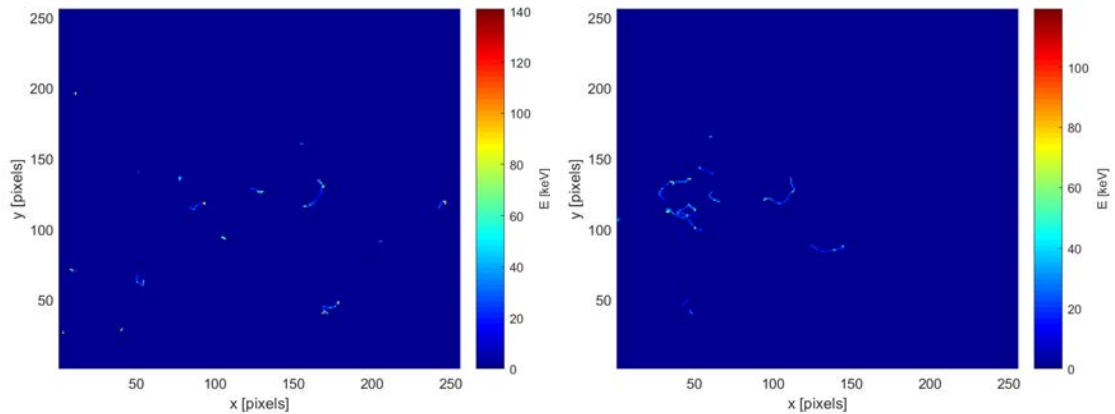


Figure 3.10: Figures representing two randomly chosen dataframes obtained during the test measurements with  $^{207}\text{Bi}$  calibration sources. The length of presented frame was set to 1 s. One can see example of different spots representing different types of particles. Typically one pixel spots are photons while long curved tracks are electrons.

provides also "clustered output" [85]. All the triggered pixels in one dataframe are grouped in clusters based on the criterion of adjacency. Cluster represents one particle. The energy of the cluster as well as its position is saved into a file. The cluster position is represented by unique number, defined as an average position of each pixel belonging to the cluster. Data contains also so-called cluster size which is number of pixels in the cluster. In my analysis software, I always took advantage of clustered output.

In order to obtain reliable data in the clustered output, we need to set length of one frame carefully. It takes 200 ms to read out the data from detector independently of the length of the frame. On one side, the longer the frame lengths is, the lower the relative dead time of the detector is. On the other side, longer frames allow the detector to collect more statistics and rise a chance to find overlapping clusters. This is something what needs to be avoided because overlapping clusters are represented as single particle in the final output causing

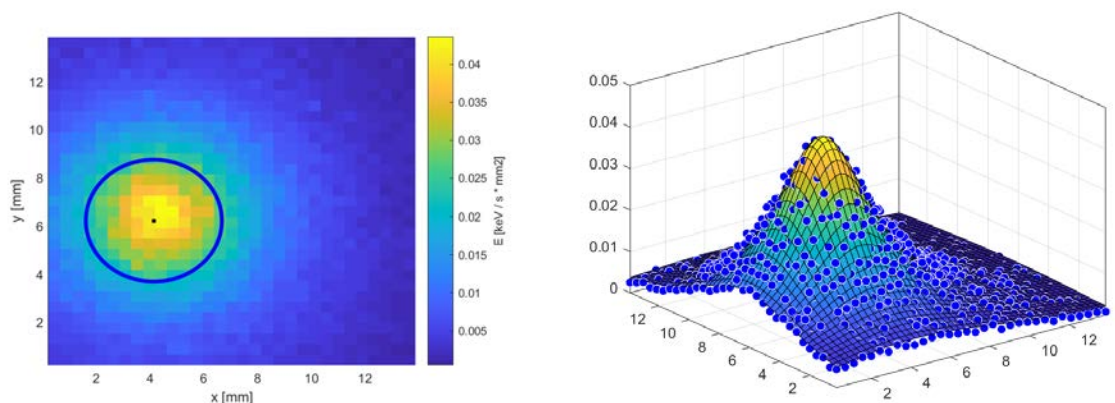


Figure 3.11: Two representations of the energy deposition for source number 133. Note that, each bin represents area of  $8 \times 8$  pixels. Left: Two-dimensional representation of the energy deposition on the chip. Right: Discrete datapoints represent values of the energy deposited in each spatial bin during the full duration of measurement. The image depicts a fit of the distribution given by equation 3.2.

distortions in data. Standard frame length can go down to fractions of a second. However, after few short testing measurements I came to a conclusion that the calibration sources are weak enough to open the frame for 1 s without affecting the data quality.

For the purpose of data analysis, I developed Matlab script capable of reading the clustered data output format. All the frames in the measurement are superimposed by the script giving the energy distribution of all the clusters as shown in the Figure 3.11 - Left. Extra blue circle represents size of the source while black dot represents its center. Both were added to the dataset after distribution was fitted by function given by Equation 3.2.

$$f(x,y) = \frac{A}{(x-x_0)^2 + (y-y_0)^2 + \gamma} \quad (3.2)$$

The center of the source is here represented by fitting parameters  $(x_0, y_0)$  and the radius of the blue circle is calculated as HWHM value of the 2D distribution, i.e.  $\sqrt{\gamma}$ . Fitting function was chosen empirically, according to the best fit criterion. As it can be seen in the Figure 3.11 - Right, fitting function describes the distribution sufficiently well.

#### 3.2.3.2 Study of the Energy Spectra

In search for proper ROI for data analysis I performed several comparative measurements. First of all, I studied the shape of the energy spectrum.  $^{207}\text{Bi}$  is a complex emitter decaying by electron capture with half-life of 31.55 yr. It produces gammas, X-rays as well as Auger electrons (Table 3.3). In Figure 3.12 one can find comparison of the energy spectra as measured by 300  $\mu\text{m}$  thick detector (H11-W0163) and 1 mm thick detector (L05-W0163).

Let us first have a look at the low energy part of the spectrum (5 keV - 30 keV) represented by Figures 3.12a and 3.12b. By looking at the Table 3.3 one can conclude that the lower part of the spectrum represents the X-rays (9.184 keV - 15.860 keV) and Auger electrons (5.327 keV - 15.817 keV) from the electron capture of  $^{207}\text{Bi}$ . In both cases X-rays and the electrons are detected very efficiently, as their energy is not sufficient to traverse the detector. However, in the high energy part of the spectrum one can expect gammas, but for them both thicknesses of Silicon layer are practically transparent. Electrons of high energy, depose energy depending on the thickness of detector. While 300  $\mu\text{m}$  detector is too thin to fully stop the electrons (Figure 3.12c), in the case of 1 mm detector, one can observe peak of electrons of 481.7 keV and 975.6 keV appearing (Figure 3.12d). As the detector was calibrated with low energy X-ray fluorescent sources, we can notice imprecision of the

Gammas		X-rays		Electrons	
E [keV]	$I_{abs}$ [%]	E [keV]	$I_{abs}$ [%]	E [keV]	$I_{abs}$ [%]
569.7	97.8	9.2 - 15.9	33.2	5.3 - 15.8	54.4
897.8	0.1	72.8	21.7	0.0 - 87.9	2.9
1064	74.5	75.0	36.5	56.3 - 61.9	1.8
1442	0.1	84.5 - 85.5	12.5	481.7	1.5
1460	1.6	84.5 - 87.6	16.2	975.6	7.1
1770	6.9	87.2 - 87.4	3.7	1047.8 - 1050.6	1.8

Table 3.3: Products from decay of  $^{207}\text{Bi}$ . Gamma line 328.1 keV gamma was omitted due to its negligible absolute intensity. The most significant X-rays and electrons were chosen. Source [86].

### 3.2: Mapping of $^{207}\text{Bi}$ Deposition Distribution in Calibration Sources

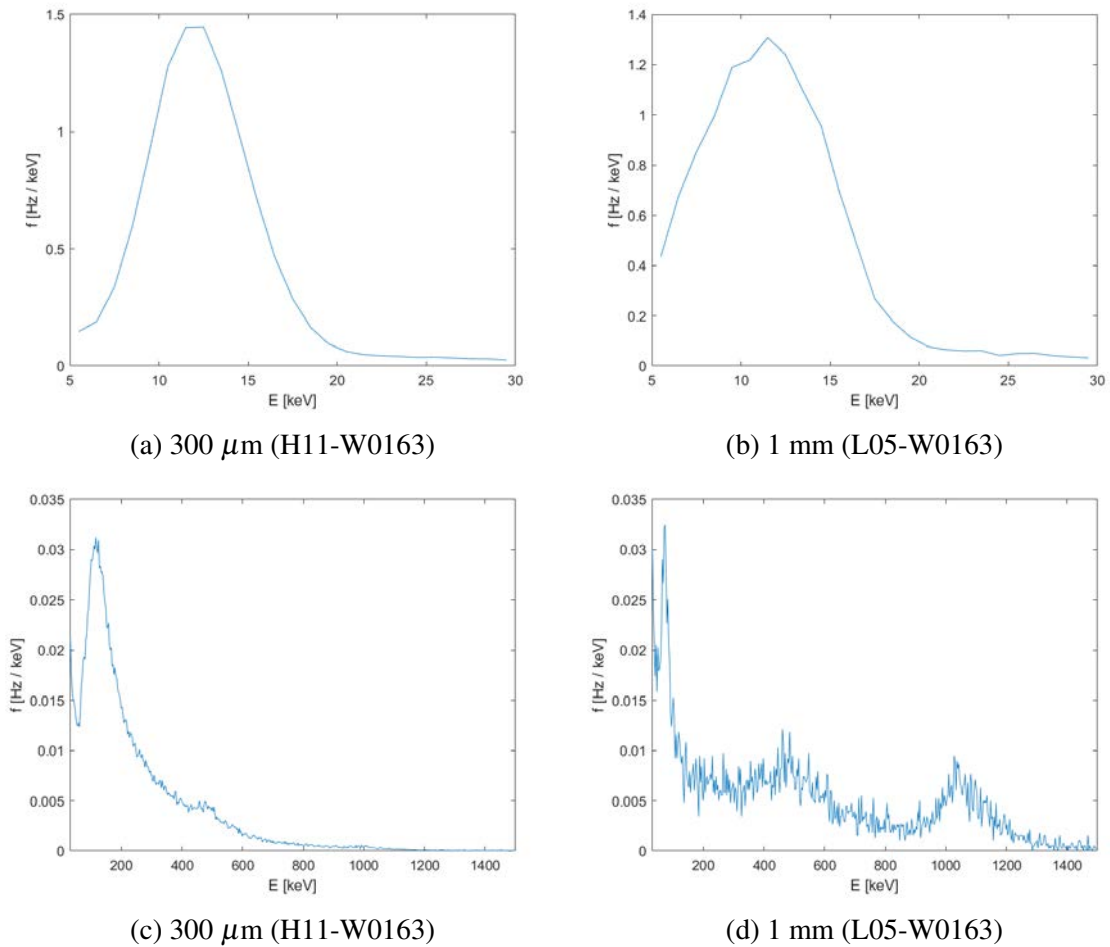


Figure 3.12: Comparison of different regions of energy spectra obtained by measurement of source number 71 with the detectors of the different thickness. While in the low part of the spectrum (5 keV - 30 keV) - figures on top - no significant difference is observed, in the high energy part of the spectrum (30 keV - 1500 keV) - figures at the bottom - we can notice peaks appearing in measurement with detector of 1 mm thickness. Reasons for the difference are discussed in the text.

calibration in high energy region which is demonstrated by second peak (975.6 keV) being displaced towards the high energy.

Based on the presented analysis of the energy spectra, I decided to choose ROI for all the measurements to be between 3 keV and 30 keV. Detectors of both thicknesses give similar spectrum in the region, therefore, we can expect comparable results regardless of the detector used in the study. Moreover, as it was discussed, energy calibration is certainly working well in the region within the energy resolution of the detector. Lower boundary of 3 keV instead of 5 keV as presented in Figures 3.12 was chosen in order to ensure that the peak in the low energy part of the spectrum is fully contained.

Chosen ROI appears to be the right choice from the point of view of final localisation of the source droplet. Figure 3.13 shows the influence of the energy cut on the localisation of the  $^{207}\text{Bi}$  droplet. It is possible to recognize that in Figure 3.13 - Right (low energy, low pixel size cut), the Bismuth droplet is better localised than in the Figure 3.13 - Left, representing high energy part of the spectrum with effectively no cut on the pixel size. The HWHM of

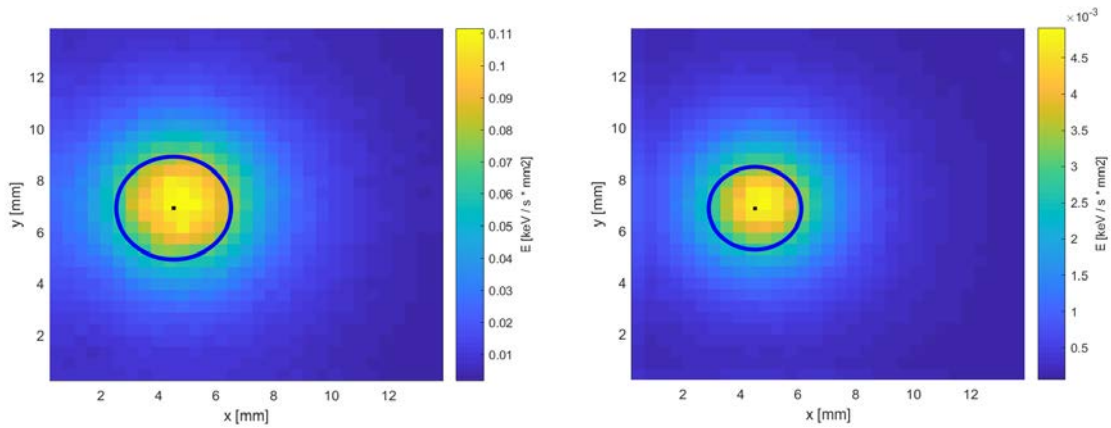


Figure 3.13: Result from measurement of source number 139. Images represent comparison of the same data with two different cuts. Left: Dataset including all the clusters with energy between 30 keV and 1300 keV and pixel size less than 100. Right: Dataset including clusters of low energy between 3 keV and 30 keV. Only clusters of pixel size 1 were included.

the droplet from low energy dataset is 1.24 times smaller. The reason for the difference lies in the interaction between electrons from high energy part of the spectrum. These electrons leave in the chip curvy tracks several pixels long. However, in the clustered output only one unique position is assigned to each cluster regardless of its size. In case of clusters composed of at least two pixels, this brings an uncertainty in the cluster localisation. The lower energy region is dominated by X-rays which typically leave only one pixel clusters. Therefore, their position is measured with precision of one pixel. In order to ensure maximal precision of the cluster position I decided to work only with clusters of the size of one pixel from the aforementioned low energy part of the spectrum. On one side, combination of both cuts decreased the measurement statistics to 43-50%, on the other side, it increased the precision of the main result of the study - the localisation of the  $^{207}\text{Bi}$  droplet.

#### 3.2.4 Detector Spatial Calibrations

If we look at the Figure 3.11 - Left we can notice another important question which has to be solved. The fit presented in the figure provides the radius (HWHM of the distribution) of the characteristic size of the source droplet as well as the position of the source. Nonetheless, the position ( $x_0, y_0$ ) is given in the frame of reference of the detector chip. In other words, position of the source is known relatively to the detector chip. However, the main aim of the study is to measure relative position of the source droplet and the Copper source frame. It was necessary to reproduce its position and represent it in the data. In order to achieve this goal, I performed spatial calibration of each detector. During all the measurements, the source was carefully positioned in the same reference position, as it is depicted in the Figure 3.14. This convention provided stable reference point for the spatial calibration. As a next step, I took laser-perforated metallic grid and placed it on the detector in the way, that top left corner of the grid (yellow point in Figure 3.15 - Left) was aligned with the measurement reference point. Subsequently, I irradiated the grid with X-rays and obtained pattern shown in the Figure 3.15 - Right. Missing hole in the measured calibration dataset helped to identify exact row and the column of each hole in otherwise symmetrical and repetitive pattern. Note that, the y axis of grid's coordinate system is orientated the opposite direction relatively to



Figure 3.14: Alignment of the measured source on the detector. Sources in all the measurements were aligned with the top left corner of black plastic holder as depicted by yellow arrows. The relative position of the red Copper frame window and the top left point were known thanks to the previous measurements of the source dimensions listed in the Tables 3.1 and 3.2.

the pixel detector y axis (Figure 3.15). Moreover, the origin of both coordinate systems are shifted relatively to each other. It implies, that the transformation between the coordinate systems won't be simple shift or rescale but one needs to employ linear algebra in order to tackle the problem mathematically.

Let me explain the mathematical background of the spatial calibration. In the following, all the vectors will be implicitly columns unless transposed. The goal of the calibration is to find a transformation matrix  $A$  and shift vector  $b = (b_1, b_2)$  providing a transformation between any vector  $v = (v_1, v_2)$  (in mm) in the calibration grid's coordinates and vector  $p = (p_1, p_2)$  in pixel detector's coordinates (in pixels) such as:

$$p = Av + b. \quad (3.3)$$

Let us now have four different vectors (points in space) in calibration grid coordinates  $v_1, v_2, v_3$  and  $v_4$  represented in pixel detector coordinates:  $p_1, p_2, p_3$  and  $p_4$ , respectively. The transformation relation from Equation 3.3, therefore holds for each vector:

$$p_i = Av_i + b, \quad i = 1, 2, 3, 4. \quad (3.4)$$

Now, if we define matrices  $V_1, V_2, P_1, P_2$  and  $B$ :

$$V_1 = (v_1, v_2); \quad V_2 = (v_3, v_4); \quad P_1 = (p_1, p_2); \quad P_2 = (p_3, p_4); \quad B = (b, b), \quad (3.5)$$

following matrix equations also hold as a consequence of the Equation 3.4:

$$P_1 = AV_1 + B; \quad P_2 = AV_2 + B. \quad (3.6)$$

If we subtract second equation from the first we eliminate the unknown matrix  $B$ :

$$P_1 - P_2 = A[V_1 - V_2]. \quad (3.7)$$

Finally, we multiply equation from the right side with matrix inverse  $[V_1 - V_2]^{-1}$  and swap sides:

$$A = [P_1 - P_2][V_1 - V_2]^{-1}. \quad (3.8)$$

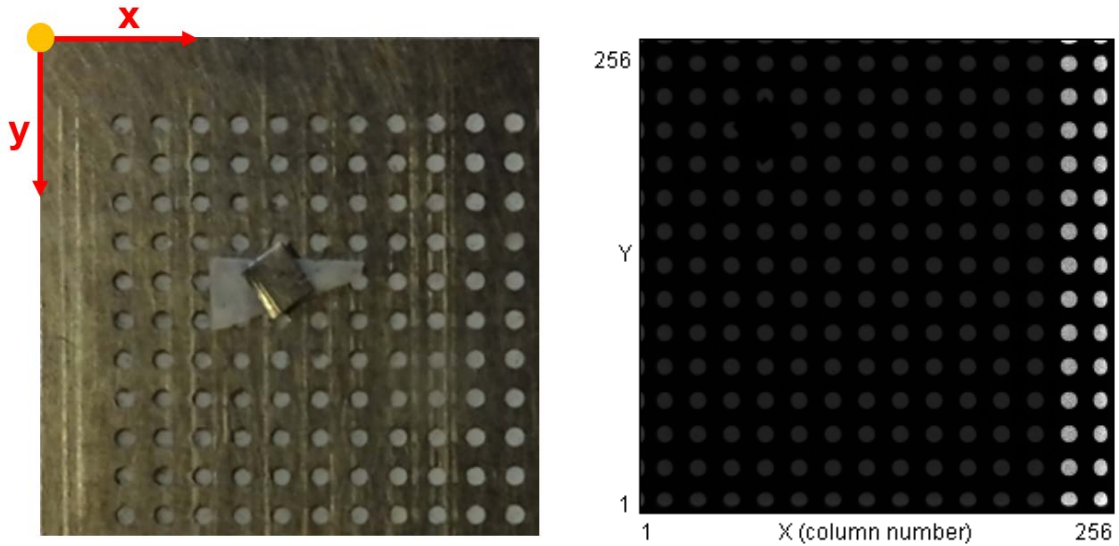


Figure 3.15: Left: Photo of the spatial calibration metallic grid. Yellow point was in the process of spatial calibration aligned with standard reference point defined in the Figure 3.14. Right: Image of the calibration grid as seen by detector L05-W0163 after exposure to X-rays. Note that, the covered hole appears in fourth column and third row instead of fifth row and fifth column (left figure) because first two rows and first column are out of the sensitive area of the detector as well as the grid's yellow reference point.

	$v_1$ (mm)	$v_2$ (mm)	$v_3$ (mm)	$v_4$ (mm)
$x$	6.16	11.58	11.58	6.16
$y$	6.08	6.08	11.06	11.06

Table 3.4: Coordinates of four chosen grid points in grid's coordinate system obtained by measurement by caliper presented in Figure 3.16 - Left.

Equation 3.8 provides recipe for calculation of the transformation matrix  $A$  given values of four points in both coordinate systems. With  $A$  already known, the shift vector  $b$  is obtained from Equation 3.4:

$$b = p_i - Av_i. \tag{3.9}$$

The calculation should work for any chosen  $i = 1, 2, 3, 4$ . Having matrix  $A$  and vector  $b$ , it is possible to transform any vector  $v$  in calibration grid coordinates into vector  $p$  in pixel detector coordinates. The opposite transformation can be achieved by inverted relation:

$$v = A^{-1}(p - b). \tag{3.10}$$

Here,  $A^{-1}$  represents inverse of matrix  $A$ .

Let me now demonstrate how the presented method works. As an example, I will use spatial calibration of detector L05-W0163. As it was already discussed, the first step to perform the spatial calibration is to choose four points and express them in both coordinate systems.

Figure 3.16 - Left shows choice of my four points represented on the photo of the grid. These four points were (thanks to the covered hole) identified in the dataset measured by the detector (3.16 - Right). Green lines represent two horizontal and two vertical linear fits and

	$p_1$ (pix.)	$p_2$ (pix.)	$p_3$ (pix.)	$p_4$ (pix.)
x	67.96	159.48	159.52	68.01
y	207.62	207.68	116.06	116.05

Table 3.5: Coordinates (rounded to two decimal places) of four chosen grid points in detector's coordinate system obtained by fit presented in Figure 3.16 - Right.

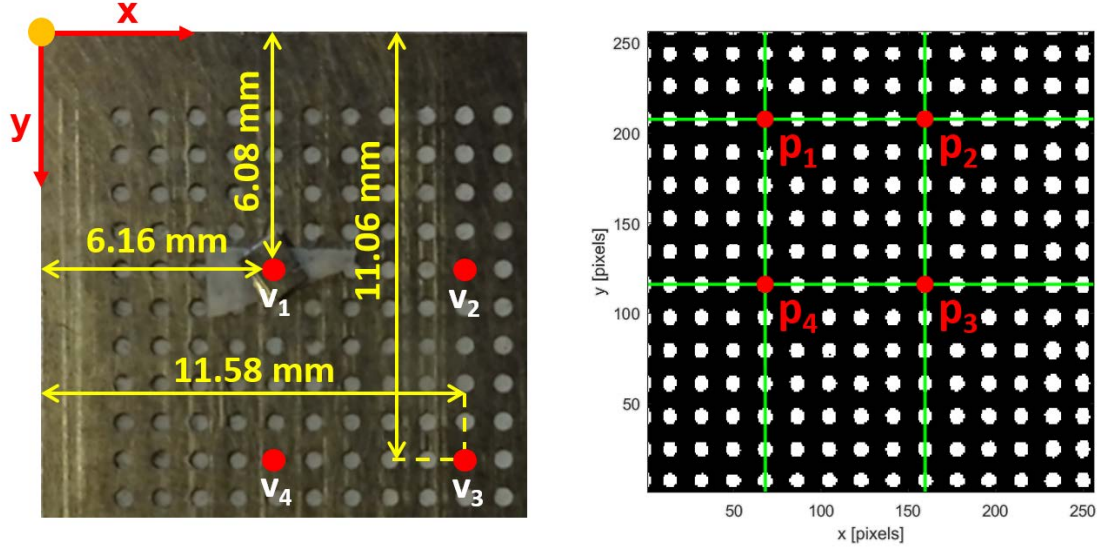


Figure 3.16: Left: Dimensions of the grid measured by calliper. They represent the coordinates of four chosen calibration vectors  $v_1$ ,  $v_2$ ,  $v_3$  and  $v_4$ . Right: Same four points identified in the dataset from exposure by X-rays in Figure 3.15 - Right. The contrast of the image was enhanced before the fitting (green lines) was performed.

their intersections represent the coordinates of my four chosen points in detector's coordinate system. All the measured (fitted) coordinates in both coordinate systems are summarized in the Table 3.4 (Table 3.5).

Having all the important ingredients for my mathematical recipe it is possible to construct matrices  $V_1$ ,  $V_2$ ,  $P_1$  and  $P_2$  from Equation 3.5:

$$V_1 = \begin{pmatrix} 6.16 & 11.58 \\ 6.08 & 6.08 \end{pmatrix}, \quad V_2 = \begin{pmatrix} 11.58 & 6.16 \\ 11.06 & 11.06 \end{pmatrix}, \quad (3.11)$$

$$P_1 = \begin{pmatrix} 67.96 & 159.48 \\ 207.62 & 207.68 \end{pmatrix}, \quad P_2 = \begin{pmatrix} 159.52 & 68.01 \\ 116.06 & 116.05 \end{pmatrix}. \quad (3.12)$$

Subsequently, I calculated  $V_1 - V_2$ ,  $P_1 - P_2$ :

$$V_1 - V_2 = \begin{pmatrix} -5.42 & 5.42 \\ -4.98 & -4.98 \end{pmatrix}, \quad P_1 - P_2 = \begin{pmatrix} -91.56 & 91.47 \\ 91.57 & 91.63 \end{pmatrix}, \quad (3.13)$$

as well as  $[V_1 - V_2]^{-1}$ :

$$[V_1 - V_2]^{-1} = \begin{pmatrix} -0.0923 & -0.1004 \\ 0.0923 & -0.1004 \end{pmatrix}. \quad (3.14)$$



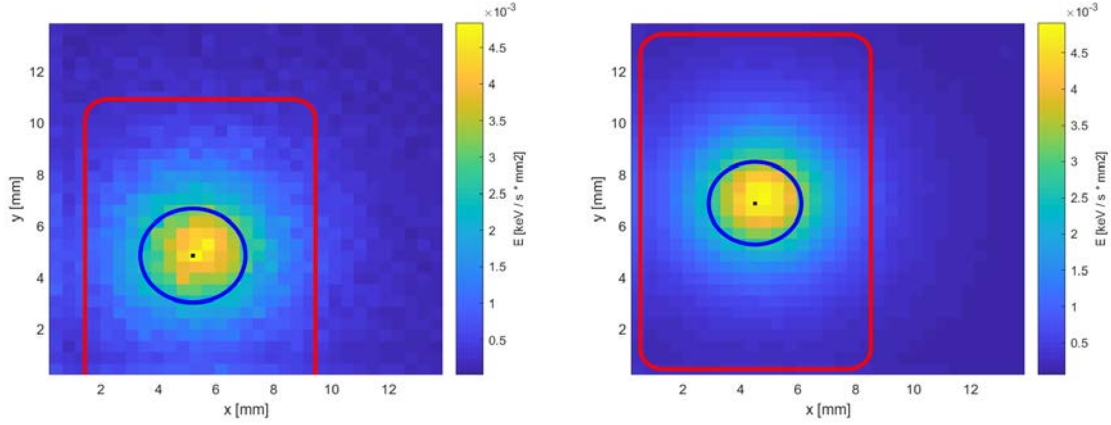


Figure 3.17: Example of two measurement results after the addition of Copper source frame window (red rectangle). Left figure represents measurement of source number 75 while figure on the right represents measurement of the source number 139. It is clearly visible that the position of the red Copper frames are in the different positions. This is expected, because source number 75 (Left) is source with plastic envelope while source number 139 (Right) has no plastic envelope. Note that both datasets are expressed in mm instead of the pixels which was achieved by using size of one pixel (0.055 mm) as a scaling factor.

It was important to choose my four points in such way, that the matrix  $V_1 - V_2$  is not singular. Finally, by application of Equation 3.8 and, subsequently, Equation 3.9, we obtain matrix  $A$  and shift vector  $b$  for transformation from grid's coordinate system to coordinate system of detector:

$$A = \begin{pmatrix} 16.885 & 0.0087 \\ 0.0062 & -18.3936 \end{pmatrix}, \quad b = \begin{pmatrix} -36.1 \\ 319.4 \end{pmatrix}. \quad (3.15)$$

For the inverse transformation defined by Equation 3.10, we can use matrix:

$$A^{-1} = \begin{pmatrix} 0.0592 & 0 \\ 0 & -0.0544 \end{pmatrix}. \quad (3.16)$$

Let me briefly discuss obtained results. Looking at matrices  $A$  and  $A^{-1}$  we can conclude that we obtained correct and expected results. Within precision of one decimal place the off-diagonal elements are zero which suggest no rotation between the two coordinate system which is indeed true. Moreover, minus sign next to the bottom right elements of the two matrices describe mathematically the fact, that the directions of  $y$  axes are mutually opposite between the two coordinate systems. In contrary, the directions of the  $x$  axes are mutually the same which is represented by positive sign of the elements in first row and first column in both matrices (Figure 3.15). Looking at the  $b$  vector we can state expected fact, that the origins of the two coordinate systems are mutually displaced.

If we look at the dimensional analysis of the values,  $b$  vector is represented in pixels. It represents the relative displacement of grid's coordinate system relatively to origin of the detector's coordinate system. Negative  $x$  value suggests displacement to the left from the chip and  $y$  which is higher than 256 (number of pixel rows) suggests that the reference measurement point is above the chip. This is exactly the situation implied by Figure 3.15. Finally, we conclude that the values of matrix  $A^{-1}$  are in mm per pixel, based on the fact that this matrix has to transform pixels in which vector  $p$  is expressed into mm, the units of

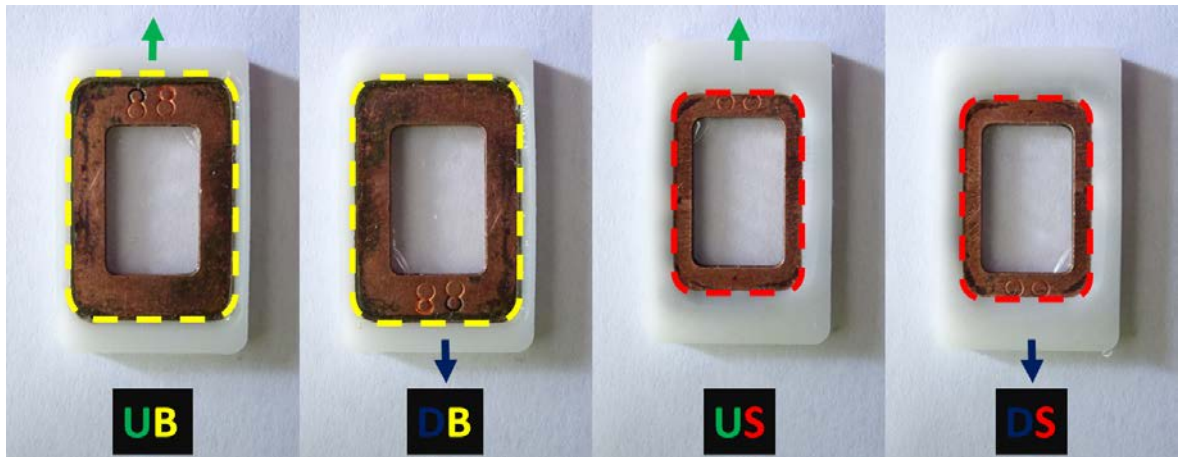


Figure 3.18: Four different positions of source number 88. U stands for upward position, D for downward position, B for the side with big opening and S for side with small opening. Further details are explained in the text.

vector  $v$ . The diagonal elements of the matrix  $A^{-1}$  provide rescaling. The values 0.0592 and 0.0544 represent the size of one pixel in mm. The two values were obtained indirectly, but still within a good precision they represent correct size of standard Timepix detector pixel (0.055 mm). The presented process was performed with each one of the detectors using my own Matlab script. With the transformation relations at disposal, it is easy to express any point in the detector (or outside) in both coordinate systems. Based on the source frame measurements (Tables 3.1 and 3.2), it was simple task to represent the red source frame window from Figure 3.14 into the measured dataset. Example is shown in Figure 3.17.

#### 3.2.4.1 Source Placement Convention

Before I will start to discuss the final results obtained in the study, one last topic remains still to be covered. As it was already mentioned, both types of calibration sources (with and without plastic envelope) are of rectangular shape and they are emitting decay products to both sides perpendicular the area of the rectangle. Therefore, in order to make unambiguous conclusion about source droplet position, it is important to clarify on which side the measurement was performed. Furthermore, once we have chosen the side of the source facing the detector, the source can still be rotated by 180 degrees in its plane. These two symmetries together define four different positions which have to be named and distinguished in order to provide replicable results.

Figure 3.18 contains photos of a source number 88 with plastic envelope. Source can be placed (with respect to predefined upward position) in four different measurement positions. In case of source with plastic envelope it is possible to distinguish a side with a big opening (positions UB and DB, B stands for big) and opposite side with a small opening (positions US and DS, S stands for small). Moreover, on each side, source number is engraved. It helps to distinguish upward placement (positions UB and US) from downward placement (positions DB and DS). Analogical positions can be defined for source without plastic envelope. However, if we look at the Figure 3.19 we can spot slight difference. Without plastic envelope there is no possibility to define each side based on the size of the plastic opening. Nevertheless, two sides of any source without plastic envelope can be distinguished thanks to the difference in colour, single colour (positions WO-SU and WO-SD) and double colour

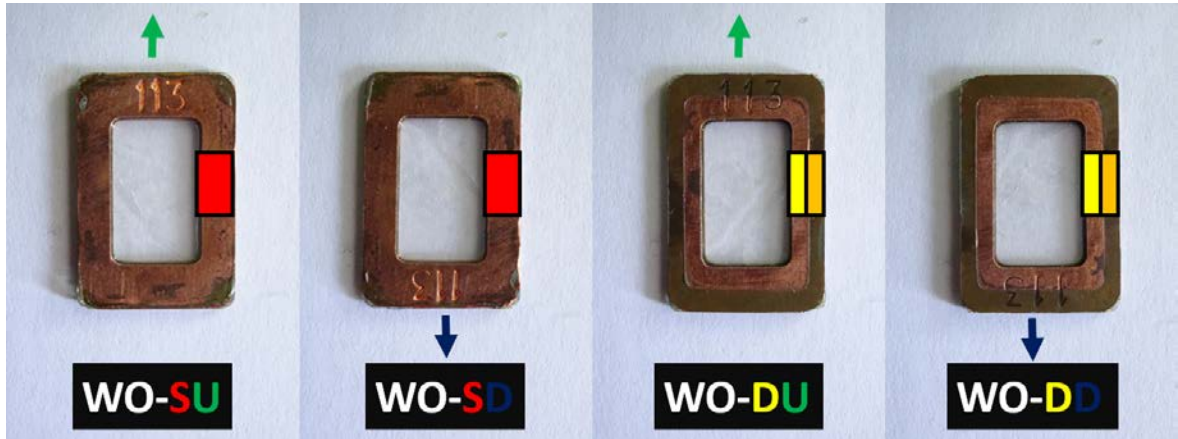


Figure 3.19: Four different positions of source number 113. U stands for upward position, (second) D for downward position, S for the side with single colour opening and (first) D for side with double colour. Prefix "WO-" is added to distinguish positions of source without plastic frame easier. Further details are explained in the text.

(positions WO-DU and WO-DD). The upward positions (WO-SU and WO-DU) and downward positions (WO-SD and WO-DD) are defined exactly in same fashion as in the case of source with plastic envelope, based on the engraved source number. Note that, for easier orientation in the convention, all the positions concerning sources without plastic frame have prefix "WO-". The convention defined in the Figures 3.18 and 3.19 has to be (and will be) strictly followed in the thesis. At this point, last important remark should be made. If we take Figure 3.14 as an example, we can state that the measured source is in position WO-SU. However, it is the double coloured side which is facing the detector. For the sake of practicality the name of the position is based on what observer sees. It is not important which side is seen by detector (unless stated otherwise).

### 3.2.5 Results

During my second stay in LSM in December 2017, I performed final measurements. During 12 days, I managed to measure 49 different sources in 52 measurements (three sources were measured two times). The duration of one measurement was variable, ranging from few hours to few days. Statistics of chosen measurements can be found in the Table 3.6.

The table includes the name of the detector involved in the measurement as well as number of counts in ROI ( $N_{\text{ROI}}$ ) and total dataset ( $N_{\text{TOT}}$ ), their fraction and the flux of energy detected per unit time ( $E_{\text{ROI}} / t_{\text{live}}$ ). Full information about all performed measurements can be found in Table A.2 in Appendix A. Based on the presented number, it is possible to distinguish two types of detector. If we look at the particle rates, we can notice that  $300 \mu\text{m}$  thick detectors (H04-W0163 and H11-W0163) detected particle rates approximately on the level of 7-9 Hz. However, 1 mm thick detector (L05-W0163) have seen higher rates of 11 or more Hz. It is another demonstration of higher detection efficiency due to the thickness of the detector. Note that, the particle rates allow us to calculate activities relatively to one chosen source. However, according to the difference in the detection efficiency which I have just discussed, it is impossible to compare activities between sources measured by thicker detector and the sources measured by thinner detectors.

The quantities of interest extracted from the measurement are depicted in Figure 3.20.

### 3.2: Mapping of $^{207}\text{Bi}$ Deposition Distribution in Calibration Sources

M.	Detector	$t_{\text{live}}$ [s]	$N_{\text{ROI}}$ [1]	$N_{\text{TOT}}$ [1]	$\frac{N_{\text{ROI}}}{N_{\text{TOT}}}$ [%]	$\frac{N_{\text{ROI}}}{t_{\text{live}}}$ [Hz]	$\frac{E_{\text{ROI}}}{t_{\text{live}}}$ [keV / s]
73	H04-W0163	5 994	49 656	114 585	43.34	8.28	92.88
74	H11-W0163	6 384	53 527	123 395	43.38	8.38	101.28
111	H11-W0163	13 813	125 124	288 873	43.31	9.06	110.18
120	L05-W0163	45 669	552 206	1 095 402	50.41	12.09	134.99
126	H04-W0163	199 776	1 474 716	3 428 264	43.02	7.38	82.38
126*	H04-W0163	166 317	1 290 921	3 038 524	42.49	7.76	86.55
132	H11-W0163	197 260	1 719 104	3 955 332	43.46	8.71	104.58
132*	H11-W0163	165 699	1 440 205	3 324 424	43.32	8.69	104.86
139	L05-W0163	197 151	2 342 662	4 723 626	49.59	11.88	133.00
139*	L05-W0163	165 604	1 965 319	3 973 773	49.46	11.87	133.82

Table 3.6: Statistics of chosen measurements. M. in the first column stands for number of measured source. Rows with asterisk denote repeated measurement under same experimental conditions.

M.	Position	$x_0$ [mm]	$y_0$ [mm]	HWHM [mm]	$x_0 - C_X$ [mm]	$y_0 - C_Y$ [mm]	$p_x$ [1]	$p_y$ [1]	r [mm]
126	WO-DU	3.02	6.79	2.44	-1.22	0.11	-0.31	0.02	1.23
126*	WO-DU	3.00	7.01	2.14	-1.24	0.33	-0.31	0.05	1.28
132	WO-DU	3.99	7.29	1.96	-0.25	0.57	-0.06	0.09	0.62
132*	WO-DU	3.94	7.46	1.95	-0.29	0.74	-0.07	0.11	0.79
139	WO-DU	4.50	6.88	1.61	-0.02	-0.07	0.00	-0.01	0.07
139*	WO-DU	4.47	7.03	1.62	-0.05	0.08	-0.01	0.01	0.10

Table 3.7: Table summarising all obtained quantities for chosen measurements. M. in the first column stands for number of measured source. Measurements with asterisk denote repeated measurement under same experimental conditions. Colour coding of dislocation vector length denotes source category described in the text.

Black point is center of  $^{207}\text{Bi}$  droplet ( $x_0, y_0$ ) obtained by fit described in Section 3.2.3.1. The fit provides also HWHM value of the distribution (characteristic dimension of the source). The droplet is symbolized in the picture by blue circle with the radius of distribution's HWHM. Red point is a center of the source frame. Its coordinates are ( $C_x, C_y$ ). Finally, green arrow represents the most important quantity, "the dislocation vector",  $r$ . It is a vector whose origin is in the center of source frame and the end in the center of  $^{207}\text{Bi}$  droplet:  $r = (x_0 - C_x, y_0 - C_y)$ . It represents the dislocation of the source droplet from the center of the source frame. Therefore, its length is a measure of this dislocation. In the right side of the same figure one can find definition of complementary dislocation parameters  $p_x$  and  $p_y$ . They represent the same information given by coordinates of dislocation vector but in relative terms with respect to source frame dimensions. Both have value from interval  $\langle -1, 1 \rangle$ .  $p_x$  ( $p_y$ ) = 0 represents situation when source is perfectly horizontally (vertically) aligned while  $p_x$  ( $p_y$ ) = -1 represents source deposition on the left (bottom) edge of the source frame and  $p_x$  ( $p_y$ ) = 1 represents source deposition on the right (top) edge of the source frame. The parameters are dimensionless.

Finally, let me discuss the results. Table 3.7 includes data from six measurements of three repeatedly measured sources. All the previously mentioned quantities can be found in the

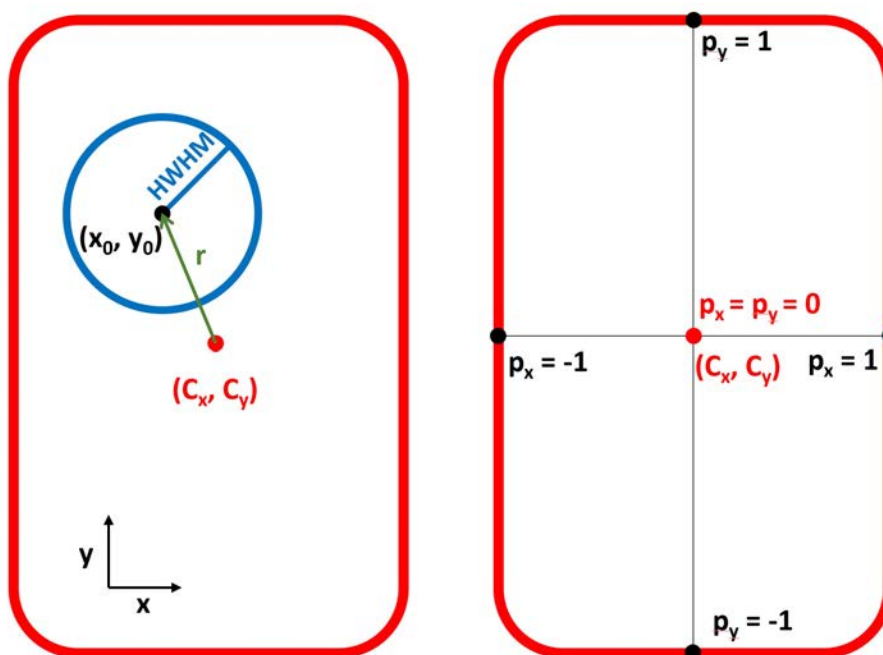


Figure 3.20: Graphical representation of the quantities extracted from the measurement. They are explained in further detail in the text.

table. The coordinates of the droplet and source frame center is expressed in the mm. Note that, their values are the coordinates in the detector coordinate system rescaled from pixels into mm by size of one pixel (0.055 mm). Last column shows a length of the dislocation vector. Majority of the sources were centred well within 1.5 mm or less. In order to simplify the description of the sources, I decided to divide them into three basic categories. Category A includes all the sources with  $r < 0.5$  mm (green category), category B all the sources with  $0.5 \text{ mm} < r < 1$  mm (yellow category). In category C (red category) the rest of the sources were placed, i.e.  $1 \text{ mm} < r$ . Full results from all the measurements can be found in Table A.4 in Appendix A.

The results have shown that 21 sources belong to the category A, 23 to category B and 5 into category C. None of the sources showed contamination on the source frame. In other words, all the tested sources are eligible to be used in the calibration. However, thanks to the study it will be possible to choose the best ones. For easier orientation in the results, I represented all the dislocation vectors in Figure 3.21.

### 3.2.5.1 Uncertainty Estimation

In order to perform uncertainty estimation I took advantage of three repeated measurements. The uncertainty was estimated by comparing the differences between dislocation vectors obtained for the same source in two different measurements. Let us have a look at the uncertainty of the x coordinate first. By comparison of the measurement 132 and 132\* the difference in x coordinate is 0.04 mm (difference between -0.25 mm and -0.29 mm). This difference is the biggest between among all the repeated measurements In Table 3.7. Measurements 126 and 126\* yield only 0.02 mm of difference while measurement 139 and 139\* yield difference of 0.03 mm. As a conservative estimate I consider final uncertainty in the x direction the one with the highest value, i.e.  $\Delta x = 0.04$  mm. I repeated exactly same

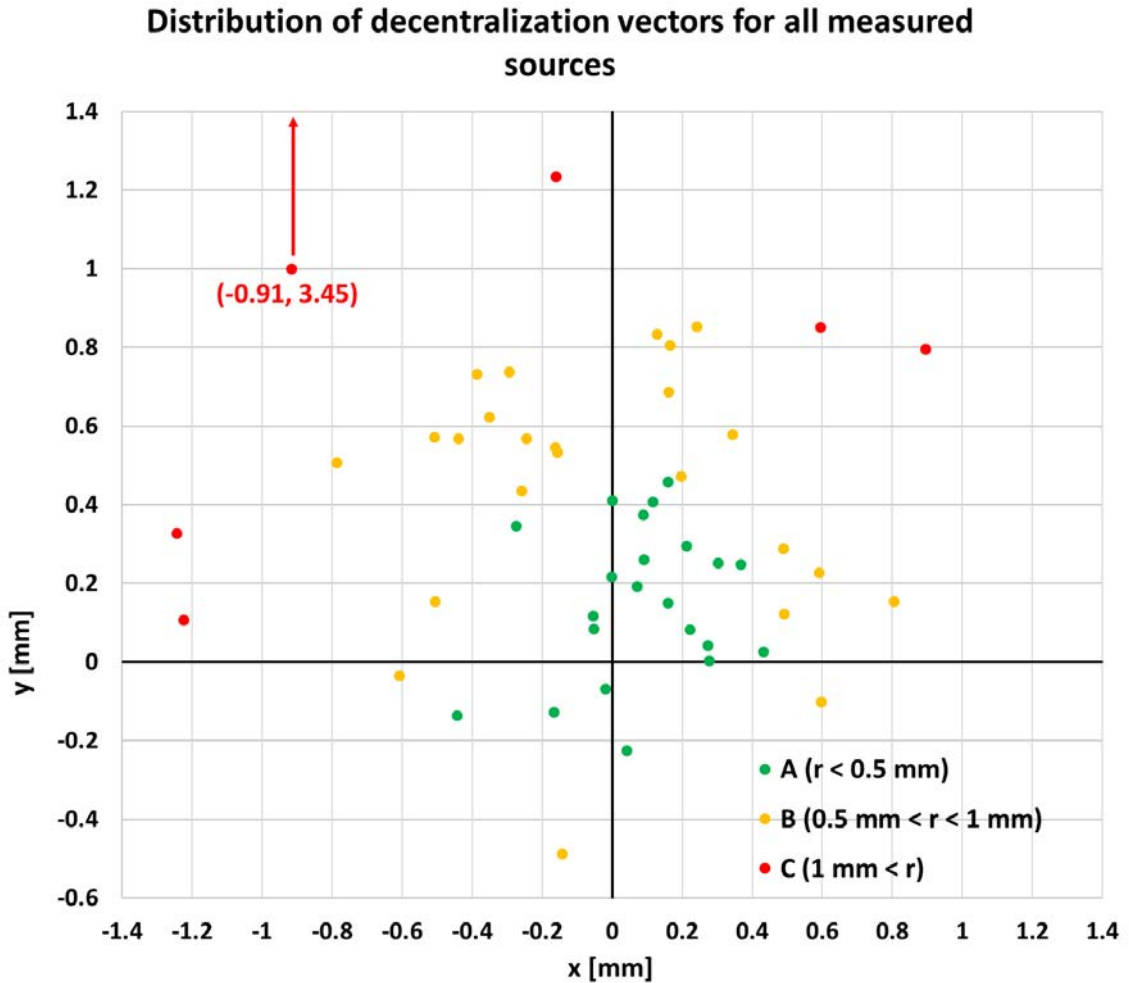


Figure 3.21: Each dot symbolizes one performed measurement. Position represents the dislocation vector coordinates. Origin represents the center of the source frame. Dot colour stands for the source category (A, B or C).

process for the y direction. Here, is the biggest difference (0.22 mm) between measurement number 126 and 126\*. Again, this value is considered as uncertainty of the measurement in the y direction, i.e.  $\Delta y = 0.22$  mm.

It is obvious, that the uncertainty in y direction is significantly larger than the one in x direction. This has simple explanation. If we look at the Figure 3.14 we can notice important detail. The figure shows alignment of the measured source to the reference measurement point (top left corner). While in the left side the source is touching black plastic chip holder and it can be aligned easily, in the horizontal (y) direction, source can move freely and has to be aligned by hand. Naturally, it brings extra uncertainty into the measurement.

### 3.3 Measurements of Source Activities

Another crucial property of calibration sources which needs to be known, is the activity. SuperNEMO demonstrator is using 42  $^{207}\text{Bi}$  sources for calibration of optical modules in main walls. It is important to ensure that all the optical modules obtain roughly the same

number of calibration electrons in order to obtain homogeneous calibration quality all over the calorimeter walls. This can be achieved by avoiding placement of the most active sources on one side of the detector. If at least relative source activities are known, the distribution of the calibration sources can be optimized. Furthermore, the knowledge of absolute activities can help to define the length and frequency of the calibration sessions. Activities serve as an input to the simulations of calibration system. In NEMO-3,  $^{207}\text{Bi}$  sources have been measured with an uncertainty on activity at the level of 5%, leading to an uncertainty of 5% on the electron reconstruction efficiency. This uncertainty was, thus dominating the uncertainty on half-life of  $2\nu\beta\beta$ . Precise measurements of calibration source activities, therefore, have potential to reduce significantly the uncertainty of the half-life.

Such measurements are the main goal of the following section. The activity was measured in two parallel sets of measurement - relative and absolute.

#### 3.3.1 Relative Measurements

Forty-one calibration  $^{207}\text{Bi}$  sources were shipped from LSM to CENBG in summer 2018 in order to perform the activity measurements.  $^{207}\text{Bi}$  is a complex emitter, emitting not only electrons (key particles for calibration), but also X-rays and gammas. The activity measurements were performed with two different Germanium detectors detecting gammas coming from the sources.  $^{207}\text{Bi}$  produces two main gamma lines: 569.7 keV (branching ratio 97.8%) and 1063.7 keV (branching ratio 74.5%). The analysis in the activity measurements was based on the analysis of these two peaks.

Let me firstly talk about relative activity measurements. They were performed by Germanium detector (I will call it detector A) depicted in Figure 3.22.

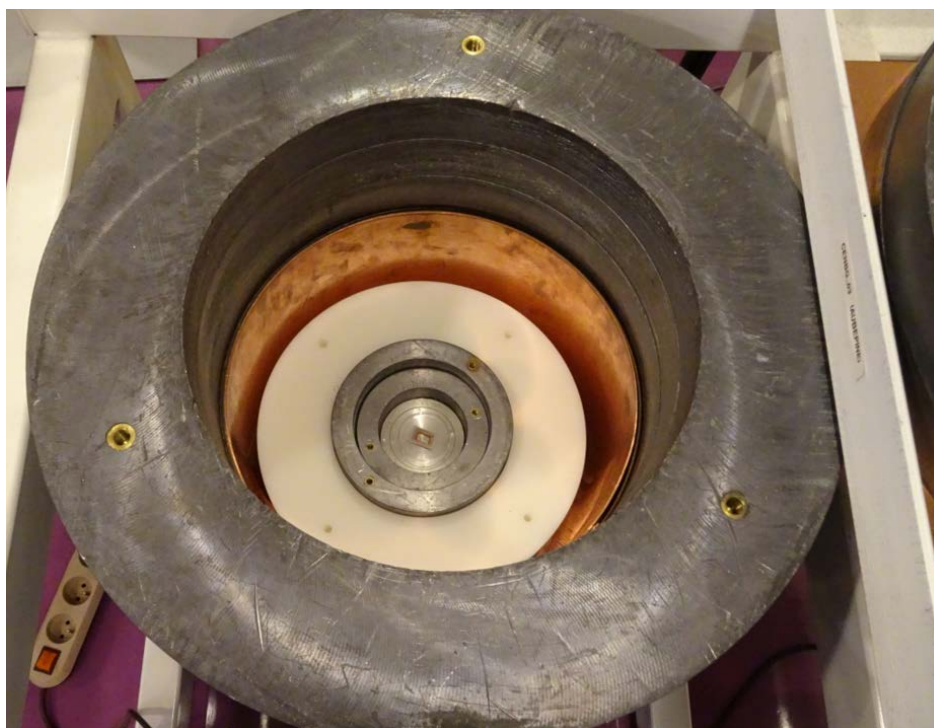


Figure 3.22: Image of the Germanium detector in CENBG employed for relative activity measurements. Inner white cylinder is polyethylene shielding while the outer grey cylinder is lead shielding.

Detector itself (not visible in the photo) is in the bottom part of the shielding shaft. It is a high-purity coaxial-type Germanium detector with a  $100 \text{ cm}^3$  volume hosted at the PRISNA platform at CENBG (Plateforme Régionale Interdisciplinaire de Spectrométrie Nucléaire en Aquitaine). This detector was initially developed by the NEMO collaboration in the early 90's in close collaboration with the Canberra company. The calibration source was placed on top of the detector (i.e. at the bottom of the shaft, shown in photo) with UB side facing the detector (Figure 3.18) in case of source with plastic and WO-SU side facing the detector (Figure 3.19) in case of source without plastic. While the side of the source facing the detector was strictly followed in each measurement, the horizontal alignment (UB vs. DB, US vs. DS, etc.) was kept only approximately.

Detector was shielded, which allowed to measure very clean spectrum shown in Figure 3.23. Figure depicts two mentioned gamma lines which were of interest in both the relative and absolute activity measurements. In the relative measurement I took advantage of only 570 keV which was fitted by Gaussian bell shape function deposited on constant background:

$$f_1(E) = \frac{N}{\sqrt{2\pi}\sigma} e^{-\frac{(E-E_0)^2}{2\sigma^2}} + c. \quad (3.17)$$

Fitting parameters were  $E_0$  (peak position),  $\sigma$  (peak width),  $c$  (background) and  $N$  (integral of the Gaussian). Integral ( $N$ ) represents the fitted value of number of events detected in 570 keV peak. Such value can be used for relative comparison of source activities. Majority of the radiation is undetected and one needs to perform simulation or measurement to extract the detection efficiency in order to calibrate the detector. The calibration of the detector to absolute activities would be, in principle, possible by measurement of detector efficiency, however, such measurement would not provide value with uncertainty better than 5%. Detection efficiency depends on the distance between the source and detector. In my study, there are two types of sources - with and without plastic envelope. Envelope changes slightly the geometry of the source. This slight, few millimeter difference (as it will be shown in following sections) causes difference in the source-detector distance between two types of sources. The difference can be in principle compensated, however, this was not the aim of the relative measurement. Without performing the correction, one should not compare results for sources with plastic envelope and for sources without the envelope.

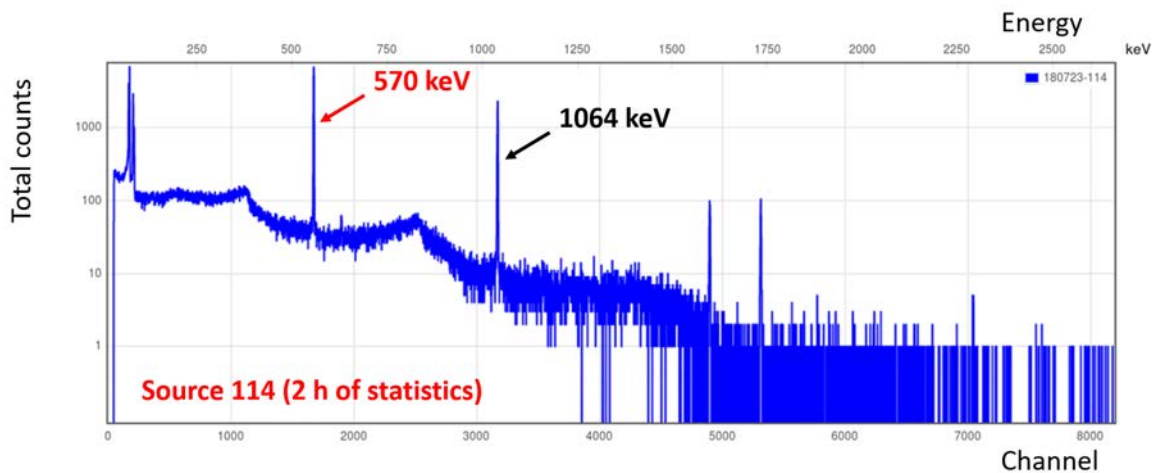


Figure 3.23: Gamma spectrum of source number 114 as measured by detector A. Figure depicts positions of 570 keV and 1064 keV peaks produced by  $^{207}\text{Bi}$ .



**3.3.1.1 First Phase**

Relative measurements were performed for 40 sources. It consisted of two phases. In first phase, all the sources were measured in previously discussed fashion collecting ~6 min of statistics. The aim of the first phase was to briefly obtain list of the most active sources. Only the most active could have been used for absolute activity measurements due to the limited time allocated for the absolute measurements.

After the spectrum measured by detector A was fitted by function in Equation 3.17 in the vicinity of peak 570 keV, integral (parameter N in fit) was considered as a measure of activity. Typically, 1400 - 1600 counts were extracted in the peak. Live time of the measurements were ranging from 330 s to 360 s. In each case, number of counts was divided by measurement's live time and compared. Statistical uncertainty of such short measurement was rather high (1 - 2%), however, sufficiently low to choose the best candidates for absolute measurements, with satisfactory precision and in minimal amount of measurement time.

In following, twenty-four the most active sources (75, 80, 81, 82, 84, 87, 88, 89, 91, 92, 93, 94, 95, 96, 111, 113, 114, 115, 116, 120, 131, 133, 135 and 138) were labelled as "golden" sources. These sources were all measured in absolute measurement. Following ten sources (76, 77, 78, 79, 83, 85, 86, 90, 119 and 139) were labelled as "silver" sources. At the time of the first phase of relative measurement these sources were candidates for absolute measurement. Finally, only one of them (76) was finally measured in precise absolute measurements. Note that, this division was only first rough comparison in order to choose sources which were later advanced for absolute measurement. Finally, there might be examples of silver sources which are more active than some of the golden sources. This is not a problem, as the final results would be based on the relative and absolute measurements with more precise approach presented in following sections.

**3.3.1.2 Second Phase**

Second phase relative measurements were simple repetition of the first phase. Nevertheless, in second phase, all the sources were measured during at least 2 h. Spectrum was measured again by detector A and fitted by the same function in Equation 3.17 in the vicinity of peak 570 keV, integral (N) was extracted. Naturally, much more statistics was collected. Typically, around 30000 counts were collected in 570 keV peak and obtained statistical uncertainty around the level of 0.1%.

Results are summarized in Figure 3.24. X-axis represents count rate extracted by fit in 570 keV peak while y-axis represents integral count rate in full spectrum. Each datapoint is labelled by the number of source. Colour of the label represents type of an source (with or without plastic envelope). It is visible that both types of the sources are distributed rather evenly all along the chart. This might be a hint that the difference in the source geometry (the plastic envelope) does not play very big role in comparison at this level of precision. Nevertheless, without proper absolute reference measurements, sources should not be compared between the categories. Finally, the colour of data point represents distinction between "golden", "silver" and the rest of the sources. All the measurement data points in the plot are aligned close to the red linear function obtained by fit. The correlation between the count rate in full spectrum and in the 570 keV is strong which is due to stable ratio between two measured values. This is a sign of good source quality, that the sources are not contaminated by other gamma emitting isotopes.

Figure 3.24 represents measurements of 40 sources in CENBG. Another three extra source measurements (numbers 123, 132 and 138) were performed in LSM. Sources 84 and

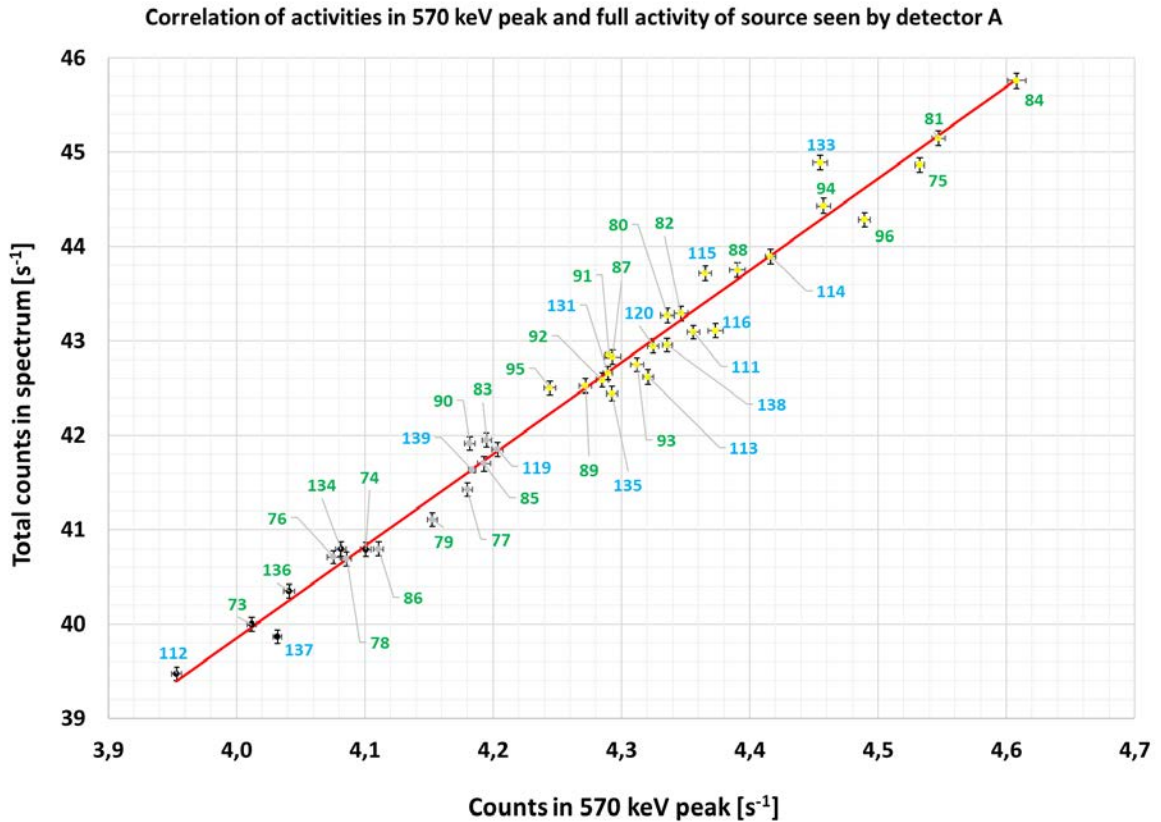


Figure 3.24: Plot representing correlation between count rate from full spectrum and count rate observed in 570 keV peak in each of the measurements of second phase. Datapoints are labelled by number of the measured source. Green label colour represents the source with plastic envelope while blue label represents source without plastic envelope. Colour of the datapoint represents distinction of the source based on the activity introduced in phase one of relative measurements. Yellow colour represents "golden" source, grey colour "silver" source and black colour all the other sources.

138 were measured as reference sources. All the results from measurements can be found in Tables A.5, A.6, A.7 and A.8 in Appendix A. Based on the relative activity measurement results, we can conclude that the difference of activities of the least and most active sources should not be larger than 15%.

### 3.3.1.3 Distribution of Calibration Sources in SuperNEMO Detector

With help of the source mapping studies and relative activity measurements presented in the chapter, it was finally possible to decide which 42 the best calibration sources are eligible for calibration of SuperNEMO calorimeter. The sources will be distributed in six columns in gaps between Selenium foils. Each column contains seven sources.

Their approximate positions are shown in Figure 3.25 obtained from simulations of tracker hit rate caused by calibration sources. Each position is denoted by its column and row. Columns are numbered from 1 to 6. If we look from the Italian side of the lab perpendicularly at the Selenium foils (having Italian-side tracker between us and sources), the Column 1 is on the left and Column 6 on the right. Rows are numbered from 1 to 7 with Row 1 at the bottom and Row 7 on the top.

Sources were distributed in 42 positions based on the results of relative activity measure-

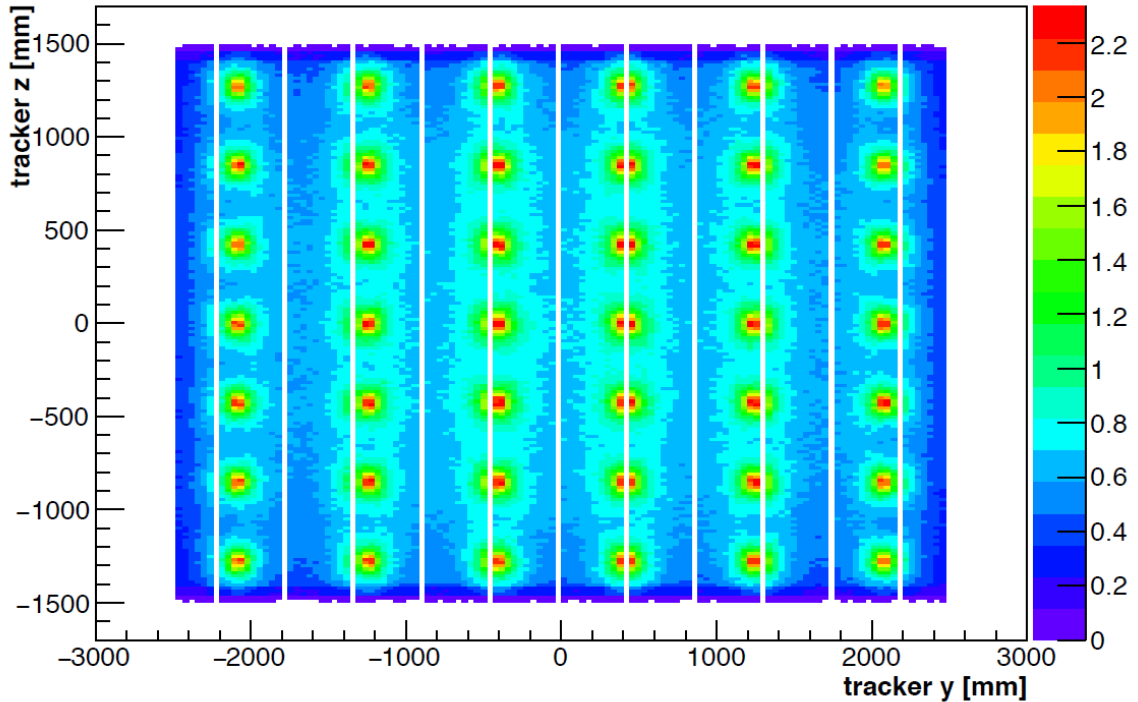


Figure 3.25: Approximate scheme of positions of calibration sources. Vertical spacing between two sources is 42.5 cm. Note that, the sources are in reality lying exactly in the gaps between selenium foils. The slight mismatch in figure is caused by the fact, that the scheme was generated in simulation of the decays of  $^{207}\text{Bi}$  and reconstructed by tracker. Therefore, the positions are influenced by precision of the tracking and also binning of the plot. Figure prepared by Carla Macolino.

ments. The final distribution of the sources is showed in Table 3.8. Both the "golden" sources which were measured with plastic envelope (green font, yellow cell colour, Tables A.5 and A.6) and "golden" sources which were measured without plastic envelope (blue font, yellow cell colour, Table A.7) are independently distributed evenly in order to achieve electron exposure as homogeneous as possible. Note that, before installation of sources, all the plastic envelopes were removed from the sources which had them. After plastic envelopes were removed, positions in Figure 3.18 were no longer relevant for those sources. These positions corresponds to the ones in Figure 3.19 according to following key: UB  $\rightarrow$  WO-SU, DB  $\rightarrow$  WO-SD, US  $\rightarrow$  WO-DU and DS  $\rightarrow$  WO-DD. All 42 sources were, after plastic envelope removal installed in WO-DU position facing the Italian side of the lab. Downwards direction was defined with the direction of gravity. Sources were installed into new envelopes developed specifically for SuperNEMO.

### 3.3.2 Absolute Measurements

All "golden" sources and "silver" source number 76 (together 25 sources) were measured with detector depicted in Figure 3.26. I call it detector B. It is a coaxial Germanium detector. It was chosen for absolute activity measurements because its detection efficiency (at 15 cm) is known within 0.2% systematic uncertainty [87].

It was impossible to measure all of them due to limited time before the sources had to be shipped from CENBG to LSM for installation.

	Column 1	Column 2	Column 3	Column 4	Column 5	Column 6
Row 7	83	88	86	75	77	120
Row 6	111	76	95	78	91	132
Row 5	73	82	135	87	139	114
Row 4	133	112	84	113	81	137
Row 3	123	80	131	93	119	116
Row 2	115	134	89	74	92	136
Row 1	79	94	85	96	90	138

Table 3.8: Final distribution of calibration sources into 42 positions. The position of viewer in scheme is on the Italian side with respect to the calibration sources. Figure takes advantage of similar colour coding to the one in Figure 3.24. Green font colour represents sources which were measured with plastic envelope while blue represents sources measured without plastic envelope. Yellow cell colour represents all the "golden" sources. Cell with no background colour are the "silver" sources and the rest.

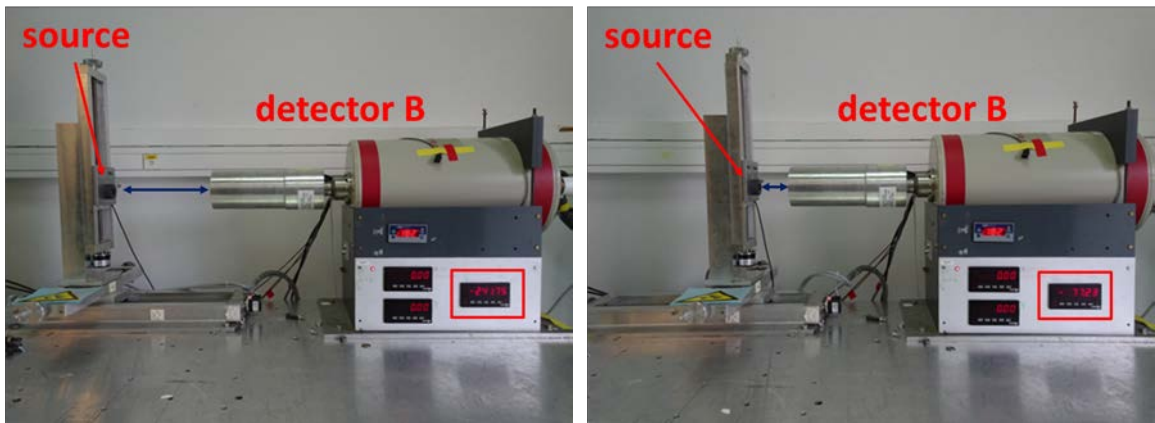


Figure 3.26: Photos of measurement of absolute source activities with detector B. The source was attached to a vertical holder. It was possible to move the holder closer and further from the detector and adapt the source-detector distance (blue arrows) with a precision of 0.01 mm.

Detector B was used for all the measurements of absolute activities. Source was placed in front of the detector in a movable holder as seen in the figure.

### 3.3.2.1 Measurements of Source Depths

It was possible to set the distance between the holder and the detector with precision of 0.01 mm. In order to compute detection efficiencies (in our case it was done by simulation) one needs to know the distance (source-detector) with high precision.

Figure 3.27 represents detailed scheme of cross-sections of two types of the sources (with and without plastic envelope. Red dashed line is a reference line to which sampler holder (grey U-shaped object in scheme) was aligned. The presence of plastic envelope in case b) causes the offset of mylar (blue line) to reference line (red dashed line) marked by green arrows to be different to case a) without plastic envelope. The difference in these offsets causes difference in distances source-detector. It was necessary to measure the difference with sufficient precision in order to correct the position of the sample holder for two different cases.

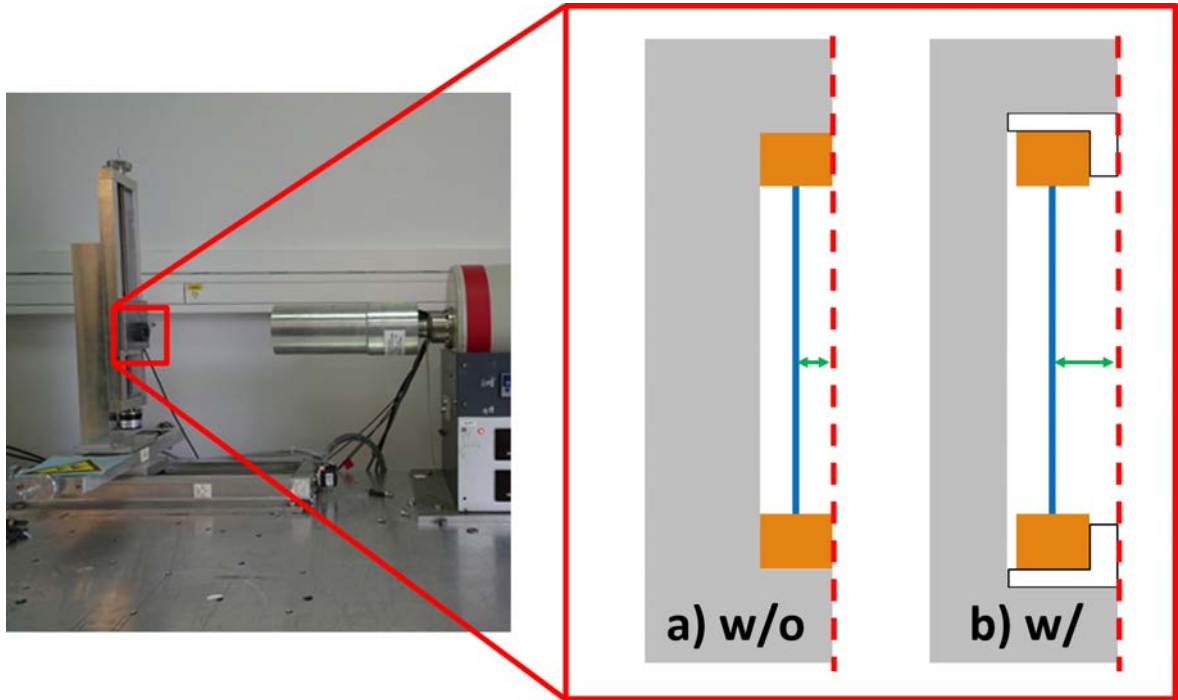


Figure 3.27: Schematic close-up cross section of source holder (grey) with source. There were two different sample holders for both types of calibration sources. Orange rectangles represent cross-section of source frame while blue line the mylar foil. Red dashed line represents an alignment level which was marking the position of source in horizontal direction. The sample holder for source w/ plastic envelope had deeper nest for source placement resulting in difference in offset (green arrows) with respect to red alignment level.

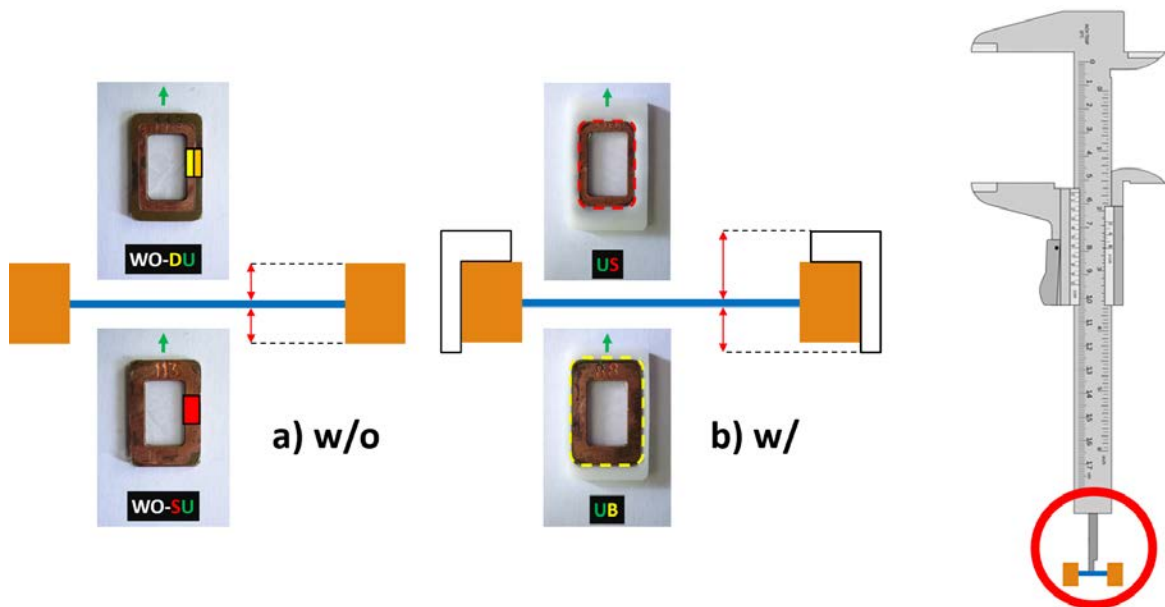


Figure 3.28: Rotated schematic cross section of calibration sources (Left) from Figure 3.27. In the scheme, the sample holders are now omitted. Red arrows depict four source depths which were measured in multiple measurements. Each photo marks the name of the side (WO-DU, WO-SU, US and UB). Right side of the figure shows scheme of the measurement of the depths (not to scale) performed by Vernier calliper.

Figure 3.28 shows schemes similar to the right side of Figure 3.27. For both types of sources (w/o and w/) the cross section of the calibration source through its thickness is shown in schematic way. The photos on top and bottom represents the name of the side of the calibration source. Red arrows are measured source "depths" whose difference result in the offset in distance source-detector explained in the Figure 3.27. Specifically, it is a difference between the depth of WO-DU and US causing the difference, as these were the sides of the calibration sources facing the detector in all absolute measurements. Even though, only WO-DU and US are relevant for the activity measurements, depths of sides WO-SU and UB were also measured in order to obtain full specification of the source dimensions. The depths were measured by depth probe of Vernier calliper as it is symbolised in the right side of the Figure 3.28. Each side was measured in ten repeated measurements in order to decrease measurement uncertainties. This gives 20 measurements per source and with 40 available sources it makes 800 measurements all together. Results can be found in Table 3.9.

Side	d [mm]	$\Delta d$ [mm]
WO-DU	0.633	0.068
WO-SU	0.603	0.054
US	1.796	0.078
UB	1.275	0.063

Table 3.9: Results of measured source depths with their estimated uncertainties.

Results for depths of sides WO-DU and WO-SU are based on 140 measurements each (14 sources without plastic envelope) while depths of sides US and UB are each based on 260 measurements (26 sources with plastic envelope). The difference between the depth of US and WO-DU is  $1.769 \text{ mm} - 0.633 \text{ mm} = 1.163 \text{ mm}$ . Looking back to Figure 3.27 we can state, that in case of the activity measurement of source without plastic envelope holder should be measured 1.163 mm further away from detector in order to compensate for the offset.

### 3.3.2.2 Activity Measurements and Analysis

Measurements of the sources with detector B were always performed at source-detector distance of 75 mm. This distance, finally, after the offset correction was applied, always represented the distance of mylar surface (where the droplet of  $^{207}\text{Bi}$  source is deposited) and the detector. Example of spectrum from measurement of source No. 114 can be seen in Figure 3.29.

Spectrum consists of many peaks originating in the natural background because in this case, the detector was not shielded. Figure also shows (in red) two ROIs containing 570 keV and 1064 keV peaks originating in the measured source. Second ROI contains only 1064 keV peak, therefore it was possible to fit it with a function in Equation 3.17. In case of 570 keV peak, ROI contains another two close peaks. It was, therefore fitted with sum of three Gaussians on top of linear background:

$$f_3(E) = \sum_{i=1}^3 \frac{N_i}{\sqrt{2\pi}\sigma_i} e^{-\frac{(E-E_0^i)^2}{2\sigma_i^2}} + aE + b. \quad (3.18)$$

$E_0^i$  stand for the peak positions,  $\sigma_i$  for their widths and parameters  $N_i$  represent each peak's integral. Parameters a and b describe background. Parameter  $N_1$  was of my interest

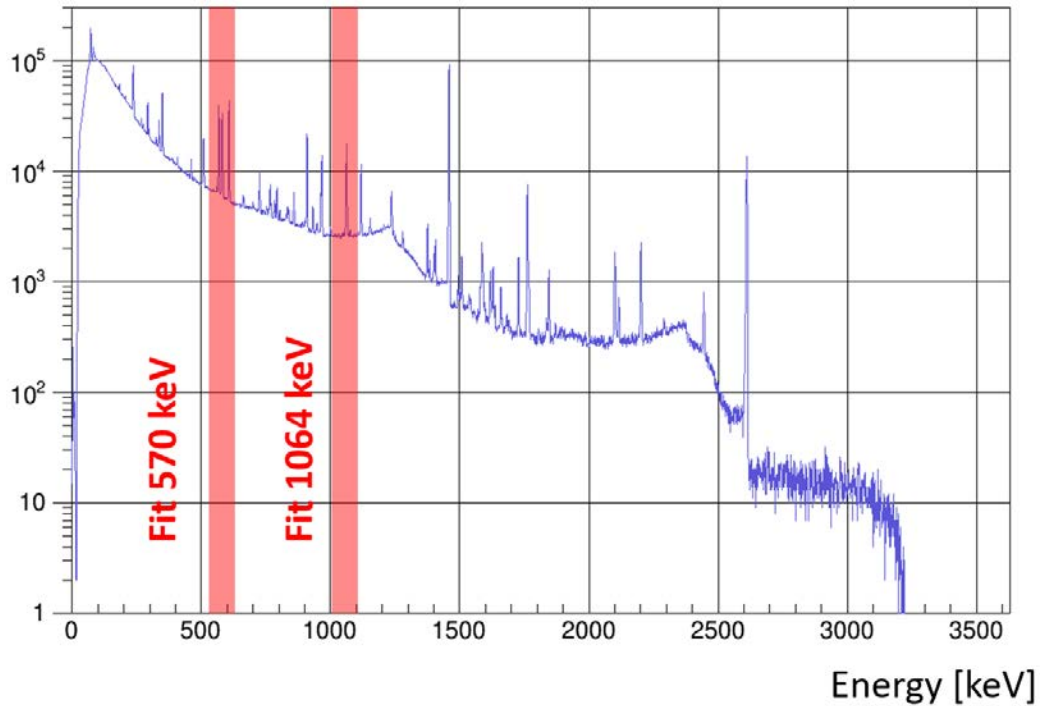


Figure 3.29: Spectrum of source number 114 as measured by detector B. Two red stripes mark the ROI used in the analyses of absolute source activities. Except for the peaks of interest (570 keV and 1064 keV) the spectrum contains many other peaks originating in natural background radiation because the detector was not shielded.

as it was representing the integral of counts in 570 keV peak. Performance of the fit can be seen in Figure 3.30.

Blue bins (width of 1 keV) represent measured data in the zoomed region while red curve represents triple Gaussian fit.

After the integral in both the 570 keV (denoted  $N_{570}$ ) and 1064 keV (denoted  $N_{1064}$ ) was extracted, the activity can be computed using following equation:

$$A = \frac{N}{t_{live}\epsilon r} \tag{3.19}$$

$N$  stands for the integral in peak of interest (for 570 keV,  $N = N_{570}$  and for 1064 keV,  $N = N_{1064}$ ). This number should be divided by live time of measurement  $t_{live}$  and corrected for detection efficiency  $\epsilon$  and branching ratio  $r$ . Both detection efficiency and branching ratio are individual for each peak. Their values which were used in the computation of activities can be found in Table 3.10.

Table displays also the absolute uncertainties of branching ratios and detection efficien-

$E_\gamma$ [keV]	$r$ [1]	$\Delta r$ [1]	$\epsilon$ [1]	$\Delta \epsilon$ [1]
<b>570</b>	0.9776	0.0003	0.0102	0.000011
<b>1064</b>	0.7458	0.0049	0.006739	0.000045

Table 3.10: Values of branching ratios (from [88]) and detection efficiencies (from simulations) with their uncertainties used in the analysis of absolute activities.

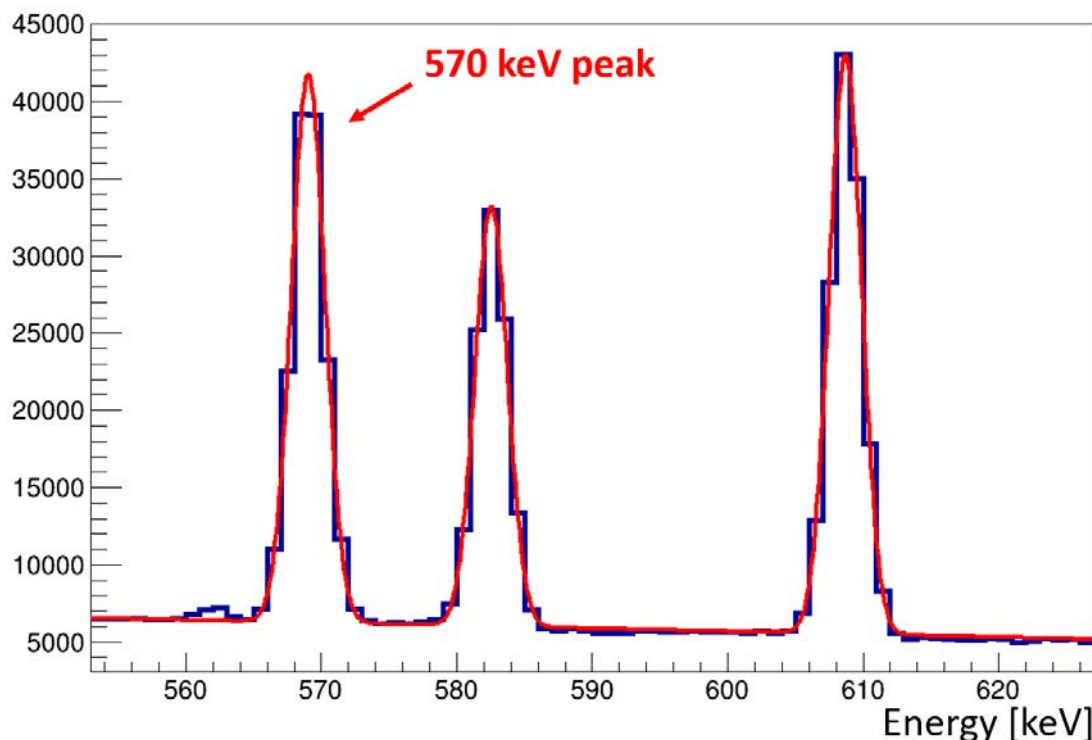


Figure 3.30: Zoom of the ROI in the vicinity of 570 keV from spectrum in Figure 3.29. Blue curve represents measured data and red curve the peak with triple Gaussian given by Equation 3.18.

cies. The live time and number of counts in integral was, naturally, source specific. The uncertainty of live time is negligible and statistical uncertainty of integral ( $\Delta N$ ) was obtained after fit was performed. Uncertainties, as well as the peak counts, are included in Tables A.9 and A.10 for my analysis and in Tables A.11 and A.12 for my colleague's analysis (discussed in following text). All the mentioned tables can be found in Appendix A.

The relative uncertainty of activity  $\Delta A/A$  was obtained by formula:

$$\frac{\Delta A}{A} = \sqrt{\left(\frac{\Delta N}{N}\right)^2 + \left(\frac{\Delta r}{r}\right)^2 + \left(\frac{\Delta \varepsilon}{\varepsilon}\right)^2} \quad (3.20)$$

For each source, two values of activity was obtained. Naturally, these two values should give the same results as they describe the same source.

Figure 3.31 includes comparison of results for all 25 sources measured for absolute activities. Results of values obtained by analysis of 1064 keV have roughly two times larger relative uncertainty. It is caused by difference in relative uncertainty of detection efficiency. While in case of 570 keV  $\Delta \varepsilon/\varepsilon \approx 0.1\%$  for 1064 keV it reaches almost seven times higher value of 0.67%! In the figure one can also notice a discrepancy on a level of three sigma between the activities obtained by two different peaks.

### 3.3.2.3 Discrepancy Between Results

Previous analysis of source activities offered two different value extracted from two different peaks. There are two possibilities how to approach such a situation. First of all it is possible to state that within 5% precision the values do agree if this kind of precision is



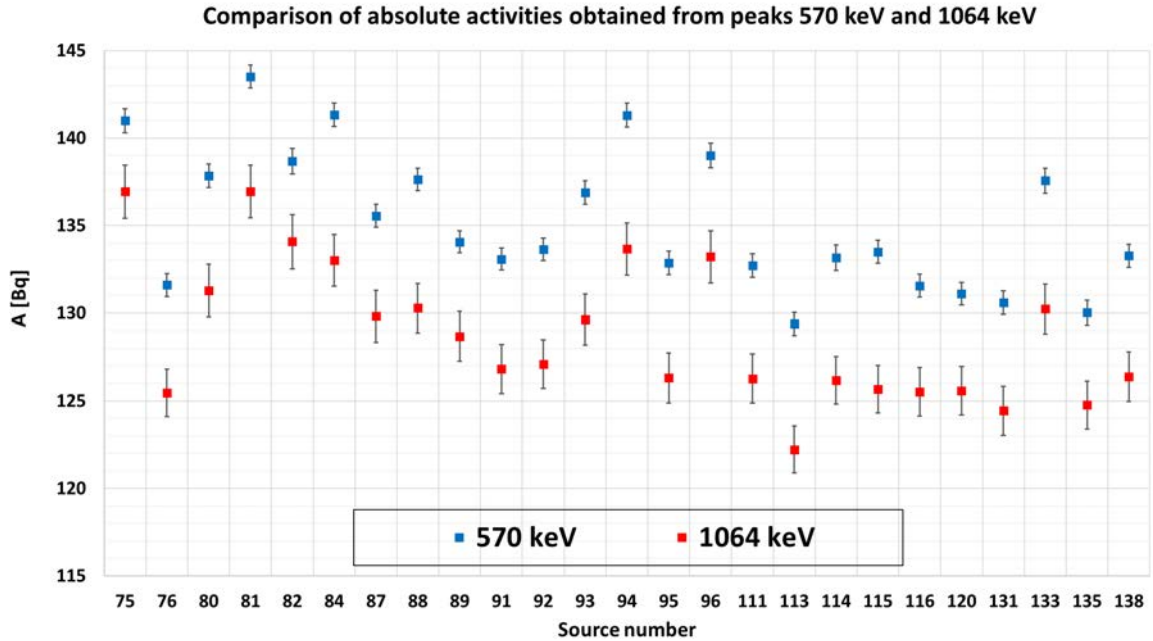


Figure 3.31: Comparison of absolute activities obtained in my analysis from two different peaks.

sufficient for our needs. Nevertheless, the aim of the study is to obtain relative uncertainties approaching 1%.

Therefore, it is important to search for the refinement of the values used in analysis. If we look at the Equation 3.19, we can find three experiment-dependent quantities in the formula. Live time of the measurement, is known effectively with perfect precision. Other two - number of counts in the peak ( $N$ ) and detection efficiency ( $\epsilon$ ) can contribute to the discrepancy. Let me discuss them in more detail.

Number of counts (integral) extracted from the peak depend on the analysis method. In order to investigate possible mistakes arising from fitting and extraction of number of counts, my colleague Frédéric Perrot set up an independent analysis method for extraction of peak counts in both the peaks 570 keV and 1064 keV. After he obtained number of counts ( $N$ ) the activity was calculated using the same equation, i.e. Equation 3.19. He also used same value of detection efficiencies and branching ratios from Table 3.10. To put it into nutshell, our analyses analysed independently both peaks, differing only in the method of extraction of peak's integral. Figures 3.32 display the ratio ( $M/F$ ) of my absolute activity values ( $M$ ) divided by the ones obtained by Frédéric ( $F$ ). In top part of the figure, comparative ratio is plotted for 570 keV peak while bottom shows the ratio for 1064 keV. Both analyses are producing consistent results well within the error. In other words, the analysis of Frédéric confirmed the discrepancy between two peaks observed in Figure 3.31. The agreement between our two methods have also shown that the explanation for discrepancy does not lie in the method of extraction of peak integrals but rather in the detection efficiency.

In the time scale of this thesis the investigations of detection efficiency values have started, however, the results are expected to be obtained after its finalisation. The issue is investigated by our colleague in CENBG, Bertram Blank, who kindly provided the Detector B which was already well calibrated for 15 cm. However, the distance source-detector we used in our measurements was 7.5 cm in order to obtain larger statistics in shorter time. For this distance, the detector is not so well calibrated and, therefore, the discrepancy occurred.

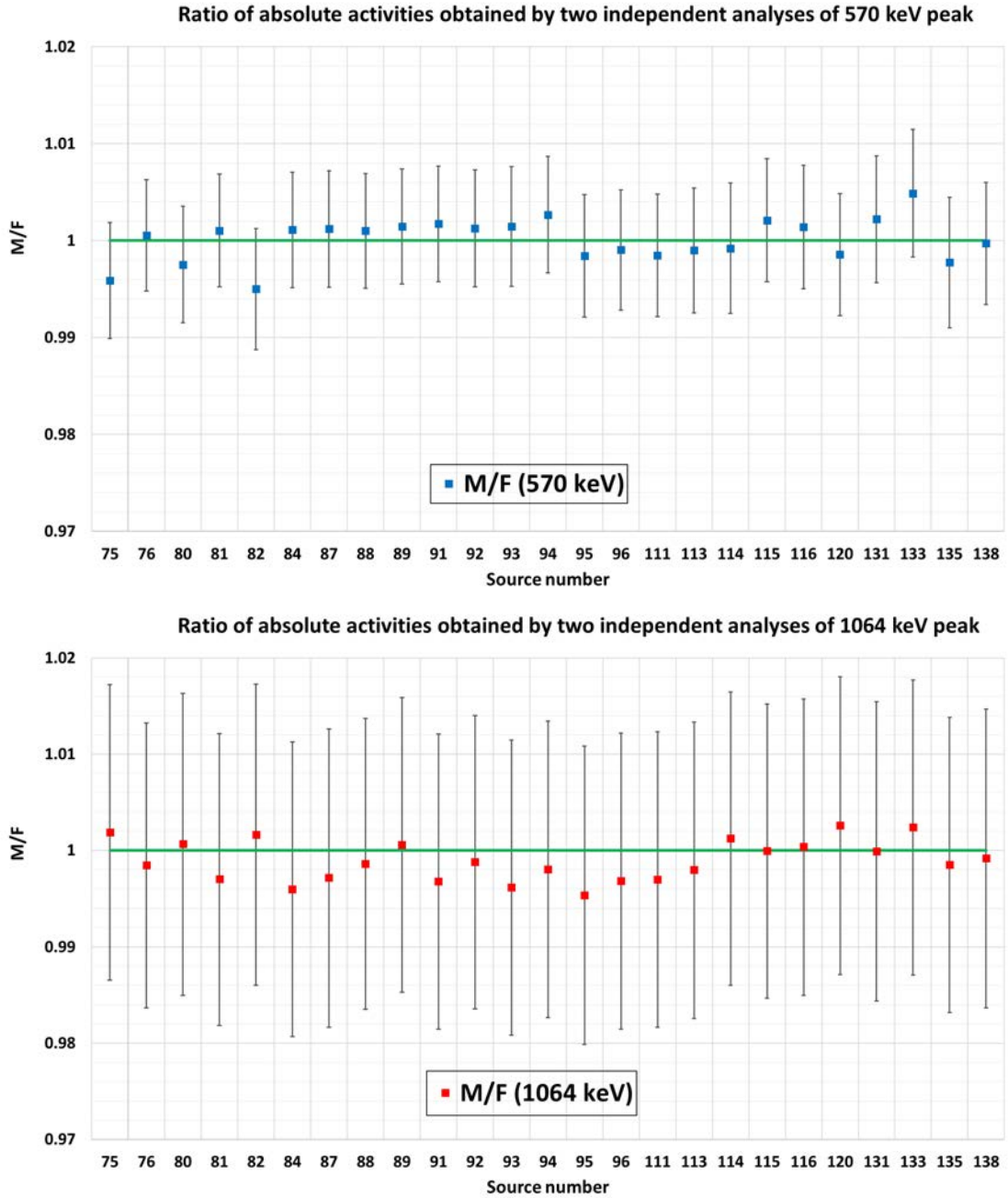


Figure 3.32: Comparisons of results of two independent analyses performed by me and Frédéric. BOTH plots show ratio between absolute activity obtained by my method divided by same number obtained by Frédéric's method. Top plot (blue points) shows comparison for peak 570 keV, bottom plot shows comparison of 1064 keV peak. Within the uncertainties, the methods are fully consistent.

The detection efficiency for 7.5 cm will be obtained by measurement of source  $^{60}\text{Co}$  with known activity. This isotope has two lines which are very close to the energies of gammas we used in our analyses.

Absolute activities were calculated and within 5% uncertainty the results obtained from two peaks are consistent. However, the study is under investigation. Relative uncertainty of activities expected to be reached after it will be finished is 1%.

## 3.4 Conclusions

In the chapter, two studies of  $^{207}\text{Bi}$  calibration sources were performed. In the first one, the source deposition quality within a source frame was studied. Study was performed by three Silicon Timepix detectors provided by IEAP CTU in Prague. Calibration, test measurements, and the final measurements were performed at the end of 2017. Analysis software was written and results were obtained at the beginning of 2018. Results have shown that no source sample had the  $^{207}\text{Bi}$  deposited outside of the mylar foil, on the Copper frame. Five measured sources had the droplet deposited more than one millimeter away from center. When it comes to deposition quality, I conclude, that all the sources were proved to be eligible for calibration, however, the differences in quality were observed within one millimeter. Database of all the results and statistics can be found in Appendix A. Currently an article about the measurements is finished and will be submitted soon for a publication, after it would be approved by collaboration.

In the second study, source activities were measured. The uncertainty of activity value is the main contributor to the final uncertainty of  $2\nu\beta\beta$  half-life. Study was separated in two measurements with two different Germanium gamma detectors, which I called A and B. With detector A in CENBG, 40 sources were measured during 2 hours each, and relative activities were obtained. Another two sources were measured in LSM with similar method. The measurements played a key role for the source installation in the detector. Based on the study, the sources were distributed in order to reach best homogeneity of exposure from sources all around the calorimeters from main wall. With detector B, provided by my colleague Bertram Blank, measurements of absolute activities were performed in CENBG. Only 25 sources could be measured in these precise measurement, due to limited time the sources could stay in CENBG. The statistics during at least one day was collected for each source. Calculated activities of the sources were ranging from 125 Bq and 145 Bq. The analysis was based on the counts obtained by fit from 570 keV and 1064 keV peaks. For each source, calculated activity extracted from 1064 keV was typically smaller than the one obtained from 570 keV peak. This is a discrepancy which has to be accounted for, in order to reach 1% uncertainty in the measurement. Independent method of study of my colleague Frédéric Perrot has shown the same behaviour, therefore, we can conclude, that the difference is not introduced in the analysis. The discrepancy arises from the detector calibration. The detection efficiency of the detector is known within uncertainty, on the level of 0.2% at the source-detector distance of 15 cm. However, the measurements were performed in a distance of 7.5 cm. After the detector efficiency for 7.5 cm will be extracted from measurements with  $^{60}\text{Co}$ , the uncertainties of the absolute activities could be reported within the 1% uncertainty. This is a work beyond the scope of the thesis.

## Simulations of SuperNEMO Neutron Shielding

Among all the other sources of background, neutrons can also cause indirectly a fake double beta event in the detector. It is, therefore, inevitable for experiments of high sensitivity such as SuperNEMO to take them into account. According to their different character we can divide background neutrons into external and internal.

**External neutrons** are produced in materials outside the detector. Their typical source in LSM is a rock surrounding the lab. The analysis have shown the presence of Uranium and Thorium in the rock. These elements produce alpha particles which are capable to produce neutrons via  $(\alpha, n)$  reactions. They also undergo spontaneous fission also capable to produce neutrons. LSM is the deepest European laboratory with overburden on the level of 4800 m.w.e. Only roughly one in a million cosmic muons reach the lab which is 1.7 km deep underground. However, these remaining high energy muons interact with the rock and can possible produce neutrons. It is necessary to develop a shielding which is able to effectively capture neutrons and lower the chance for observation of fake double beta decay event caused by neutron.

**Internal neutrons**, as the name suggests, are produced inside of the detector materials. Each material for SuperNEMO demonstrator is carefully chosen and tested for radiopurity in order to eliminate any source of internal background to maximal possible level. Naturally, it is not possible to eliminate internal neutrons completely and, therefore, their sources have to be well known and described. In SuperNEMO, there are two main sources of internal neutrons. First of all, it is roughly 286 kg of glass used in the PMTs. The glass contains  $^{238}\text{U}$  which fissions spontaneously by production of roughly 2 neutrons per fission. The activity of the glass was measured to be on the level of 1 Bq/kg. The glass is expected to account for roughly  $10^4$  neutrons produced every year. Second main source of internal neutrons can be found in a small metallic component of feedthroughs on top and bottom of the demonstrator used for gas ventilation. These feedthroughs contain Beryllium as well as Uranium. Uranium produces neutrons via spontaneous fission, while Beryllium is capable to effectively capture alpha particles and produce neutrons via  $(\alpha, n)$  reactions. Total mass of these tiny metallic parts in demonstrator will account for roughly 12 kg but is still expected to contribute to roughly  $5 \times 10^3$  internal background neutrons every year. Even though, radiopure detector materials produce orders of magnitude less neutrons every year than the ones coming from external sources, they are almost impossible to be shielded which makes them in general potentially more dangerous.

The background neutrons can be thermalized in the shielding and/or detector materials.

Subsequently, they can be captured while gammas of few MeV are produced. For these high energy gammas, positron-electron pair production is dominating process. Due to uncertainties in track reconstruction positron might be reconstructed as an electron. Such an event represent fake (background) double beta decay event.

The tasks presented in the current chapter were performed during early works on the design of SuperNEMO demonstrator shielding. It represent first rough estimations of external neutron backgrounds which contributed to the discussion of the neutron shielding design. The goal of the chapter is to perform a first comparison between scenarios with different shielding materials. The fluxes passing through shielding are estimated based on the realistic background measured in LSM. Materials capturing the most of the neutrons in the detectors were identified.

## 4.1 Simulations of the Shielding

Following study is dedicated uniquely to the external neutron background. The main goal is to compare a shielding performance of three different materials (polyethylene, water and wood) of three different thicknesses (10 cm, 20 cm and 30 cm). Combination of these materials and their thicknesses represent nine "wall scenarios" ("shielding scenarios"). The simulation was performed in two phases. In the first phase, background neutrons from spectrum measured in LSM was propagated through a simple wall for each one of the nine wall scenarios. In second phase, the neutron spectrum which passed the wall was used as an input spectrum for Falaise simulation in order to identify the materials and regions of the demonstrator which captured the majority of the neutrons.

External neutrons are induced in the rock surrounding LSM by cosmic muons which have to pass 4800 m.w.e. overburden. They are also produced by Uranium and Thorium isotopes in the rock. They produce neutrons directly in spontaneous fission or alpha particles able to induce neutrons via ( $\alpha, n$ ) reactions.

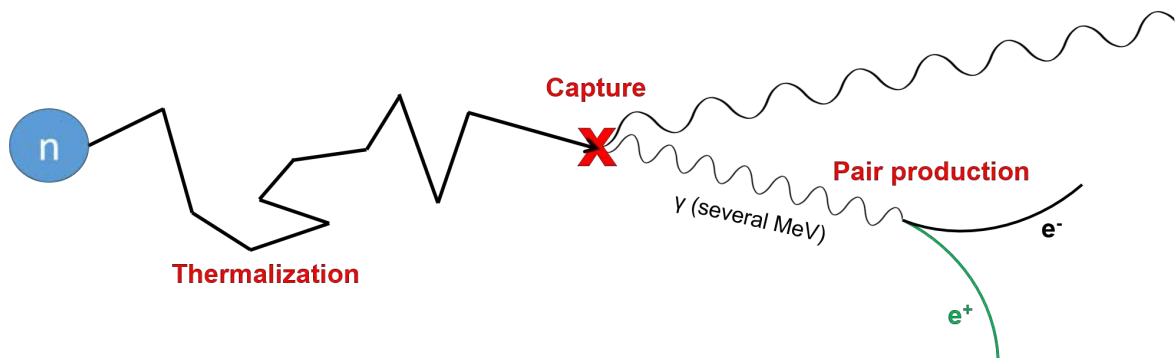


Figure 4.1: Scheme describing the process which leads to the production of fake double-beta events induced by neutrons. The process is described in more detail in the text.

Figure 4.1 depicts simplified scheme of production of fake double-beta signal in the demonstrator caused by neutron. Neutron originating in the rock surrounding the lab loses kinetic energy in a sequence of collisions. These collisions occur either in the shielding or in the demonstrator construction material. In each collision the neutron undergoes, there is a chance that the neutron would be captured by nucleus it collides with. Majority of the neutrons are slowed all the way down to thermal energy (0.3 eV) before they are captured. At

the thermal energy neutron's cross section for capture increases drastically. However, neutrons with higher energies can also be captured before thermalization is finished. Nucleus which captured neutron has changed its structure and now it has excess excitation energy which has to be released. It does so, typically, in a form of one or few gamma rays of several MeV. Each gamma with energy superior to 1.022 MeV (two electron or positron masses) is capable to produce electron-positron pair. The probability of the process is raising with the gamma energy. The magnetic field present in the demonstrator ensures opposite clockwise-ness of trajectories belonging to the particles with opposite charge. However, if trajectories are straight enough, positron trajectory can be misreconstructed as an electron. The sequence of events composed of a neutron thermalization, followed by neutron capture, pair production and misreconstruction of positron as electron might seem very unlikely. Nevertheless, neutrons are particles without charge which are very difficult to stop. There are millions of neutrons emitted from rock every year into the lab and each can potentially produce fake signal. It is important to estimate not only their numbers but also how often they are captured in the detector.

### 4.1.1 Phase One: Neutrons Passing Through Shielding

As a first step towards the estimation of effects of external neutron background, it is important to know the neutron energy spectrum produced by rock in LSM. In my simulations I used spectrum estimated by [89]. The resulting spectrum is depicted in Figure 4.2.

Note that, the spectrum provided by the article was estimated for all neutrons with energy higher than 1 MeV. Therefore, the spectrum in lowest roughly 1 MeV (before first red data point) was obtained by simple linear extrapolation. Total integral flux of neutrons measured

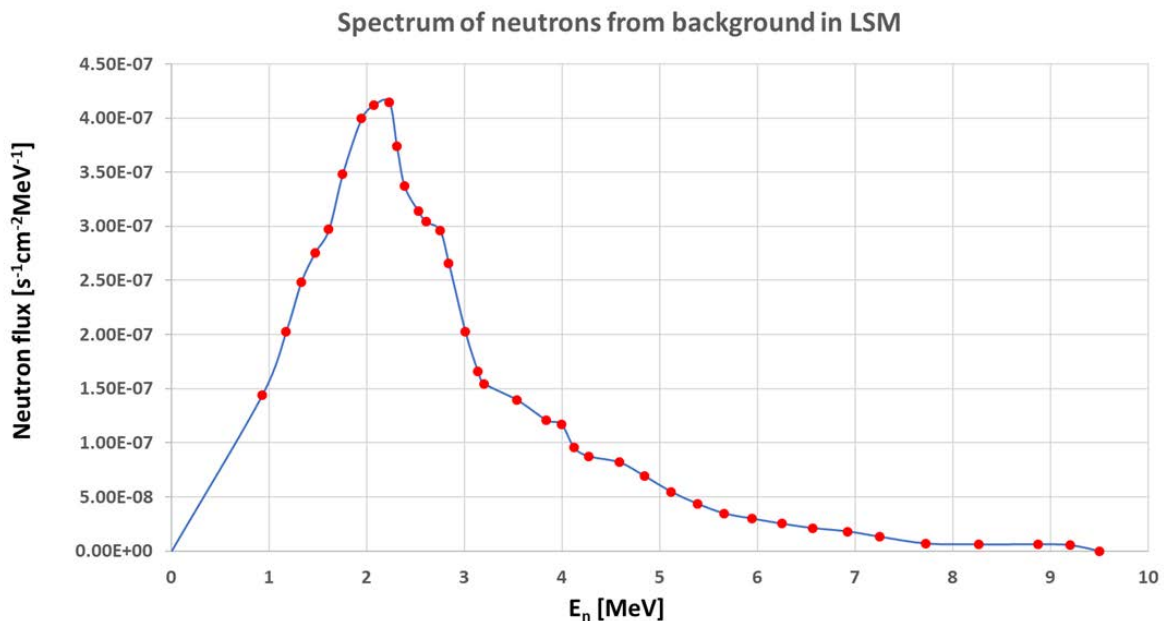


Figure 4.2: Spectrum of external neutrons  $B_{LSM}(E_n)$  as measured in [89]. Red dots represent data points obtained from the article. Blue lines represent simple linear interpolations of the function in order to obtain continuous spectrum. Note that, the region for the lowest energy region  $(0 \text{ MeV}, 1 \text{ MeV})$  is not covered in the article and was extrapolated towards  $B_{LSM}(0) = 0$ .

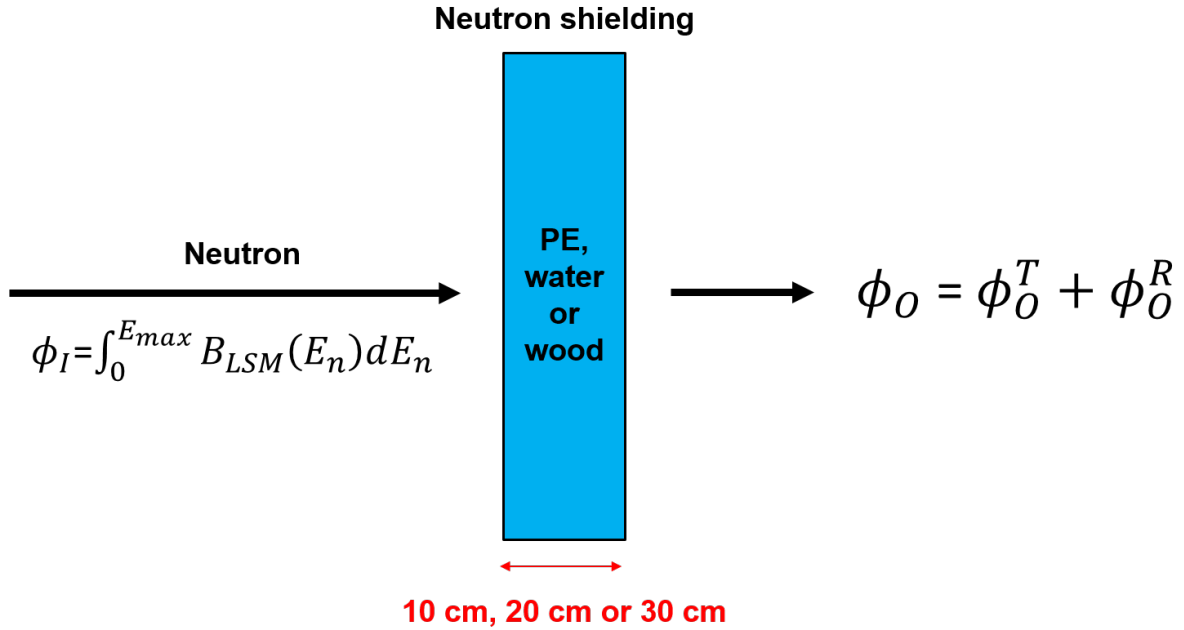


Figure 4.3: Schematic representation of first phase simulation geometry. Neutron was shot perpendicularly (in vacuum) towards a wall composed of one of three materials named in the figure. Each simulated neutron sample represented proportion of total flux  $\Phi_I$  with given weight. Its calculation is explained in text. Thickness of the wall was set either to 10 cm, 20 cm or 30 cm in dependence on the wall scenario. Total outgoing flux  $\Phi_O$  was accumulated as a total sum of all neutron sample weights which passed the wall. Those samples which passed to the other side with remaining energy of  $E < 0.3$  eV were scored also to thermal flux  $\Phi_O^T$ , the rest was scored into flux  $\Phi_O^R$ . The size of wall in both directions perpendicular to impacting neutron was 1 m which was sufficient to prevent neutrons leaking to the side.

in LSM is  $10^{-6} \text{ s}^{-1} \text{ cm}^{-2}$ , therefore, the spectrum in Figure 4.2 is normalized to this value.

Interest of the first phase of the neutron simulation is in the test of different shielding materials. Three materials were chosen: polyethylene, water and wood. Simulation was performed using Geant software package, version 4.10.02.b01. Geometry of the simulation is depicted and briefly explained in Figure 4.3.

Inside of the wall, neutrons were slowed down in the wall or, possibly, stopped. Only neutrons which passed through were scored in a spectrum. This spectrum represents spectrum of neutrons which could be seen behind shielding made of chosen material. Nine different simulations were performed each containing  $8 \times 10^6$  samples. Water in simulation was composed of Hydrogen and Oxygen atoms in ratio 2:1. Water is standard material already defined in the Geant package as well as polyethylene. Polyethylene in Geant is composition of Carbon and Hydrogen in ratio 1:2. The only material which I had to define by hand was wood. In my simulation, wood was composed of Hydrogen, Carbon and Oxygen in following respective ratio 4:2:1.

Energy spectrum was sampled by neutrons from flat energy distribution between 0 MeV and  $E_{max} = 9.5$  MeV. Flat distribution of samples is useful to obtain homogeneous sample coverage (and also statistical uncertainty) all over the neutron spectrum. In order to take into account the shape of the background distribution (Figure 4.2), different simulated neutron samples did not represent same proportion of flux. Proportion of neutron flux carried by neutron sample was expressed by weight  $w$ . Sample with random energy  $E_n$  represented a

Mat.	d [cm]	$\Phi_O^T \times 10^9$ [s <sup>-1</sup> cm <sup>-2</sup> ]	$\Phi_O^R \times 10^9$ [s <sup>-1</sup> cm <sup>-2</sup> ]	$\Phi_O^T / \Phi_O^R$ [1]	$\Phi_O \times 10^9$ [s <sup>-1</sup> cm <sup>-2</sup> ]	$\Phi_I \times 10^9$ [s <sup>-1</sup> cm <sup>-2</sup> ]
PE	10	114	285	0.401	399	1000.1
water	10	114	391	0.292	505	1000.1
wood	10	96	479	0.201	575	999.9
PE	20	37	48	0.778	85	1000.2
water	20	64	95	0.673	159	999.8
wood	20	91	150	0.605	241	999.7
PE	30	7	9	0.805	16	999.6
water	30	19	23	0.813	42	1000.3
wood	30	38	44	0.863	83	999.8

Table 4.1: Results of the first phase of shielding simulation. For each of the nine wall scenarios flux which passed through the shielding is displayed. Fluxes marked with index "O" represent the flux behind the wall. Index  $\Phi_O^T$  represents flux of all neutrons which passed wall with remaining energy of  $E < 0.3$  eV (thermal). In contrary,  $\Phi_O^R$  represents the rest of the spectrum behind the wall, i.e.  $E > 0.3$  eV.  $\Phi_I$  displays flux impacting the wall. The value is within statistical precision equal to  $10^{-6}$  s<sup>-1</sup>cm<sup>-2</sup> in each wall scenario.

flux given by value  $B_{LSM}(E_n)$  given by function in Figure 4.2. The weight  $w$  is, however, not yet complete. The numerical value  $B_{LSM}(E_n)$  of LSM neutron background spectrum represents number of neutrons per unit energy (and unit area and unit time). Therefore, it is crucial to know which fraction of energy spectrum each generated sample is representing. As it was already mentioned, in each (out of nine) wall scenarios  $N_S = 8 \times 10^6$  neutron samples were simulated. They homogeneously covered energy interval  $\langle 0 \text{ MeV}, 9.5 \text{ MeV} \rangle$ . Therefore, each simulated sample represented a  $\Delta E/N_S$  of energy interval. Here,  $\Delta E = E_{\max} - E_{\min}$  is an energy range covered by generator's interval (i.e.  $E_{\min} = 0 \text{ MeV}$  and  $E_{\max} = 9.5 \text{ MeV}$ ). Finally, the weight of each sample was given by

$$w = \frac{B_{LSM}(E_n)\Delta E}{N_S}. \quad (4.1)$$

Weight  $w$  represents a fraction of integral flux per unit area and unit time ( $\Phi_I = 10^{-6}$  s<sup>-1</sup>cm<sup>-2</sup>) contributed by sample with energy  $E_n$ . Therefore, the sum of all weights over all samples should (within a negligible statistical error for large samples) give total integral flux (in the bracket). It is a confirmation of proper performance of the simulation which can be observed in Table 4.1.

After the weight of sample was calculated, the neutron sample was propagated through the wall of given material and thickness. Let me remind at this point, once again, that while the thickness of the wall was finite, the other two dimensions were effectively infinite, meaning that the other two dimensions were large enough in order to prevent neutron exiting on a side of the wall. Fraction of the neutron flux was captured inside of the wall or deflected back, however, many of the neutrons were only slowed down and propagated to the other side of the wall. These neutrons were scored, according to their remaining energy after moderation, into resulting output spectrum. Integral flux of the neutrons which passed the wall in each of the nine wall setups is shown in the Table 4.1.

Table contains values of total flux of thermal neutrons ( $E_n < 0.3$  eV)  $\Phi_O^T$  which passed the wall,  $\Phi_O^R$  - flux of all the rest of neutrons ( $E_n > 0.3$  eV) passing the wall, total outgoing flux



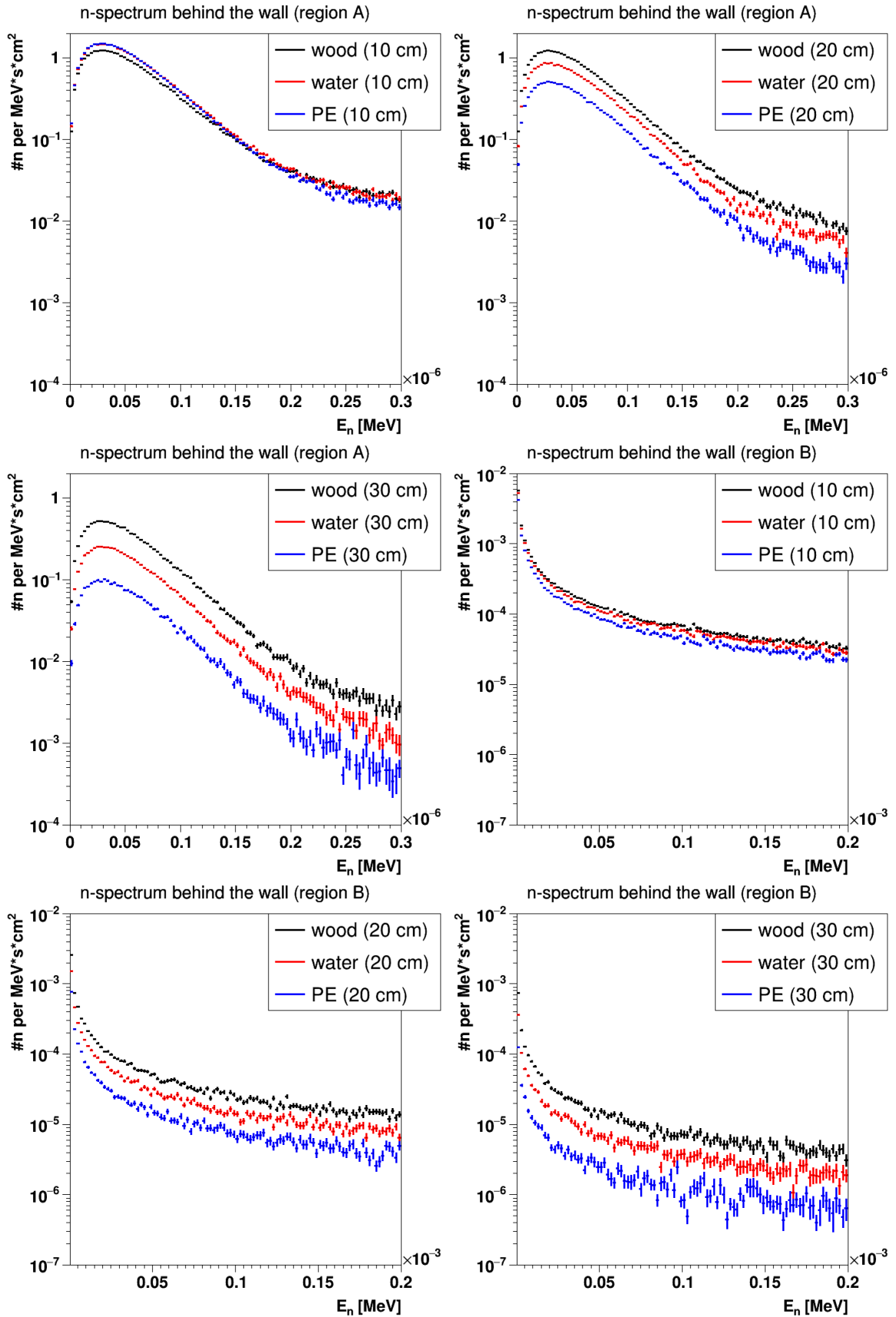


Figure 4.4: Spectrum of neutrons which passed the shielding in nine different wall scenarios. Figures represent first two energy regions: A - (0 eV, 0.3 eV) and B - (0.3 eV, 200 eV). Every single figure depicts three wall scenarios with the same thickness in order to compare performance of the materials.

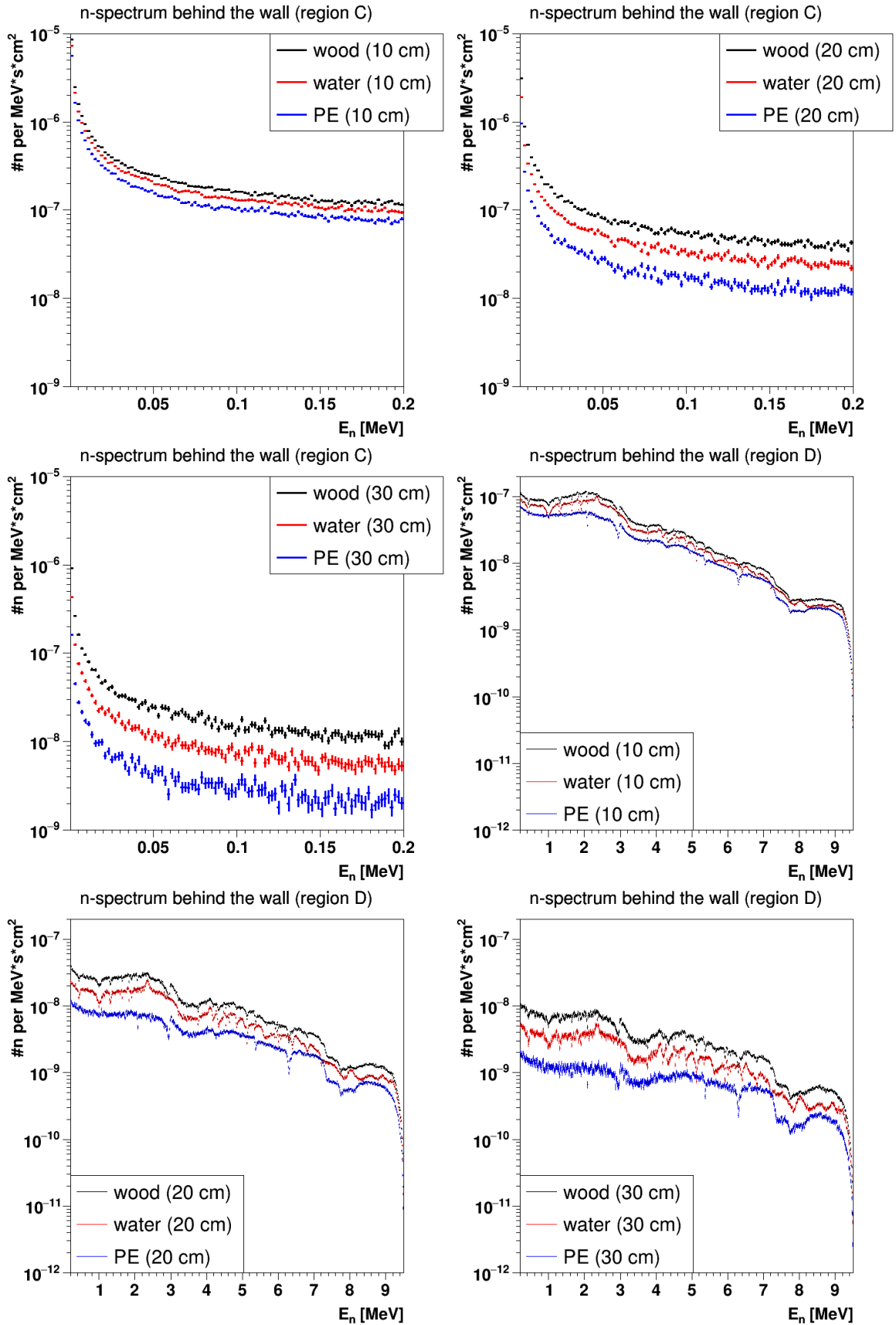


Figure 4.5: Spectrum of neutrons which passed the shielding in nine different wall scenarios. Figures represent first two energy regions: C - (0.2 keV, 200 keV) and D - (0.2 MeV, 9.5 MeV). Every single figure depicts three wall scenarios with the same thickness in order to compare performance of the materials.

on the other side of the wall  $\Phi_O = \Phi_O^T + \Phi_O^R$  and total incoming flux  $\Phi_I$  given by spectrum of background neutrons in LSM. Incoming spectrum is obtained as a sum of weights of all the generated particle samples and can serve as estimation of precision of the simulation.

For a given thickness polyethylene is shown to be the best shielding material. With only 10 cm thickness, polyethylene is capable to stop roughly 60% neutrons, while water and wood of the same thickness only less than 50%. In scenarios with wall of 10 cm thickness polyethylene seems to produce the largest contribution of thermal neutron flux. Polyethylene does not only stop the neutrons of any energy more effectively than water or wood, it is also very effective in thermalization of neutrons passing the wall. In scenarios with 30 cm thick wall, almost half of the remaining neutron flux is thermalized. This is similar for all the three materials. Nevertheless, polyethylene stops neutrons more than twice as effectively than water and more than four times as effectively as wood. For any given thickness, polyethylene performs the best while wood shows the worst results. It is also important to note at this point, that the results of wood shielding in my simulation are dependent on the definition of wood as a material. Definition of such an amorphous material like wood, can be, in principle, chosen in many different ways. Wet wood contains more water (more Hydrogen) than dry wood and composition of other elements might differ as well. It has to be taken into account when comparisons are discussed.

The neutron which passed the wall have access to the detector and can potentially cause fake double beta-signal. Not only fluxes but also spectra of neutrons behind the wall were saved in the simulations. They are plotted in Figures 4.4 and 4.5. The neutron spectrum, typically, covers several orders of magnitudes in energy. Therefore, I decided to split it into four different energy regions called A, B, C and D which I have plotted separately. Their limits are following: A - (0 eV, 0.3 eV), B - (0.3 eV, 200 eV), C - (0.2 keV, 200 keV), D - (0.2 MeV, 9.5 MeV). Weight of each generated neutron sample was scored into one of these four regions in dependence on the remaining neutron's kinetic energy after passing the wall. Sample of weight  $w$  represents a fraction of integral flux (in  $s^{-1}cm^{-2}$ ) not normalized to energy. Energy regions A, B, C and D cover different proportions of full spectrum and, therefore they contain, in principle, different number of samples. In order to be capable to compare fluxes between the regions it was necessary to normalize flux again back to the unit of energy. The width of bin  $b_w$  was different in each region. The energy normalization is performed simply by dividing the weight of neutron sample by bin width into which it was scored, i.e. ( $w/b_w$ ). Outcoming energy spectra behind wall for all wall scenarios in regions A, B, C and D, respectively, are shown in Figures 4.4 and 4.5.

### **4.1.2 Phase Two: Mapping of Demonstrator**

Phase one of the neutron simulation provided very useful information about spectra of remaining neutrons behind the shielding (Figures 4.4 and 4.5). These neutrons have access to detector and have possibility to produce fake double-beta events. They were used as an input spectra in the second phase of the simulation. The question of interest in this phase is to determine number of neutrons per year which are captured in demonstrator. It is important to evaluate the number of neutrons captured every year in the different demonstrator construction materials and compare their contribution.

The simulation was performed by Falaise version 2.0.0. As it was mentioned in the introduction to the chapter, this work was performed at the early works on the shielding design for demonstrator, therefore, shielding was not yet included. It is a reason why the passage of neutrons through wall was simulated separately in phase one using Geant package. Neutron

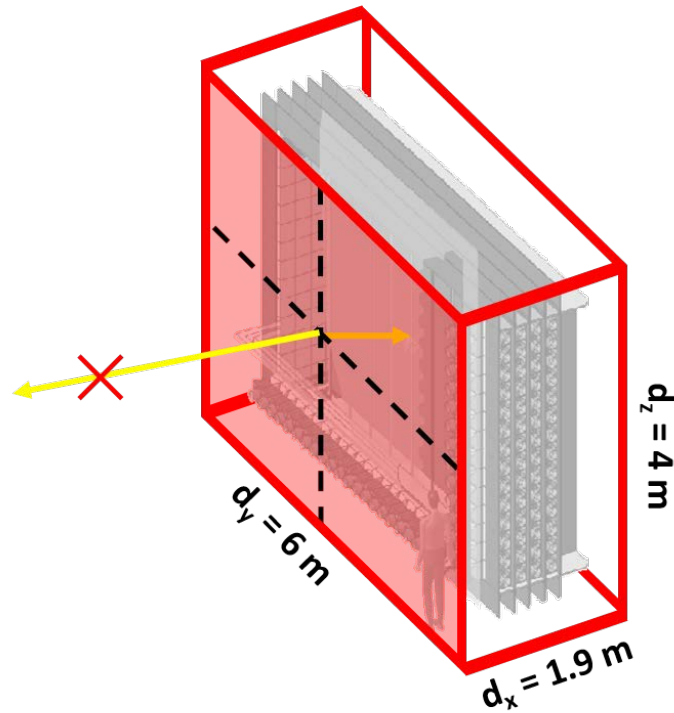


Figure 4.6: Schematic representation of simulation's setup in phase two. Figure shows wire model of box surrounding the demonstrator. From each of six surfaces neutrons were shot homogeneously to  $4\pi$  solid angle. Yellow arrows represent example of two neutrons originating in same point in the box. Neutron which was emitted inside was followed in the simulation while neutron exiting out of the box was immediately rejected (symbolized by red cross). The box was for the purposes of display negligibly expanded. Real box was touching the demonstrator from each side.

spectrum which passed the wall in one of nine wall scenarios was a starting point for phase two. Similarly to first phase, neutrons were generated in a flat spectrum to ensure homogeneous exposure of the spectrum. Neutrons were generated in box tightly surrounding the demonstrator. The box's center matched the center of demonstrator. The size of the box was  $187 \times 600 \times 406 \text{ cm}^3$ . Neutrons were shot from random positions distributed on the surface of the box into  $4\pi$  angle directions. Those with initial momentum heading out of the box were not taken into account.

Figure 4.6 represents simple scheme of setup in simulation in phase two. Rejection of neutrons emitted outside caused loss of 50% of the simulated sample, however, the version of Falaise in use lacked possibility to generate particles into predefined solid angles.

In phase one simulation, I concluded that spectra of neutrons passing the shielding span over many orders of magnitude in energy. Thermal neutrons have a much larger probability to be captured due to their cross sections. They represent, however, crucial but extremely narrow stripe of the spectrum. This give rise to a difficulty to properly sample all the energies properly. In the second phase, I sampled energy range of 0 MeV to 8 MeV. Version of Falaise in use (2.0.0) allowed to generate only flat energy spectrum for generated particles. Such an generator generates samples homogeneously. Therefore, if we generate  $N$  samples homogeneously in energy interval (0 MeV, 8 MeV), only a fraction of them would fall into interval (0 eV, 0.3 eV) which is seven orders of magnitude smaller. The chance, that sample would be generated as thermal neutron is equal to proportion between the widths of two

intervals which is equal to  $0.3 \text{ eV} / 8 \times 10^6 \text{ eV} = 3.75 \times 10^{-8}$ . Probability to generate thermal neutron in flat distribution is then only  $3.75 \times 10^{-6} \%$ ! In order to generate one single thermal neutron one would need to generate in average more than 26 million samples. It was necessary to modify approach to properly sample the thermal neutrons which are probably the most crucial contribution of neutron captures. I decided to divide phase two into two smaller similar simulations. In first one, simulation  $S^T$ , only thermal neutrons from energy region of A (defined previously) were simulated. In second one, simulation  $S^R$ , the rest of the spectrum was simulated, i.e. energy regions B, C and D together. Neutrons in both of them, as pre-announced, were simulated as a flat spectrum. In  $S^T$  neutrons were simulated from energy range of  $\langle 0.001 \text{ eV}, 0.3 \text{ eV} \rangle$ , in  $S^R$  from energy range of  $\langle 0.3 \text{ eV}, 8 \text{ MeV} \rangle$ .

Weight of each data sample was calculated exactly the same way as I have shown in phase one simulation. In this case, however, the flux was entering through the surface of roughly  $S = 90 \text{ m}^2$  of the box around the demonstrator and the simulation represented the background collected during period  $t = 3.15 \times 10^7 \text{ s}$  (one year). The weight from Equation 4.1, expressed flux in  $\text{s}^{-1} \text{cm}^{-2}$  had to be multiplied by period  $t$  and surface  $S$  to give number of neutrons passing through box surface  $S$  captured in demonstrator during one year. Therefore, the weight in phase two was calculated as

$$w = \frac{B_{\text{WALL}}^i(E_n) \Delta E S t}{N_S}. \quad (4.2)$$

$B_{\text{WALL}}^i(E_n)$  represents spectrum passed through the wall in wall scenario of interest (Figures 4.4 and 4.5).  $\Delta E$  is a width of the energy range from which neutrons were randomly generated. In the simulation ( $S^T$ ), simulated range covered interval  $\langle 0.001 \text{ eV}, 0.3 \text{ eV} \rangle$ , therefore, its  $\Delta E = 0.299 \text{ eV}$ . Furthermore, simulation  $S^R$  covered neutron from range of  $\langle 0.3 \text{ eV}, 8 \text{ MeV} \rangle$ , which gives  $\Delta E = 7.9999997 \text{ MeV}$ .  $N_S$  represents number of samples in the simulation. This number was also different for both  $S^T$  and  $S^R$ . In simulation  $S^T$ , sample number of  $N_S = 1.9997 \times 10^7$  was left after outward going neutrons were eliminated. The real simulated number of generated events was exactly  $4 \times 10^7$ . In case of simulation  $S^R$ ,  $3.2 \times 10^7$  samples were generated out of which  $N_S = 1.59979 \times 10^7$  were heading inside of the box. The final weight assigned to the neutron sample represents a number of neutrons per year. It is important to remind, that the same neutron sample was used for each of nine scenarios, the difference between the results comes only from the difference in the shape of the spectra given by  $B_{\text{WALL}}^i(E_n)$  represented by plots in Figures 4.4 and 4.5.

In both simulations, I was interested in the locations of neutron captures inside of the demonstrator. If generated neutron sample was captured, name of the material, in which capture happened, was saved. Weights of neutrons were scored into separate data containers, each representing one of the materials. Finally, the sum inside of each container represent number of captures expected in the material during one year of operation of detector.

Tables 4.2 and 4.3 represent simulated neutron captures inside of four materials with the most neutron captures. Both tables are expressed in thousands of neutron counts per year. Table 4.2 represents all the captures of neutrons initiated by neutrons from thermal part of the spectrum ( $E < 0.3 \text{ eV}$ , region A) in simulation  $S^T$ . On the other side, Table 4.3 represents all the captures of neutrons initiated by neutrons from rest of the spectrum ( $E > 0.3 \text{ eV}$ , regions B, C and D) from simulation  $S^R$ .

The results clearly show that the vast majority of neutrons from both parts of spectrum are captured in Iron. Iron captures roughly 93% of all neutrons from thermal part of the spectrum and roughly 88% of all neutrons from the rest of the spectrum. Iron is a very widely used material in the demonstrator. It is used in all supporting constructions which hold the module

$E_n \leq 0.3 \text{ eV (S}^T)$		Wall scenario								
		30 cm			20 cm			10 cm		
		PE	water	wood	PE	water	wood	PE	water	wood
Detector material	<b>All</b>	168	437	896	874	1494	2121	2666	2667	2250
	<b>Iron</b>	157	409	837	817	1396	1982	2492	2493	2103
	<b>Plexiglass</b>	4.8	12	25	25	42	60	76	76	64
	<b>SN-metal</b>	4.5	12	24	23	40	57	71	71	60
	<b>Copper</b>	0.8	2.2	4.5	4.4	7.5	11	13	13	11

Table 4.2: Table displays number of expected captured neutrons inside of the demonstrator per year caused by thermal neutrons behind the wall (flux  $\Phi_O^T$ , energy region A). Columns represent nine different shielding wall scenarios. First row displays number of all captures in detector followed by four lines representing detector materials with most captures. Values are represented in thousands of neutrons per year.

$E_n > 0.3 \text{ eV (S}^R)$		Wall scenario								
		30 cm			20 cm			10 cm		
		PE	water	wood	PE	water	wood	PE	water	wood
Detector material	<b>All</b>	103	274	539	579	1150	1843	3450	4658	5626
	<b>Iron</b>	91	242	478	513	1019	1635	3063	4132	4992
	<b>Plexiglass</b>	3.8	10	19	20	40	62	118	165	205
	<b>SN-metal</b>	5.3	14	28	30	60	97	176	234	275
	<b>Copper</b>	1.8	4.6	9.1	10	20	32	60	81	97

Table 4.3: Table displays number of expected captured neutrons inside of the demonstrator per year caused by neutrons with energy superior to 0.3 eV after they passed the wall (flux  $\Phi_O^R$ , energy regions B, C and D). Columns represent nine different shielding wall scenarios. First row displays number of all captures in detector followed by four lines representing detector materials with most captures. Values are represented in thousands of neutrons per year.

together. Plexiglass is used in calorimeter - for instance, in side calorimeter (xcalo) it serves as a light guide and it has a form of cubic blocks. Furthermore, material denoted as SN-metal is composed of Nickel (77 %), Iron (16 %), Cobalt (0.05 %) and Molybdenum (0.02 %). The material is used for shielding of PMTs against magnetic field (to ensure their proper performance). Copper is used in all parts where good electrical conductivity is needed, for example in Geiger cell endcaps shown in Figure 4.13.

After a sample was captured, coordinates x,y and z of position of the capture was also saved. Such an information is useful to build a 3D map of all neutron captures in demonstrator. The demonstrator volume (and part of its vicinity) was divided into cubic bins of  $4 \times 4 \times 4 \text{ cm}^3$ . When neutron was captured, its weight was scored into the bin in which neutron capture occurred. With addition of information about the material where capture occurred, I was able to produce such 3D maps for each material separately.

Maps in Figure 4.7 show 2D projections of 3D distribution of all captures in the demonstrator. Projections are always projected into xy plane (top view), xz plane (X-calo side view) and yz plane (main calorimeter view from side). The projections represent sum of all neutron captures in direction perpendicular to the plane of projection. This give rise to apparent red hot spots in some projections. These hot spots are caused by the integration of bins over

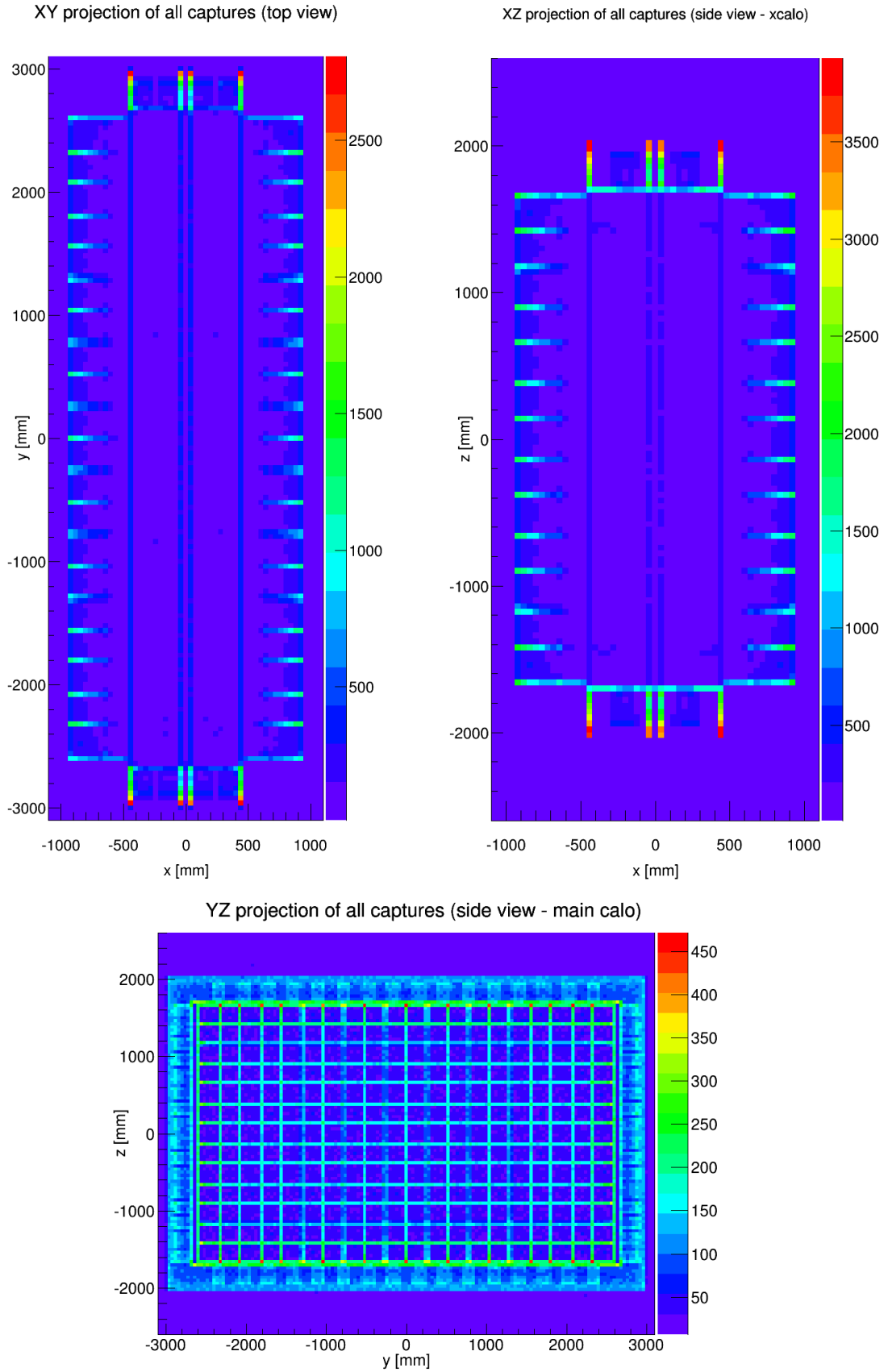


Figure 4.7: Projections of 3D maps of neutron captures in the demonstrator. All captures (regardless of material) caused by thermal neutron flux behind shielding  $\Phi_0^T$  are included. Numerical value represents number of captures per year in 16 cm<sup>2</sup> (surface of bin). Results represent wall scenario with PE shielding of 10 cm thickness.

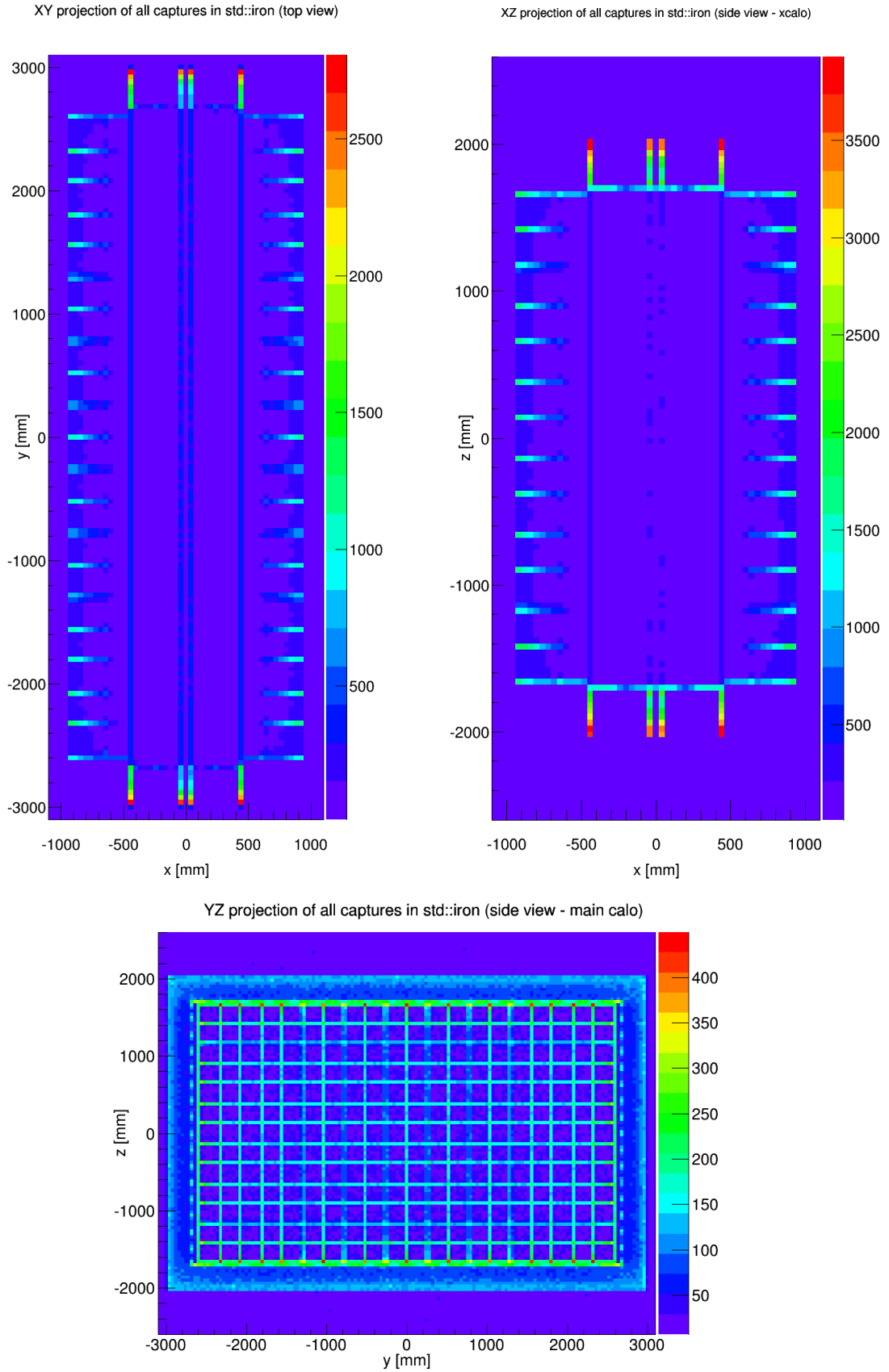


Figure 4.8: Projections of 3D maps of neutron captures in the demonstrator. Only captures in Iron caused by thermal neutron flux behind shielding  $\Phi_0^T$  are included. Numerical value represents number of captures per year in 16 cm<sup>2</sup> (surface of bin). Results represent wall scenario with PE shielding of 10 cm thickness.



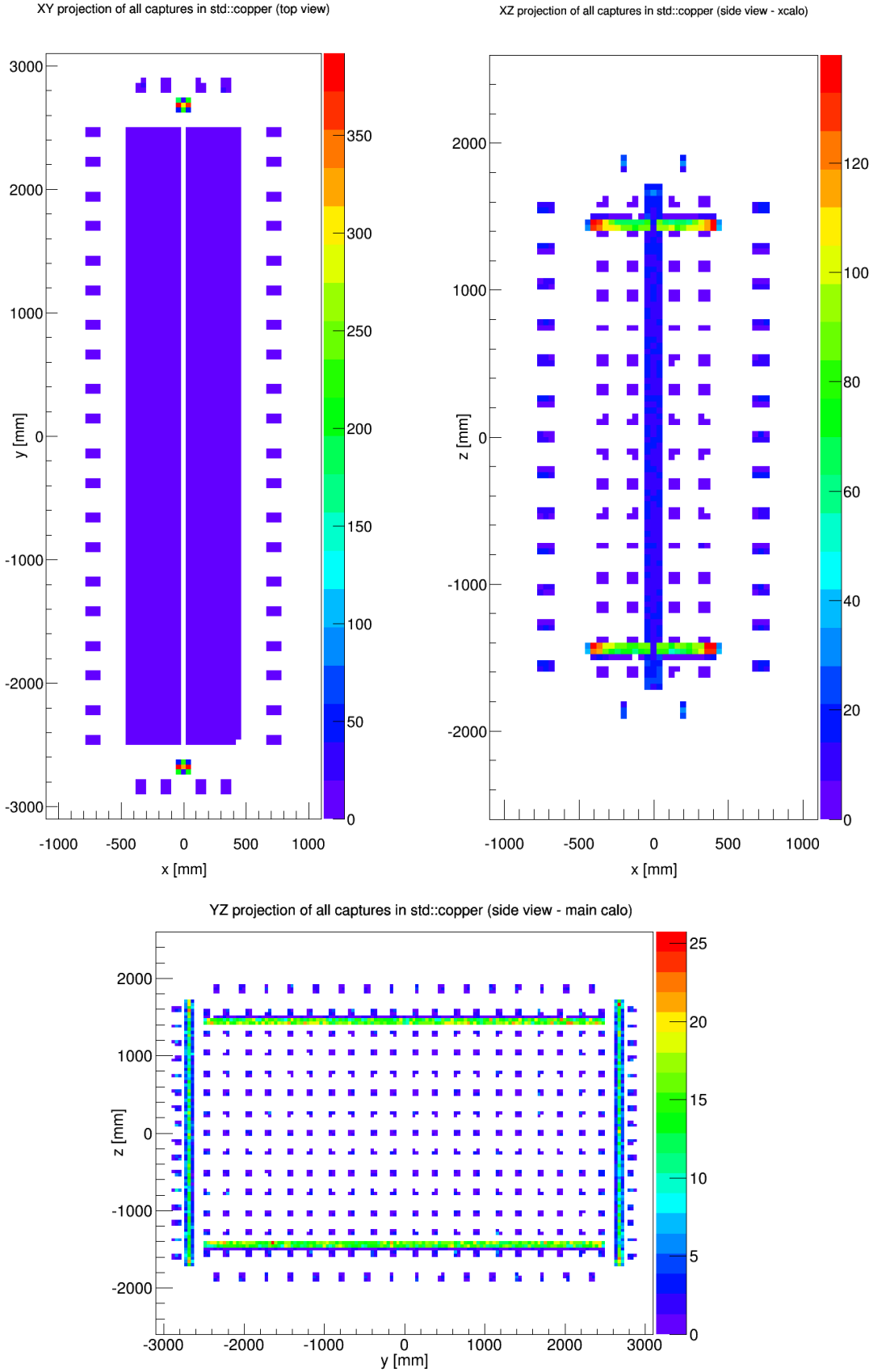


Figure 4.9: Projections of 3D maps of neutron captures in the demonstrator. Only captures in Copper caused by thermal neutron flux behind shielding  $\Phi_0^T$  are included. Numerical value represents number of captures per year in  $16 \text{ cm}^2$  (surface of bin). Results represent wall scenario with PE shielding of 10 cm thickness.

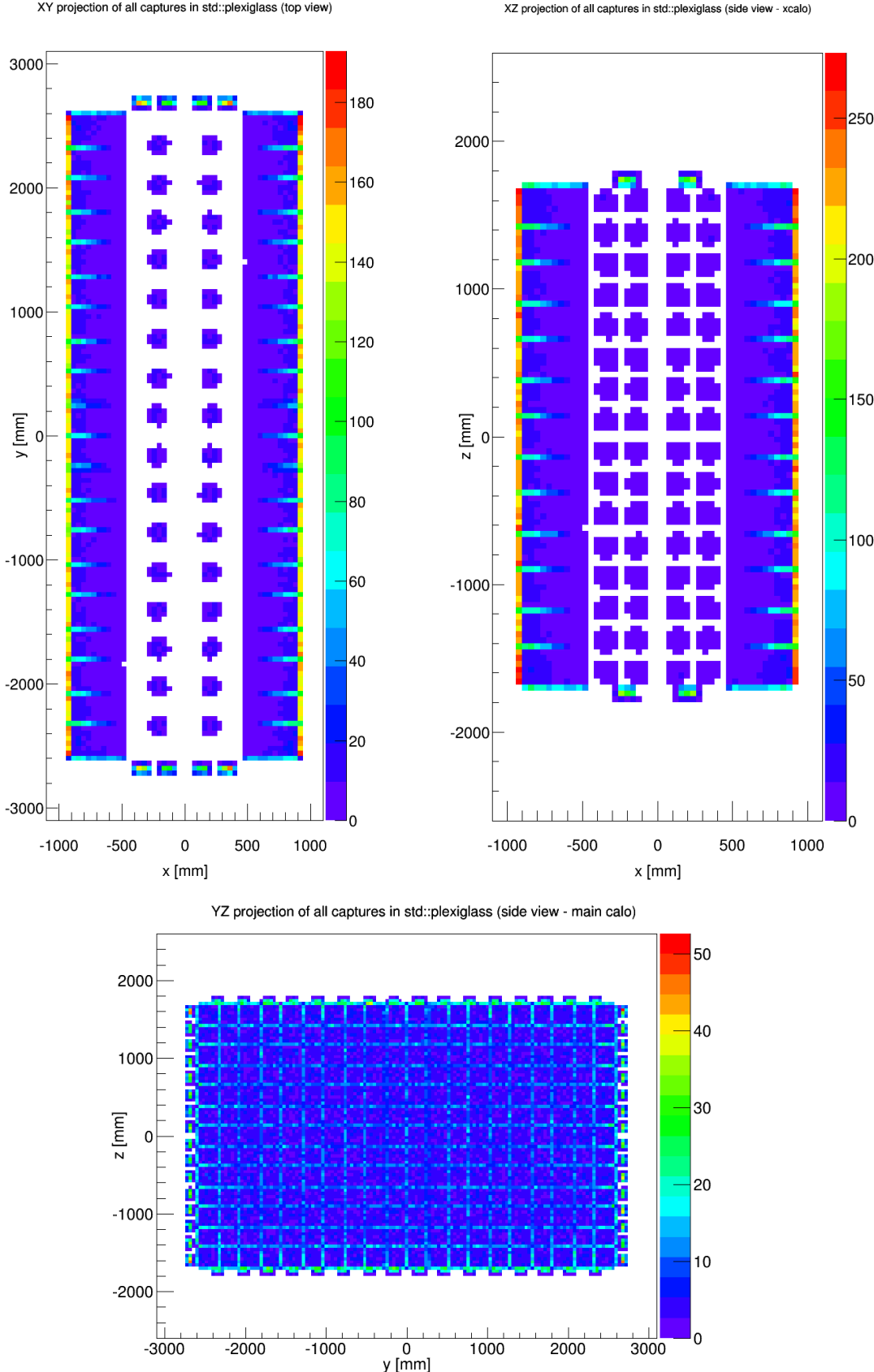


Figure 4.10: Projections of 3D maps of neutron captures in the demonstrator. Only captures in Plexiglass caused by thermal neutron flux behind shielding  $\Phi_0^T$  are included. Numerical value represents number of captures per year in 16 cm<sup>2</sup> (surface of bin). Results represent wall scenario with PE shielding of 10 cm thickness.

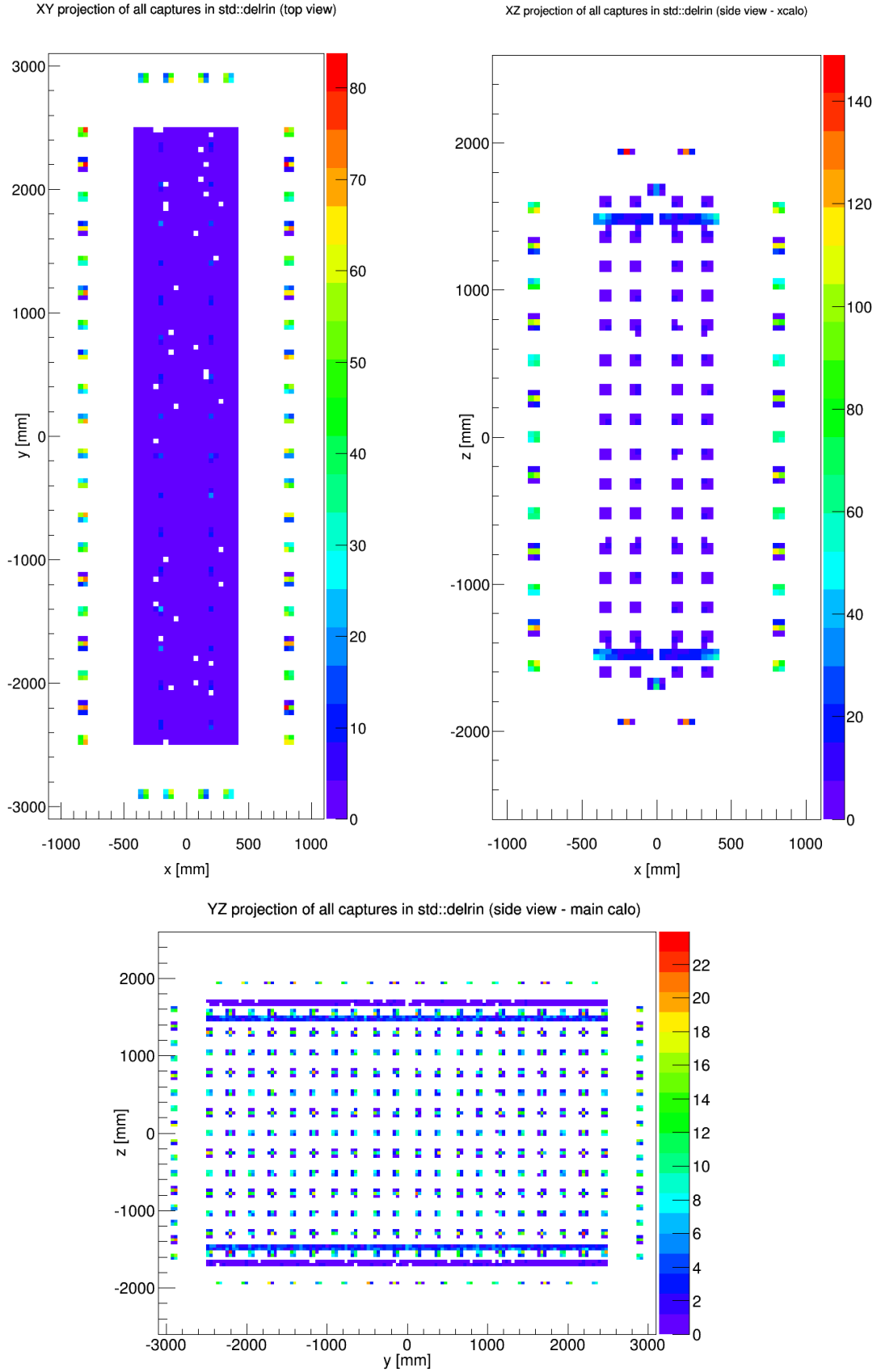


Figure 4.11: Projections of 3D maps of neutron captures in the demonstrator. Only captures in Delrin caused by thermal neutron flux behind shielding  $\Phi_O^T$  are included. Numerical value represents number of captures per year in  $16 \text{ cm}^2$  (surface of bin). Results represent wall scenario with PE shielding of 10 cm thickness.

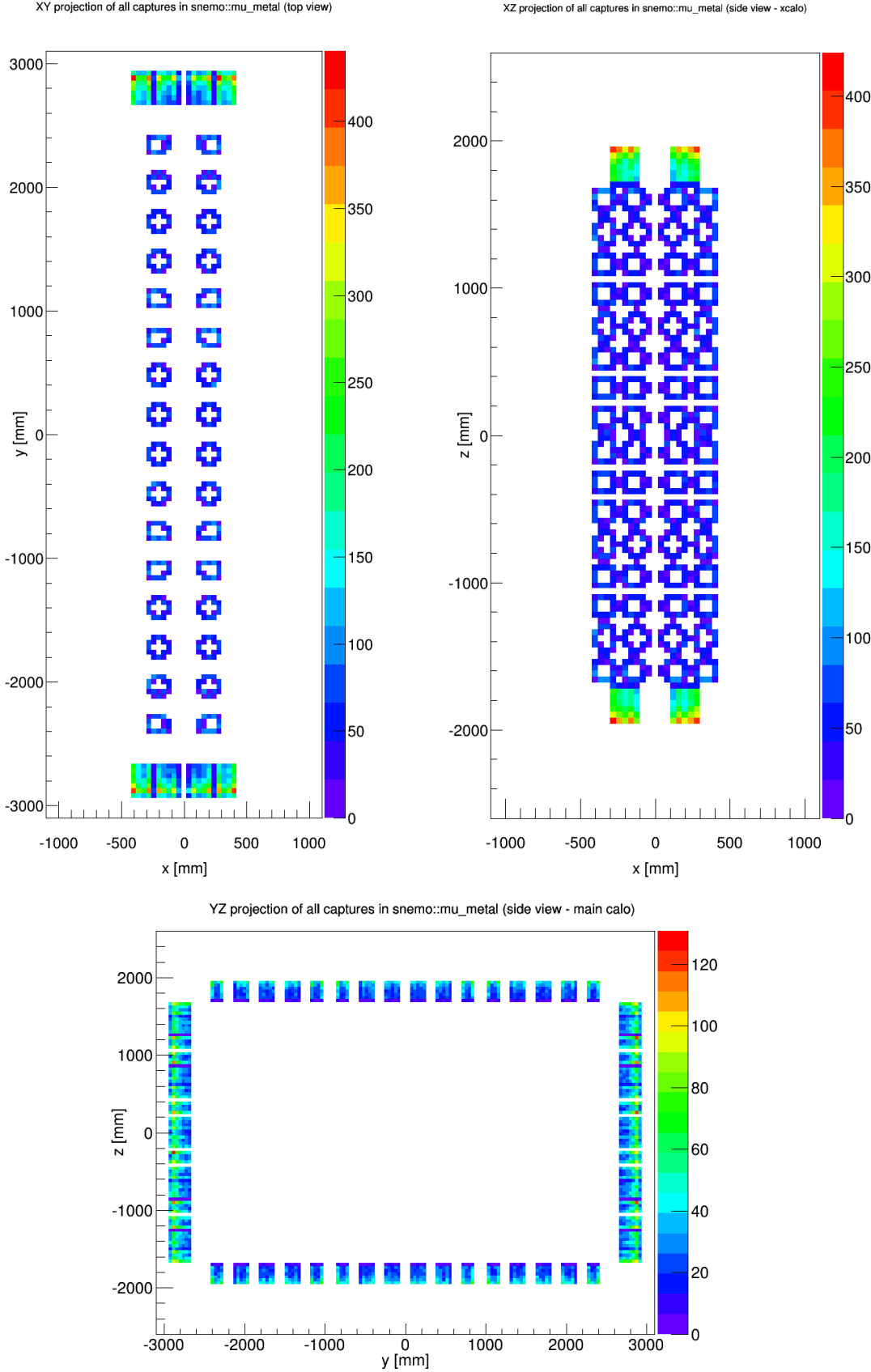


Figure 4.12: Projections of 3D maps of neutron captures in the demonstrator. Only captures in SN-metal caused by thermal neutron flux behind shielding  $\Phi_O^T$  are included. Numerical value represents number of captures per year in 16 cm<sup>2</sup> (surface of bin). Results represent wall scenario with PE shielding of 10 cm thickness.

the third dimension. The frequency of the captures have to be considered by comparison of all three projections in order to avoid wrong conclusions. Each 2D bin is represented in number of neutrons captured during one year per  $16 \text{ cm}^2$ . Figures 4.8, 4.9, 4.10, 4.11 and 4.12 represent same type of projections, this time for captures in Iron, Copper, Plexiglass, Delrin and SN-metal, respectively. In case of Iron it is possible to recognize the supporting structures of the detector. Delrin is a material not included in the Tables 4.2 and 4.3. Delrin is used as radiopure insulator which can be found for example in the endcap of each Geiger cell. Its photo can be found in Figure 4.13. SN-metal structures, as already discussed, serve as a magnetic field shielding in order to protect PMTs (for X-calor and G-veto). They can be clearly recognized in Figure 4.12. Figures 4.7 to 4.12 provide great demonstration of the distribution of materials in the detector.

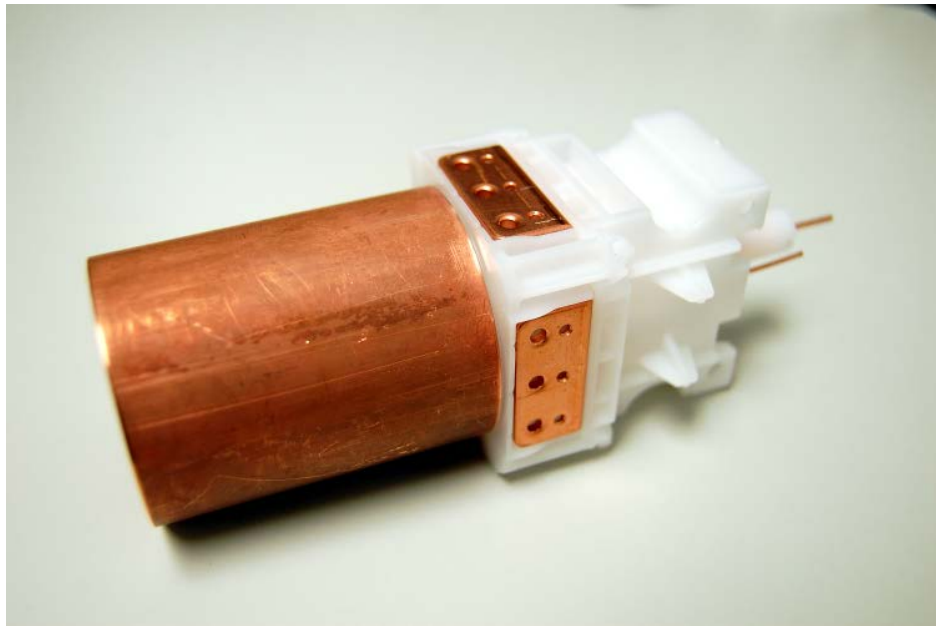


Figure 4.13: Photo of Geiger cell endcap. White part, made of Delrin, serves as an insulator.

Neutron simulations represent first estimation of neutron fluxes which could be expected with use of different types of shielding. The information was used to form first design proposals for the neutron shielding. Simulation in second phase was performed without physical presence of the shielding in the simulation's setup. This approximation, however, cannot reproduce effects of neutrons which are scattered back into the wall after they have already passed it. They can be subsequently thermalized and re-emitted back into the volume of demonstrator. The phase two of the simulation accounts only for neutrons directly traversing shielding and interacting in the module or leaving. Full realistic simulations will be performed after the shielding will be implemented into the Falaise. For the moment the result proposed in this section are sufficient approximation demonstrating the behaviour of neutrons in the detector and giving a reference point for future work.

## 4.2 Problem of Neutron Capture Generators

Neutron simulations performed in previous sections studied the effects of neutron propagation and capture in the detector. It gives an information about the potential of the captures to generate fake double-beta signal. In order to obtain real estimation of background from

neutrons one would need to follow the gammas produced in the capture. Even though, the process of gamma deexcitation is fully implemented in Geant package, the performance used model is not sufficient. In following section, I will briefly explain the pitfalls of generators of gammas originating from thermal neutron capture.

Neutron interactions are probably the most difficult processes to be reliably simulated. Used interaction models are frequently only phenomenological. Data describing the nuclear levels and the transitions are frequently not precise enough to give results of the highest precision. All these factors contribute to complexity of computational tasks involving neutrons.

It is, therefore, important to be familiar with the performance of the simulation code in conditions of the problem in question. For majority of the applications (especially problems including high energy neutrons) available codes for simulation work precisely enough to give reliable final results. However, the central, and most important process of this chapter is the neutron capture of thermal neutrons. Due to their large cross sections for neutron capture, thermal neutrons are potentially the biggest contributor to the detector's background out of all the neutron spectrum.

### 4.2.1 Thermal Neutrons in Geant4

Simulation of all the physics in Falaise (simulation code for SuperNEMO demonstrator) is delegated to Geant4 [90, 91, 92]. Therefore, in order to test the performance of neutron simulation, I decided to test it directly in Geant4.

I set up very simple simulation. Thermal neutrons (i.e.  $E_n = 0.3$  eV) were produced in the center of  $1 \times 1 \times 1$  m<sup>3</sup> cube made of <sup>54</sup>Fe. Their initial momentum was isotropic. The neutrons were scattered in the cube until they were captured. The dimensions of cube were large enough to ensure that all the neutrons are captured inside of it. I generated  $5 \times 10^5$  neutrons. Example of ten events from the simulation are shown in Figure 4.14. After each

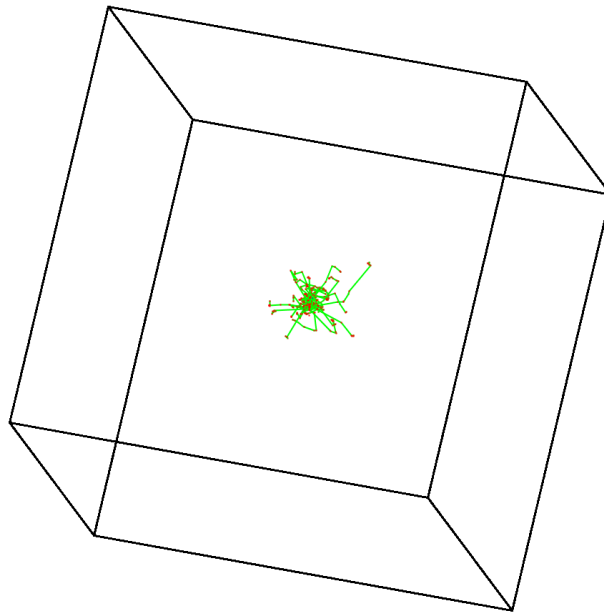


Figure 4.14: Example of 10 thermal neutron events. Neutrons (green tracks) at thermal energy ( $E = 0.3$  eV) were shot from the center of the cube ( $1 \times 1 \times 1$  m<sup>3</sup>) into full ( $4\pi$ ) solid angle. Cube was sufficiently large to capture all the generated neutrons.

$E_\gamma$ [MeV]	$I_{G4}$ [ $\frac{\gamma}{100\text{ev.}}$ ]	$I_{NDS}$ [ $\frac{\gamma}{100\text{ev.}}$ ]	$I_{G4}/I_{NDS}$ [1]	$E_\gamma$ [MeV]	$I_{G4}$ [ $\frac{\gamma}{100\text{ev.}}$ ]	$I_{NDS}$ [ $\frac{\gamma}{100\text{ev.}}$ ]	$I_{G4}/I_{NDS}$ [1]
0.412	15.23	19	<b>0.80</b>	3.792	1.47	1.8	<b>0.82</b>
0.931	1.73	2.1	<b>0.83</b>	4.455	1.27	1.6	<b>0.79</b>
1.24	0.79	1	<b>0.79</b>	4.495	2.70	3.4	<b>0.79</b>
1.638	1.38	1.7	<b>0.81</b>	4.589	2.12	2.6	<b>0.82</b>
1.918	1.69	2.1	<b>0.81</b>	4.707	0.98	1.8	<b>0.54</b>
2.052	1.60	2	<b>0.80</b>	4.802	2.30	2.9	<b>0.79</b>
2.47	3.15	3.9	<b>0.81</b>	5.391	0.97	1.2	<b>0.81</b>
2.618	1.89	2.4	<b>0.79</b>	5.507	1.89	2.4	<b>0.79</b>
2.67	1.22	1.5	<b>0.81</b>	5.745	1.86	2.3	<b>0.81</b>
2.873	0.89	1.1	<b>0.81</b>	6.268	2.59	3.2	<b>0.81</b>
3.005	0.81	1	<b>0.81</b>	6.826	1.50	1.9	<b>0.79</b>
3.028	2.12	2.6	<b>0.82</b>	7.246	1.61	2	<b>0.81</b>
3.38	1.21	1.5	<b>0.81</b>	8.886	9.95	12.3	<b>0.81</b>
3.508	0.81	1	<b>0.81</b>	9.297	111.61	66	<b>1.69</b>
3.552	1.15	1.4	<b>0.82</b>				

Table 4.4: Results from thermal neutron simulation represented in Figure 4.14. Each line represents one of the gamma lines emitted after thermal neutron capture on  $^{54}\text{Fe}$ . Table compares intensities of the line obtained from Geant4 simulation ( $I_{G4}$ ) to intensities in Nuclear Data Sheets ( $I_{NDS}$ ) obtained from [93]. Intensities are represented in number of observed gammas per 100 events.

neutron was captured, it produced one or several gammas. I scored each gamma energy into single gamma spectrum. Energies of all gammas produced in one capture were summed up, and the result was scored in another spectrum.

Table 4.4 shows a summary of the obtained intensities for all gammas of intensity superior or equal to one gamma per 100 events. The results are compared to the expected intensities based on nuclear data. In last column, ratio of intensity obtained by simulation and expected intensity is shown. The comparison shows that gamma of highest energy is overestimated by almost 70% while all the other gammas are underestimated by roughly 20%. Moreover, energy of the highest gamma line ( $E_\gamma = 9.297$  MeV) represents situation when nucleus is deexcited by one gamma all the way to the ground state. The intensity of this gamma obtained from simulation is  $I_{G4} = 111.61$  gammas per 100 events. The value of intensity implies, that this gamma occurs in average more than once per event. Therefore, simulation produces events when this gamma is emitted at least twice. The energy released by this highest gamma line is equal to the difference between highest possible state and ground state. It represents the Q-value of the neutron capture. Emission of two 9.297 MeV gammas, therefore represent non-conservation of the energy in the event.

Problem of non-conservation of energy is clearly visible in Figure 4.15. Figure shows spectrum of energies released per one event.

The region of the energy spectrum marked by blue rectangle represents all the events in which more energy was emitted than it should have been. It is possible to find examples when energy twice as higher than Q-value was released. Naturally, this is unwanted feature. The study was repeated for  $^{56}\text{Fe}$ ,  $^{63}\text{Cu}$  and  $^{65}\text{Cu}$  and compared with [94], [95] and [96]. The results showed violation of energy conservation in all of these cases.

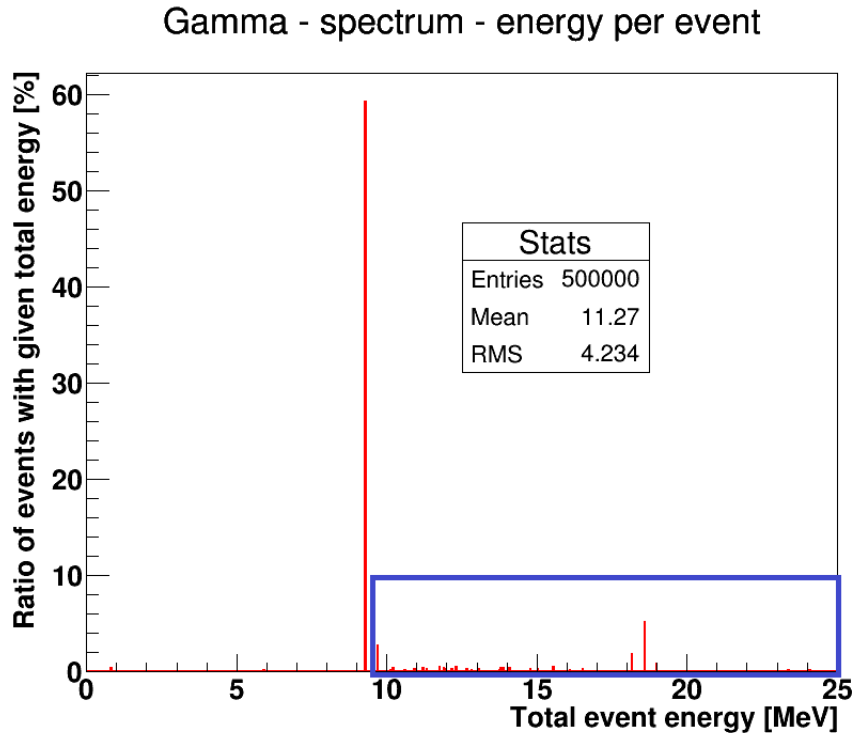


Figure 4.15: Spectrum of energies per event obtained from thermal neutron simulation represented in Figure 4.14. Region of spectrum marked by blue rectangle represents all the events in which energy emitted by gammas is higher than Q-value of neutron capture. These events violate conservation of energy.

## 4.2.2 Stair Generator

The non-conservation of the energy in the thermal neutron capture is caused by neglecting the correlations between the gammas. The excess excitation energy can be released by one gamma or several gammas in a cascade.

Figure 4.16 - Left shows the simplest non-trivial deexcitation scheme with one intermediate level. Energy difference between the highest energy state  $E_H$  and ground state  $E_0$  can be released in two possible ways. Either via one gamma ( $\gamma_0$ ) or two gammas in coincidence ( $\gamma_{10} + \gamma_{11}$ ). Regardless of the fact, whether the excitation energy  $E_H - E_0$  was released by one or several gammas, the energy released by deexcitation must be always the same. The generator in Geant4, however, did not fulfil this condition. If we look at the right side of the Figure 4.16, we can see an illustration of the scheme from left for a randomly chosen cascade probabilities  $x_{101}$  and  $x_{111}$  in a form of single gamma energy spectrum.  $\gamma_{10}$  and  $\gamma_{11}$  originate in the same cascade, therefore, their intensities will always be equal. The proportions of intensities  $\gamma_{10}/\gamma_0$  and  $\gamma_{11}/\gamma_0$  depends only on the proportion of cascade probabilities  $x_{101}/x_{111}$ .

Let us assume now, that both cascades  $x_{101}$  and  $x_{111}$  happen exactly 50% of the time. It means that the intensity of each of two gammas  $\gamma_{10}$  and  $\gamma_{11}$  are the same as the intensity of  $\gamma_0$ . Moreover, we know that average number of gammas per capture would be 1.5 because 50% of time nucleus is deexcited by one gamma and rest of the time by two gammas.

Now, let me propose a simple neutron capture generator. First of all, the generator chooses randomly (based on the gamma per event distributions) a number of emitted gammas. In our example we have 50% chance to generate two gammas. Say, the generator



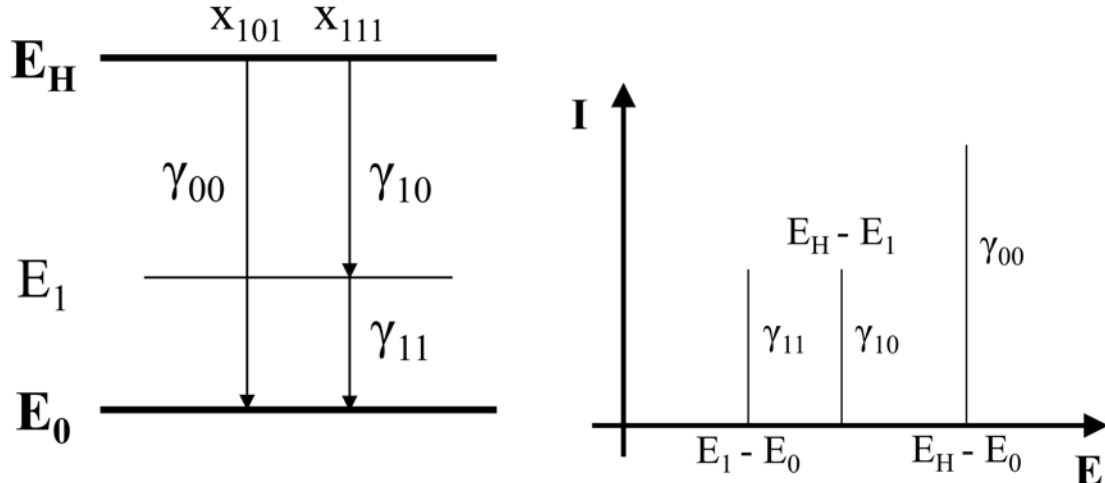


Figure 4.16: Left: Example of simple system with three nuclear states.  $E_0$  denotes energy of ground state,  $E_1$  energy of first excited state and by  $E_H$  we understand the energy of the highest excited state.  $E_H$  is always a state of nucleus immediately after the thermal neutron is captured. Right: Representation of decay scheme from left as it would be seen in the energy spectrum (for specific choice of cascade probabilities  $x_{101}$  and  $x_{111}$ ). Naming convention of cascades and gammas is explained in the text.

have chosen two gammas in first event. In next step, the generator has to choose (randomly) the gammas which are emitted. If we pick them only based on the intensities in the energy spectrum in the right side of Figure 4.16, we could pick, for example, emission of  $\gamma_{00}$  along with  $\gamma_{11}$ . Both gammas emit together energy larger than difference  $E_H - E_0$ , therefore, energy is not conserved. However, in our example, the mean number of emitted gammas, as well as single gamma energy spectrum, is preserved. Such an approximation causes energy non-conservation in Geant4 generator. Moreover, it is possible to obtain  $\gamma_{00}$  repetitively in the same event, which causes events with emission of several Q-values of energy. While such an statistical, average approach is acceptable as a good approximation for some high energy applications, it is not suitable for the study of neutron background in SuperNEMO demonstrator. Energy of gamma emitted after neutron capture influences cross section of the pair production, in other words, how likely is it to obtain potential fake double-beta event. If several gammas are emitted in a cascade, there is a chance that both would produce pair and violate proper signature of fake double-beta decay event. Creation of several gammas in a cascade increase chance of rejection of fake-double beta signal. Therefore, it is important to have generator with proper simulation of both, the gamma multiplicities in cascade (gamma correlations) as well as energy conservation. This is however, very difficult task to fulfil.

In order to preserve energy, the gammas have to be generated in correlation, i.e. as a whole cascade. Such an approach could be achieved by generator which I call "Stair Generator". The principle is simple. The generator takes a database of single gammas and their intensities (data obtained from measurement) as an input. Each gamma has a designated level of origin. In example from Figure 4.16  $\gamma_{00}$  and  $\gamma_{10}$  would have origin state  $E_H$  while  $\gamma_{11}$ 's origin state would be  $E_1$ . The generator starts generating always at the highest level  $E_H$ . Among all the gammas which originate in  $E_H$ , first gamma in cascade would be chosen randomly. The probability is proportional to the intensity of the gamma. Gamma subsequently leads to lower energy level, where another gamma is randomly chosen among all those which

$E_\gamma$ [MeV]	$I_{SG}$ [ $\frac{\gamma}{100\text{ev.}}$ ]	$I_{NDS}$ [ $\frac{\gamma}{100\text{ev.}}$ ]	$I_{SG}/I_{NDS}$ [1]	$E_\gamma$ [MeV]	$I_{SG}$ [ $\frac{\gamma}{100\text{ev.}}$ ]	$I_{NDS}$ [ $\frac{\gamma}{100\text{ev.}}$ ]	$I_{SG}/I_{NDS}$ [1]
0.412	19.9599	19	<b>1.05</b>	3.792	0.4857	1.8	<b>0.27</b>
0.931	0	2.1	<b>0.00</b>	4.455	0	1.6	<b>0.00</b>
1.24	0	1	<b>0.00</b>	4.495	2.16	3.4	<b>0.64</b>
1.638	1.661	1.7	<b>0.98</b>	4.589	2.99	2.6	<b>1.15</b>
1.918	0	2.1	<b>0.00</b>	4.707	0.7729	1.8	<b>0.43</b>
2.052	2.02	2	<b>1.01</b>	4.802	2.16	2.9	<b>0.74</b>
2.47	0.6708	3.9	<b>0.17</b>	5.391	1.99	1.2	<b>1.66</b>
2.618	1.12	2.4	<b>0.47</b>	5.507	2.32	2.4	<b>0.97</b>
2.67	0	1.5	<b>0.00</b>	5.745	2.06	2.3	<b>0.90</b>
2.873	0	1.1	<b>0.00</b>	6.268	3.74	3.2	<b>1.17</b>
3.005	0	1	<b>0.00</b>	6.826	1.51	1.9	<b>0.79</b>
3.028	1.62	2.6	<b>0.62</b>	7.246	2.0693	2	<b>1.03</b>
3.38	0.8999	1.5	<b>0.60</b>	8.886	12.65	12.3	<b>1.03</b>
3.508	0	1	<b>0.00</b>	9.297	67.6032	66	<b>1.02</b>
3.552	2.06	1.4	<b>1.47</b>				

Table 4.5: Results obtained by Stair Generator. Each line represents one of the gamma lines emitted after thermal neutron capture on  $^{54}\text{Fe}$ . Table compares intensities of the lines obtained from Stair Generator ( $I_{SG}$ ) to intensity in Nuclear Data Sheets ( $I_{NDS}$ ) obtained from [93]. Intensities are represented in number of observed gammas per 100 events.

originate in the level. The process is repeated until the ground state is reached. Such an approach preserves energy in the event by generation of full cascades, the correlations between gammas are taken into account.

Table 4.5 shows gamma intensities  $I_{SG}$  obtained by simulation of  $10^6$  events with Stair Generator. The results are compared with values  $I_{NDS}$  obtained from nuclear data sheets [93]. The correspondence for many gammas is very precise. However, many gammas are underestimated or overestimated by several tens of %. Note that, by the nature of generator, it is ensured, that energy is preserved exactly in each event. However, except for gammas, whose intensities are overestimated or underestimated, we can find examples of gammas which are not generated at all. These gammas originate in states lower than  $E_H$ . Problem of the generator is that, it relies strongly on the consistency of data. However, the data contains several gammas unassociated with any of the states. Therefore, many of the gammas are not accessible by generator because their origin states are never reached. Let me show an example based on Figure 4.16 - Left.  $\gamma_{11}$  is produced only if generator reaches excited level  $E_1$ . Only possibility to reach the state is by emission of  $\gamma_{10}$ . If this gamma is missing from the experimental dataset, the state  $E_1$  is never reached and  $\gamma_{11}$  never produced. In principle, the generator should work reliably with perfectly consistent dataset (all gammas are associated and properly connected). It is, however, rarely true.

### 4.2.3 Possible Solution

As we learned in the previous section, it is important to have a generator which accounts not only for correlations of gammas, but also for imprecisions in the input datasets. For this purpose, I propose a possible solution. It represents interesting proposal to solve the

problems with gammas from thermal neutron capture and might help in the future to pave a road for precise estimation of fake double-beta decay rates originating from neutrons.

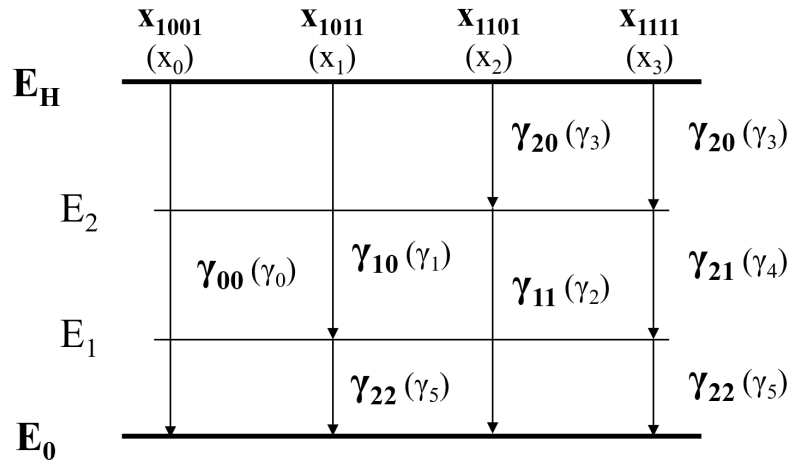


Figure 4.17: Scheme of gamma deexcitation cascades after thermal neutron capture. The scheme represents situation with two intermediate excited states  $E_1$  and  $E_2$ .

#### 4.2.3.1 Naming Convention

In order to describe proposed generator, let me first clarify naming conventions used in the problem. Figure 4.17 represent cascade scheme similar to the one in Figure 4.16 - Left, but this time with two intermediate states  $E_1$  and  $E_2$ .

First of all, let us discuss the convention used to designate full gamma cascades. In the example, there are four different cascades:  $x_{1001}$ ,  $x_{1011}$ ,  $x_{1101}$  and  $x_{1111}$ . The index holds a full information about the structure of cascade. Let me take cascade  $x_{1011}$  as an example. The cascade starts with transition  $E_H \rightarrow E_1$  followed by transition  $E_1 \rightarrow E_0$ . The cascade involves states  $E_H$ ,  $E_1$  and  $E_0$ . If we list all four states involved in our system in order of descending energy ( $E_H$ ,  $E_2$ ,  $E_1$ ,  $E_0$ ) and then represent each state by 0 or 1, we obtain the naming convention. 1 is assigned, if state is involved in the cascade, 0 is assigned otherwise. Therefore, cascade involving chain of transitions:  $E_H \rightarrow E_2 \rightarrow E_0$  is designated by  $x_{1101}$ . The number of indices always corresponds to number of all states in the system. Note that, all the cascades start and end by ones simply because the highest state  $E_H$  and ground state  $E_0$  has to be always involved. These two indices might be omitted. If we do so, we can define one-to-one correspondence between binary numbers and cascades. We just need to rewrite binary number (after omission of leading and final one in the index) in decimal system. Such an alternative notation is shown in bracket under the original (binary) notation in Figure 4.17. In decimal notation the structure of the cascade is not obviously visible just by looking at the index, however, it is much more practical when it comes to calculations. For systems with many intermediate states, binary notation becomes lengthy and cumbersome. In following, I will always follow decimal notation for simplicity.

With decimal notation in mind, it is trivial task to calculate how many possible cascades can be expected in the system given the number of intermediate levels. In my example, there are two intermediate levels  $E_1$  and  $E_2$ . In each cascade, none of the levels might be involved ( $x_{1001}$  /  $x_0$ ), one level might be involved ( $x_{1011}$  /  $x_1$  and  $x_{1101}$  /  $x_2$ ), or both of them might be involved ( $x_{1111}$  /  $x_3$ ). There is no other possibility unless we add another intermediate level.

If we omit the ones at the beginning and the end of cascade each one can be represented by any two digit combination of 0 and 1. Therefore, there is  $2^2$  cascades in the example. Accordingly, with  $n$  intermediate states one could draw  $2^n$  different cascades.

In case of single gammas, the convention is bit more complicated. Different gammas are shared between the cascades, so their naming convention cannot be derived from the name of the cascade they belong to. As a first step, I divided the gammas into classes. Zero class gamma is the one which connects the highest state  $E_H$  with the ground state  $E_0$  ( $\gamma_{00}$ ). In each system, regardless of the number of intermediate states, there is only one zero class gamma. It is always the one which skips all the intermediate states. First class gamma, I call the gamma which skips one level less than zero class gamma ( $\gamma_{10}$  and  $\gamma_{11}$ ). Zero class gamma was skipping two states, therefore, first class gamma (in system with two intermediate states) skips one level. Every higher class skips one less state. In our system with two intermediate states the last class is second class when gammas do not skip any intermediate level ( $\gamma_{20}$ ,  $\gamma_{21}$  and  $\gamma_{22}$ ). In other words, such gamma connects neighbouring levels. Number of classes depends on number of intermediate states. Each gamma has two indices. First index denotes class to which gamma belongs. Second index serves to differ between the gammas in same class. The lowest index is always 0 and it denotes gamma of highest energy of level from which it originates. For instance,  $\gamma_{10}$  and  $\gamma_{11}$  both belong to first class, but  $\gamma_{10}$  originates in level  $E_H$  which is higher level of origin than in case of  $\gamma_{11}$  (level  $E_2$ ). In this sense, the gammas belonging to the same class are denoted by increasing second index as their state of origin is lower. Index of last gamma in the class always equals the number of class. If we keep that in mind, we can easily calculate number of single gammas for given number of intermediate states. There is always one zero-class gamma. First class includes always two gammas and class  $i$  contains  $i+1$  gammas. The highest class is always  $n$ -th class (where  $n$  is number of intermediate states in the system) with  $n+1$  gammas. To obtain total number of single gammas in the system we have to sum up all the gammas from all classes, i.e. numbers from 1 up to  $n+1$  (including). The total sum is  $(n+1)(n+2)/2$ . Two index convention is very useful in order to easily cover all possible gammas for given system, however, one index is more practical to be used. Example of such convention can be found in brackets next to each gamma in Figure 4.17. In following examples, I will keep on using the simpler one-index notation.

Table 4.6 summarizes number of cascades ( $N_C$ ) and unique single gamma transitions ( $N_\gamma$ ) as a function of number of intermediate states in the system ( $n$ ).

<b>n</b>	<b>0</b>	<b>1</b>	<b>2</b>	<b>3</b>	<b>4</b>	<b>5</b>	<b>6</b>	<b>7</b>	<b>8</b>	<b>9</b>	<b>10</b>	<b>11</b>	<b>12</b>	<b>13</b>
<b><math>N_C</math></b>	1	2	4	8	16	32	64	128	256	512	1024	2048	4096	8192
<b><math>N_\gamma</math></b>	1	3	6	10	15	21	28	36	45	55	66	78	91	105

Table 4.6: Table displays number of all possible cascades  $N_C$  and single gamma transitions  $N_\gamma$  in a system with  $n$  intermediate states.

### 4.2.3.2 Description of Generator

Cascade variables  $x_i$  can be used to store probabilities of cascade occurrence. If we would have the proper values, we would be able to generate thermal neutron capture gammas properly in the coincidence and with energy conserved in the event. On the other side, standard nuclear tables provide intensities of single gammas in form of  $\gamma_j$  variables. As

an additional information, usually, the level of origin for each gamma is provided. The intensities are represented in number of gammas per 100 events (i.e. in %).

The task is, therefore, to find a relationship between cascade variables  $x_i$  and single gamma intensities  $\gamma_j$ . As it was discussed already, this is possible only to a certain precision, as the data might miss some gamma transitions causing the exact generators to fail.

Imagine, we know the probabilities  $x_i$  for each single cascade to occur (with infinite precision). In such case, we would be able to easily calculate how often gamma occurs. For instance, probability of  $\gamma_3$  to occur in random event is given by probability  $p_3 = x_2 + x_3$ . It can be created by any of these two cascades. Such an relation can be written for each of the gammas:

$$\begin{aligned}
 p_0 &= x_0 \\
 p_1 &= x_1 \\
 p_2 &= x_2 \\
 p_3 &= x_2 + x_3 \\
 p_4 &= x_3 \\
 p_5 &= x_1 + x_3.
 \end{aligned} \tag{4.3}$$

Here,  $p_j$  represents probability (ideal intensity) of  $\gamma_j$  to occur. Composition of the equations is clear from Figure 4.17. These are the equation for case with two intermediate states. Note that, cascade probabilities are normalized to one:

$$x_0 + x_1 + x_2 + x_3 = 1, \tag{4.4}$$

because in each event any cascade should always occur. Cascades are also mutually exclusive. However, this does not hold for single gammas:

$$p_0 + p_1 + p_2 + p_3 + p_4 + p_5 > 1. \tag{4.5}$$

Sum of their probabilities is always higher than one (except for the trivial case with no intermediate state) and represents the average number of gammas per 100 events. However, all we have available are the gamma intensities  $\gamma_j$  which might not be perfectly consistent due to experimental uncertainties. Nevertheless, if they were, the measured intensities  $\gamma_j$  should be exactly same as gamma probabilities ( $p_j$ ) obtained by ideal measurement:

$$\gamma_j = p_j. \tag{4.6}$$

Equations 4.6 form a set of "Structure Equations" (SE). Six SE encode all the necessary relations for the case of two intermediate states. Such equations could be written for case with any number of intermediate states.

As the name suggest, cascade probabilities are probability variables, therefore their values should be always in the interval  $\langle 0, 1 \rangle$ . At this point, I would like to point out specific property of SE. Let us have a look back to Equation 4.3. Based on the previous remark, non-observation of  $\gamma_3$  in experimental data (i.e.  $p_3 = 0$ ) would imply  $x_2 = 0$  and  $x_3 = 0$ . As neither of the cascade variables can be negative, this is the only possibility. However,  $x_3 = 0$  would imply  $p_2 = p_4 = 0$ . It is a (welcomed) consequence of the correlations between the gammas in the cascades.

Experimental datasets usually originate from sets of different experiment with different experimental uncertainties or sensitivities of measurement setups. Therefore, it is no surprise

that situation when  $\gamma_3 = 0$  and  $\gamma_2 \neq 0$  can occur even though it should not (see Figure 4.17). Strictly speaking, for such a combination of single gamma probabilities, no solution in form of (non-negative) cascade probabilities  $x_i$  would exist. The Stair Generator worked on bit different principle, however, this was exactly the reason why it did not work properly.

In order to account for experimental uncertainties in the input datasets, we have to take an approximative approach. It is important to have an approach which would allow us to reproduce measured intensities as precise as possible while preserving the cascades and, the most importantly, the energy.

Let me start with Equation 4.6. It represents (in case of two intermediate states) exact relations between the cascade probabilities and single gamma intensities in ideal case. Let me define a function  $\delta_j(x_i)$ :

$$\delta_j(x_i) = \gamma_j - p_j. \quad (4.7)$$

In case of ideal data, obviously,  $\delta_j = 0$ . Based on the experimental uncertainties discussed above, it is impossible to reach such a solution, however,  $\delta_j^2(x_i)$  expresses the imprecision of the solution.  $p_j$  is a linear function of cascade probabilities  $x_i$ . Therefore,  $\delta_j^2(x_i)$  is also a function of cascade probabilities. It is always non-negative, which is ensured by raising  $\delta_j$  to a second power. Single gamma intensities  $\gamma_j$  serve as functional parameters given by data. Finally, variation of all the cascade probabilities  $x_i$ , within the allowed interval  $\langle 0, 1 \rangle$ , influences a variation of  $\delta_j^2(x_i)$  values. The values of interest are those as close to zero as possible. Nevertheless, each  $\delta_j^2(x_i)$  function reaches the minimal value for different set of cascade coefficients. To ensure, that we have found the minimal global value, it is necessary to minimize sum of all the contributions:

$$\Delta(x_i) = \sum_{\text{allgammas}}^{N_\gamma} \Delta_j^2(x_i). \quad (4.8)$$

In case of two intermediate states  $\Delta(x_i)$  function has a following form:

$$\Delta(x_0, x_1, x_2, x_3) = \delta_0^2 + \delta_1^2 + \delta_2^2 + \delta_3^2 + \delta_4^2 + \delta_5^2, \quad (4.9)$$

where

$$\begin{aligned} \delta_0(x_0) &= \gamma_0 - x_0, \\ \delta_1(x_1) &= \gamma_1 - x_1, \\ \delta_2(x_2) &= \gamma_2 - x_2, \\ \delta_3(x_2, x_3) &= \gamma_3 - x_2 - x_3, \\ \delta_4(x_3) &= \gamma_4 - x_3, \\ \delta_5(x_1, x_3) &= \gamma_5 - x_1 - x_3. \end{aligned} \quad (4.10)$$

$\gamma_j$  are gamma intensities given by experimental measurements. Finally, solution to the problem is a quadruplet of cascade probabilities  $x_0^s, x_1^s, x_2^s, x_3^s$  fulfilling all the following conditions:

$$\begin{aligned} 0 \leq x_0^s, x_1^s, x_2^s, x_3^s &\leq 1, \\ x_0^s + x_1^s + x_2^s + x_3^s &= 1, \\ \Delta(x_0^s, x_1^s, x_2^s, x_3^s) &= \min[\Delta(x_i)]. \end{aligned} \quad (4.11)$$

This is a well known problem of finding constrained functional extremes. It can be approached by method of Lagrange multiplier. The whole presented approach can be applied

to systems with arbitrary number of intermediate levels, limited only by amount of computing power. Each extra intermediate level adds to the complexity of the problem factor of two (number of cascades). Nevertheless, vast majority of the cascades could be considered as zero for each  $\gamma_j$  which is equal to zero (as already discussed). Once, all the cascade probabilities are obtained, random number generator can choose between the cascades randomly. The conservation of energy is guaranteed. One has to be careful about appearance of non-existing gamma lines in the spectrum, however, this effect is a price to be paid for incompleteness of data.

The generator proposed in this section has ability to improve with improved data precision, which I consider as the most important feature.

### 4.2.3.3 Solution for a System with Two Intermediate States

In the current section, I will show an explicit solution for a problem defined in Equation 4.11. It will be solved for a particular example of system with two intermediate states (depicted in Figure 4.17). In the process, I will develop a matrix formalism which will, finally, make it applicable to a problem with arbitrary number of intermediate states.

During the whole derivation to follow, I will work in the space of column vectors, e.g.  $v$  represents column vector while  $v^T$  stands for a row vector. Before I will start the main derivation, let me define "cascade vector"  $x$ , "probability vector"  $p$ , "gamma intensity vector"  $\gamma$  and "delta difference vector"  $\delta$  in following way:

$$x = \begin{pmatrix} x_0 \\ x_1 \\ x_2 \\ x_3 \end{pmatrix}, \quad p = \begin{pmatrix} p_0 \\ p_1 \\ p_2 \\ p_3 \\ p_4 \\ p_5 \end{pmatrix}, \quad \gamma = \begin{pmatrix} \gamma_0 \\ \gamma_1 \\ \gamma_2 \\ \gamma_3 \\ \gamma_4 \\ \gamma_5 \end{pmatrix}, \quad \delta = \begin{pmatrix} \delta_0 \\ \delta_1 \\ \delta_2 \\ \delta_3 \\ \delta_4 \\ \delta_5 \end{pmatrix}. \quad (4.12)$$

Note the dimensions of each vector. Cascade vector  $x$  has 4 components (number of cascades) while the other two contain 6 components (number of gammas). Such definitions will be useful later in the derivation. Equation 4.3 can be rewritten in vector form  $p_j = s_j^T x$ . Here,  $s_j$  is one of six vectors which keep information about the structure of the cascades. For our system their specific form is as follows:

$$s_0 = \begin{pmatrix} 1 \\ 0 \\ 0 \\ 0 \end{pmatrix}, \quad s_1 = \begin{pmatrix} 0 \\ 1 \\ 0 \\ 0 \end{pmatrix}, \quad s_2 = \begin{pmatrix} 0 \\ 0 \\ 1 \\ 0 \end{pmatrix}, \quad s_3 = \begin{pmatrix} 0 \\ 0 \\ 1 \\ 1 \end{pmatrix}, \quad s_4 = \begin{pmatrix} 0 \\ 0 \\ 0 \\ 1 \end{pmatrix}, \quad s_5 = \begin{pmatrix} 0 \\ 1 \\ 0 \\ 1 \end{pmatrix} \quad (4.13)$$

Furthermore, if we define matrix  $S$ :

$$S = (s_0, s_1, s_2, s_3, s_4, s_5) = \begin{pmatrix} 1 & 0 & 0 & 0 & 0 & 0 \\ 0 & 1 & 0 & 0 & 0 & 1 \\ 0 & 0 & 1 & 1 & 0 & 0 \\ 0 & 0 & 0 & 1 & 1 & 1 \end{pmatrix}, \quad (4.14)$$

we can express Equations 4.3 in simple and compact matrix form:

$$p = S^T x. \quad (4.15)$$

Following the definitions of vector  $p$ ,  $\gamma$  and  $\delta$  we can also rewrite delta differences  $\delta_i$  given by Equation 4.10 into matrix form:

$$\delta = \gamma - p = \gamma - S^T x. \quad (4.16)$$

Finally, the global difference function  $\Delta$  given by Equation 4.9 takes form of dot product<sup>1</sup> of  $\delta$  vector with itself:

$$\Delta = \delta^T \delta = (\gamma^T - p^T)(\gamma - p) = \gamma^T \gamma - 2p^T \gamma + p^T p. \quad (4.17)$$

In the equation, I took advantage of Equation 4.16. In last step, I used the symmetry of dot product,  $\gamma^T p = p^T \gamma$ . Matrix formalism introduced in text above is applicable for any system regardless of the number of intermediate states. Even though, I am focusing on the particular case, the final result will be applicable for any problem of this type.

With the formalism at the place, it is possible to discuss the problem given in Equation 4.11. One needs to find a minimum of function  $\Delta$  for values of vector  $x$  whose components add up to one. It is an optimization problem when extremes of the function of multiple variables have to be found given a constraint. It can be solved by method of Lagrange multiplier.

First of all, let me remind the method of Lagrange multiplier. If we want to find extreme(s) of (for instance) two-dimensional function  $f(x,y)$  in region given by equation  $g(x,y) = 0$ , one should define so-called Lagrange function first:

$$\mathcal{L}(x, y, \lambda) = f(x, y) + \lambda g(x, y). \quad (4.18)$$

Here,  $\lambda$  is so-called Lagrange multiplier. Extreme(s) of function  $f$  in the region  $g = 0$  are all lying in points obtained as a solution to a system of equations:

$$\frac{\partial \mathcal{L}}{\partial x} = 0, \quad \frac{\partial \mathcal{L}}{\partial y} = 0, \quad \frac{\partial \mathcal{L}}{\partial \lambda} = 0. \quad (4.19)$$

For each  $\lambda$  obtained as a solution, vector  $(x, y)$  represents sought constrained extreme. The method is applicable to functions  $f$  of arbitrary number of variables.

Let me now apply the method to our problem. The function  $f$  which we need to minimize is function  $\Delta$ , depending on all the components (variables) of vector  $x$ . The constraint  $g = 0$  in our problem is given by the sum of all components of vector  $x$  which should always add to one (full probability), i.e.

$$g(x_0, x_1, x_2, x_3) = 1 - x_0 - x_1 - x_2 - x_3 = 0. \quad (4.20)$$

Therefore, the Lagrange function defining the problem is following:

$$\mathcal{L}(x_0, x_1, x_2, x_3, \lambda) = \Delta(x_0, x_1, x_2, x_3) + \lambda g(x_0, x_1, x_2, x_3). \quad (4.21)$$

Putting all the partial derivation of Lagrange function to zero (according to recipe from Equation 4.19) yields a set of equations:

$$\frac{\partial \mathcal{L}}{\partial x_0} = 0, \quad \frac{\partial \mathcal{L}}{\partial x_1} = 0, \quad \frac{\partial \mathcal{L}}{\partial x_2} = 0, \quad \frac{\partial \mathcal{L}}{\partial x_3} = 0, \quad \frac{\partial \mathcal{L}}{\partial \lambda} = 0. \quad (4.22)$$

---

<sup>1</sup>Note that, whenever dot product of two vector appears throughout the derivation, it stands for the standard vector dot product known from classical geometry, i.e.  $v_1^T v_2 = v_1^T \mathbb{1}_N v_2$ .  $N$  is a number of components of vectors  $v_1$  and  $v_2$  and  $\mathbb{1}_N$  stands for square unity matrix of dimension  $N$ .



Now, if we realize that

$$\frac{\partial g}{\partial x_a} = \frac{\partial(1 - x_0 - x_1 - x_2 - x_3)}{\partial x_a} = -1, \quad a = 0, 1, 2, 3, \quad (4.23)$$

we can rewrite Equations 4.22 into form

$$\frac{\partial \Delta}{\partial x_0} = \lambda, \quad \frac{\partial \Delta}{\partial x_1} = \lambda, \quad \frac{\partial \Delta}{\partial x_2} = \lambda, \quad \frac{\partial \Delta}{\partial x_3} = \lambda, \quad g = 0. \quad (4.24)$$

It is possible to eliminate (in our case) unwanted  $\lambda$  multiplier by subtraction of second, third and fourth equation from the first one and obtaining set of four equations (of four variables):

$$\frac{\partial \Delta}{\partial x_0} - \frac{\partial \Delta}{\partial x_1} = 0, \quad \frac{\partial \Delta}{\partial x_0} - \frac{\partial \Delta}{\partial x_2} = 0, \quad \frac{\partial \Delta}{\partial x_0} - \frac{\partial \Delta}{\partial x_3} = 0, \quad g = 0. \quad (4.25)$$

As it will turn out soon, this is a set of linear equations which can be solved by application of basic linear algebra. Note that, all the process presented until this point was not dependent on the number of cascades, neither the number of gammas involved in the problem. The specific case of two intermediate states (4 cascades, 6 gammas) is chosen as an example clarifying the general matrix notation and the calculation process.

In steps to follow, it is necessary to evaluate all the partial derivations of  $\Delta$  function with respect to cascade probability  $x_a$ . Before I do that, it is important to express some intermediate relations. Let me, firstly, define four-component base vectors  $e_0 - e_3$ :

$$e_0 = \begin{pmatrix} 1 \\ 0 \\ 0 \\ 0 \end{pmatrix}, \quad e_1 = \begin{pmatrix} 0 \\ 1 \\ 0 \\ 0 \end{pmatrix}, \quad e_2 = \begin{pmatrix} 0 \\ 0 \\ 1 \\ 0 \end{pmatrix}, \quad e_3 = \begin{pmatrix} 0 \\ 0 \\ 0 \\ 1 \end{pmatrix}. \quad (4.26)$$

Number of these vectors is given by number of cascades (cascade probabilities) assumed in the problem. It is also useful to underline that for any vector  $v$  (or matrix  $M$ ) and its transpose  $v^T$  ( $M^T$ ), following relation holds:

$$\left(\frac{\partial v}{\partial \alpha}\right)^T = \frac{\partial v^T}{\partial \alpha}, \quad \left(\frac{\partial M}{\partial \alpha}\right)^T = \frac{\partial M^T}{\partial \alpha} \quad (4.27)$$

for any variable  $\alpha$ . It is easily to see, that by performing partial derivation with respect to any of the cascade probabilities  $x_a$ , on vector  $x$  we obtain one of the base vectors  $e_a$ :

$$\frac{\partial x}{\partial x_a} = e_a. \quad (4.28)$$

Furthermore, vector  $\gamma$  and matrix  $S$  are constant and they yield zero when derived with respect to  $x_a$ :

$$\frac{\partial \gamma}{\partial x_a} = 0, \quad \frac{\partial S}{\partial x_a} = 0. \quad (4.29)$$

Given the Equations 4.15, 4.28 and 4.29, following holds:

$$\frac{\partial p}{\partial x_a} = S^T e_a. \quad (4.30)$$

Finally, we have all the ingredients in order to compute derivations of global difference function  $\Delta$ . By putting Equations 4.17, 4.27, 4.29, 4.30 and symmetry of dot product together, we can write:

$$\frac{\partial \Delta}{\partial x_a} = 2e_a^T S S^T x - 2e_a^T S \gamma. \quad (4.31)$$

First three in Equations 4.25 have a form of difference of derivations of  $\Delta$ . Using Equation 4.31 we can write:

$$\frac{\partial \Delta}{\partial x_a} - \frac{\partial \Delta}{\partial x_b} = 2(e_a^T - e_b^T) S S^T x - 2(e_a^T - e_b^T) S \gamma, \quad (4.32)$$

and Equations 4.25 gain form:

$$\begin{aligned} (e_0^T - e_1^T) S S^T x &= (e_0^T - e_1^T) S \gamma, \\ (e_0^T - e_2^T) S S^T x &= (e_0^T - e_2^T) S \gamma, \\ (e_0^T - e_3^T) S S^T x &= (e_0^T - e_3^T) S \gamma, \\ (e_0^T + e_1^T + e_2^T + e_3^T) x &= 1. \end{aligned} \quad (4.33)$$

In last equation  $g = 0$ , I took advantage of the fact that  $(e_0^T + e_1^T + e_2^T + e_3^T) x = x_0 + x_1 + x_2 + x_3$ . Having a closer look at the system in Equation 4.33 it is possible to spot hidden matrix equation of form  $Ax = b$  where

$$A = \begin{pmatrix} (e_0^T - e_1^T) S S^T \\ (e_0^T - e_2^T) S S^T \\ (e_0^T - e_3^T) S S^T \\ e_0^T + e_1^T + e_2^T + e_3^T \end{pmatrix}, \quad b = \begin{pmatrix} (e_0^T - e_1^T) S \gamma \\ (e_0^T - e_2^T) S \gamma \\ (e_0^T - e_3^T) S \gamma \\ 1 \end{pmatrix}. \quad (4.34)$$

Finally, the sought vector  $x$  is, therefore, calculated as:

$$x = A^{-1} b \quad (4.35)$$

where  $A^{-1}$  is inverse of matrix  $A$ . Matrix  $A$  is a square matrix of dimension equal to number of cascades involved in the system in question. It is relatively straightforward to extend matrix  $A$  and vector  $b$  into systems with higher number of intermediate states, namely, systems with  $N_C$  cascades and  $N_\gamma$  gammas:

$$A = \begin{pmatrix} (e_0^T - e_1^T) S S^T \\ (e_0^T - e_2^T) S S^T \\ \vdots \\ (e_0^T - e_{N_C}^T) S S^T \\ \sum_{i=0}^{N_C} e_i^T \end{pmatrix}, \quad b = \begin{pmatrix} (e_0^T - e_1^T) S \gamma \\ (e_0^T - e_2^T) S \gamma \\ \vdots \\ (e_0^T - e_{N_C}^T) S \gamma \\ 1 \end{pmatrix}. \quad (4.36)$$

Structure matrix  $S$  and vector  $\gamma$  are expanded accordingly, following the definition at the beginning of the section.

#### 4.2.3.4 Proof of the Concept by Analytical Solution

In order to prove the concept I will present solution of two (intermediate) state system which was used as an example throughout the whole discussion about the generator. The task is simple. We need to compose the matrix  $A$  and vector  $b$  from Equation 4.34, find

the inverse matrix  $A^{-1}$  and subsequently calculate  $A^{-1}b$ . Let me start with matrix A. As a first step, it is helpful to compose row vectors of form  $e_a^T - e_b^T$ . Following the definition in Equations 4.26 we can write:

$$\begin{aligned} e_0^T - e_1^T &= (1 \ -1 \ 0 \ 0), \\ e_0^T - e_2^T &= (1 \ 0 \ -1 \ 0), \\ e_0^T - e_3^T &= (1 \ 0 \ 0 \ -1). \end{aligned} \quad (4.37)$$

Taking advantage of definition of matrix S in Equation 4.14 we can write:

$$SS^T = \begin{pmatrix} 1 & 0 & 0 & 0 & 0 & 0 \\ 0 & 1 & 0 & 0 & 0 & 1 \\ 0 & 0 & 1 & 1 & 0 & 0 \\ 0 & 0 & 0 & 1 & 1 & 1 \end{pmatrix} \begin{pmatrix} 1 & 0 & 0 & 0 \\ 0 & 1 & 0 & 0 \\ 0 & 0 & 1 & 0 \\ 0 & 0 & 1 & 1 \\ 0 & 0 & 0 & 1 \\ 0 & 1 & 0 & 1 \end{pmatrix} = \begin{pmatrix} 1 & 0 & 0 & 0 \\ 0 & 2 & 0 & 1 \\ 0 & 0 & 2 & 1 \\ 0 & 1 & 1 & 3 \end{pmatrix}. \quad (4.38)$$

Following the recipe in Equation 4.34, with help of Equations 4.37 and 4.38 we can evaluate matrix A and vector b:

$$A = \begin{pmatrix} 1 & -2 & 0 & -1 \\ 1 & 0 & -2 & -1 \\ 1 & -1 & -1 & -3 \\ 1 & 1 & 1 & 1 \end{pmatrix}, \quad b = \begin{pmatrix} \gamma_0 - \gamma_1 - \gamma_5 \\ \gamma_0 - \gamma_2 - \gamma_3 \\ \gamma_0 - \gamma_3 - \gamma_4 - \gamma_5 \\ 1 \end{pmatrix}. \quad (4.39)$$

It is now simple task to calculate matrix inverse  $A^{-1}$ :

$$A^{-1} = \begin{pmatrix} 1/4 & 1/4 & 0 & 1/2 \\ -1/2 & 0 & 1/4 & 1/4 \\ 0 & -1/2 & 1/4 & 1/4 \\ 1/4 & 1/4 & -1/2 & 0 \end{pmatrix}. \quad (4.40)$$

Finally, the solution  $x = A^{-1}b$  has a following form:

$$\begin{aligned} x_0 &= \frac{1}{2} + \frac{1}{2}\gamma_0 - \frac{1}{4}\gamma_1 - \frac{1}{4}\gamma_2 - \frac{1}{4}\gamma_3 - \frac{1}{4}\gamma_5, \\ x_1 &= \frac{1}{4} - \frac{1}{4}\gamma_0 + \frac{1}{2}\gamma_1 - \frac{1}{4}\gamma_3 - \frac{1}{4}\gamma_4 + \frac{1}{4}\gamma_5, \\ x_2 &= \frac{1}{4} - \frac{1}{4}\gamma_0 + \frac{1}{2}\gamma_2 + \frac{1}{4}\gamma_3 - \frac{1}{4}\gamma_4 - \frac{1}{4}\gamma_5, \\ x_3 &= -\frac{1}{4}\gamma_1 - \frac{1}{4}\gamma_2 + \frac{1}{4}\gamma_3 + \frac{1}{2}\gamma_4 + \frac{1}{4}\gamma_5. \end{aligned} \quad (4.41)$$

As it could be expected, solution has form  $x = c + M\gamma$  where c is a constant vector with dimension of x vector and M is matrix which is mixing all the gammas together to form cascade probabilities  $x_i$ . Note that, each column (therefore all the elements) of matrix M add up to zero while all the components of the vector c add up to one exactly. It is a consequence of constraint  $x_0 + x_1 + x_2 + x_3 = 1$  which ensures that at least one of the cascades happens regardless of the experimental values which are stored in  $\gamma$  vector.

Let me now demonstrate the performance of obtained result. The whole discussion was motivated by the imprecisions in experimental data. As it was discussed, inconsistent input

in form of  $\gamma_i$  intensities (missing transitions) made some of the transitions unreachable by previously presented stair generator. Solution proposed in this section should not only conserve energy and  $\gamma$  correlations but the limit of its performance is given only by consistency of the  $\gamma$  transition values plugged into it. This also implies that, for perfectly consistent data set the generator should give exact solution. Let me check this property. Let us have a following input dataset:

$$\gamma^T = ( \gamma_0 \ \gamma_1 \ \gamma_2 \ \gamma_3 \ \gamma_4 \ \gamma_5 ) = ( 0.5 \ 0.05 \ 0.4 \ 0.45 \ 0.05 \ 0.1 ). \quad (4.42)$$

I will call this dataset ideal and denotes it by letter I because it represents perfectly consistent data as if they were measured by ideal experiment. If we now plug these  $\gamma$  (I) values into solution in Equation 4.41 we obtain following cascade probability vector:

$$x^T = ( x_0 \ x_1 \ x_2 \ x_3 ) = ( 0.5 \ 0.05 \ 0.4 \ 0.05 ), \quad (4.43)$$

Taking advantage of structural equations given in Equation 4.3 we can calculate all the gamma probabilities  $p_i$  which would be produced by the generator.

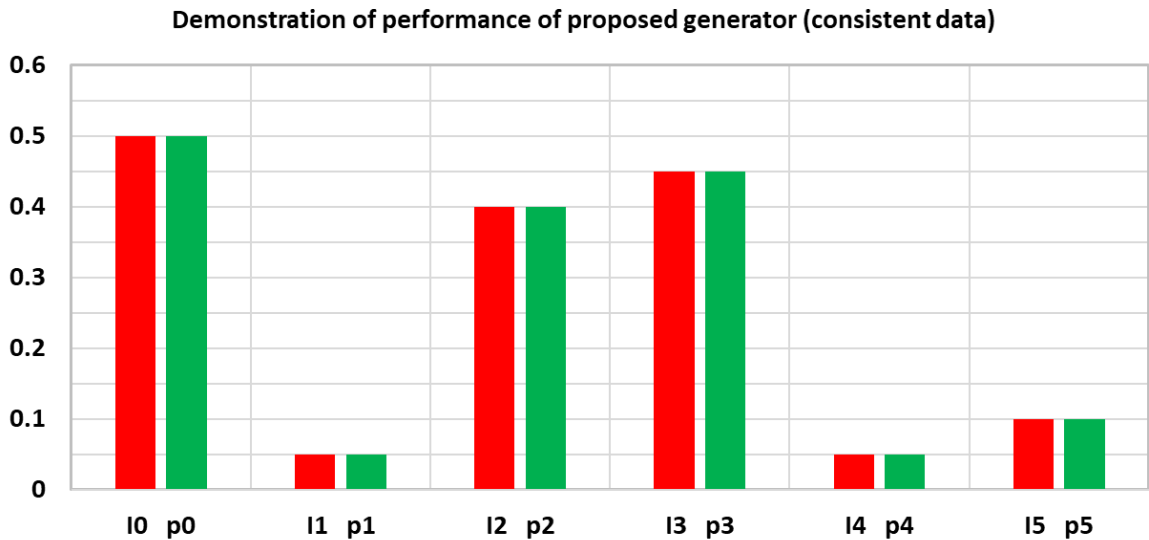


Figure 4.18: Comparison of ideal gamma intensities (red) with intensities generated by my generator (green).

Figure 4.18 contains comparison of ideal gamma intensities (red) from Equation 4.42 compared to intensities computed by the generator (green) based on Equations 4.41 and structure equations. Generator is exactly matching the intensities provided by dataset. Even though, this example is necessary check of basic performance, it does not yet reveal the real power of the generator. If ideal data were plugged into stair generator, the result would be also exact.

However, the main advantage of my generator is the possibility to work with imprecise data. Imagine that (ideal) intensities in Equation 4.42 would be measured with realistic detector giving rise to experimental uncertainties. Imagine that detector would measure slightly biased values:

$$\gamma^T = ( \gamma_0 \ \gamma_1 \ \gamma_2 \ \gamma_3 \ \gamma_4 \ \gamma_5 ) = ( 0.53 \ 0.05 \ 0.43 \ 0.48 \ 0 \ 0.1 ). \quad (4.44)$$

These values are strictly speaking inconsistent, as it is not possible to find cascade probabilities  $x_0, x_1, x_2$  and  $x_3$  such that, the resulting gamma probabilities  $p_i$  obtained from Equations

4.3 would be matching these measured values. Intensities of  $\gamma_0$ ,  $\gamma_2$  and  $\gamma_3$  are off by 0.03 while  $\gamma_4$  is missing completely. After we plug the  $\gamma$  values into the generator (Equation 4.41) we obtain following cascade probabilities:

$$x^T = (x_0 \ x_1 \ x_2 \ x_3) = (0.5 \ 0.0475 \ 0.4275 \ 0.025). \quad (4.45)$$

As usual, these probabilities can be turned into gamma probabilities (intensities) as produced by generator by using structure equations. Figure 4.19 is comparing the ideal data (I, red), measured experimental generator input ( $\gamma$ , blue) and gamma intensities obtained by generator given the input (p, green). In case of  $\gamma_0$ ,  $\gamma_2$  and  $\gamma_3$  the generator (green) was capable to

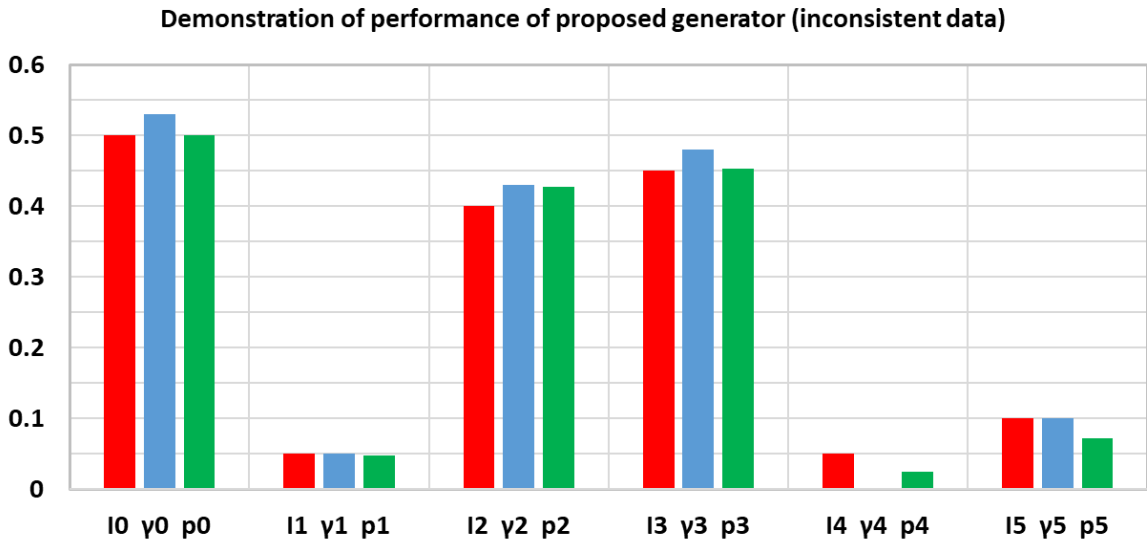


Figure 4.19: Comparison of ideal gamma intensities (red) with intensities biased by measurement uncertainties (blue) and resulting gamma intensities generated by my generator (green).

totally or partially compensate the mismatch of measurement (blue) and ideal data (red). In case of  $\gamma_0$ , the errors cancelled out perfectly resulting in generator being more precise than the input dataset. In other two cases, results from generator are closer to reality than measurement. This is thanks to the structure of the cascades encoded in the generator's equations. Furthermore,  $\gamma_4$  is not present in experimental dataset. However, the generator reproduces this transition at least partially. It is for a price of underestimation of  $\gamma_5$ , nevertheless, it is inevitable effect which we pay for imprecise data. Appearance of  $\gamma_4$  in my example is a triumph of my generator. If we remind the structure of the cascades from Figure 4.17 we see that  $\gamma_4$  is intermediate link between  $\gamma_3$  and  $\gamma_5$  in cascade  $x_3$ . Stair generator would be capable of generating  $\gamma_3$  but after it would fall to the  $E_2$  excited state it would not be capable of reaching ground state  $E_0$ , causing not only  $\gamma_4$  to be left out but  $\gamma_5$  being suppressed.

It is possible to conclude, that my proposed generator represents a possibility to reconstruct gamma correlations as precisely as the input dataset allows. The presented example for two intermediate states was chosen for simplicity and clarity, however, Equation 4.36 offers recipe for solution of any system. One only needs to compose the matrix of structure  $S$  specific for the system. After matrix  $A$  is composed, it needs to be inverted. The dimension of the matrix is  $N_C \times N_C$  where  $N_C$  is a number of possible cascades in the system. Based on the Table 4.6 we can see that, the number of cascades grows exponentially with the number of intermediate states in the system. However, even for complex systems, the

diagonalization of large matrices is achievable with computers nowadays. Furthermore, the structure equations can be simplified significantly based on the selection rules which might prohibit some particular gamma transitions to occur. The calculation needs to be performed only once. After the vector of cascade probabilities  $x$  is obtained for given dataset, it does not have to be recalculated, unless more precise experimental data are obtained as an input. Proposed generator is conceptually general and it can be also applied for any systems where decay cascades occur (regardless of particles produced in the transitions). It is also possible to generalize the generator in order to work with transitions originating from lower than the highest excited state  $E_H$ .

### **4.3 Conclusions**

The estimation of neutron background is generally difficult task to perform. In the chapter, I compared neutron fluxes which could be expected to pass through shielding for nine specific cases. Subsequently, estimation of neutron capture counts inside of the demonstrator was performed. Materials with most of the captures were identified and mapped in form of three dimensional capture maps.

The neutrons were followed all the way to the capture. Physics implemented in Geant software package is sufficient and well implemented for such task. However, in second part of the chapter it was shown, that the model of production of gammas produced in thermal neutron capture is not sufficient for the task of estimation of background caused by neutrons. Energy conservation and gamma coincidences are not preserved. New potential approach which could take these two features into account was proposed. The performance of the generator was demonstrated on a simple example. In future, I plan to apply the approach on the real data for chosen isotopes and use it to estimate fake double-beta events caused by neutron capture.

## Estimation of Sensitivity of SuperNEMO to $0\nu\beta\beta$ with Majoron Emission

Main interests of double beta decay experiments are usually focused towards yet unobserved  $0\nu\beta\beta$  or  $2\nu\beta\beta$  which was already proven to exist experimentally for various different nuclei. However, there exist another more exotic double beta decay theories predicting existence of  $0\nu\beta\beta$  with emission of so-called Majoron(s):

$$0\nu\beta\beta\chi^0 : (A, Z) \rightarrow (A, Z + 2) + 2e^- + \chi^0, \quad (5.1)$$

$$0\nu\beta\beta\chi^0\chi^0 : (A, Z) \rightarrow (A, Z + 2) + 2e^- + 2\chi^0. \quad (5.2)$$

Here,  $\chi^0$  stands for a Majoron. Majoron is a massless Goldstone boson which arise due to a violation of global B-L symmetry assumed in certain models. Its existence might have important implications in Cosmology [97, 98, 99] or Astrophysics [100, 101, 102, 103].

Different Majoron models result in different electron energy spectra. They are denoted by "spectral index". Theoretical spectra for spectral indices  $n=1,2,3,5$  and  $7$  resulting from proposed models are shown in Figure 5.1. In the whole thesis, under symbol  $0\nu\beta\beta\chi^0$  we understand process with spectral index  $n = 1$  and symbol  $0\nu\beta\beta\chi^0\chi^0$  stands for process with spectrum of index  $n = 3$ .

NEMO-3, set the limit for half life of  $0\nu\beta\beta\chi^0$  to  $1.5 \times 10^{22}$  yr (90% CL) and limit for  $0\nu\beta\beta\chi^0\chi^0$  at  $3.1 \times 10^{21}$  yr (90% CL) [104]. The goal of the chapter is to evaluate how much can SuperNEMO improve these values.

### 5.1 Calculation of Half-Life of Rare Processes

Double-beta decay processes are very rare and difficult to observe. Their half lives are extremely long, measured in millions of ages of universe. It makes such processes extremely difficult to observe. In case when the decay is observed, it is possible to calculate its half life based on the number of detected decays. Any type of nuclear decay follows universal law of radioactive decay:

$$N(t) = N_0 e^{-\lambda t}. \quad (5.3)$$

Number of remaining nuclei which have not yet decayed,  $N(t)$ , fall exponentially with time.  $N_0$  represents number of initial nuclei at the beginning of the observation. The rate at

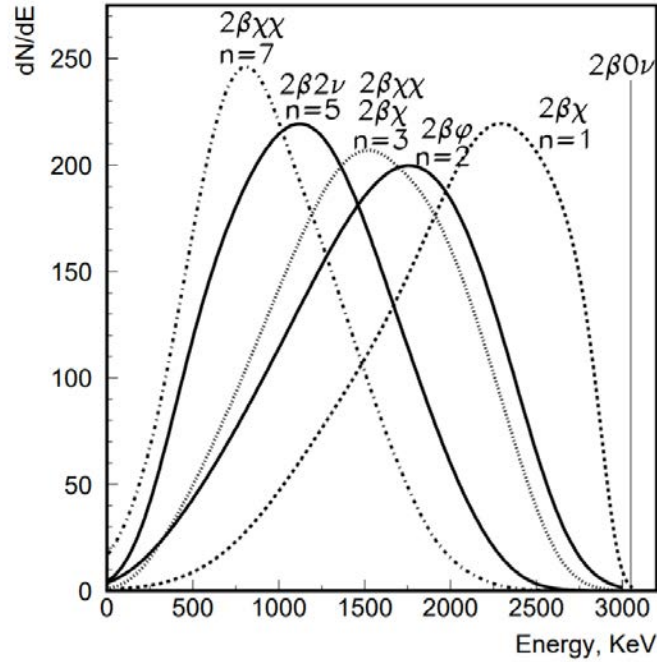


Figure 5.1: Theoretical electron energy spectra of different types of double beta decay. Spectral index  $n$  serves for distinction between the spectral types. Source: [104]

which system of nuclei decay is influenced by decay constant  $\lambda$ . Decay constant is related to half life ( $T_{1/2}$ ) via very well known relation:

$$\lambda = \frac{\ln(2)}{T_{1/2}}. \quad (5.4)$$

Large values of  $\lambda$  describe fast decays with short half lives. In contrary, low values, describe decays which are very slow with large half lives. The latter is exactly a case for any type of double-beta process. By multiplication of both sides of Equation 5.4 by measurement period  $t$ , we can conclude, that exponent  $\lambda t$  in Equation 5.3 is proportional to ratio of measurement period and decay's half life:  $t/T_{1/2}$ . Shortest half lives of double-beta decay processes are on the level of  $10^{15}$  years while standard duration of double beta decay experiment is measured in years, rarely in decades. The ratio between measurement period and half life of double beta decay process is at maximum at the level of  $t/T_{1/2} \approx 10^{-14}$ . Exponent  $\lambda t$  is, therefore, always extremely tiny as well and we can write:

$$1 \gg \lambda t \gg (\lambda t)^2 \gg \dots \gg (\lambda t)^i, \quad i = 3, 4, 5, \dots \quad (5.5)$$

Number of decayed nuclei  $n_D$  during a period  $t$  can be calculated as difference in numbers of nuclei at the beginning of measurement  $N_0$  and remaining nuclei  $N(t)$  given by Equation 5.3:

$$n_D = N_0 - N_0 e^{-\lambda t} = N_0 \left( \lambda t - \frac{(\lambda t)^2}{2!} + \frac{(\lambda t)^3}{3!} - \dots \right) \approx N_0 \lambda t. \quad (5.6)$$

Exponential decay formula was expanded into Taylor polynomial. Thanks to Equation 5.5 it was possible to neglect all the terms except for the first one and obtain very simple relation (for very rare decays). Number of initial nuclei at the beginning of the measurement



$N_0$  can be estimated if we know amount - mass ( $m$ ) of the observed isotope in the source. For given isotope, molar mass  $W$  expresses mass of one mole of the isotope. Therefore, ratio  $m/W$  expresses number of moles of the isotope in given source sample. Furthermore, Avogadro's constant  $N_A$  defines number of objects (in our case nuclei) needed to compose one mole. Therefore,  $m/W$  moles of observed isotope contains

$$N_0 = \frac{mN_A}{W} \quad (5.7)$$

nuclei. If we know mass of the observed source we can estimate number of nuclei at the beginning of observation. It is important to keep in mind, that the mass of the isotope of interest is not the same as mass of the source which contains the isotope. Typically, sources are composed of many different isotopes and only fraction of their mass, given by their abundance ( $a$ ), is composed of the isotope of interest. It is important to keep in mind, therefore, that  $m$  in my equations represents the fraction of mass belonging to pure isotope in the source of mass. One can also express  $m$  in terms of full source mass  $m_s$  as a product of source mass and abundance of isotope in the source, i.e.

$$m = am_s. \quad (5.8)$$

If we now combine Equations 5.4, 5.6, 5.7 and 5.8 we obtain:

$$n_D = \ln(2) \frac{N_A}{W} \frac{am_s t}{T_{1/2}}. \quad (5.9)$$

The equation expresses number of decays  $n_D$  for rare process with half life  $T_{1/2}$  if  $m_s$  kilograms of isotope with molar mass of  $W$  and abundance  $a$  is observed during period of time  $t$ . Equation gives us the direct recipe to improve chances to observe sought decay. Number of decays is proportional to abundance of the isotope in the source  $a$ , mass of the source  $m_s$  and length of the measurement  $t$ . Number of decays can be enhanced by observation of larger source masses during longer period of times. On top of that, the chances are improved if source is enriched, i.e. abundance of observed isotope  $a$  in source is higher. Quantity  $am_s t$  (mt) is called exposure and it serves for comparison of different double beta decay experiments.

In Equation 5.9,  $n_D$  stands for real number of decays given the experimental parameters explained above. However, number of observed decays  $n_{OS}$  is lower. Some of the decays are not detected due to imprecisions in reconstruction or simply by imposing various different data cuts. The relation between number of real decays  $n_D$  and number of observed decays  $n_{OS}$  can be expressed via detection efficiency  $\epsilon$ . It is a ratio of observed signal events to all decays:  $\epsilon = n_{OS} / n_D$ .  $\epsilon$  can be obtained from simulations. Finally, let me express half life from Equation 5.9:

$$T_{1/2} = \ln(2) \frac{N_A}{W} \epsilon \frac{am_s t}{n_{OS}}. \quad (5.10)$$

Here,  $n_D$  was substituted by number of observed signal events  $n_{OS}$  by experiment. Due to the presence of background in experiments, it is not possible to tell with 100% certainty how many real decays  $n_{OS}$  were observed (and how many detected events have origin in background). However, having precise background model, it can be estimated to a certain confidence level as a value denoted  $\mu^1$ . Strictly speaking  $n_{OS}$  cannot be measured, therefore,

<sup>1</sup>Methodology to calculate  $\mu$  if number of background counts  $b$  is given will be discussed in following sections

Equation 5.10 is used for calculation of half life in double beta decay experiments where  $\mu$  is plugged instead of  $n_{OS}$ .

## 5.2 Statistical Nature of Observed Counts

Equation 5.10 gives a recipe for calculation of half life of rare decay if number of observed counts is given. Radioactive decay is, however, statistical process. Two perfectly identical copies of the same experiment might, therefore, provide different observed counts, due to the statistical fluctuations. It is important to take this fact into account in order to avoid mistakes in analysis and avoid dependence of the result on random factor. Discussion to follow is based on the one presented in [105].

### 5.2.1 Experiments Without Background

In order to avoid random factor in calculation of half life, one needs to consider ensemble of identical experiments instead of single measurement done by one particular example. In average, such experiment detects  $n_O$  total counts (signal + background). In case of background-less experiments, therefore, each count represents true signal. Estimation of true detected signals  $\mu$  is, therefore, identical to number of all observed counts, i.e.  $n_O = \mu$ . As it was already discussed, identical experiments yield different number of counts due to the statistical fluctuations. Probability to observe  $n$  counts in specific experiment (if average of  $\mu$  true signals are expected) is given by Poisson distribution:

$$P(n, \mu) = \frac{\mu^n}{n!} e^{-\mu}. \quad (5.11)$$

For example, with  $\mu = 3$  expected true signals, 42.3% of identical experiments would observe less counts and roughly 5% unfortunate experiments would not observe a single count! What conclusion can a single experiment draw about average value of true expected signals given from observation of  $n$  events? Common method to report a result is given in terms of so-called confidence intervals proposed by Neyman in [106]. The idea is to propose interval  $\mu \in (\mu_L, \mu_U)$  instead of single value. Here,  $\mu_U$  represents number of expected true events such that, only  $\alpha$  fraction of identical experiments would report lower or equal observed number of counts. Similarly,  $\mu_L$  is value of true expected signals such that only  $\beta$  fraction of identical experiments would observe higher or equal number of counts. Fractions  $\alpha$  and  $\beta$  represent scenarios of experiments not covered by the interval. In contrary,  $1 - \alpha - \beta$  represent all the scenarios covered in the interval. It expresses the level of belief that the interval covers the true value. That is where term confidence level comes from.

Let me demonstrate with an example, how confidence intervals are calculated. I will assume background-less experiment, which observed  $n = 3$  counts, as an example. Let me choose  $\alpha = \beta = 0.05$  (5%). Upper limit,  $\mu_U$  in such case is a value for which cumulative probability to observe number of counts less or equal to three is 5%. Limit can be obtained, therefore, if we solve following equation:

$$\alpha = 0.05 = \sum_{i=0}^3 P(i, \mu_U). \quad (5.12)$$

Equation can be solved numerically with result  $\mu_U = 7.754$ . Subsequently, we can calculate lower limit  $\mu_L$  in similar fashion. We search for a mean value of true signals  $\mu_L$  for

which 5% of experiments would report three or more counts. The value is a solution to the equation:

$$\beta = 0.05 = \sum_{i=3}^{\infty} P(i, \mu_L). \quad (5.13)$$

Numerical solution provides value  $\mu_L = 0.818$ . Finally, we say that confidence interval (0.818, 7.754) covers value of true expected signals  $\mu$  at the confidence level (CL) of 90% ( $1 - \alpha - \beta$ ). Note that, choice  $\alpha = 0.03$  and  $\beta = 0.07$  would yield different confidence interval but with a same confidence level. Such an interval is also valid, however, it is common choice to set symmetric intervals. In case when  $\alpha \neq 0$  and  $\beta \neq 0$  we talk about central interval. There are situations when only one-sided interval is preferable. If we repeat the same procedure, this time with  $\alpha = 0$  and  $\beta = 0.05$ , we obtain interval (0, 7.554). Such interval offers uniquely upper limit at the confidence level of 95%. Furthermore, choice  $\alpha = 0.05$  and  $\beta = 0$  yields interval (0.818,  $\infty$ ) again on 95% confidence level. However, in this case only lower limit is reported. It is always important to precise what kind of interval (one-sided or central) is presented along with confidence level, when reporting result of such experiment.

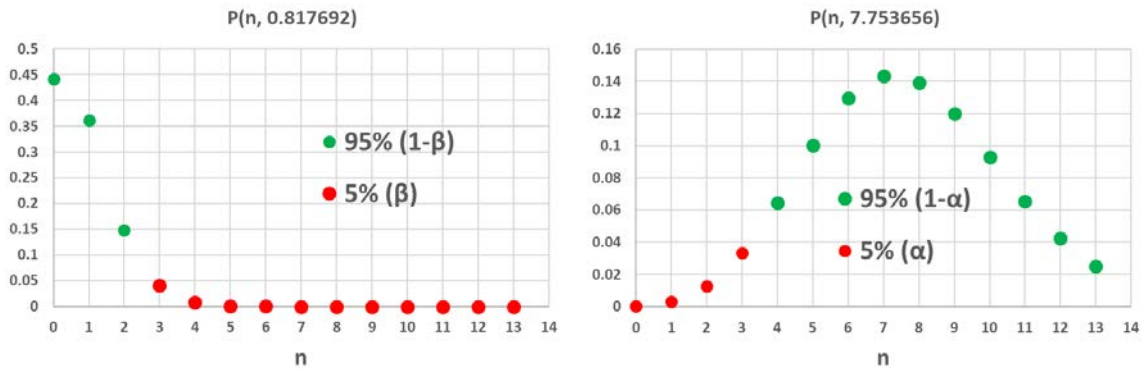


Figure 5.2: Left: Poisson distribution for  $\mu = 0.817692$ . Value  $\mu$  represents lower limit of confidence interval  $\mu_L$ . It was chosen in a way, that all the scenarios  $n \geq n_0 = 3$  (red dots) give a cumulative probability of  $\beta$ : 5%. Right: Poisson distribution for  $\mu = 7.753656$ . Value  $\mu$  represents upper limit of confidence interval  $\mu_U$ . It was chosen in a way, that all the scenarios  $n \leq n_0 = 3$  (red dots) give a cumulative probability of  $\alpha$ : 5%.

Let me briefly summarize the method for calculation of confidence intervals. Background-less experiment with  $n_0$  observed counts should report mean expected number of true signals  $\mu$  from interval  $(\mu_L, \mu_U)$ . Here, the limits of the interval are calculated in following way:

$$\alpha = \sum_{i=0}^{n_0} P(i, \mu_U),$$

$$\beta = \sum_{i=n_0}^{\infty} P(i, \mu_L). \quad (5.14)$$

Here,  $\alpha$  and  $\beta$  are chosen constants which decide between scenarios when only lower, upper or both limits are given. The confidence level of the presented interval is given in % and is calculated as  $1 - \alpha - \beta$ .

### 5.2.2 Experiments with Background - Collapse of Classical Method

In following, I will assume more realistic situation of experiments with non-zero background. Mean expected number of counts is in such case composed of two components, the mean expected signal  $\mu$  (same as in case of background-less experiments) and mean expected number of background counts  $b$ . If we average over ensemble of identical experiments, in average we expect to observe  $n_0 = \mu + b$  counts. Following the same logic as in previous section, the probability to observe  $n$  counts in one of the experiments is again given by Poisson distribution:

$$P(n, \mu + b) = \frac{(\mu + b)^n}{n!} e^{-(\mu + b)}. \quad (5.15)$$

Compared to Equation 5.11, number of mean expected counts  $n_0$  is higher by number of expected background counts  $b$ . After addition of expected background counts, Equations 5.14 get following form:

$$\begin{aligned} \alpha &= \sum_{i=0}^{n_0} P(i, \mu_U + b), \\ \beta &= \sum_{i=n_0}^{\infty} P(i, \mu_L + b). \end{aligned} \quad (5.16)$$

By setting  $\alpha = 0.05$ ,  $\beta = 0$ , one can calculate one-sided confidence intervals  $(0, \mu_U)$  in similar fashion as in background-less case. Let me assume experiment with four expected background counts,  $b = 4$ . I will compare experiments which observed number of counts lower than background, i.e four different experiment scenarios  $n = 3, 2, 1, 0$ . For each of four scenarios, plot similar to Figure 5.2 - Right was produced and shown in Figure 5.3.

Value of mean total expected counts  $\mu + b$  differs in dependence of scenario. Experiment with three measured counts calculates  $\mu + b = 7.754$  counts as a solution to first equation in Equation 5.16. If we subtract background (four counts), we obtain upper limit of confidence interval  $\mu_U = 3.754$ . It is no surprise that, the lower the number of measured counts is the lower  $\mu_U$  is. However, for experiment scenarios  $n = 2, 1, 0$  we obtain  $\mu_U = 2.296, 0.744, -1.004$ , respectively. Case, when no count is measured, gives a non-physical negative value of upper limit. Moreover, if we try to correct such value and report  $\mu_U = 0$ , the confidence interval would be an empty set. Due to the presence of background, value  $\mu_U$  is "pushed" out of the physical region. Classical method provides absurd results for measurements observing much less counts  $n$  than expected background  $b$ .

## 5.3 Feldman-Cousins Method

Previously presented problem with construction of reasonable confidence intervals is not the only pitfall of classical method.

Experiments which observe number of counts lower than background, are, quite naturally, able to report only upper limit on the expected mean signal  $\mu_U$ . Such an upper boundary can be plugged into Equation 5.10 in order to calculate respective half-life. Half-life and number of signal counts  $\mu$  are inversely proportional. Therefore, plugging upper limit on expected mean signal  $\mu_U$  into Figure 5.10 yields lower boundary on half life as follows:

$$T_{1/2} \geq \ln(2) \frac{N_A}{W} \varepsilon \frac{am_s t}{\mu_U}. \quad (5.17)$$

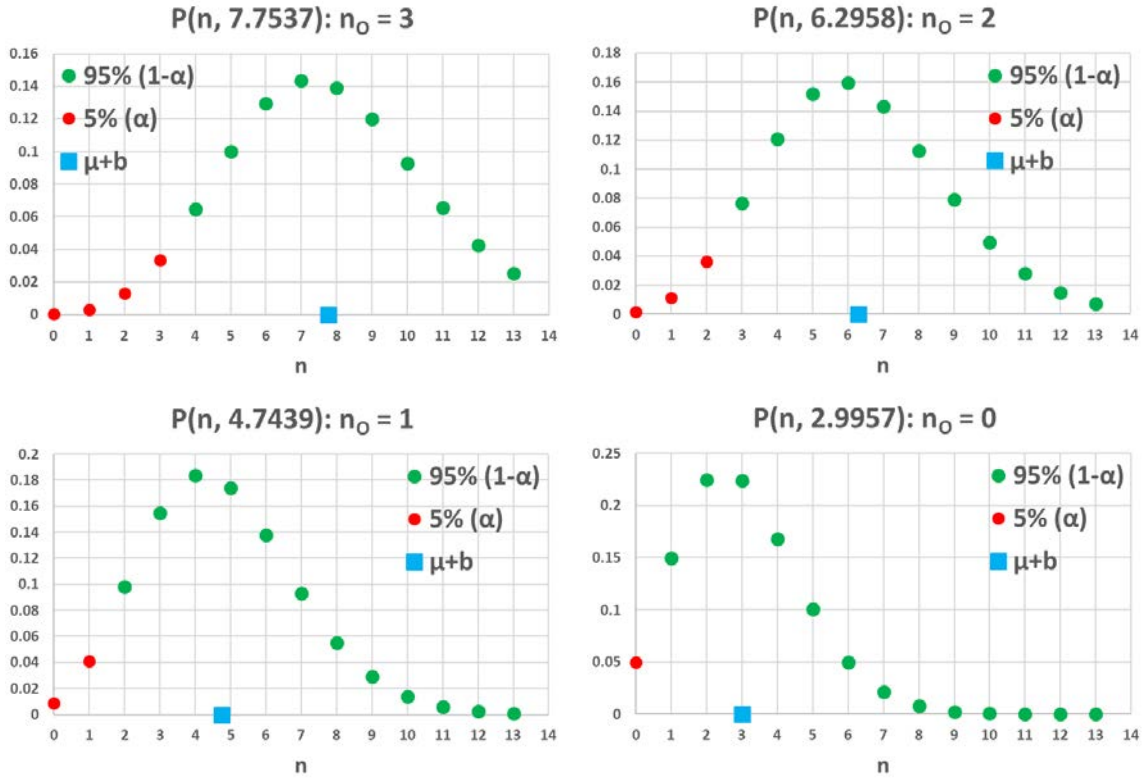


Figure 5.3: Poisson distributions of four different values of mean expected counts  $\mu + b$ . Value  $\mu + b$  was chosen in a way that cumulative probability of  $n \leq n_0$  (red dots) is equal exactly to chosen  $\alpha$  (5%). Blue dot marks position of  $\mu + b$  on x-axis (numerical value is given in each title). Each plot represents different measured number of counts  $n_0$  of identical experiments with expected background  $b = 4$ .

Using a classical method, two experiments which observe same number of total counts but expect different backgrounds, would report different upper limits of true mean signal ( $\mu_U$ ). This is not surprising, however, if both experiments observed less counts than background (no discovery), the one with higher expected background would report lower value of  $\mu_U$ , i.e. higher low limit on half life. This is an anomaly of the method, because experiment with larger expected background should not get better results than one with lower background.

All of the previous fundamental problems with classical method were solved by Feldman and Cousin in their famous article from 1997 [107]. Their method takes advantage of construction of so-called confidence belts. Construction of confidence belts in some sense resembles the process of construction of confidence intervals from classical method.

Let me describe the process in detail. As previously, let us have an experiment with expected background  $b$ . The experiment detects  $n$  counts. Probability, that an experiment with  $b$  background counts observes  $n$  total counts is governed by Poisson probability  $P(n, \mu + b)$  given by Equation 5.15.  $\mu$ , the mean true signal count, is unknown and has to be extracted. In classical method the approach was rather direct. We attempted to adapt limits of confidence interval ( $\mu_L, \mu_U$ ) in a way that cumulative probability of  $P(i, \mu_U + b)$  ( $P(i, \mu_L + b)$ ) for all  $i \leq n$  ( $i \geq n$ ) covered  $\alpha$  ( $\beta$ ) portion of probability. Feldman-Cousins method is not as straightforward. In this method, intervals ( $n_j^{\min}, n_j^{\max}$ ) are constructed for equidistantly distributed succession of values  $\mu_j$ . Calculation is performed for variety of chosen values  $\mu_j$ .

Such intervals are called confidence belts.

Calculation of confidence belts proceeds in following steps:

1. Value of  $\mu_j$  is chosen.
2. Values of integer quantities  $n_j^{\min}$  and  $n_j^{\max}$  are calculated. They should satisfy following relations:

$$1 - \alpha \leq \sum_{i=n_j^{\min}}^{\infty} P(i, \mu_j + b), \quad (5.18)$$

$$1 - \beta \leq \sum_{i=0}^{n_j^{\max}} P(i, \mu_j + b). \quad (5.19)$$

Coefficients  $\alpha$  and  $\beta$  are chosen based on the type of interval and confidence level which we would like to reach (central or one-sided). For given  $\alpha$  and  $\beta$ , solution is a couple of  $n_j^{\min}$  and  $n_j^{\max}$  where  $n_j^{\min}$  is minimal value satisfying the Equation 5.18 while, simultaneously  $n_j^{\max}$  is maximal value satisfying the Equation 5.19.

3. Values  $n_j^{\min}$  and  $n_j^{\max}$  are kept.
4.  $\mu_j$  is incremented by a small chosen amount  $\Delta\mu$ ,  $\mu_{j+1} = \mu_j + \Delta\mu$  is obtained. Algorithm continues with  $\mu_{j+1}$  at point 2.
5. When sufficient interval of values of  $\mu_j$  is calculated, the algorithm stops.

Figure 5.4 contains clarification of Equations 5.18 and 5.19 for  $\mu_j + b = 8.56$ . Note that, similarly to confidence intervals from classical method, confidence level  $CL = 1 - \alpha - \beta$ . In the classical method, we adapted value of variables  $\mu_L$  and  $\mu_U$  in order to solve Equations 5.16.  $\mu_L$  and  $\mu_U$  are real numbers so the equations are solvable exactly (within numerical

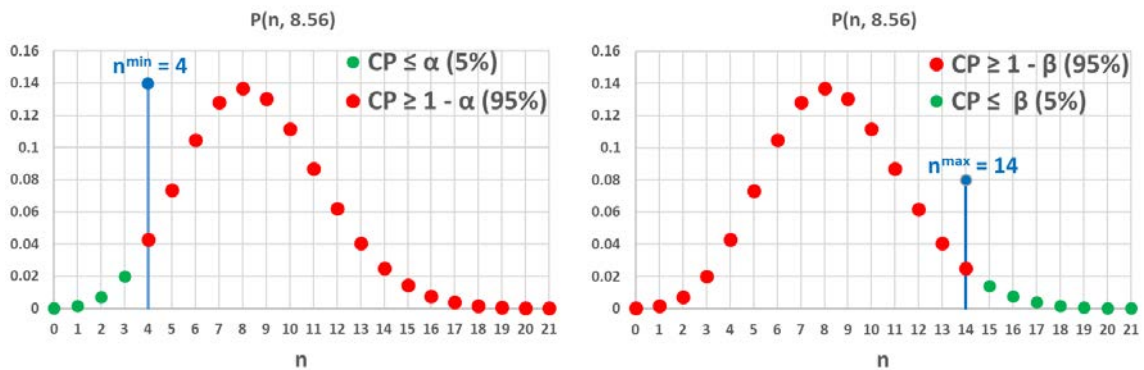


Figure 5.4: Example of calculation of (central) confidence belt for  $\mu_j = 8.56 - b$ . Left: According to Equation 5.18,  $n_j^{\min} = 4$  because cumulative probability (CP) of red dots is superior to  $1 - \alpha = 95\%$ . At the same time, value  $n = 5$  would cause CP of red dots drop below 95%. Right: According to Equation 5.19,  $n_j^{\max} = 14$  because cumulative probability (CP) of red dots is superior to  $1 - \beta = 95\%$ . At the same time, value  $n = 13$  would cause CP of red dots drop below 95%.

imprecision). However, in problem of confidence belts, values  $n_j^{\min}$  and  $n_j^{\max}$  are integers. The cumulative probability of  $P(n, \mu_j + b)$  for all  $n_j^{\min} \leq n \leq n_j^{\max}$  will practically always exceed  $CL = 1 - \alpha - \beta$ . Such conservativeness is unavoidable effect.

Result of the whole algorithm is a set of  $\mu_0, \mu_1, \dots, \mu_N$  values with respective confidence belts  $(n_0^{\min}, n_0^{\max}), (n_1^{\min}, n_1^{\max}), \dots, (n_N^{\min}, n_N^{\max})$ . The confidence belts can be represented in two-dimensional plots which can be found in Figure 5.5.

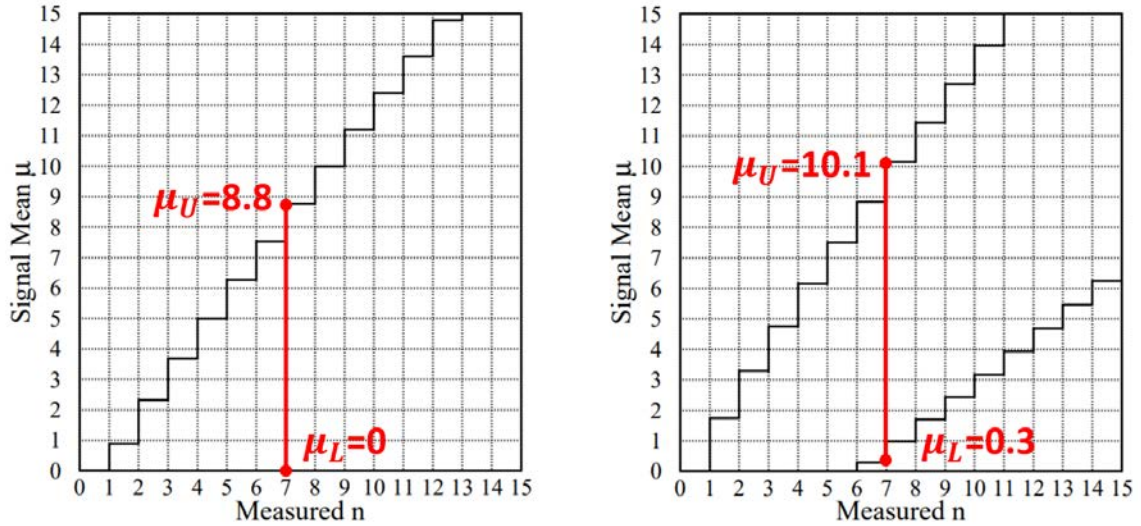


Figure 5.5: Representation of confidence belts as a function of  $\mu_j$  (y-axis). X-axis represents number of total counts  $n$  observed by experiment. Source: [107]. Both plots are generated for case with  $b = 3$ . They are described in more detail in the text. Left: Plot showing confidence level low limits  $n_j^{\min}$  in dependence on  $\mu_j$  for one-sided intervals with  $\beta = 0$ . Right: Plot showing confidence level limits  $n_j^{\min}$  and  $n_j^{\max}$  in dependence on  $\mu_j$  for central interval.

The plots represent two different type of belt intervals. Left one, with  $\alpha = 0.1$  (10%) and  $\beta = 0$  represents one-sided belts where only  $n_j^{\min}$  is finite and  $n_j^{\max} = \infty$ . They are generated for case with three expected background counts ( $b = 3$ ). If experiment observes, for instance,  $n = 7$ , it reports confidence interval given by vertical section in value  $n = 7$ , as depicted in Figure 5.5. Experimentalist in the scenario on the left side would report confidence interval of  $\mu = (0, 8.8)$  while the same experiment with the same expected background would report interval  $(0.3, 10.1)$ . Both cases offer interval on a confidence level  $CL = 1 - \alpha - \beta$  of 90%. The difference lies in the choice whether experimentalist prefer to publish only upper limit or central interval. Such a degree of freedom creates ambiguity in reported results. What is even worse, the plots offer empty confidence interval in case if experiment observed zero counts ( $n = 0$ ). The solution which is a triumph of Feldman-Cousins method is in the ordering principle presented in following section.

### 5.3.1 Ordering Principle

Confidence belts in Figure 5.5 represent two possible analyses methods for the same experiment with three background counts. Moreover, if we keep confidence level at the same value of 90% we can shift the belts to the left or right in dependence on  $\alpha$  and  $\beta$ . This becomes clear if we have a look at the Figure 5.4. Imagine that we keep the sum of  $\alpha + \beta$

= 0.1 constant. If we gradually decrease  $\alpha$ , value  $n^{\min}$  would decrease as well.  $\beta$ , however, would be increased, pushing  $n^{\max}$  to lower values.

Choice of  $\alpha$  and  $\beta$  is distinguishing between scenario when central interval or one-sided interval is reported. Nevertheless, it makes sense to expect only upper limit  $\mu_U$  when measured number of counts is less or equal to expected background and central interval otherwise. Such an option is not possible with the method proposed in the latest section. Method which would change  $\alpha$  and  $\beta$  dynamically for different  $\mu_j$  is needed.

Solution how  $n_j^{\min}$  and  $n_j^{\max}$  in Figure 5.4 was found, can be reformulated bit differently. In order to find value  $n^{\max} = 14$  we can say that we had to gradually sum the probabilities  $P(0, 8.56) + P(1, 8.56) + \dots$ , until cumulative sum exceeded value of  $1 - \beta$ . This happened when  $P(14, 8.56)$  was added so we concluded that  $n^{\max} = 14$ . We added values  $P(i, 8.56)$  in well defined order ( $i = 0, 1, 2, \dots$ ). It is example of type of ordering based on which, we accept or reject individual values. Another type of ordering can be observed in the same figure, on the left side, in case when  $n^{\min} = 4$  was calculated. All the probabilities  $P(i, 8.56)$  were added in descending order  $\infty \rightarrow 4$ . Term  $P(4, 8.56)$  caused the sum to exceed 95% ( $1 - \alpha$ ) and, therefore,  $n^{\min} = 4$ .

### 5.3.1.1 Likelihood Ratio Ordering Principle

The ordering principles of ascending / descending order are not the only possibilities. More sophisticated principles can be proposed. Feldman and Cousins proposed likelihood ratio ordering principle as a core of their universal method presented in this section.

The principle is tailored to build the interval from the center by adding terms  $P(i, \mu_j + b)$  to the left and right based on their likelihood ratios  $R$  given by:

$$R = \frac{P(i, \mu_j + b)}{P(i, \mu_j^{\text{best}} + b)}. \quad (5.20)$$

Here,  $\mu_j^{\text{best}}$  is a value which maximizes  $P(i, \mu_j + b)$  for given  $i$  and  $b$ . Method of likelihood ratio ordering, adds the terms  $P(i, \mu_j + b)$  with highest likelihood ratio into cumulative sum. The method gives priority to values of  $P(i, \mu_j + b)$  as close as possible to the most probable value  $\mu_j^{\text{best}}$ .

It is easiest to demonstrate the principle with an example. In order to obtain a direct comparison with Figure 5.4, I will assume construction of interval given by  $\mu_j + b = 8.56$ . While the calculation of case (descending / ascending order) presented in the figure did not rely on the value of  $b$  (only on  $\mu_j + b$ ), we did not have to precise it. However, in case of likelihood ratio ordering the result depends on both  $\mu_j$  and  $b$ . In the following, I will assume expected background of three counts,  $b = 3$ . I will present example of case  $\mu_5 = 0.5$  (I skipped  $\mu_0 = 0, \mu_1 = 0.1, \dots, \mu_4 = 0.4$ ).

Detailed clarification of such calculation is displayed in Table 5.1. Each row represents one value of total counts observed by experiment. Second column displays Poisson probability of obtaining  $n$  counts if  $\mu_5 + b$  are expected. Following column shows  $\mu_5^{\text{best}}$  which is a value of  $\mu$  which maximizes  $P(n, \mu + b)$  for given  $n$  and  $b$ . This value cannot be negative. In following column  $P(n, \mu_5^{\text{best}} + b)$  is calculated. Fifth column holds value of likelihood ratio  $R$  given in Equation 5.20. Finally, last column displays order of descending value of  $R$ . The order in which values  $P(n, \mu_5 + b)$  are added to cumulative sum is great demonstration of the method of likelihood ratios. First term added to the sum is  $n = 4$  followed by  $n = 3, 2, 5, 1, 0$  and 6. Their cumulative sum is equal to 0.935 and it just enough terms to exceed value of 0.9 which is 90% CL. On this confidence level, therefore, we calculated that for  $\mu_5 = 0.5$  ( $b$



$\mu_5 = 0.5, b = 3$					
<b>n</b>	<b>P(n, <math>\mu_5+b</math>)</b>	<b><math>\mu_5^{best}</math></b>	<b>P(n, <math>\mu_5^{best}+b</math>)</b>	<b>R</b>	<b>Order</b>
0	0.030	0	0.050	0.607	6
1	0.106	0	0.149	0.708	5
2	0.185	0	0.224	0.826	3
3	0.216	0	0.224	0.963	2
4	0.189	1	0.195	0.966	1
5	0.132	2	0.175	0.753	4
6	0.077	3	0.161	0.480	7
7	0.039	4	0.149	0.259	8
8	0.017	5	0.140	0.121	9
9	0.007	6	0.132	0.050	
10	0.002	7	0.125	0.018	
11	0.001	8	0.119	0.006	

Table 5.1: Example of calculation of confidence belt for experiment which expects 3 background counts. The calculation is performed for  $\mu_5 = 0.5$ . More information about the calculation and content of the table is provided in text.

= 3),  $n_5^{\min} = 0$  and  $n_5^{\max} = 6$ . If we added following term in order ( $n = 7$ ) cumulative sum would reach 0.973, exceeding also 0.95 (95%), in such scenario,  $n_5^{\min} = 0$  and  $n_5^{\max} = 7$ . By addition of yet another term ( $n = 8$ ) sum reaches 0.99 which results into  $n_5^{\min} = 0$  and  $n_5^{\max} = 8$  at 99% confidence level.

Method of likelihood ratio ordering builds confidence belts from center and expands it to the left and right simultaneously. Note that, the algorithm might lead into intervals when some value in the middle is not included in the cumulative sum while reaching wanted CL. In such case conservative approach should be chosen and the missing value should be included also to achieve continuous interval.

I performed calculation such as the one presented in Table 5.1 for many different values of  $0 \leq \mu_j \leq 15$  with step  $\Delta\mu = \mu_{j+1} - \mu_j = 0.01$ . The resulting intervals ( $n_j^{\min}, n_j^{\max}$ ) I represented in form of confidence belts similar to Figure 5.5. The result for 90% and 95% can be found in Figure 5.6.

As the value of  $\mu$  is rising, we can notice that interval ( $n_j^{\min}, n_j^{\max}$ ) changes from one-sided regime ( $n_j^{\min} = 0$ ) into central interval regime ( $n_j^{\min} \neq 0$ ). Vertical cross section in given value  $n$ , bounded from the bottom by blue curve ( $\mu_L$ ) and from top by red curve ( $\mu_U$ ), represent confidence intervals reported by experiment. Confidence intervals ( $\mu_L, \mu_U$ ) for experiment which observed  $n = 0$  were empty in Figure 5.5. This was due to the ordering method used to produce confidence belts. Such a behaviour is not present in case of likelihood ratio ordering as can be seen in Figure 5.6. This is a triumph of likelihood ratio method. Moreover, the method also automatically generates one sided confidence interval ( $0, \mu_U$ ) or central interval ( $\mu_L, \mu_U$ ), depending on how significant the number of observed counts is relatively to the background.

### 5.3.1.2 Numerical Artefacts

Confidence belts, like those presented in Figure 5.6 can be produced for any value of background  $b$ . For given number of observed events  $n$ , we can extract confidence interval ( $\mu_L, \mu_U$ ) as a function of expected background  $b$ .

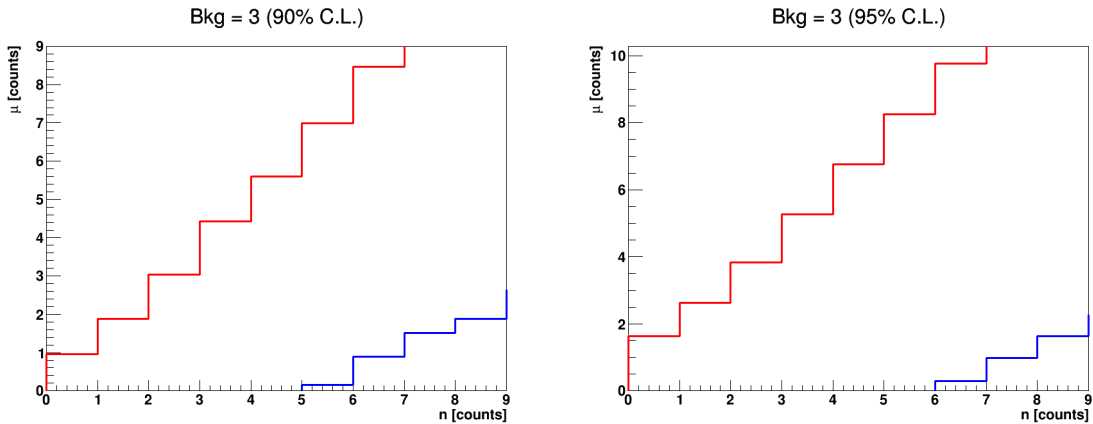


Figure 5.6: Results from my own implementation of Feldman-Cousins recipe. Plots represent example of confidence belts generated for 90% CL (left) and 95% CL (right) for experiment which expects 3 background counts. Likelihood ratio ordering method was implemented. In comparison to Figure 5.5 likelihood ratio method provides non-empty confidence interval for experiment observing zero counts.

Figure 5.7 shows how upper limit  $\mu_U$  of confidence interval (90% CL) changes with increasing expected background  $b$  for  $n = 0, 2, 4$ . Black dashed line represents calculation based on the previously presented method of likelihood ratio ordering. Limit tends to be improved (lower) with higher expected background. However, the functions in the plot are not perfectly smooth. They contain sharp local peaks where functional value grows a little and then continue decreasing again. These are effects caused by discreteness of Poisson distribution. In order to obtain nicely smooth, never increasing function, we need to apply a correction. The values in the regions between two peaks are set to a value of next peak in order to flatten the curve. The curves after the application of correction are presented as solid red lines. Proposed correction is something what we can afford to do, as it overestimates the upper limit of confidence interval, setting it to more conservative value. Such a correction were applied in my simulations presented in following text.

### 5.3.2 Experiments with no Discovery

Method of likelihood ratio ordering proved itself to be effective, preventing the appearance of empty confidence intervals. The method relaxes the requirement to choose  $\alpha$  and  $\beta$  thresholds from method with ascending / descending ordering. One only needs to choose CL and perform the calculation.

In this section, I am interested in experiments which did not observe the process of interest and cannot claim the discovery. Such an experiment observes less or equal number of counts than the expected background,  $n \leq b$ . With a method of likelihood ratio ordering, such experiment is always capable to report upper limit  $\mu_U$ . Thanks to the Equation 5.17 the limit can be transformed into low limit on a half-life. Figure 5.6 implies that, the lower the number of counts  $n$  observed by experiment is under the expected background, the better upper limit  $\mu_U$  experiment is able to report. Experiment with higher expected background would report better limit than experiment with lower background if both experiments measured same number of counts. This is an unwanted anomaly already discussed to arise in classical method.

Experiment expecting 4 background counts during given period of time has a 19.5%

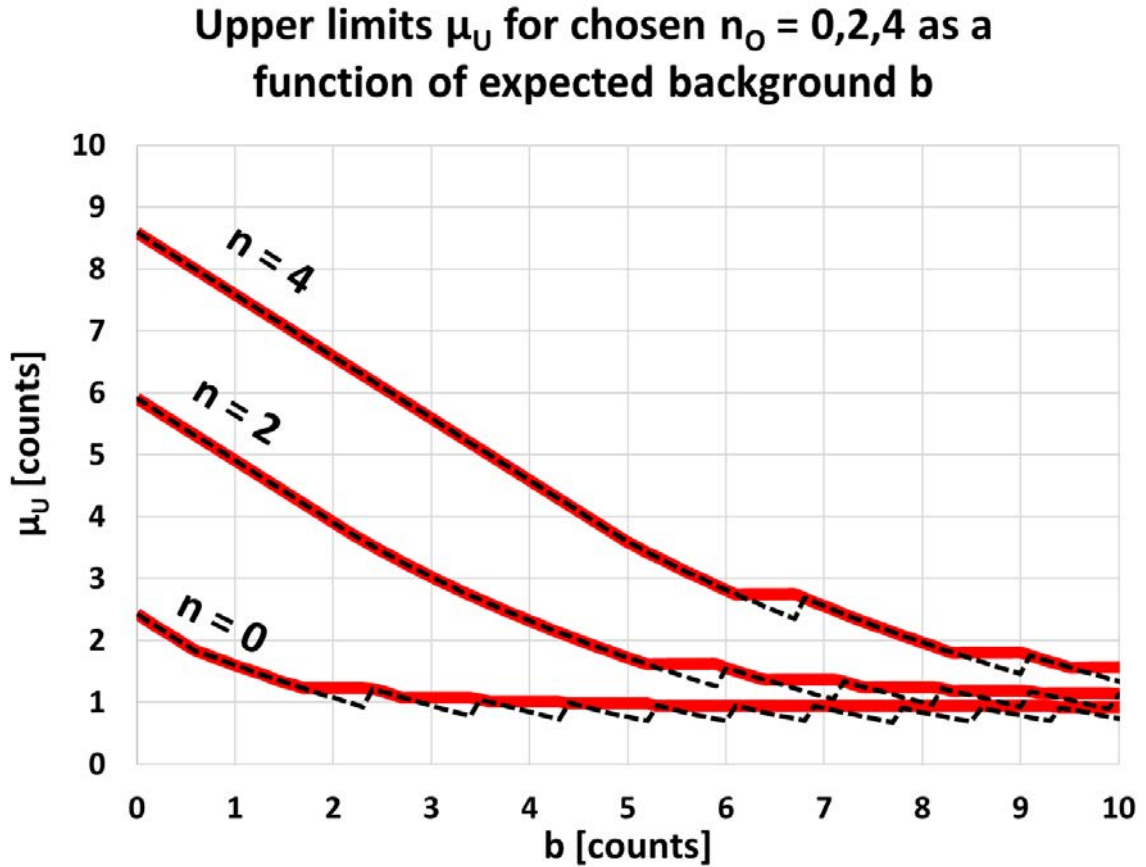


Figure 5.7: Plots of upper limits  $\mu_U$  as a function of background expected by experiment. Plot is constructed for experiments observing  $n = 0, 2$  or  $4$  total counts. Calculation represents 90% CL. Dashed black lines show calculation with no correction obtained by application of likelihood ratio ordering method to Feldman-Cousins recipe. Red solid lines are same results after correction was applied in order to prevent intervals where function increases.

chance to observe four counts assuming no other source of counts,  $P(4,4) = 0.195$ . It also has a probability of 19.5% to observe 3 counts,  $P(3,4) = 0.195$ , 14.7% to observe 2 counts,  $P(2,4) = 0.147$ , etc.. To some extent, number of events which experiment detects, is partially random, only governed by Poisson distribution. We need a method which assigns unique value of upper limit  $\mu_U$  to experiments with no discovery only based on the expected background  $b$ , regardless of number of counts it has detected. Solution is, to report a mean value of all upper limits over all experiments with the same expected background and different detected counts. The value is calculated as follows:

$$\mu_U = \sum_{n=0}^{\infty} P(n, b) U(n, b). \quad (5.21)$$

Here,  $U(n, b)$  is an upper limit which experiment would report based on the likelihood ratio ordering method if it observed  $n$  events and expected background  $b$  (for given CL). Such a limit is weighted by probability  $P(n, b)$ , that the experiment measures  $n$  counts if only background is present.

Such a calculation method ensures that the experiments with better background suppression but no discovery, would be able to publish better limit than the one with more background.

Feldman-Cousins method presented above is standard frequentist method used to evaluate exclusion regions for half-life of undiscovered processes. The upper value  $\mu_U$  calculated by method presented in this chapter and represented by Equation 5.21 can be plugged into Equation 5.17 and provide a lower limit on half life of the undiscovered process. If real half-life of the sought (existing) process is lower than this limit, the experiment should be able to observe it. In following section, I applied the method to estimate expected limit achievable by SuperNEMO experiment to  $0\nu\beta\beta$  with Majoron emission.

## 5.4 Calculation of Half-Life Limits

In the first part of the chapter, I extensively described, all the ingredients needed for calculation of half-life limit of rare processes.

First of all, it is important to study energy spectrum of processes of interest ( $0\nu\beta\beta$  decay channels with emission of Majoron ( $0\nu\beta\beta\chi^0$  and  $0\nu\beta\beta\chi^0\chi^0$ ) along with their backgrounds, in order to find regions of interest (ROI) where one would have the best chance to observe the decay. Subsequently, I will apply the previously presented recipe of Feldman and Cousins to estimate sensitivity of SuperNEMO experiments to  $0\nu\beta\beta\chi^0$  and  $0\nu\beta\beta\chi^0\chi^0$ . The sensitivity will be studied for two different CL as a function of background activities of  $^{208}\text{Tl}$  and  $^{214}\text{Bi}$ .

### 5.4.1 Calculation of Detection Efficiencies $\varepsilon$

Among other parameters, Equation 5.17 includes detection efficiency  $\varepsilon$ . Parameter  $\varepsilon$  expresses a fraction of all events of a particular process which were successfully detected and reconstructed and which passed all the eventual data cuts. The parameter can naturally be obtained only from a simulation. Simulation is performed for  $N$  events of every single process (for example  $2\nu\beta\beta$ ) with application of all the detection imperfection (e.g. energy resolution, track reconstruction, etc.) and data cuts of interest. Only  $N_p$  events pass the requirements of data cuts. Detection efficiency is then simply the ratio of events which passed over all the events which were simulated:

$$\varepsilon = \frac{N_p}{N}. \quad (5.22)$$

Before I will discuss the sensitivities of SuperNEMO, it is important to extract detection efficiencies. In order to eliminate events of arguable quality, I will always apply so-called Standard Double Beta Decay Reconstruction Criteria (SDBDRC) to accept or reject event. The list of five conditions which event has to meet is following: exactly two calorimeter hits, exactly two associated calorimeter hits (with track), exactly two vertices on foil, exactly two reconstructed particles, exactly two negatively charged particles.

In this study, I consider  $0\nu\beta\beta\chi^0$  and  $0\nu\beta\beta\chi^0\chi^0$  as a signal events. On the other side,  $0\nu\beta\beta$ ,  $2\nu\beta\beta$  or decay of  $^{208}\text{Tl}$  or  $^{214}\text{Bi}$  can mimic the decay and will be considered as major contributors to background. It is important to find a cut (on energy) which favours the signal and suppress the background the most.

Each of these six processes have different shape of energy spectrum. Therefore, by variation of energy cut  $E_{\min} \leq E < E_{\max}$  one can observe the change in ratio of detection efficiencies between signal and background processes.

I established such study by using Falaise 2.0.0 (software specialized for simulations for SuperNEMO). Each of the six samples from Table 5.2 were passed through SDBDRC with extra energy cut accepting only events with energy in interval  $(E_{\min}, E_{\max})$ . I was varying

Samp.	Process	Nucleus	Magnetic field [G]	Number of simulated events
S3	$0\nu\beta^-\beta^-$	$^{82}\text{Se}$	25	$1.04 \times 10^8$
S4	$0\nu\beta^-\beta^-\chi^0$	$^{82}\text{Se}$	25	$1.04 \times 10^8$
S5	$0\nu\beta^-\beta^-\chi^0\chi^0$	$^{82}\text{Se}$	25	$1.038 \times 10^8$
S7	$2\nu\beta^-\beta^-$	$^{82}\text{Se}$	25	$1.04 \times 10^8$
S9	$\beta^-$	$^{208}\text{Tl}$	25	$1.04 \times 10^8$
S10	$\beta^-$	$^{214}\text{Bi}$	25	$1.04 \times 10^8$

Table 5.2: List of simulated samples produced by Falaise 2.0.0 used in the study.

values of  $E_{\min}$  and  $E_{\max}$  from 0 keV to 3500 keV by a step of 100 keV. I combined all the values while keeping  $E_{\min} < E_{\max}$ . For each cut detection efficiency coefficient  $\varepsilon$  was calculated.

Results are presented in Figure 5.8. Energy distributions with peak at the end of the spectrum tend to produce  $\varepsilon$  plots with highest values on top while the ones with peak towards the low energies produce  $\varepsilon$  plots with maximums on the left side. Six presented arrays of  $\varepsilon$  values serve as an input for calculation of signal-to-background ratios in following section.

## 5.4.2 Calculation of Signal-to-Background Ratios

Detection efficiencies  $\varepsilon$  give us very important information about capabilities of energy cut to suppress background and favour signal. Nevertheless, in order to find out what will be the real ratio between signal counts and background counts this is not yet full information. For a given process, number of observed counts, for an exposure  $am_s t$ , depends not only on  $\varepsilon$  but also on a half life  $T_{1/2}$  of the process. This becomes clear if we invert Equation 5.10:

$$n = \ln(2) \frac{N_A}{W} \varepsilon \frac{am_s t}{T_{1/2}}. \quad (5.23)$$

This formula I used for estimation of expected background counts originating from  $0\nu\beta\beta$  and  $2\nu\beta\beta$  of  $^{82}\text{Se}$ . Half life of  $2\nu\beta\beta$  is already observed process and its half life is known. The one I used was  $T_{1/2}^{2\nu} = 0.92 \times 10^{20}$  yr [108]. In case of  $0\nu\beta\beta$ , only lower limit is available, so I used value of  $T_{1/2}^{0\nu} = 2.4 \times 10^{24}$  yr published in [109]. Furthermore, isotopical mass of  $^{82}\text{Se}$  is  $W = 81.92$  g/mol. Exposure  $am_s t$  was variable and is discussed later.

In case of  $^{208}\text{Tl}$  and  $^{214}\text{Bi}$  decays, the approach is bit different. These two processes are standard backgrounds for observation of  $0\nu\beta\beta$ . These isotopes can be found directly in source foil and, therefore, it is important to suppress their presence. The radiopurity of material is expressed typically in terms of activity (A) per kilogram of source foil. The total observed counts from such decay (assuming that the activity does not change with time) can be calculated following way:

$$n = \varepsilon A am_s t. \quad (5.24)$$

Goal of SuperNEMO is to keep the activities of  $^{208}\text{Tl}$  and  $^{214}\text{Bi}$  below  $2 \mu\text{Bq/kg}$  and  $10 \mu\text{Bq/kg}$ , respectively. In order to discuss the contribution of  $^{208}\text{Tl}$  and  $^{214}\text{Bi}$  on choice of ROI with the best signal-to-background ratio, I performed studies of 4 (extreme) scenarios when activities  $A_{\text{Tl}}$  and  $A_{\text{Bi}}$  had all possible combinations of values 0 and  $300 \mu\text{Bq/kg}$ .

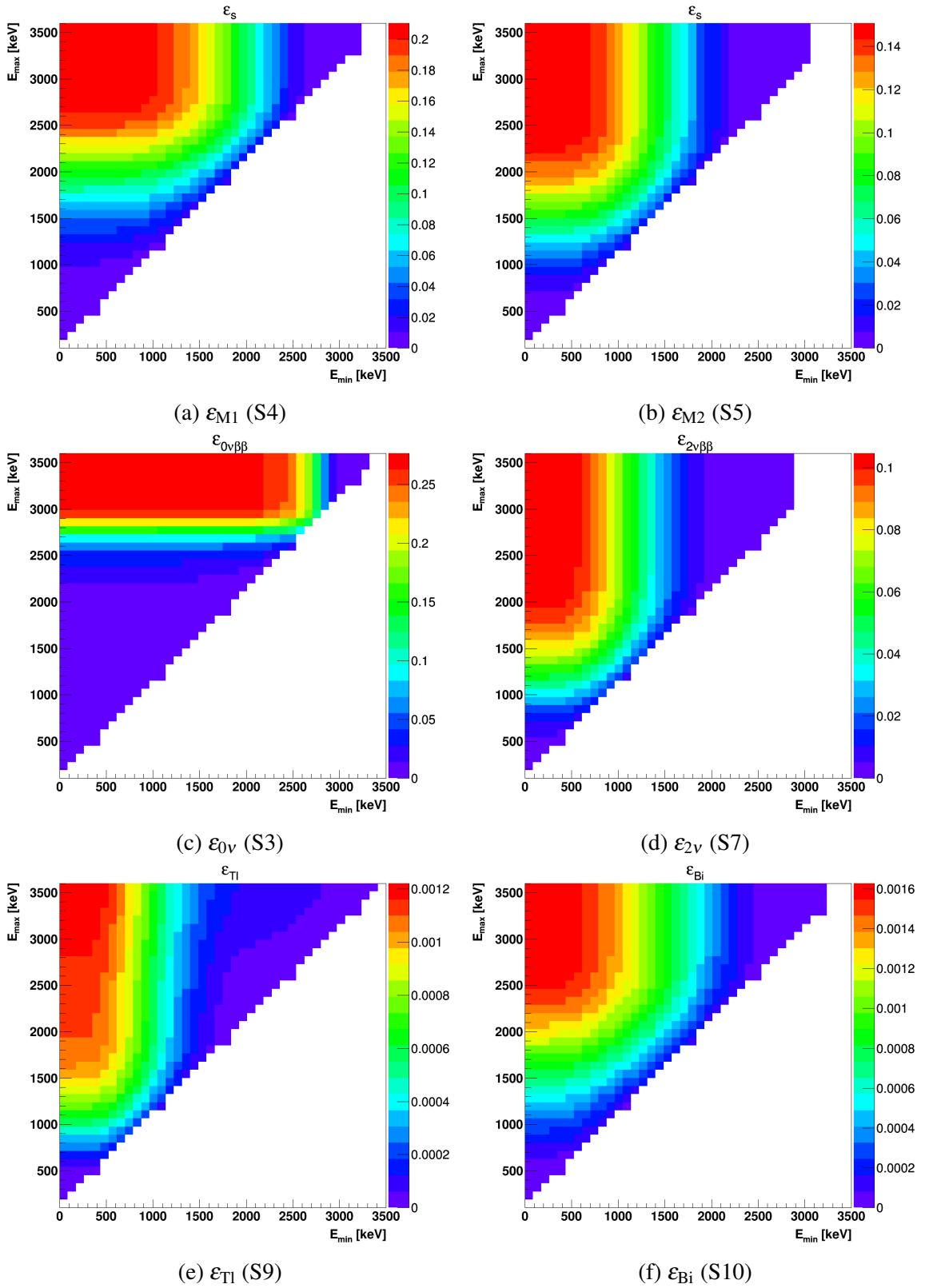


Figure 5.8: Detection efficiencies of six processes for different energy intervals obtained by simulation.

Calculation of background counts is simple summation through all the sources, i.e.  $2\nu\beta\beta$ ,  $0\nu\beta\beta$  and decays of  $^{208}\text{Tl}$  and  $^{214}\text{Bi}$ . If we want to evaluate ratio of signal and background counts we need to provide also number of counts produced by  $0\nu\beta\beta\chi^0$  ( $0\nu\beta\beta\chi^0\chi^0$ ). One of the possibilities would be, to take advantage of half-life limit given for both processes. However, this is not necessary. In the analysis, we need to find the most suitable energy ROI which would maximize the signal to background ratio  $r$ . We need to compare  $r$  for different scenarios, however, we are not interested in its value in absolute terms. The half life of the signal process does not make a difference in the study. Therefore, I decided to express the number of counts in terms of Equation 5.24. The frequency of occurrence of both decay channels  $0\nu\beta\beta\chi^0$  and  $0\nu\beta\beta\chi^0\chi^0$  I express via activities  $A_1 = A_2 = 1000 \mu\text{Bq/kg}$ . Such a choice was made for esthetical reasons, in order to obtain signal-to-background ratios in units, tens or larger orders of magnitude.

Finally, if we combine all the signal and background counts expressed via Equations 5.23 and 5.24 into signal-to-background ratio  $r$ , we obtain:

$$r = \frac{\varepsilon_i A_i}{\ln(2) \frac{N_A}{W} \left( \frac{\varepsilon_{2\nu}}{T_{1/2}^{2\nu}} + \frac{\varepsilon_{0\nu}}{T_{1/2}^{0\nu}} \right) + \varepsilon_{\text{Tl}} A_{\text{Tl}} + \varepsilon_{\text{Bi}} A_{\text{Bi}}}. \quad (5.25)$$

Numerator stands for number of counts of  $0\nu\beta\beta\chi^0$  ( $i = 1$ ) or  $0\nu\beta\beta\chi^0\chi^0$  ( $i = 2$ ) depending on which of the two we are studying at the moment. Denominator combines all four sources of background. All the detection efficiencies  $\varepsilon$  depend on chosen energy cut and is provided by results in Figure 5.8.

Similarly to detection efficiencies, the signal-to-background ratio is changing as a function of chosen ROI and can be represented in form of plots similar to Figure 5.8. Figures 5.9a - 5.9d represent distributions of signal-to-background ratios for  $0\nu\beta\beta\chi^0$  process for four different constellations of activities  $A_{\text{Tl}}$  and  $A_{\text{Bi}}$ . Constellation, without Bi and Tl backgrounds ( $A_{\text{Tl}} = A_{\text{Bi}} = 0 \mu\text{Bq/kg}$ ) in Figure 5.9a shows how  $2\nu\beta\beta$  and  $0\nu\beta\beta$  contribute to the distribution of signal-to-ratio plots for different ROI. Other three plots are scenarios when at least Tl or Bi background is present. The change in shape is negligible, which implies that either  $2\nu\beta\beta$  or  $0\nu\beta\beta$  is a major contribution for background for  $0\nu\beta\beta\chi^0$ . The situation is clarified in Figure 5.9e. It contains spectra of  $0\nu\beta\beta\chi^0$  in comparison to all relevant backgrounds in SuperNEMO after experiment would run for half a year observing 7 kg of  $^{82}\text{Se}$ . The spectrum assumes scenario of  $A_{\text{Tl}} = A_{\text{Bi}} = 300 \mu\text{Bq/kg}$ . Red dashed line represent sum of all backgrounds while blue dashed line the spectrum of  $0\nu\beta\beta\chi^0$ . It is obvious, that in energies below 2500 keV  $2\nu\beta\beta$  is hugely dominating. Above this value, in region of signal's peak,  $2\nu\beta\beta$  spectrum dramatically drops and we can observe contributions of roughly the same order of magnitude from  $0\nu\beta\beta$ , Bi and Tl. Nevertheless, activity values of Bi and Tl are very extreme, exceeding the SuperNEMO design values tens, up to hundred of times. In standard situation, therefore, the most important background contribution around peak of  $0\nu\beta\beta\chi^0$  comes from  $0\nu\beta\beta$ . Regardless of the activities of Tl or Bi the ROI in all scenarios is interval (2600 keV, 2700 keV). This is the interval with the highest chance to observe the decay if it exist.

Analogical signal-to-background ratio plots but for  $0\nu\beta\beta\chi^0\chi^0$  can be found in Figures 5.10a - 5.10d. Background scenarios remained exactly the same. It is possible to notice roughly forty-fold drop in  $r$  in the hot spots (peak value) in comparison to scenarios with  $0\nu\beta\beta\chi^0$ . The reason is clear, if we compare Figure 5.9e with 5.10e. Background spectra in both plots are generated under exactly the same conditions ( $A_{\text{Tl}} = A_{\text{Bi}} = 300 \mu\text{Bq/kg}$ ,  $t = 0.5 \text{ yr}$ , exposure 7 kg), however, the shape of the signal (blue dashed line) changed. Peak of

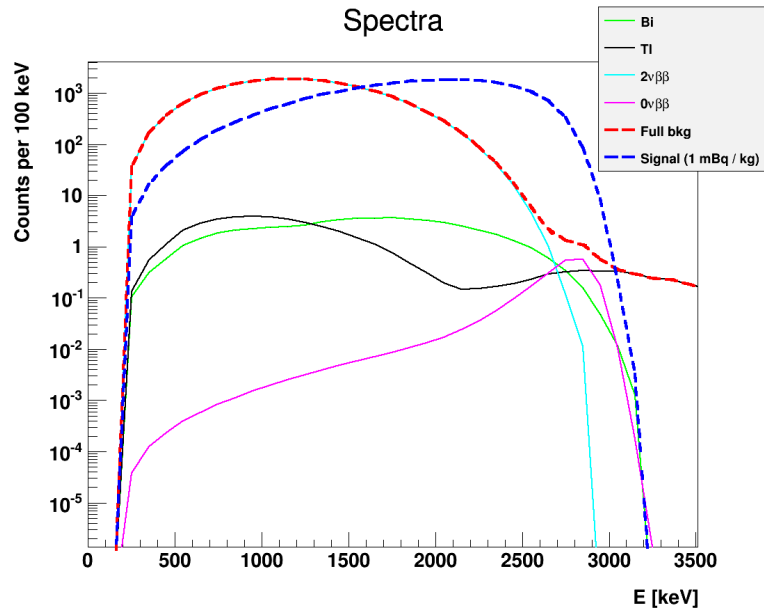
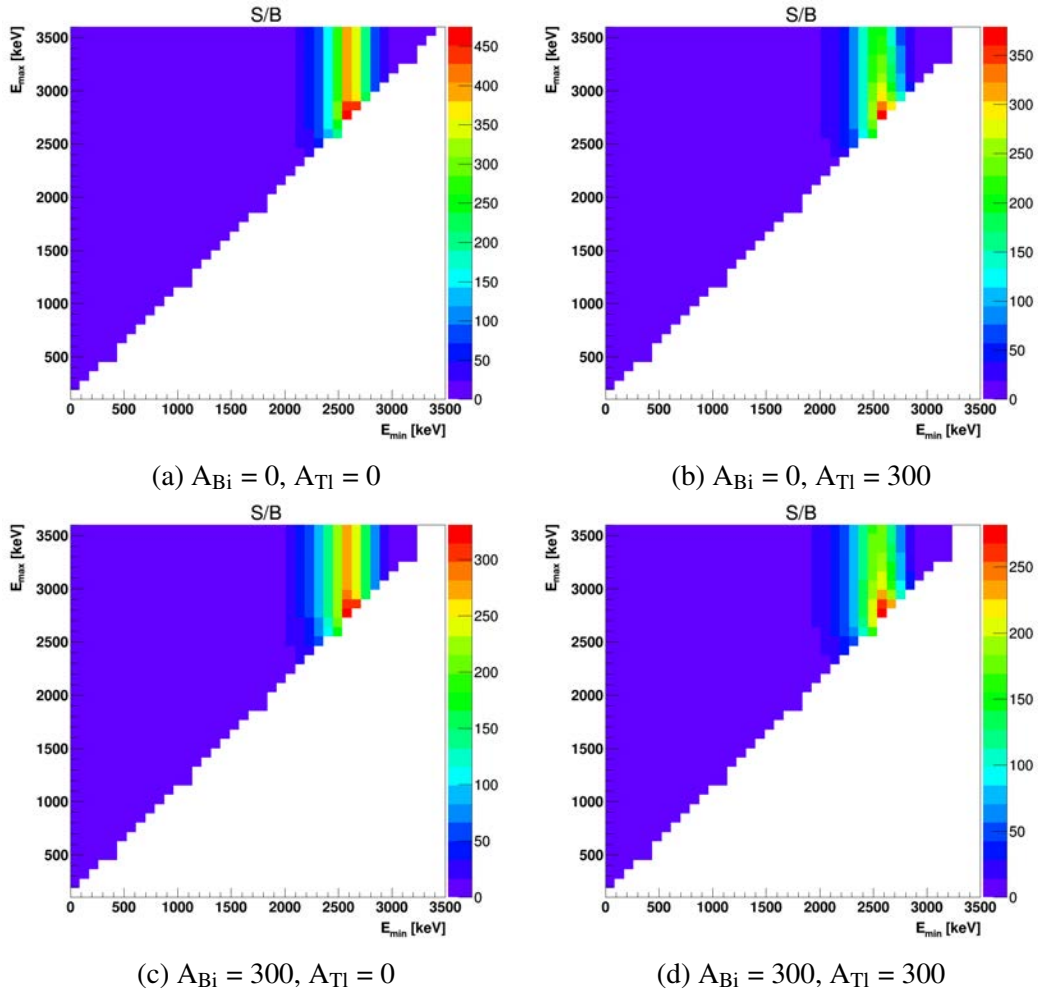


Figure 5.9: Expected signal ( $0\nu\beta\beta\chi^0$ ) to background ratio (a-d) as a function of chosen energy interval. Figure e) represents a energy spectra of  $0\nu\beta\beta\chi^0$  and all the background processes. Red dashed line represents sum of all background contributions while blue dashed line represents spectrum of  $0\nu\beta\beta\chi^0$ . Spectrum generated for exposure of 3.5 kg·yr.  $A_{Tl}$  and  $A_{Bi}$  in captions are expressed in  $\mu\text{Bq/kg}$ .



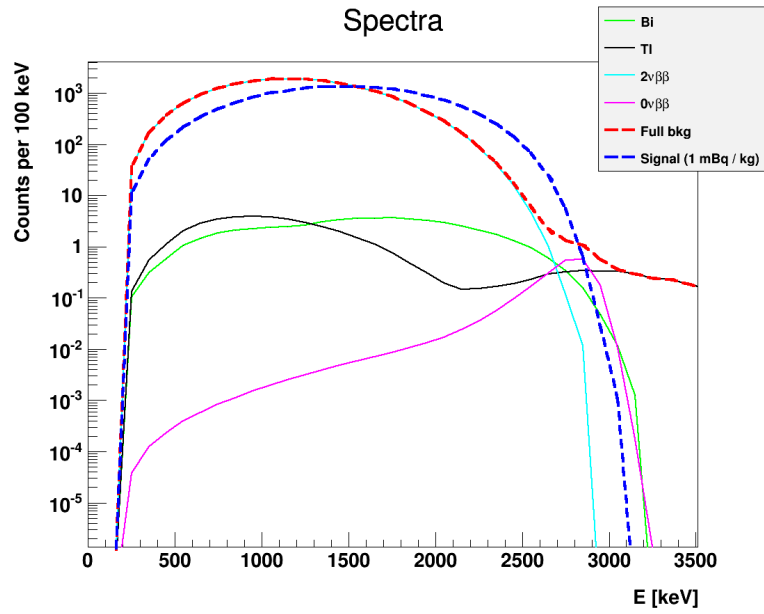
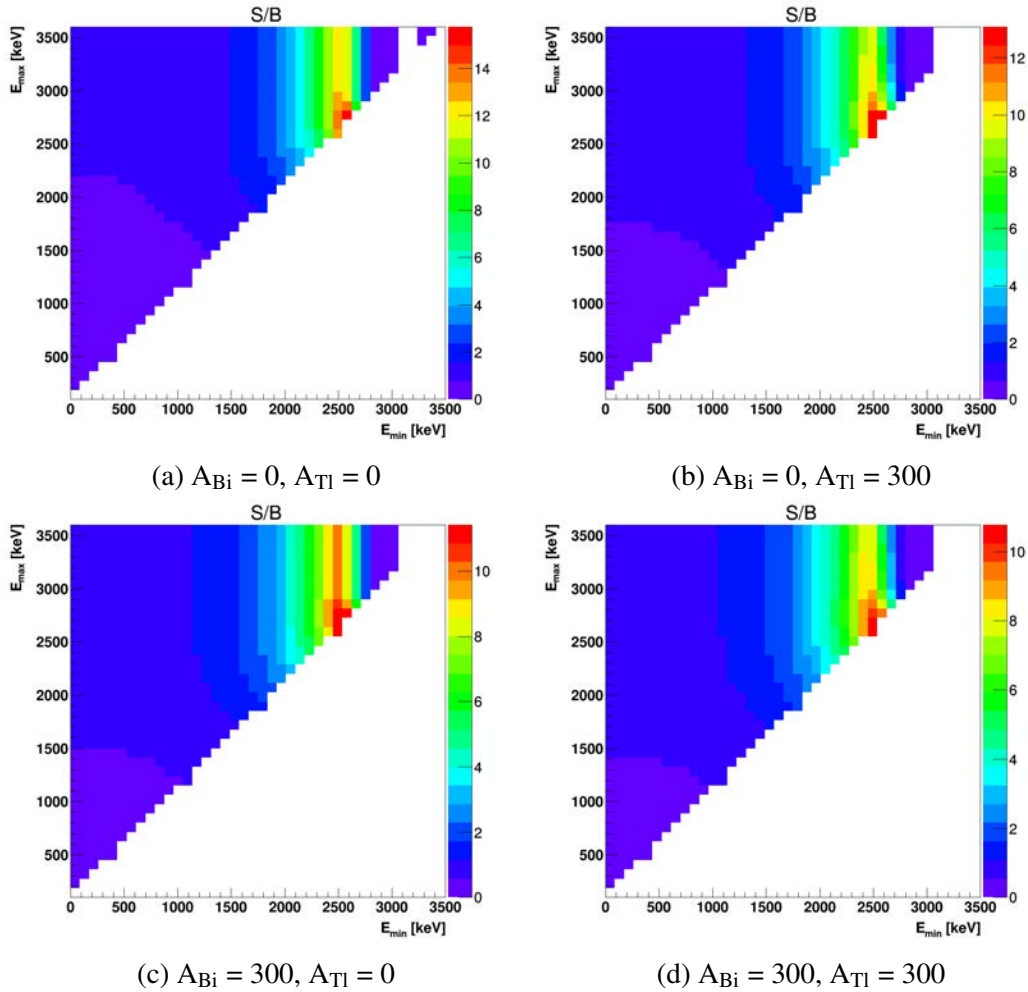


Figure 5.10: Expected signal ( $0\nu\beta\beta\chi^0\chi^0$ ) to background ratio (a-d) as a function of chosen energy interval. Figure e) represents a energy spectra of  $0\nu\beta\beta\chi^0\chi^0$  and all the background processes. Red dashed line represents sum of all background contributions while blue dashed line represents spectrum of  $0\nu\beta\beta\chi^0\chi^0$ . Spectrum generated for exposure of 3.5 kg·yr.  $A_{Tl}$  and  $A_{Bi}$  in captions are expressed in  $\mu\text{Bq/kg}$ .

spectrum of  $0\nu\beta\beta\chi^0\chi^0$  is shifted to the lower energies relatively to  $0\nu\beta\beta\chi^0$ . This region is strongly dominated by spectrum  $2\nu\beta\beta$  causing dramatic drop in signal-to-background ratio. It is much more difficult to distinguish  $0\nu\beta\beta\chi^0\chi^0$  from  $2\nu\beta\beta$  than it was in case of  $0\nu\beta\beta\chi^0$ . We should, therefore, expect much lower sensitivity values for  $0\nu\beta\beta\chi^0\chi^0$  than for  $0\nu\beta\beta\chi^0$ . ROI with best signal-to-background ratio and, therefore, the best region to search for the decay was, similarly to  $0\nu\beta\beta\chi^0$ , computed as (2600 keV, 2700 keV).

### 5.4.3 Sensitivity Results

Signal-to-background ratio plots presented in previous section are crucial inputs in order to find the energy cut with the best chance for observation of  $0\nu\beta\beta\chi^0$  or  $0\nu\beta\beta\chi^0\chi^0$ . The ROIs extracted in previous section are useful, if we obtain significant signal over the background. Such an ROI would give the observation of highest significance. In case when discovery could not be claimed, it is important to set lower limit on the decay's half-life. The best possible limit experiment can provide, however, does not necessarily have to be extracted from ROI with best signal-to-background ratio.

In what follows, I will, finally, employ previously discussed Feldman-Cousins recipe in order to compute half-life limits of SuperNEMO with respect to these two processes.

The recipe takes number of expected background counts  $b$  as an input. Four contributions to  $0\nu\beta\beta\chi^0$  and  $0\nu\beta\beta\chi^0\chi^0$  backgrounds discussed previously produce total counts which can be calculated by following equation:

$$b = am_s t \left[ \ln(2) \frac{N_A}{W} \left( \frac{\varepsilon_{2\nu}}{T_{1/2}^{2\nu}} + \frac{\varepsilon_{0\nu}}{T_{1/2}^{0\nu}} \right) + \varepsilon_{Tl} A_{Tl} + \varepsilon_{Bi} A_{Bi} \right]. \quad (5.26)$$

Here, set of four  $\varepsilon$  values (detection efficiencies) are again taken from result in Figure 5.8. Half-lives of  $2\nu\beta\beta$  and  $0\nu\beta\beta$  were set to values of  $T_{1/2}^{2\nu} = 0.92 \times 10^{20}$  yr [108] and  $T_{1/2}^{0\nu} = 2.4 \times 10^{24}$  yr [109], as discussed in previous section. In all the performed calculations, the mass of the pure  $^{82}\text{Se}$  in Selenium foils was set to  $m = 7$  kg.

Number of background counts is the only input for Feldman-Cousins recipe. For each value of expected background one obtains upper values of expected signal counts  $\mu_U$ . Relationship of expected background counts and limit given by the recipe can be found in Figure 5.11.

Green and purple dots represent the values which I obtained after I implemented the recipe for 90% and 95 % CL, respectively. I performed calculations for range of (non-equidistant) values up to  $b = 276.6$ . Under 276.6, each upper limit was extracted by interpolation between two closest calculated values. For values higher than  $b = 276.6$ , I extrapolated the function by using:

$$\mu_U = \alpha \sqrt{b}. \quad (5.27)$$

For 90% CL, I used function where  $\alpha = 1.81$  and for 95% CL, I used function where  $\alpha = 2.13$ . The two extrapolation functions are also shown in Figure 5.11 as red and yellow dashed lines. We can observe that in the region  $b = (120, 276.6)$  these extrapolation functions overlap very precisely with the values obtained by Feldman-Cousins calculation. Furthermore, the choice of extrapolation was not based only on the similarity with performed calculated green and purple functions. For given number of background counts, the statistical fluctuations can be described by Poisson distribution. However, as we reach higher values, the distribution starts to resemble Gaussian bell. Expected fluctuations of background on a level of one standard deviation is simply given by  $\sqrt{b}$  in such case. This represents notoriously known

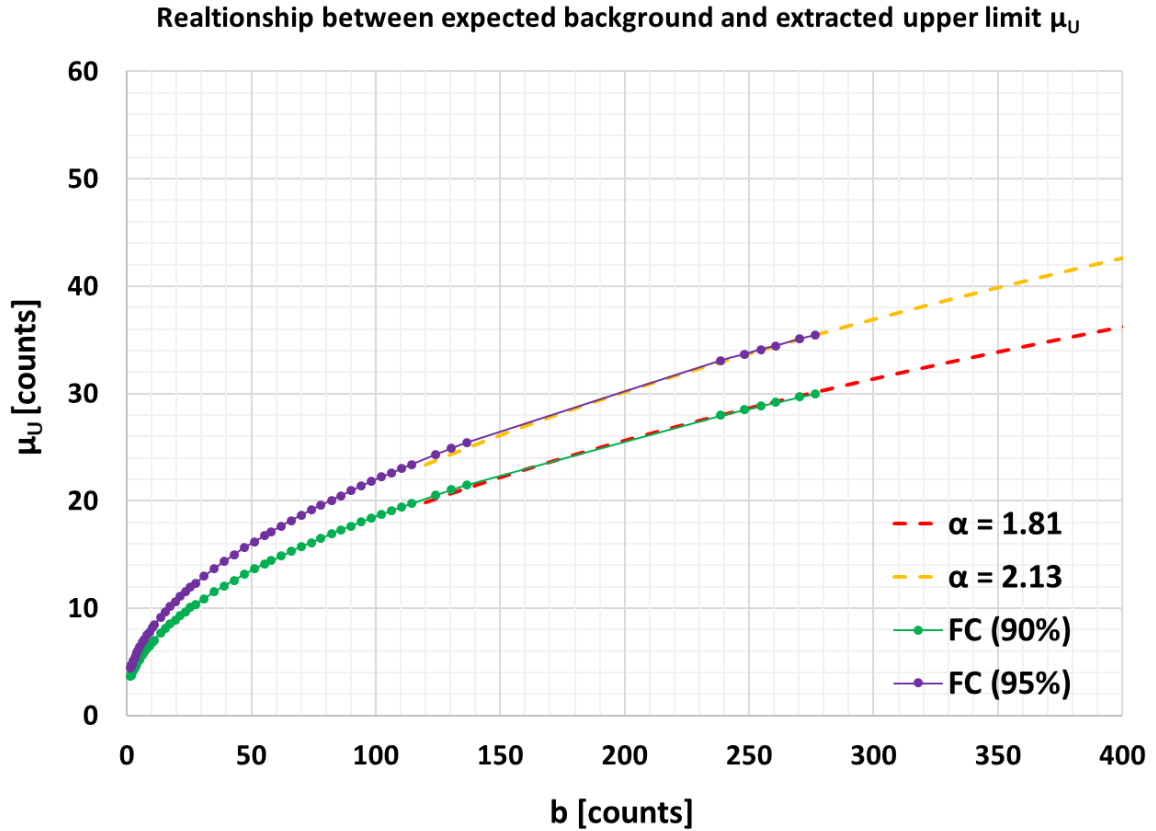


Figure 5.11: Plot showing relationship between expected number of background counts and upper limit on signal counts resulting from two different approaches. The details are commented in the text.

CL of 68.27%. For 90% CL we need 1.64 standard deviations (i.e.  $1.64\sqrt{b}$ ) and for 95% CL we need 1.96 standard deviations ( $1.96\sqrt{b}$ ). Such an approach to calculation of half-life limit was already presented in Equation 1.24 without further discussion.

I can conclude, that my extrapolation curves follow this trend. Instead of obtaining  $\alpha = 1.64$  for 90% CL and  $\alpha = 1.96$  for 95% CL, I received little higher factors of  $\alpha = 1.81$  and  $\alpha = 2.13$ , respectively. This is not a fault, it is acceptable result, coming from conservatism introduced in several steps of the Feldman-Cousins recipe. Obtained limit is slightly overestimated, which result into little lower half-life limits. It is an acceptable effect.

After the number of background counts was calculated, functions from Figure 5.11 were used to extract the limit. Last necessary input for the calculation were the Tl and Bi activities. Studies were performed for various scenarios of different Tl and Bi activities and lengths of measurement. These values are explicitly noted in each plot. Background spectrum for both studied processes with Majoron(s) is mainly dominated by  $2\nu\beta\beta$ . In order to observe effect of presence of Tl and Bi, several scenarios were studied. The most extreme cases assumed up to 20 times higher Bi activity and 50 times higher Tl activity in comparison to design goal of SuperNEMO ( $A_{Tl} < 2 \mu\text{Bq/kg}$ ,  $A_{Bi} < 10 \mu\text{Bq/kg}$ ).

Half-life limit was always computed based on  $\mu_U$  extracted from plot in Figure 5.11. Afterwards,  $\mu_U$  was plugged into Equation 5.17. The limit was obtained for same set of  $\text{ROI}^2$  as it was previously performed with detection efficiencies  $\epsilon$ . In each case, the result

<sup>2</sup>It was combination of all different possible lower and upper boundaries on interval 0 keV - 3600 keV with step of 100 keV.

from ROI with the highest limit was chosen and plotted. Results were produced for both 90% and 95% CL using my own code fully implementing every detail of the calculation.

Figures 5.12 represent half-life limits achievable for  $0\nu\beta\beta\chi^0$  after 0.5, 1, 2, 5, 10 or 15 years. Plots are showing the decrease of achievable limit with raising activity of Bi. Red scenario always represent situation with no background from Tl and green one with  $A_{Tl} = 100 \mu\text{Bq/kg}$  (50 times larger than expected in SuperNEMO).

Sensitivity to  $0\nu\beta\beta\chi^0$  starts at a level of  $5.67 \times 10^{22}$  yr (90% CL) for an extreme case scenario  $A_{Tl} = 100 \mu\text{Bq/kg}$   $A_{Bi} = 200 \mu\text{Bq/kg}$  only after a half year of measurement (exposure of 3.5 kg·yr). This value is already almost four times larger than value  $1.5 \times 10^{22}$  yr (90% CL) published by previous NEMO-3 result in [104]. In some of the plots, it is possible to observe non-linear behaviour of the limit as a function of Bi background. This is usually due to change of ROI between two points. ROI containing the highest half-life limit is represented by cell colour in Tables B.1 and B.2 in Appendix B. The tables contain all the values plotted in Figures 5.12.

Figure 5.13a shows potential of improvement of the half-life limit as a function of measurement time for both CL and the most extreme scenarios (background-less and scenario with the most extreme Bi and Tl background). We can observe, that the limit can overpass value of  $10^{23}$  yr (90% CL) in less than 1.5 years which represents almost one order of magnitude improvement in comparison to NEMO-3 result.

While for  $0\nu\beta\beta\chi^0$  six different ROI were offering the best half-life limit in dependence on time of measure CL and activities of Bi and Tl in case of  $0\nu\beta\beta\chi^0\chi^0$  situation was very different. ROI yielding the best half-life limit for this process was always (1000 keV, 2900 keV) due to different spectral shape, shifted to low energies relatively to  $0\nu\beta\beta\chi^0$ . In this ROI, Bi and Tl contamination contributed negligibly (compared to largely dominating  $2\nu\beta\beta$ ) to the background and the resulting limits remained almost unchanged even for extreme values<sup>3</sup> of Bi and Tl contamination. Therefore, the calculation was performed only for one scenario - the scenario assuming the SuperNEMO design contamination limits of  $A_{Bi} = 10 \mu\text{Bq/kg}$  and  $A_{Tl} = 2 \mu\text{Bq/kg}$ .

The results for CL = 90% and CL = 95% are plotted in Figure 5.13b. We can observe that the limit  $3.1 \times 10^{21}$  yr (90% CL) on  $0\nu\beta\beta\chi^0\chi^0$  from [104] obtained by NEMO-3 should be improved even faster than the one for  $0\nu\beta\beta\chi^0$ . In Table B.4 in Appendix B we can find that this limit should be improved after less than 0.1 yr and improved by one order of magnitude after less than 4.5 yr!

Note that, the ideal scenario (no Tl or Bi background), is much closer to expected Tl and Bi activities than any of the other scenarios, as the expected SuperNEMO design activities of Tl and Bi are on the level of  $A_{Tl} < 2 \mu\text{Bq/kg}$ ,  $A_{Bi} < 10 \mu\text{Bq/kg}$ . The ideal scenario can be, therefore, considered with a good approximation as a reliable estimation. However, in both cases also the realistic scenarios are computed as well.

## 5.5 Conclusions

The goal of chapter was to discuss the methodology of half life limit calculations for rare processes and to apply them in order to estimate expected sensitivities which could be reached by SuperNEMO for  $0\nu\beta\beta\chi^0$  and  $0\nu\beta\beta\chi^0\chi^0$ .

The construction of classical confidence intervals was discussed. As the method collapses for experiments with expected non-zero background, Feldman-Cousins method was

<sup>3</sup>Hundreds of times higher than SuperNEMO design values.

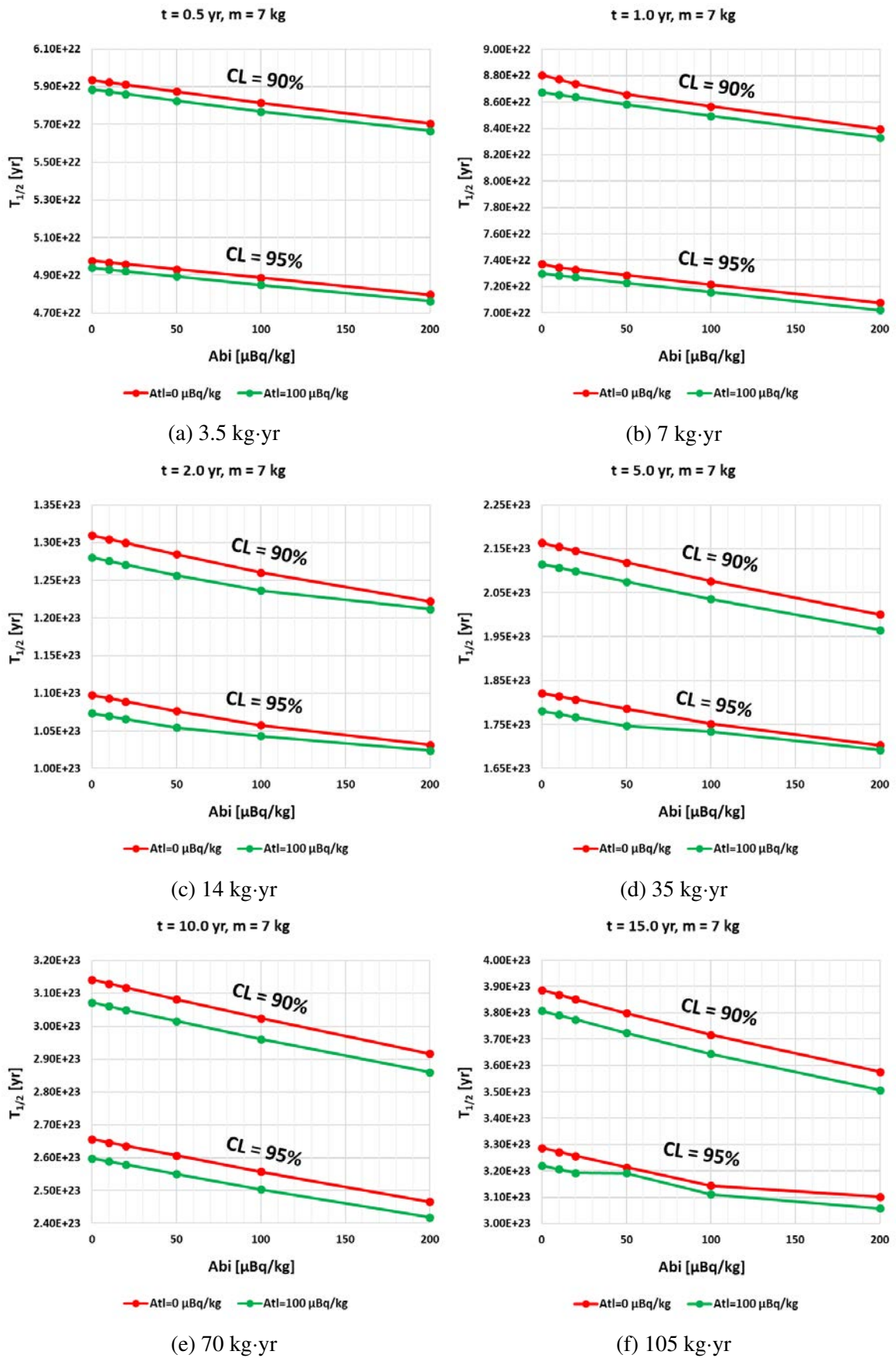
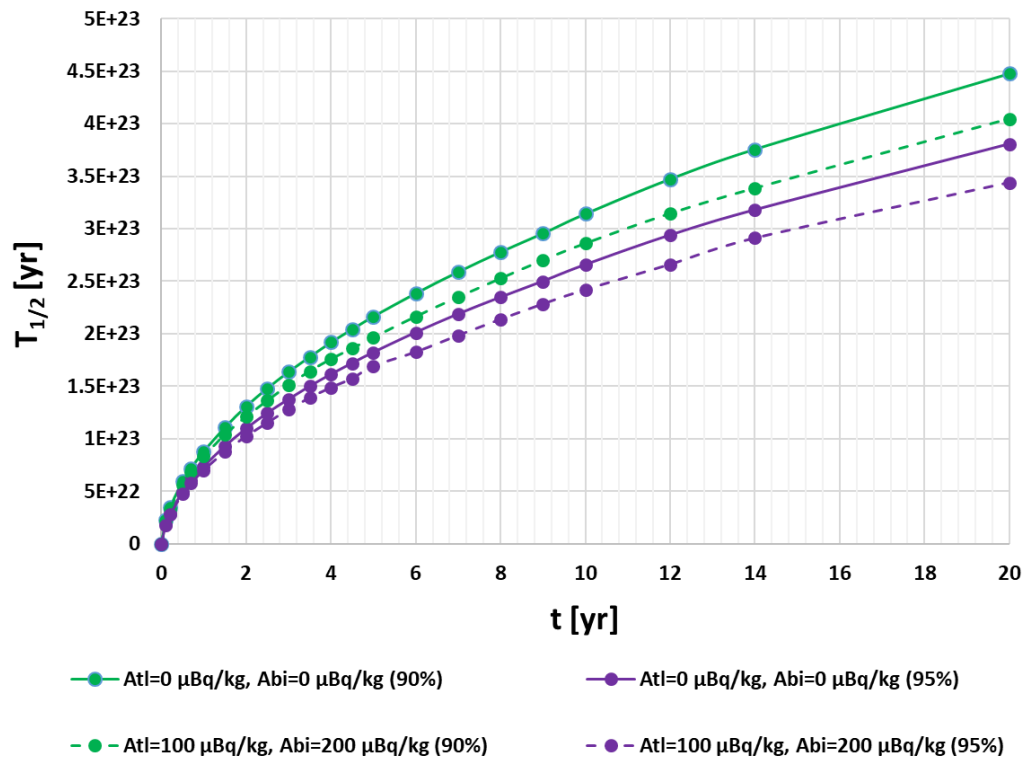
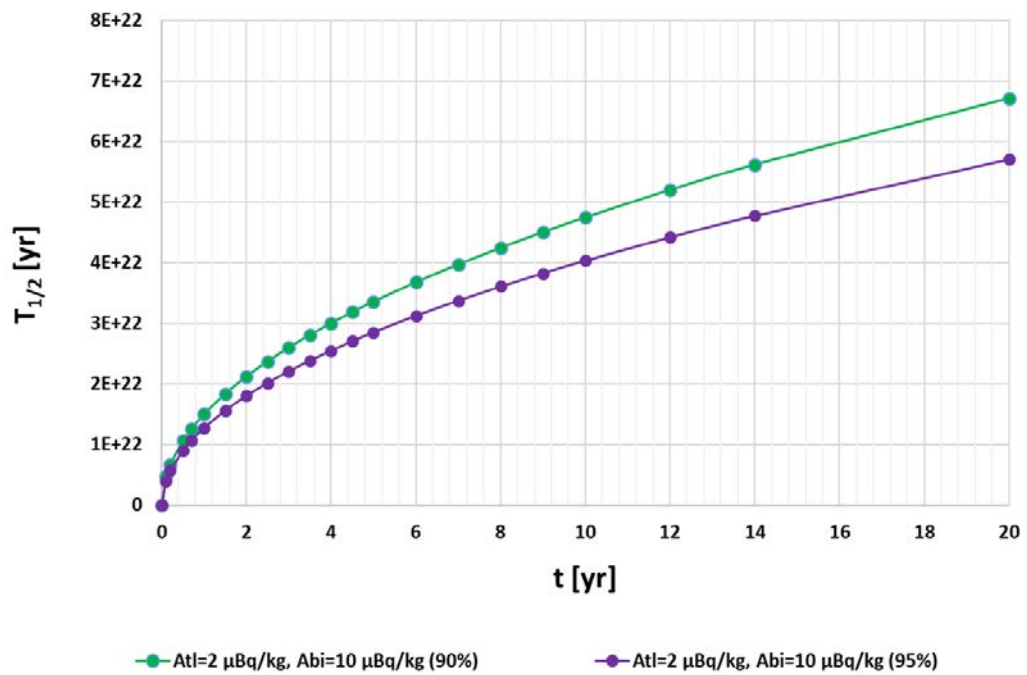


Figure 5.12: Plots of half life limits calculated for different exposures confidence levels and Bi and TI background activities. Half life limits calculated for  $0\nu\beta\beta\chi^0$ .



(a)  $0\nu\beta\beta\chi^0$



(b)  $0\nu\beta\beta\chi^0\chi^0$

Figure 5.13: Plots of half life limit as a function of SuperNEMO measurement time for the worst case scenario and ideal case scenario on two different confidence levels.

developed, solving the problems with classical method. The algorithm of Feldman-Cousins was discussed in detail and subsequently applied for calculations of  $0\nu\beta\beta\chi^0$  and  $0\nu\beta\beta\chi^0\chi^0$ .

In second part of the chapter, I have shown a methodology to estimate detection efficiencies and signal-to-background ratios using simulation in Falaise (software package for simulations of SuperNEMO module). The results led to choice of energy interval (2600 keV, 2700 keV) as a ROI with best signal-to-background ratio for both  $0\nu\beta\beta\chi^0$  and  $0\nu\beta\beta\chi^0\chi^0$ . Expected sensitivities were calculated for both processes for different exposures, background activities of Tl and Bi and different CL. Results presented in Figures 5.12 and 5.13 have shown that major improvement of half life limit for both the processes can be expected already after few months even in the worst case scenario.

# Conclusions

Proof of existence of  $0\nu\beta\beta$  decay would without doubt represent very important sought step beyond the physics of Standard Model. Such a discovery would also represent a large development in nuclear theory, especially in calculation of nuclear matrix elements. Period of 2020-2030 will be a decade of astonishing ton scale experiments in the field of  $0\nu\beta\beta$ . It gives a possibility to probe its half-life up to  $10^{28}$  years and effective neutrino mass down to few meV in dependence on the nuclear matrix elements calculations.

Presented thesis contributed to these efforts by variety of different results. At the end of 2016, it was possible to finish construction of main calorimeters in LSM with my contribution to the assembly process and quality testing of optical modules.

Mapping measurements of  $^{207}\text{Bi}$  calibration sources helped to reject the possibility of the accidental deposition of  $^{207}\text{Bi}$  outside of the mylar foil, on the copper source frame. The copper frame in such case would be an obstacle for the electrons on their flight to the calorimeter in calibration. Frame would reduce their energy which would lead to imprecisions in energy calibration. All controlled sources were from this point of view without problems. Thanks to the study, it was also possible to choose sources with the  $^{207}\text{Bi}$  droplet deposited very close (within one millimeter) from the center of the frame. Furthermore, the precise knowledge of exact source positions (along with the introduction of positioning conventions) serves as an input for precise simulations of calibration system. On the other side, the relative activity measurements helped to rank the sources and subsequently distribute them in the demonstrator in order to optimize homogeneity of exposure of the calorimetric walls during calibration. Absolute activity measurements provide information helpful for decision on duration of calibration. What is the most important, in NEMO-3 the activities of calibration sources were known with a 5% precision. This uncertainty is the main contributor to the final uncertainty on the half-life of  $2\nu\beta\beta$ . After the refinement of uncertainties presented in the chapter about activity measurements, the uncertainty of half-life of  $2\nu\beta\beta$  could be reduced not only for future SuperNEMO results but after recalculation also for results given by NEMO-3, because the sources were used for its calibration.

Studies of neutron shielding represent twofold contribution. Firstly, it is a first estimation of the quality of shielding in design phase. It was possible to conclude that the polyethylene is a material of preference. Furthermore, it was shown that the parts of detector made of Iron will represent the major contribution to all the gamma radiation produced by neutron capture inside of the shielding. Software for all these tasks was developed and is routinely used. Secondly, the presented neutron simulations contributed to more general question of neutron generators. Problem of the proper generation of gammas from thermal neutron capture was addressed and demonstrated. Theoretical basis for new approach to generation of neutron



captures was presented and demonstrated on illustrative example.

Within the discussion of half-life limits of  $0\nu\beta\beta$  mode with Majoron emission I took opportunity to present the famous Feldman-Cousins method in detail and discussed the reasons why it was introduced. The best ROI for observation of both types of  $0\nu\beta\beta$  with Majoron emission (with one and also two Majorons) was shown to be (2600 keV, 2700 keV) in the case when the decay would be observed. In case SuperNEMO demonstrator would not observe the decay, it was shown, that limits on both the decay channels obtained by NEMO-3 could be improved within few months or less. Within up to 5 years of measurement one can expect the improvement of both results by at least one order of magnitude.

After several years of preparation, next year, 2019, SuperNEMO demonstrator enters the well deserved phase of data taking. No one can predict whether the  $0\nu\beta\beta$  will be observed or not, but finally, it is clear that SuperNEMO detector will once again push the limits of our knowledge closer to new discoveries. After all, who knows what will be the next big discovery in neutrino physics?

# Complete Results of Measurements of $^{207}\text{Bi}$ Calibration Sources

This appendix contains full database of all the results obtained in measurements of  $^{207}\text{Bi}$  calibration sources in Chapter 3.

## A.1 Mapping Results

In this section, I present statistics (Tables A.1 and A.2) and the final measured quantities (Tables A.3 and A.4) obtained by source mapping by pixel detectors. All the necessary information concerning the measurements and analysis can be found in Section 3.2.

M.	Detector	$t_{live}$ [s]	$N_{ROI}$ [cnts]	$N_{TOT}$ [cnts]	$\frac{N_{ROI}}{N_{TOT}}$ [%]	$\frac{N_{ROI}}{t_{live}}$ [Hz]	$\frac{E_{ROI}}{t_{live}}$ [keV / s]
73	H04-W0163	5 994	49 656	114 585	43.34	8.28	92.88
74	H11-W0163	6 384	53 527	123 395	43.38	8.38	101.28
75	L05-W0163	6 392	81 876	161 538	50.69	12.81	143.86
76	H04-W0163	5 894	46 150	104 733	44.06	7.83	87.35
77	H11-W0163	5 852	51 400	118 735	43.29	8.78	106.09
78	L05-W0163	5 837	68 141	134 683	50.59	11.67	130.98
79	H04-W0163	6 074	50 034	115 418	43.35	8.24	91.72
80	H11-W0163	6 047	53 649	124 042	43.25	8.87	108.39
81	L05-W0163	6 045	76 828	151 907	50.58	12.71	142.19
82	H04-W0163	13 848	118 802	276 970	42.89	8.58	97.38
83	H11-W0163	5 836	48 506	113 138	42.87	8.31	102.19
84	L05-W0163	5 835	75 618	150 765	50.16	12.96	145.45
85	H04-W0163	6 531	55 041	126 510	43.51	8.43	95.21
86	H11-W0163	6 430	53 571	125 558	42.67	8.33	101.54
87	L05-W0163	6 427	78 772	154 925	50.85	12.26	138.21
88	H04-W0163	6 912	60 879	139 663	43.59	8.81	99.39
89	H11-W0163	6 745	59 920	141 226	42.43	8.88	109.31

Table A.1: See caption of Table A.2.

M.	Detector	$t_{live}$ [s]	$N_{ROI}$ [cnts]	$N_{TOT}$ [cnts]	$\frac{N_{ROI}}{N_{TOT}}$ [%]	$\frac{N_{ROI}}{t_{live}}$ [Hz]	$\frac{E_{ROI}}{t_{live}}$ [keV / s]
90	L05-W0163	6 774	80 838	158 929	50.86	11.93	134.37
91	H04-W0163	5 540	48 098	111 111	43.29	8.68	98.68
92	H11-W0163	5 425	48 289	113 016	42.73	8.90	109.29
93	L05-W0163	5 410	65 486	129 454	50.59	12.10	135.48
94	H04-W0163	2 874	26 003	59 589	43.64	9.05	101.37
95	H11-W0163	2 809	24 183	55 942	43.23	8.61	104.32
96	L05-W0163	2 822	34 871	68 967	50.56	12.36	139.01
111	H11-W0163	13 813	125 124	288 873	43.31	9.06	110.18
112	H11-W0163	5 602	46 438	106 760	43.50	8.29	100.79
113	L05-W0163	5 605	68 085	135 183	50.37	12.15	135.97
114	H04-W0163	7 622	68 413	158 181	43.25	8.98	100.87
115	H11-W0163	7 525	71 050	163 248	43.52	9.44	113.96
116	L05-W0163	7 539	92 141	185 290	49.73	12.22	136.50
118	H04-W0163	45 816	414 630	957 375	43.31	9.05	101.76
119	H11-W0163	45 671	396 247	929 737	42.62	8.68	103.72
120	L05-W0163	45 669	552 206	1 095 402	50.41	12.09	134.99
121	H04-W0163	45 375	367 970	853 014	43.14	8.11	90.69
122	H11-W0163	44 766	404 234	941 025	42.96	9.03	111.26
123	L05-W0163	44 762	542 330	1 070 742	50.65	12.12	135.26
124	H04-W0163	43 554	390 466	904 988	43.15	8.97	101.72
125	H11-W0163	41 787	343 470	784 633	43.77	8.22	99.51
126	H04-W0163	199 776	1 474 716	3 428 264	43.02	7.38	82.38
126*	H04-W0163	166 317	1 290 921	3 038 524	42.49	7.76	86.55
127	L05-W0163	41 480	500 823	982 522	50.97	12.07	135.98
128	H04-W0163	15 920	133 303	310 626	42.91	8.37	95.11
130	H11-W0163	15 546	128 427	294 117	43.67	8.26	100.12
131	L05-W0163	15 564	183 819	365 429	50.30	11.81	133.09
132	H11-W0163	197 260	1 719 104	3 955 332	43.46	8.71	104.58
132*	H11-W0163	165 699	1 440 205	3 324 424	43.32	8.69	104.86
133	H04-W0163	34 414	310 293	724 374	42.84	9.02	101.63
135	H11-W0163	37 880	333 898	763 859	43.71	8.81	105.33
137	L05-W0163	37 579	425 656	839 072	50.73	11.33	127.27
138	L05-W0163	13 224	159 769	318 364	50.18	12.08	137.11
139	L05-W0163	197 151	2 342 662	4 723 626	49.59	11.88	133.00
139*	L05-W0163	165 604	1 965 319	3 973 773	49.46	11.87	133.82

Table A.2: Statistics of all performed  $^{207}\text{Bi}$  deposition distribution measurements. M. in the first column stands for number of measured source.  $N_{ROI}$  stands for number of counts in ROI during measurement,  $N_{TOT}$  number of all measured counts and  $E_{ROI}$  represents energy integrated in ROI during the measurement. Rows with asterisk denote repeated measurement under same experimental conditions. Type of the source (with or without plastic envelope) can be extracted from second column of Tables A.3 and A.4.

M.	Position	$x_0$ [mm]	$y_0$ [mm]	HWHM [mm]	$x_0 - C_X$ [mm]	$y_0 - C_Y$ [mm]	$p_x$ [1]	$p_y$ [1]	r [mm]
73	US	5.31	4.56	2.06	0.12	0.41	0.03	0.06	0.42
74	US	5.79	4.09	2.18	0.60	-0.10	0.15	-0.02	0.61
75	US	5.19	4.85	1.83	-0.26	0.44	-0.06	0.07	0.51
76	US	5.35	4.31	2.51	0.16	0.15	0.04	0.02	0.22
77	US	5.03	4.74	2.01	-0.16	0.55	-0.04	0.08	0.57
78	US	5.66	4.71	2.11	0.21	0.29	0.05	0.05	0.36
79	US	5.03	5.39	2.14	-0.16	1.23	-0.04	0.19	1.24
80	US	5.42	4.27	2.21	0.22	0.08	0.06	0.01	0.24
81	US	5.49	4.19	1.90	0.04	-0.23	0.01	-0.03	0.23
82	US	4.75	4.72	2.26	-0.44	0.57	-0.11	0.09	0.72
83	US	5.47	4.23	2.48	0.27	0.04	0.07	0.01	0.28
84	US	5.79	5.00	1.85	0.34	0.58	0.09	0.09	0.67
85	US	5.49	4.41	2.23	0.30	0.25	0.08	0.04	0.39
86	US	5.04	4.72	2.15	-0.16	0.53	-0.04	0.08	0.56
87	US	5.54	4.79	1.92	0.09	0.37	0.02	0.06	0.38
88	US	5.78	4.38	2.19	0.59	0.23	0.15	0.03	0.63
89	US	5.36	5.00	2.11	0.17	0.81	0.04	0.12	0.82
90	US	4.95	4.57	1.88	-0.50	0.15	-0.13	0.02	0.53
91	US	5.28	4.42	2.13	0.09	0.26	0.02	0.04	0.28
92	US	5.36	4.88	2.14	0.16	0.69	0.04	0.11	0.71
93	US	4.94	4.99	1.97	-0.51	0.57	-0.13	0.09	0.76
94	US	4.84	4.78	2.15	-0.35	0.62	-0.09	0.10	0.71
95	US	5.14	4.31	2.09	-0.05	0.12	-0.01	0.02	0.13
96	US	5.28	4.29	1.89	-0.17	-0.13	-0.04	-0.02	0.21
111	WO-DU	4.61	6.97	2.09	0.37	0.25	0.09	0.04	0.44
112	WO-DU	4.67	6.74	2.09	0.43	0.03	0.11	0.00	0.43
113	WO-DU	4.80	6.95	1.79	0.28	0.00	0.07	0.00	0.28
114	WO-DU	4.73	6.97	2.03	0.49	0.29	0.12	0.04	0.57
115	WO-DU	4.73	6.84	2.21	0.49	0.12	0.12	0.02	0.51
116	WO-DU	4.59	7.14	1.62	0.07	0.19	0.02	0.03	0.20
118	WO-DU	5.05	6.84	2.05	0.81	0.15	0.20	0.02	0.82
119	WO-DU	3.45	7.22	1.71	-0.79	0.51	-0.20	0.08	0.93
120	WO-DU	4.52	7.36	1.79	0.00	0.41	0.00	0.06	0.41
121	WO-DU	4.84	7.54	2.07	0.60	0.85	0.15	0.13	1.04
122	WO-DU	4.37	7.55	2.09	0.13	0.83	0.03	0.13	0.84
123	WO-DU	4.72	7.42	1.80	0.20	0.47	0.05	0.07	0.51
124	WO-DU	5.14	7.48	2.06	0.90	0.79	0.22	0.12	1.20
125	WO-DU	4.48	7.57	2.06	0.24	0.85	0.06	0.13	0.89
126	WO-DU	3.02	6.79	2.44	-1.22	0.11	-0.31	0.02	1.23
126*	WO-DU	3.00	7.01	2.14	-1.24	0.33	-0.31	0.05	1.28
127	WO-DU	3.91	6.91	1.94	-0.61	-0.03	-0.15	-0.01	0.61
128	WO-DU	3.86	7.42	2.08	-0.39	0.73	-0.10	0.11	0.83
130	WO-DU	3.32	10.17	2.63	-0.91	3.45	-0.23	0.53	3.57

Table A.3: See caption of Table A.4.

M.	Position	$x_0$ [mm]	$y_0$ [mm]	HWHM [mm]	$x_0 - C_X$ [mm]	$y_0 - C_Y$ [mm]	$p_x$ [1]	$p_y$ [1]	r [mm]
131	WO-DU	4.08	6.81	1.85	-0.44	-0.14	-0.11	-0.02	0.46
132	WO-DU	3.99	7.29	1.96	-0.25	0.57	-0.06	0.09	0.62
132*	WO-DU	3.94	7.46	1.95	-0.29	0.74	-0.07	0.11	0.79
133	WO-DU	4.10	6.20	2.03	-0.14	-0.49	-0.04	-0.08	0.51
135	WO-DU	4.40	7.18	2.03	0.16	0.46	0.04	0.07	0.48
137	WO-DU	4.25	7.29	1.81	-0.27	0.35	-0.07	0.05	0.44
138	WO-DU	4.52	7.16	1.79	0.00	0.22	0.00	0.03	0.22
139	WO-DU	4.50	6.88	1.61	-0.02	-0.07	0.00	-0.01	0.07
139*	WO-DU	4.47	7.03	1.62	-0.05	0.08	-0.01	0.01	0.10

Table A.4: Results of all performed  $^{207}\text{Bi}$  deposition distribution measurements. M. in the first column stands for number of measured source. Next column represents the position of measurement defined in Figures 3.18 and 3.19. Based on the position it is possible to know of which type the source was (with or without plastic envelope). Following two columns show positions of source in the pixel detector coordinates. Column number five represents the characteristic droplet size. Finally, in rows six and seven one can find coordinates of dislocation vector followed by two dislocation parameters  $p_x$  and  $p_y$ . Last column shows the length of the dislocation vector. Its colour coding symbolizes source quality category (A, B or C) defined in Section 3.2.5. Rows with asterisk denote repeated measurement under same experimental conditions.

## A.2 Results of Activity Measurements

### A.2.1 Results of Relative Activity Measurements

Section contains all the results of relative activity measurements of  $^{207}\text{Bi}$  sources. Tables A.5 and A.6 represent relative activities of all sources which were measured with white plastic envelope while Tables A.7 and A.8 represent same results for the sources without the envelope. The tables use two different reference sources (84 for type w/ and 138 for type w/o). The comparison of absolute activities of sources 84 and 138 can be obtained from absolute activity measurements.

Type	No.	$t_{live}$ [s]	$N_{570}$ [cnts]	$\frac{\Delta N_{570}}{N_{570}}$ [%]	$N_{TOT}$ [cnts]	$\frac{N_{570}}{t_{live}}$ [ $s^{-1}$ ]	$\frac{N_{TOT}}{t_{live}}$ [ $s^{-1}$ ]	$A_{rel}$ [S84 = 1]
w/	84	7390	34053	0.154	338162	4.61	45.8	1.000
w/	81	7394	33621	0.110	333834	4.55	45.1	0.987
w/	75	7619	34533	0.081	341826	4.53	44.9	0.984
w/	96	7218	32405	0.104	319655	4.49	44.3	0.974
w/	94	7314	32603	0.116	324974	4.46	44.4	0.967
w/	88	7410	32533	0.136	324199	4.39	43.8	0.953
w/	82	7267	31586	0.120	314609	4.35	43.3	0.943
w/	80	7448	32294	0.120	322290	4.34	43.3	0.941

Table A.5: See caption of Table A.6.

Type	No.	$t_{live}$ [s]	$N_{570}$ [cnts]	$\frac{\Delta N_{570}}{N_{570}}$ [%]	$N_{TOT}$ [cnts]	$\frac{N_{570}}{t_{live}}$ [s <sup>-1</sup> ]	$\frac{N_{TOT}}{t_{live}}$ [s <sup>-1</sup> ]	$A_{rel}$ [S84 = 1]
w/	93	8196	35342	0.118	350392	4.31	42.8	<b>0.936</b>
w/	87	7428	31889	0.148	318155	4.29	42.8	<b>0.932</b>
w/	91	56102	240690	0.063	2404055	4.29	42.9	<b>0.931</b>
w/	92	7258	31101	0.116	309094	4.29	42.6	<b>0.930</b>
w/	95	7428	31526	0.108	315701	4.24	42.5	<b>0.921</b>
w/	89	7517	32112	0.112	319652	4.27	42.5	<b>0.927</b>
w/	83	7602	31889	0.084	318915	4.19	42.0	<b>0.910</b>
w/	85	7454	31254	0.119	310831	4.19	41.7	<b>0.910</b>
w/	90	7498	31355	0.096	314275	4.18	41.9	<b>0.908</b>
w/	77	8205	34297	0.088	339887	4.18	41.4	<b>0.907</b>
w/	79	7493	31115	0.092	308023	4.15	41.1	<b>0.901</b>
w/	86	7593	31213	0.092	309770	4.11	40.8	<b>0.892</b>
w/	74	7669	31449	0.098	312844	4.10	40.8	<b>0.890</b>
w/	78	7420	30316	0.094	301933	4.09	40.7	<b>0.887</b>
w/	134	7328	29909	0.103	298950	4.08	40.8	<b>0.886</b>
w/	76	7859	32030	0.124	319952	4.08	40.7	<b>0.884</b>
w/	136	7684	31052	0.105	310044	4.04	40.3	<b>0.877</b>
w/	73	7452	29897	0.090	298045	4.01	40.0	<b>0.871</b>

Table A.6: Results of relative activity measurements of all sources with plastic envelope. First two columns represent source type,  $t_{live}$  is a live measurement time,  $N_{570}$  stands for number of counts extracted from 570 keV peak and  $\Delta N_{570}/N_{570}$  is its relative uncertainty.  $N_{TOT}$  represents total number of counts in full spectrum. Finally,  $A_{rel}$  is relative activity of the source, where source number 84 (red letters) is reference for all the sources with plastic envelope. Yellow cell colour (source number) represents category of "golden" source, and gray represents "silver" source. Definition of "golden" and "silver" source is introduced in Section 3.3.1.1.

Type	No.	$t_{live}$ [s]	$N_{570}$ [cnts]	$\frac{\Delta N_{570}}{N_{570}}$ [%]	$N_{TOT}$ [cnts]	$\frac{N_{570}}{t_{live}}$ [s <sup>-1</sup> ]	$\frac{N_{TOT}}{t_{live}}$ [s <sup>-1</sup> ]	$A_{rel}$ [S138 = 1]
w/o	133	7586	33795	0.123	340533	4.45	44.9	<b>1.028</b>
w/o	114	7522	33219	0.094	330179	4.42	43.9	<b>1.019</b>
w/o	116	7372	32240	0.131	317808	4.37	43.1	<b>1.009</b>
w/o	115	7571	33050	0.107	330979	4.37	43.7	<b>1.007</b>
w/o	111	7726	33655	0.112	332957	4.36	43.1	<b>1.005</b>
w/o	138	7627	33068	0.089	327634	4.34	43.0	<b>1.000</b>
w/o	138*	3746	30289	0.575	-	8.09	-	<b>1.000</b>
w/o	120	7410	32046	0.095	318219	4.32	42.9	<b>0.997</b>
w/o	113	7348	31749	0.096	313164	4.32	42.6	<b>0.997</b>
w/o	135	7712	33105	0.101	327312	4.29	42.4	<b>0.990</b>
w/o	131	7817	33531	0.083	333485	4.29	42.7	<b>0.989</b>

Table A.7: See caption of Table A.8.

Type	No.	$t_{live}$ [s]	$N_{570}$ [cnts]	$\frac{\Delta N_{570}}{N_{570}}$ [%]	$N_{TOT}$ [cnts]	$\frac{N_{570}}{t_{live}}$ [s <sup>-1</sup> ]	$\frac{N_{TOT}}{t_{live}}$ [s <sup>-1</sup> ]	$A_{rel}$ [S138 = 1]
w/o	132*	3702	29501	0.582	-	7.97	-	<b>0.986</b>
w/o	123*	3644	28812	0.589	-	7.91	-	<b>0.978</b>
w/o	119	7414	31165	0.100	310274	4.20	41.8	<b>0.970</b>
w/o	139	81670	341677	0.064	3399944	4.18	41.6	<b>0.965</b>
w/o	137	7574	30538	0.085	301950	4.03	39.9	<b>0.930</b>
w/o	112	7386	29199	0.099	291560	3.95	39.5	<b>0.912</b>

Table A.8: Results of relative activity measurements of all sources without plastic envelope. All the measurements were done in CENBG except for three marked by asterisk. Meaning of all the columns and cell colours (yellow, gray) remains the same as in Table A.6. For all the sources without plastic envelope, source number 138 (red letters) is a reference. Measurement of source number 138 without asterisk serves as reference for all measurements performed in CENBG and the one with asterisk is reference for measurements done in LSM.

### A.2.2 Results of Absolute Activity Measurements

Tables A.9 and A.10 contain data of absolute activity measurements obtained in my analysis while Tables A.11 and A.12 contain results obtained in independent analysis by my colleague Frédéric Perrot. Graphical comparison of both results are presented in Section 3.3.2.

My results									
		570 keV				1064 keV			
No.	$t_{live}$ [s]	S [cnts]	$\Delta S$ [cnts]	A [Bq]	$\Delta A$ [Bq]	S [cnts]	$\Delta S$ [cnts]	A [Bq]	$\Delta A$ [Bq]
75	82855	116491	551	<b>141.0</b>	<b>0.68</b>	57019	335	<b>136.9</b>	<b>1.52</b>
76	166203	218103	1051	<b>131.6</b>	<b>0.65</b>	104795	566	<b>125.5</b>	<b>1.36</b>
80	82911	113954	539	<b>137.8</b>	<b>0.67</b>	54700	367	<b>131.3</b>	<b>1.52</b>
81	83144	118993	534	<b>143.5</b>	<b>0.66</b>	57223	321	<b>136.9</b>	<b>1.50</b>
82	82765	114450	580	<b>138.7</b>	<b>0.72</b>	55765	367	<b>134.1</b>	<b>1.54</b>
84	83130	117165	544	<b>141.3</b>	<b>0.67</b>	55572	328	<b>133.0</b>	<b>1.48</b>
87	83145	112393	522	<b>135.6</b>	<b>0.65</b>	54247	343	<b>129.8</b>	<b>1.47</b>
88	83147	114116	517	<b>137.6</b>	<b>0.64</b>	54440	286	<b>130.3</b>	<b>1.40</b>
89	83137	111141	506	<b>134.1</b>	<b>0.63</b>	53767	307	<b>128.7</b>	<b>1.42</b>
91	83139	110327	502	<b>133.1</b>	<b>0.62</b>	52990	310	<b>126.8</b>	<b>1.40</b>
92	83142	110803	516	<b>133.6</b>	<b>0.64</b>	53104	292	<b>127.1</b>	<b>1.38</b>
93	83134	113476	549	<b>136.9</b>	<b>0.68</b>	54164	320	<b>129.6</b>	<b>1.44</b>
94	83105	117105	546	<b>141.3</b>	<b>0.68</b>	55823	339	<b>133.7</b>	<b>1.50</b>
95	83105	110106	550	<b>132.9</b>	<b>0.68</b>	52758	334	<b>126.3</b>	<b>1.43</b>
96	83108	115202	567	<b>139.0</b>	<b>0.70</b>	55635	340	<b>133.2</b>	<b>1.49</b>
111	83106	109979	553	<b>132.7</b>	<b>0.68</b>	52740	311	<b>126.3</b>	<b>1.40</b>
113	83080	107195	527	<b>129.4</b>	<b>0.65</b>	51030	293	<b>122.2</b>	<b>1.35</b>
114	83036	110262	585	<b>133.2</b>	<b>0.72</b>	52661	275	<b>126.2</b>	<b>1.36</b>

Table A.9: See caption of Table A.10.

My results									
		570 keV				1064 keV			
No.	$t_{live}$ [s]	S [cnts]	$\Delta S$ [cnts]	A [Bq]	$\Delta A$ [Bq]	S [cnts]	$\Delta S$ [cnts]	A [Bq]	$\Delta A$ [Bq]
<b>115</b>	83025	110519	528	<b>133.5</b>	<b>0.65</b>	52438	285	<b>125.7</b>	<b>1.36</b>
<b>116</b>	83137	109065	526	<b>131.6</b>	<b>0.65</b>	52441	302	<b>125.5</b>	<b>1.38</b>
<b>120</b>	83120	108656	516	<b>131.1</b>	<b>0.64</b>	52456	304	<b>125.6</b>	<b>1.39</b>
<b>131</b>	83078	108195	543	<b>130.6</b>	<b>0.67</b>	51958	319	<b>124.4</b>	<b>1.40</b>
<b>133</b>	83118	114013	587	<b>137.6</b>	<b>0.72</b>	54398	302	<b>130.2</b>	<b>1.42</b>
<b>135</b>	83143	107808	570	<b>130.0</b>	<b>0.70</b>	52135	294	<b>124.8</b>	<b>1.37</b>
<b>138</b>	83110	110446	527	<b>133.3</b>	<b>0.65</b>	52788	323	<b>126.4</b>	<b>1.42</b>

Table A.10: Absolute activities of 25 measured calibration sources obtained in my own analysis. The table contains the source number, live time of the measurement, number of counts in peak (S) and activity (A) with their absolute uncertainties. Analysis was done for two gamma peaks (570 keV and 1064 keV) as explained in Section 3.3.2.

Frédéric's results									
		570 keV				1064 keV			
No.	$t_{live}$ [s]	S [cnts]	$\Delta S$ [cnts]	A [Bq]	$\Delta A$ [Bq]	S [cnts]	$\Delta S$ [cnts]	A [Bq]	$\Delta A$ [Bq]
<b>75</b>	82855	116973	392	<b>141.6</b>	<b>0.50</b>	56912	273	<b>136.7</b>	<b>1.44</b>
<b>76</b>	166203	217984	595	<b>131.5</b>	<b>0.39</b>	104958	385	<b>125.7</b>	<b>1.27</b>
<b>80</b>	82911	114237	389	<b>138.2</b>	<b>0.49</b>	54665	268	<b>131.2</b>	<b>1.39</b>
<b>81</b>	83144	118869	400	<b>143.4</b>	<b>0.51</b>	57396	275	<b>137.4</b>	<b>1.45</b>
<b>82</b>	82765	115025	390	<b>139.4</b>	<b>0.50</b>	55674	270	<b>133.9</b>	<b>1.42</b>
<b>84</b>	83130	117036	400	<b>141.2</b>	<b>0.51</b>	55797	272	<b>133.6</b>	<b>1.41</b>
<b>87</b>	83145	112259	392	<b>135.4</b>	<b>0.50</b>	54403	270	<b>130.2</b>	<b>1.38</b>
<b>88</b>	83147	114001	393	<b>137.5</b>	<b>0.50</b>	54516	269	<b>130.5</b>	<b>1.38</b>
<b>89</b>	83137	110980	388	<b>133.9</b>	<b>0.49</b>	53735	268	<b>128.6</b>	<b>1.37</b>
<b>91</b>	83139	110137	387	<b>132.8</b>	<b>0.49</b>	53161	267	<b>127.2</b>	<b>1.36</b>
<b>92</b>	83142	110664	389	<b>133.5</b>	<b>0.49</b>	53168	266	<b>127.2</b>	<b>1.35</b>
<b>93</b>	83134	113311	393	<b>136.7</b>	<b>0.50</b>	54374	269	<b>130.1</b>	<b>1.38</b>
<b>94</b>	83105	116793	399	<b>140.9</b>	<b>0.51</b>	55933	273	<b>133.9</b>	<b>1.42</b>
<b>95</b>	83105	110280	391	<b>133.1</b>	<b>0.49</b>	53005	268	<b>126.9</b>	<b>1.35</b>
<b>96</b>	83108	115313	397	<b>139.1</b>	<b>0.50</b>	55812	273	<b>133.6</b>	<b>1.42</b>
<b>111</b>	83106	110147	389	<b>132.9</b>	<b>0.49</b>	52900	267	<b>126.7</b>	<b>1.35</b>
<b>113</b>	83080	107304	418	<b>129.5</b>	<b>0.52</b>	51134	270	<b>122.5</b>	<b>1.32</b>
<b>114</b>	83036	110350	425	<b>133.3</b>	<b>0.53</b>	52596	272	<b>126.0</b>	<b>1.35</b>
<b>115</b>	83025	110288	426	<b>133.2</b>	<b>0.53</b>	52442	272	<b>125.7</b>	<b>1.35</b>
<b>116</b>	83137	108912	416	<b>131.4</b>	<b>0.52</b>	52422	271	<b>125.5</b>	<b>1.35</b>
<b>120</b>	83120	108812	419	<b>131.3</b>	<b>0.53</b>	52320	272	<b>125.2</b>	<b>1.35</b>
<b>131</b>	83078	107957	417	<b>130.3</b>	<b>0.52</b>	51962	271	<b>124.5</b>	<b>1.34</b>

Table A.11: See caption of Table A.12.



<b>Frédéric's results</b>									
		<b>570 keV</b>				<b>1064 keV</b>			
<b>No.</b>	$t_{live}$ [s]	<b>S</b> [cnts]	$\Delta S$ [cnts]	<b>A</b> [Bq]	$\Delta A$ [Bq]	<b>S</b> [cnts]	$\Delta S$ [cnts]	<b>A</b> [Bq]	$\Delta A$ [Bq]
<b>133</b>	83118	113458	426	<b>136.9</b>	<b>0.54</b>	54269	276	<b>129.9</b>	<b>1.39</b>
<b>135</b>	83143	108053	420	<b>130.3</b>	<b>0.53</b>	52212	271	<b>125.0</b>	<b>1.34</b>
<b>138</b>	83110	110478	421	<b>133.3</b>	<b>0.53</b>	52832	273	<b>126.5</b>	<b>1.36</b>

Table A.12: Absolute activities of 25 measured calibration sources obtained in analysis of Frédéric Perrot. The table contains the source number, live time of the measurement, number of counts in peak (S) and activity (A) with their absolute uncertainties. Analysis was done for two gamma peaks (570 keV and 1064 keV) as explained in Section 3.3.2.

---

Appendix **B**

## Numerical Values of Half-Life Limits for $0\nu\beta\beta\chi^0$ and $0\nu\beta\beta\chi^0\chi^0$

The appendix is dedicated to all the half-life limit values calculated in Chapter 5. Values are plotted in Figures 5.12 and 5.13 in aforementioned chapter. Tables B.1 and B.2 contain all the half-life limits obtained for  $0\nu\beta\beta\chi^0$ . Colour of each cell represents the ROI for which the limit was obtained. The definition of colour coding is introduced in Table B.3.

<b>t = 0.5 yr</b>			<b><math>A_{Bi}</math> [<math>\mu\text{Bq/kg}</math>]</b>					
			<b>0</b>	<b>10</b>	<b>20</b>	<b>50</b>	<b>100</b>	<b>200</b>
<b>CL = 90%</b>	<b><math>A_{Tl}</math> [<math>\mu\text{Bq/kg}</math>]</b>	<b>0</b>	0.594	0.592	0.591	0.587	0.582	0.570
		<b>100</b>	0.589	0.587	0.586	0.583	0.577	0.567
<b>CL = 95%</b>		<b>0</b>	0.498	0.497	0.496	0.493	0.489	0.480
		<b>100</b>	0.494	0.493	0.492	0.489	0.485	0.476
<b>t = 1 yr</b>			<b><math>A_{Bi}</math> [<math>\mu\text{Bq/kg}</math>]</b>					
			<b>0</b>	<b>10</b>	<b>20</b>	<b>50</b>	<b>100</b>	<b>200</b>
<b>CL = 90%</b>	<b><math>A_{Tl}</math> [<math>\mu\text{Bq/kg}</math>]</b>	<b>0</b>	0.880	0.877	0.874	0.866	0.857	0.839
		<b>100</b>	0.867	0.866	0.864	0.858	0.849	0.833
<b>CL = 95%</b>		<b>0</b>	0.737	0.735	0.733	0.729	0.722	0.708
		<b>100</b>	0.730	0.729	0.727	0.723	0.716	0.702
<b>t = 2 yr</b>			<b><math>A_{Bi}</math> [<math>\mu\text{Bq/kg}</math>]</b>					
			<b>0</b>	<b>10</b>	<b>20</b>	<b>50</b>	<b>100</b>	<b>200</b>
<b>CL = 90%</b>	<b><math>A_{Tl}</math> [<math>\mu\text{Bq/kg}</math>]</b>	<b>0</b>	1.310	1.305	1.300	1.285	1.260	1.222
		<b>100</b>	1.281	1.276	1.271	1.256	1.236	1.212
<b>CL = 95%</b>		<b>0</b>	1.098	1.093	1.089	1.077	1.057	1.031
		<b>100</b>	1.073	1.070	1.066	1.054	1.043	1.024
<b>t = 5 yr</b>			<b><math>A_{Bi}</math> [<math>\mu\text{Bq/kg}</math>]</b>					
			<b>0</b>	<b>10</b>	<b>20</b>	<b>50</b>	<b>100</b>	<b>200</b>
<b>CL = 90%</b>	<b><math>A_{Tl}</math> [<math>\mu\text{Bq/kg}</math>]</b>	<b>0</b>	2.164	2.154	2.145	2.119	2.076	2.001
		<b>100</b>	2.115	2.107	2.099	2.075	2.036	1.965
<b>CL = 95%</b>		<b>0</b>	1.822	1.814	1.807	1.786	1.752	1.703
		<b>100</b>	1.781	1.774	1.767	1.747	1.734	1.692

Table B.1: See caption of Table B.2.

$t = 10$ yr			$A_{Bi} [\mu Bq/kg]$					
			0	10	20	50	100	200
CL = 90%	$A_{Tl} [\mu Bq/kg]$	0	3.141	3.129	3.117	3.082	3.024	2.916
		100	3.072	3.061	3.049	3.015	2.960	2.860
CL = 95%	$A_{Tl} [\mu Bq/kg]$	0	2.656	2.646	2.636	2.606	2.558	2.466
		100	2.598	2.588	2.579	2.550	2.504	2.419
$t = 15$ yr			$A_{Bi} [\mu Bq/kg]$					
			0	10	20	50	100	200
CL = 90%	$A_{Tl} [\mu Bq/kg]$	0	3.887	3.869	3.851	3.799	3.716	3.576
		100	3.808	3.791	3.774	3.724	3.644	3.507
CL = 95%	$A_{Tl} [\mu Bq/kg]$	0	3.287	3.272	3.257	3.214	3.144	3.102
		100	3.221	3.206	3.192	3.192	3.112	3.057

Table B.2: Half-life limits of  $0\nu\beta\beta\chi^0$  achievable by SuperNEMO as a function of Bi ( $A_{Bi}$ ) and Tl ( $A_{Tl}$ ) contamination, time of measurement ( $t$ ) and confidence level (CL). The ROI with the best half-life limit were varying, therefore, colour of the cell represents the ROI for given value. Colours are defined in Table B.3. Half-life limit values in table are expressed in  $10^{23}$  yr.

Color codes of the best ROI intervals		
(2500 keV, 2800 keV)	(2500 keV, 2900 keV)	(2400 keV, 2900 keV)
(2500 keV, 3000 keV)	(2400 keV, 3000 keV)	(2400 keV, 3100 keV)

Table B.3: Colour coding definition for intervals with the best obtained half-life limit. Each cell colour in Tables B.1 and B.2 represents different ROI for which the half-life limit was obtained.

ROI yielding the best half-life limit for  $0\nu\beta\beta\chi^0$  was always (1000 keV, 2900 keV) due to different spectral shape, shifted to low energies relatively to  $0\nu\beta\beta\chi^0$ . In this ROI, Bi and Tl contamination contributed negligibly (compared to dominating  $2\nu\beta\beta$ ) to the background and the resulting limits remained almost unchanged even for extreme values<sup>1</sup> of Bi and Tl contamination. Therefore, the calculation was performed only for scenario with the SuperNEMO design contamination limits of  $A_{Bi} = 10\mu Bq/kg$  and  $A_{Tl} = 2\mu Bq/kg$ . Resulting half-life limits are represented in Tables B.4, B.5 and B.6.

$t$ [yr]	0.1	0.2	0.5	0.7	1	1.5	2
CL = 90%	0.475	0.671	1.061	1.256	1.501	1.838	2.123
CL = 95%	0.403	0.570	0.902	1.067	1.275	1.562	1.804

Table B.4: See caption of Table B.6.

$t$ [yr]	2.5	3	3.5	4	4.5	5	6
CL = 90%	2.373	2.600	2.808	3.002	3.184	3.356	3.676
CL = 95%	2.017	2.209	2.386	2.551	2.706	2.852	3.124

Table B.5: See caption of Table B.6.

<sup>1</sup>Hundreds of times higher than SuperNEMO design values.

---

<b>t [yr]</b>	<b>7</b>	<b>8</b>	<b>9</b>	<b>10</b>	<b>12</b>	<b>14</b>	<b>20</b>
<b>CL = 90%</b>	3.971	4.245	4.503	4.746	5.199	5.616	6.712
<b>CL = 95%</b>	3.374	3.607	3.826	4.033	4.418	4.772	5.704

Table B.6: Half-life limits of  $0\nu\beta\beta\chi^0\chi^0$  achievable by SuperNEMO as a function of time of measurement (t) and confidence level (CL). The ROI with the best half-life limit was in each case (1000 keV, 2900 keV). Bi and Tl contaminations were set to  $A_{\text{Bi}} = 10\mu\text{Bq/kg}$  and  $A_{\text{Tl}} = 2\mu\text{Bq/kg}$  in the calculation. Half-life limit values in table are expressed in  $10^{22}$  yr.

# Bibliography

- [1] Becquerel, H., Comptes-rendus de l'Académie des sciences, séance du 24 février 1896 (in French) (1896) 420.
- [2] Becquerel, H., Comptes-rendus de l'Académie des sciences, séance du 1er mars 1896 (in French) (1896) 501.
- [3] Chadwick, J., Verhandlungen der Deutschen Physikalischen Gesellschaft (in German) (1914) 383.
- [4] and, Proceedings of the Royal Society of London A: Mathematical, Physical and Engineering Sciences **141** (1933) 502.
- [5] Pauli, W., letter to the nuclear conference in tuebingen on the 4-th of december, in *Pauli Archive at CERN.*, 1930.
- [6] Cowan, C. L., Reines, F., Harrison, F. B., Kruse, H. W., and McGuire, A. D., *Science* **124** (1956) 103.
- [7] Wang, K. C., *Phys. Rev.* **61** (1942) 97.
- [8] Glashow, S. L., *Nuclear Physics* **22** (1961) 579 .
- [9] Englert, F. and Brout, R., *Phys. Rev. Lett.* **13** (1964) 321.
- [10] Higgs, P. W., *Phys. Rev. Lett.* **13** (1964) 508.
- [11] Guralnik, G. S., Hagen, C. R., and Kibble, T. W. B., *Phys. Rev. Lett.* **13** (1964) 585.
- [12] Weinberg, S., *Phys. Rev. Lett.* **19** (1967) 1264.
- [13] Salam, A. and Svartholm, N., *Elementary particle theory: Relativistic groups and analyticity. Proceedings of the Eighth Nobel Symposium held May 19-25, 1968 at Aspenäs garden, Lerum, in the county of Älvsborg, Sweden*, Nobel symposium, Almqvist & Wiksell, 1968.
- [14] Abe, F. et al., *Phys. Rev. Lett.* **74** (1995) 2626.
- [15] Abachi, S. et al., *Phys. Rev. Lett.* **74** (1995) 2422.
- [16] Kodama, K. et al., *Physics Letters B* **504** (2001) 218 .
- [17] Aad, G. et al., *Physics Letters B* **716** (2012) 1 .

- [18] Chatrchyan, S. et al., *Physics Letters B* **716** (2012) 30 .
- [19] Ahmad, Q. R. et al., *Phys. Rev. Lett.* **87** (2001) 071301.
- [20] Danby, G. et al., *Phys. Rev. Lett.* **9** (1962) 36.
- [21] Anicin, I. V., *ArXiv Physics e-prints* (2005).
- [22] Perl, M. L. et al., *Phys. Rev. Lett.* **35** (1975) 1489.
- [23] Aartsen, M. G. et al., *Phys. Rev. Lett.* **117** (2016) 071801.
- [24] Katz, U. and Spiering, C., *Progress in Particle and Nuclear Physics* **67** (2012) 651 .
- [25] Salaris, M. and Cassisi, S., *Evolution of Stars and Stellar Populations*, Wiley, 2005.
- [26] Cleveland, B. T. et al., *The Astrophysical Journal* **496** (1998) 505.
- [27] Inoue, K., *Nuclear Physics B - Proceedings Supplements* **59** (1997) 267 , *Proceedings of the Fourth KEK Topical Conference on Flavor Physics*.
- [28] Abdurashitov, J. N. et al., *Phys. Rev. C* **80** (2009) 015807.
- [29] Cribier, M. et al., *Nuclear Physics B - Proceedings Supplements* **70** (1999) 284 , *Proceedings of the Fifth International Workshop on topics in Astroparticle and Underground Physics*.
- [30] Gribov, V. and Pontecorvo, B., *Physics Letters B* **28** (1969) 493 .
- [31] Pontecorvo, B., *Sov. Phys. JETP* **7** (1958) 172, [*Zh. Eksp. Teor. Fiz.*34,247(1957)].
- [32] Maki, Z., Nakagawa, M., and Sakata, S., *Progress of Theoretical Physics* **28** (1962) 870.
- [33] Fukuda, Y. et al., *Phys. Rev. Lett.* **81** (1998) 1562.
- [34] Mikheyev, S. P. and Smirnov, A. Y., *Yadernaya Fizika* **42** (1985) 1441.
- [35] West, R. M., Lauberts, A., Jorgensen, H. E., and Schuster, H. E., *Astronomy and Astrophysics* **177** (1987) L1.
- [36] Podsiadlowski, P., *Publications of the Astronomical Society of the Pacific* **104** (1992) 717.
- [37] Hirata, K. et al., *Phys. Rev. Lett.* **58** (1987) 1490.
- [38] Haines, T. et al., *Nuclear Instruments and Methods in Physics Research Section A: Accelerators, Spectrometers, Detectors and Associated Equipment* **264** (1988) 28 .
- [39] Alexeyev, E., Alexeyeva, L., Krivosheina, I., and Volchenko, V., *Physics Letters B* **205** (1988) 209 .
- [40] Arnett, W. D., Bahcall, J. N., Kirshner, R. P., and Woosley, S. E., *Annual Review of Astronomy and Astrophysics* **27** (1989) 629.

- 
- [41] Bilenky, S. M., Giunti, C., and Grimus, W., *The European Physical Journal C* **1** (1998) 247.
- [42] Goeppert-Mayer, M., *Phys. Rev.* **48** (1935) 512.
- [43] Barabash, A., *Physics Procedia* **74** (2015) 416 , *Fundamental Research in Particle Physics and Cosmophysics*.
- [44] Center, N. N. D., (2017).
- [45] Furry, W. H., *Phys. Rev.* **56** (1939) 1184.
- [46] Agostini, M. et al., *Phys. Rev. Lett.* **111** (2013) 122503.
- [47] Arnold, R. et al., *Phys. Rev. D* **92** (2015) 072011.
- [48] Domizio, S. D. and the Cuoricino collaboration, *Journal of Physics: Conference Series* **375** (2012) 042014.
- [49] Gando, A. et al., *Phys. Rev. Lett.* **110** (2013) 062502.
- [50] Caurier, E., Zuker, A. P., Poves, A., and Martínez-Pinedo, G., *Phys. Rev. C* **50** (1994) 225.
- [51] Macko, M., QRPA with Nonlinear Phonon Operator: Can It Work?, Master's thesis, Comenius University in Bratislava, 2015.
- [52] Yao, J. M., Song, L. S., Hagino, K., Ring, P., and Meng, J., *Phys. Rev. C* **91** (2015) 024316.
- [53] Klapdor-Kleingrothaus, H. et al., *The European Physical Journal A - Hadrons and Nuclei* **12** (2001) 147.
- [54] Aalseth, C. E. et al., *Phys. Rev. D* **65** (2002) 092007.
- [55] Klapdor-Kleingrothaus, H., Krivosheina, I., Dietz, A., and Chkvorets, O., *Physics Letters B* **586** (2004) 198 .
- [56] Andreotti, E. et al., *Astroparticle Physics* **34** (2011) 822 .
- [57] Sisti, M. et al., *Nuclear and Particle Physics Proceedings* **273–275** (2016) 1719 , 37th International Conference on High Energy Physics (ICHEP).
- [58] Beeman, J. W. et al., *Adv. High Energy Phys.* **2013** (2013) 237973.
- [59] Albert, J. B. et al., *Nature* **510** (2014) 229.
- [60] Mott, J., *Search for double beta decay of  $^{82}\text{Se}$  with the NEMO-3 detector and development of apparatus for low-level radon measurements for the SuperNEMO experiment*, PhD thesis, University College London, 2013.
- [61] Dassie, D. et al., *Nuclear Instruments and Methods in Physics Research Section A: Accelerators, Spectrometers, Detectors and Associated Equipment* **309** (1991) 465 .
- [62] Arnold, R. et al., *Nuclear Instruments and Methods in Physics Research Section A: Accelerators, Spectrometers, Detectors and Associated Equipment* **354** (1995) 338 .
-

- [63] LAL preprints **94–29** (1994).
- [64] Arnold, R. et al., Nuclear Instruments and Methods in Physics Research Section A: Accelerators, Spectrometers, Detectors and Associated Equipment **536** (2005) 79 .
- [65] Arnold, R. et al., Phys. Rev. D **93** (2016) 112008.
- [66] Argyriades, J. et al., Nuclear Physics A **847** (2010) 168 .
- [67] Simard, L. and the Nemo-3 collaboration, Journal of Physics: Conference Series **375** (2012) 042011.
- [68] Arnold, R. et al., Nuclear Physics A **781** (2007) 209 .
- [69] Arnold, R. et al., Phys. Rev. D **95** (2017) 012007.
- [70] Arnold, R. et al., Phys. Rev. Lett. **107** (2011) 062504.
- [71] Argyriades, J. et al., Phys. Rev. C **80** (2009) 032501.
- [72] Arnold, R. et al., The European Physical Journal C **70** (2010) 927.
- [73] Blondel, S. et al., Conseil Scientifique de l'IN2P3 (2011).
- [74] Hodák, R. et al., Improvement of the energy resolution of the scintillating detectors for the low background measurement, in *American Institute of Physics Conference Series*, volume 1672 of *American Institute of Physics Conference Series*, page 130003, 2015.
- [75] Marquet, C. et al., Journal of Instrumentation **10** (2015) P09008.
- [76] Salazar, R. and Bryant, J., PoS **ICHEP2016** (2016) 808.
- [77] Jakubek, J., Journal of Instrumentation **4** (2009) P03013.
- [78] Platkevic, M. et al., Nuclear Instruments and Methods in Physics Research Section A: Accelerators, Spectrometers, Detectors and Associated Equipment **591** (2008) 245 , Radiation Imaging Detectors 2007.
- [79] Llopart, X., Ballabriga, R., Campbell, M., Tlustos, L., and Wong, W., Nuclear Instruments and Methods in Physics Research Section A: Accelerators, Spectrometers, Detectors and Associated Equipment **581** (2007) 485 , VCI 2007.
- [80] Ballabriga, R., Campbell, M., and Llopart, X., Nuclear Instruments and Methods in Physics Research Section A: Accelerators, Spectrometers, Detectors and Associated Equipment **878** (2018) 10 , Radiation Imaging Techniques and Applications.
- [81] Turecek, D., Jakubek, J., Kroupa, M., and Soukup, P., Energy calibration of pixel detector working in time-over-threshold mode using test pulses, in *2011 IEEE Nuclear Science Symposium Conference Record*, pages 1722–1725, 2011.
- [82] Jakubek, J., Nuclear Instruments and Methods in Physics Research Section A: Accelerators, Spectrometers, Detectors and Associated Equipment **607** (2009) 192 , Radiation Imaging Detectors 2008.



- 
- [83] Jakubek, J., Nuclear Instruments and Methods in Physics Research Section A: Accelerators, Spectrometers, Detectors and Associated Equipment **633** (2011) S262 , 11th International Workshop on Radiation Imaging Detectors (IWORID).
- [84] Turecek, D., Holy, T., Jakubek, J., Pospisil, S., and Vykydal, Z., Journal of Instrumentation **6** (2011) C01046.
- [85] Holy, T. et al., Nuclear Instruments and Methods in Physics Research Section A: Accelerators, Spectrometers, Detectors and Associated Equipment **591** (2008) 287 , Radiation Imaging Detectors 2007.
- [86] IAEA, Live chart of nuclides, <https://www-nds.iaea.org/relnsd/vcharthtml/VChartHTML.html>.
- [87] Blank, B. et al., Nuclear Instruments and Methods in Physics Research Section A: Accelerators, Spectrometers, Detectors and Associated Equipment **776** (2015) 34 .
- [88] INTERNATIONAL ATOMIC ENERGY AGENCY, *Update of X Ray and Gamma Ray Decay Data Standards for Detector Calibration and Other Applications*, INTERNATIONAL ATOMIC ENERGY AGENCY, Vienna, 2007.
- [89] Chazal, V. et al., Astroparticle Physics **9** (1998) 163 .
- [90] Agostinelli, S. et al., Nuclear Instruments and Methods in Physics Research Section A: Accelerators, Spectrometers, Detectors and Associated Equipment **506** (2003) 250 .
- [91] Allison, J. et al., IEEE Transactions on Nuclear Science **53** (2006) 270.
- [92] Allison, J. et al., Nuclear Instruments and Methods in Physics Research Section A: Accelerators, Spectrometers, Detectors and Associated Equipment **835** (2016) 186 .
- [93] Junde, H., Nuclear Data Sheets **109** (2008) 787 .
- [94] Bhat, M., Nuclear Data Sheets **85** (1998) 415 .
- [95] Singh, B., Nuclear Data Sheets **108** (2007) 197 .
- [96] Browne, E. and Tuli, J., Nuclear Data Sheets **111** (2010) 1093 .
- [97] Berezinsky, V. and Valle, J. W. F., Physics Letters B **318** (1993) 360.
- [98] Dolgov, A. D. and Takahashi, F., ArXiv High Energy Physics - Phenomenology e-prints (2004).
- [99] Kazanas, D., Mohapatra, R. N., Nasri, S., and Teplitz, V. L., Phys. Rev. D **70** (2004) 033015.
- [100] Kachelriess, M., Tomàs, R., and Valle, J. W. F., Phys. Rev. D **62** (2000) 023004.
- [101] Tomàs, R., Päs, H., and Valle, J. W. F., Phys. Rev. D **64** (2001) 095005.
- [102] Hannestad, S., Keränen, P., and Sannino, F., Phys. Rev. D **66** (2002) 045002.
- [103] Farzan, Y., Phys. Rev. D **67** (2003) 073015.
-

- [104] Arnold, R. et al., Nuclear Physics A **765** (2006) 483.
- [105] Gómez-Cadenas, J. et al., Journal of Cosmology and Astroparticle Physics **2011** (2011) 007.
- [106] Philosophical Transactions of the Royal Society of London A: Mathematical, Physical and Engineering Sciences **236** (1937) 333.
- [107] Feldman, G. J. and Cousins, R. D., Phys. Rev. D **57** (1998) 3873.
- [108] Barabash, A. S., ArXiv e-prints (2017).
- [109] Azzolini, O. et al., Phys. Rev. Lett. **120** (2018) 232502.
- [110] Macko, M., Acta Phys. Polon. Supp. **9** (2016) 797.
- [111] Brun, R. and Rademakers, F., Nuclear Instruments and Methods in Physics Research Section A: Accelerators, Spectrometers, Detectors and Associated Equipment **389** (1997) 81 , New Computing Techniques in Physics Research V.

Place for your notes